galaxies

Special Issue Reprint

Stellar Spectroscopy, Molecular Astronomy and Atomic Astronomy

Edited by
Fan Liu

mdpi.com/journal/galaxies

MDPI

Stellar Spectroscopy, Molecular Astronomy and Atomic Astronomy

Stellar Spectroscopy, Molecular Astronomy and Atomic Astronomy

Guest Editor

Fan Liu

MDPI

Basel • Beijing • Wuhan • Barcelona • Belgrade • Novi Sad • Cluj • Manchester

Guest Editor
Fan Liu
School of Physics and
Astronomy
Monash University
Melbourne
Australia

Editorial Office
MDPI AG
Grosspeteranlage 5
4052 Basel, Switzerland

This is a reprint of the Special Issue, published open access by the journal *Galaxies* (ISSN 2075-4434), freely accessible at: https://www.mdpi.com/journal/galaxies/special_issues/SWLO44T4B4.

For citation purposes, cite each article independently as indicated on the article page online and as indicated below:

Lastname, A.A.; Lastname, B.B. Article Title. *Journal Name* **Year**, *Volume Number*, Page Range.

ISBN 978-3-7258-8117-8 (Hbk)
ISBN 978-3-7258-8118-5 (PDF)
https://doi.org/10.3390/books978-3-7258-8118-5

Contents

About the Editor

Fan Liu

Fan Liu, School of Physics and Astronomy, Monash University, Australia; National Astronomical Observatories, CAS, China. My studies focus on high-precision stellar spectroscopy. I am searching for chemical signatures of planet formation and engulfment in field and open cluster stars using high quality spectra from large telescopes such as Keck, VLT, Gemini and Magellan. I am also interested in binary stars, thin/thick disc stars, Galactic chemical evolution and Galactic archeology.

galaxies

MDPI

Article

LAMOST Spectroscopy and Gaia Photo-Astrometry for an Interstellar Extinction Study

Oleg Malkov *, Aleksandra Avdeeva and Dana Kovaleva

Institute of Astronomy of RAS, Moscow 119017, Russia; volosatykh.as14@physics.msu.ru (A.A.); dana@inasan.ru (D.K.)

* Correspondence: malkov@inasan.ru; Tel.: +7-495-951-7993

Abstract: The aim of this work is to establish the present accuracy and convergence of available estimates of galactic extinction. We determine the galactic interstellar extinction in selected high-latitude areas of the sky based on Gaia DR3 astrometry and photometry and spectroscopic data from the LAMOST survey. For this purpose, we choose 42 northern high-latitude sky areas surrounding supernovae that allowed establishing the accelerated expansion of the universe. We compare our results with the estimates accepted in that paper and find that they agree well, within observational errors. Simultaneously, the estimates for galactic extinction by other authors along the same sightlines show systematic differences, which can cause the distance to the extragalactic object to change by ±3–5%.

Keywords: interstellar extinction; surveys

1. Introduction

Dust produced by the nuclear burning of stars scatters and absorbs light according to the dust-reddening law. Consequently, mapping the dust is one of the central problems in astronomy. In previous works, various models have been proposed to describe interstellar extinction. The first one, developed by [1], considers a barometric (exponential) function:

$$A_V(b,d) = \frac{a_0 \cdot \beta}{sin|b|} \cdot \left(1 - exp\left(\frac{-d \cdot sin|b|}{\beta}\right)\right). \quad (1)$$

It represents the classical model of a homogeneous, semi-infinite absorbing layer with a density exponentially distributed with height. Here b and d are galactic latitude and distance from the observer to the star. The parameter β is the scale height, and a_0 is the extinction per unit length in the Galactic plane. In the original model [1], a_0 and β were constants; however, in subsequent publications, they are treated as functions of galactic coordinates (l, b) or galactocentric coordinates (r, ϕ, z). Other models have been proposed in the works of [2–7] (hereafter G23). In addition, 3D maps of dust distribution in the galaxy have been developed and published by various authors: [8–12].

LAMOST stellar spectra can be used to independently test the reddening. Stellar spectra are a sensitive test of the reddening because the broadband photometry of a star is almost entirely determined by three parameters: gravity, metallicity, and effective temperature. These atmospheric parameters can be determined using only the line information in the spectra, allowing the intrinsic broadband colors of the star to be predicted independently of the observed colors of the star. However, dust between the observer and the star will bias the observed colors relative to the intrinsic colors. The difference between the predicted intrinsic and measured colors is a measurement of the reddening of the star.

The cosecant (barometric) law (1) was used in our previous work [13] to describe the variation of the interstellar extinction in the radial direction, like most of the models mentioned above, but the variations on the sphere were described using harmonic functions. In that work, we used Gaia EDR3 photometry [14] and spectroscopic parameters from LAMOST data [15,16]. Since LAMOST data only cover the Northern Celestial Hemisphere [13], lacks approximation points in the Southern sky, which reduces the reliability of the model in this region. In [17], we used the RAVE DR6 [18] data, which cover the southern sky, to conduct similar studies and improve the [13] model. We calculated the visual extinction in different high-latitude regions of the southern sky based on the temperatures of stars from RAVE DR6 and Gaia EDR3 photometry and astrometry [14]. We then estimated the parameters a_0 and β from Equation (1) for each of the selected regions. We approximated the parameters estimated in [17] together with those found in [13] using spherical harmonics across the entire sky.

Special attention is paid in the literature to a parameter called total galactic visual extinction, or galactic extinction, A_{gal}. It can be estimated from the galactic dust reddening for a sightline, assuming a standard extinction law. The reddening estimates were published by [19] who based their results on HI and galaxy counts, by [20] (hereafter SFD98), who combined results of IRAS and COBE/DIRBE, while [21] (hereafter SF11) provide new estimates of galactic dust extinction from an analysis of the Sloan Digital Sky Survey. A_{gal} plays an important role in the construction of the extragalactic distance scale, as it provides us with the extinction of extragalactic objects to make proper allowance for the dimming of the primary distance indicators in external galaxies by interstellar dust in our own galaxy. Galactic extinction can be derived from (1) under the assumption that $d \to \infty$:

$$A_{gal}(b) = \frac{a_0 \beta}{\sin|b|}. \tag{2}$$

The main goal of the present study is the development of software for the approximation of A_V(d)-relations for various areas in the sky, and its application to a set of selected areas. We assume that (1) satisfactorily reproduces the observed V-band interstellar extinction A_V for high galactic latitudes. Besides the a_0, β parameters, A_{gal} values (2) are determined for each area and compared with values published in the literature. Obviously, getting total extinction A_{gal} we are forced to ignore any inhomogeneities beyond the distance of the Gaia stars, such as the high latitude cirrus.

The paper is organized as follows: In Section 2, we describe the data that were used and calculate the visual extinction of objects at individual areas of the sky. In Section 3, we present the results of calculations and compare them with other publications. Finally, in Section 4, we draw our conclusions.

2. Data and Method

2.1. Observational Data

The present study used the stars contained in LAMOST DR5 [16] and Gaia DR3 [22] surveys for which the distances from Bailer-Jones catalogue [23] are presented. We selected all objects from LAMOST DR5 in 42 regions, each with a radius of 1.5 degrees, centered on the positions of 42 SNe Ia listed in Table 1 of [24]. These selected regions are plotted in Figure 1. We applied quality cuts to the LAMOST data by imposing SNRR > 30 AND SNRG > 30 conditions on the signal-to-noise ratio in the r and g bands accordingly. Next, we cross-matched the Gaia DR3 catalog using the XMatch service from CDS, with a matching radius of 1 arcsecond. Figure 2 shows the distribution of angular distances between matched objects, where the identification peak is observed at 0.1 arcseconds. The distances corresponding to the objects we selected from Gaia DR3 were obtained from [23].

The visual extinction A_V for each star has been computed using the following relation:

$$A_V = c_1/c_2 \times [(BP - RP)_0 - (BP - RP)]. \tag{3}$$

Here $c_2 \equiv A_G/A_V$, where A_G is the interstellar extinction in the Gaia G-band. Bono et al. [25] give 0.840 for c_2. We use the mean value of $c_1 \equiv A_G/E_{BP-RP}$ equal to 2.02. This value is calculated for a G2V star using the extinction curve by [26] with $R_V \equiv A_V/E_{B-V} = 3.1$. Passband characteristics were taken from [27].

Only MS-stars with Gaia (BP, RP) photometry were used for the analysis. Luminosity class was estimated from LAMOST atmospheric parameters: only stars with a gravity value of $\log g \geq 4$ were selected. Intrinsic color index $(BP - RP)_0$ for MS-stars was estimated from $T_{\rm eff}$(LAMOST) with Mamajek's relations http://www.pas.rochester.edu/~emamajek/EEM_dwarf_UBVIJHK_colors_Teff.txt (accessed on 16 October 2024), see also [28].

To mitigate potential inaccuracies in the following results, whether arising from distance errors or biases in photometry and spectroscopy, we conducted a consistency check. We calculated the absolute magnitudes of the stars using the reddening estimated in (3) and distances from [23]. We then compared these calculated absolute magnitudes with the values predicted by [28] for the corresponding effective temperatures. Objects showing a discrepancy greater than 0.1 mag were excluded from further analysis. As a result of this procedure, one of the 42 areas (SN 1997F) did not contain a sufficient number of stars, and we excluded this area from further study. Other areas each contain 22 to 284 stars with known d and A_V values, altogether 4960 stars.

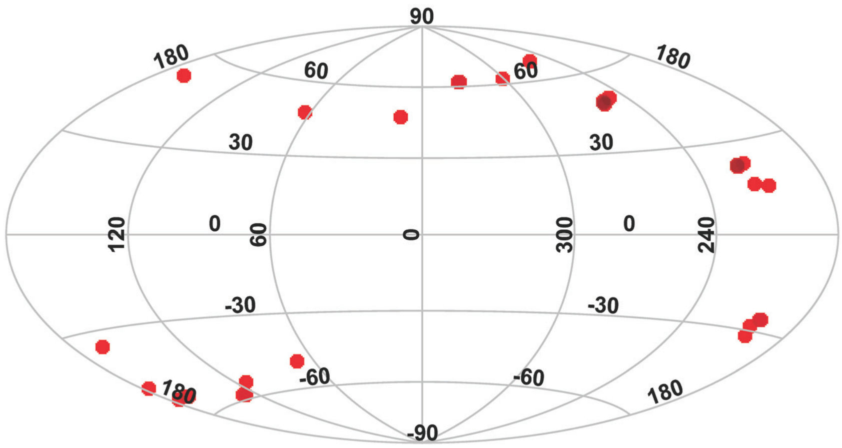

Figure 1. Selected areas. Galactic coordinates, Aitoff projection.

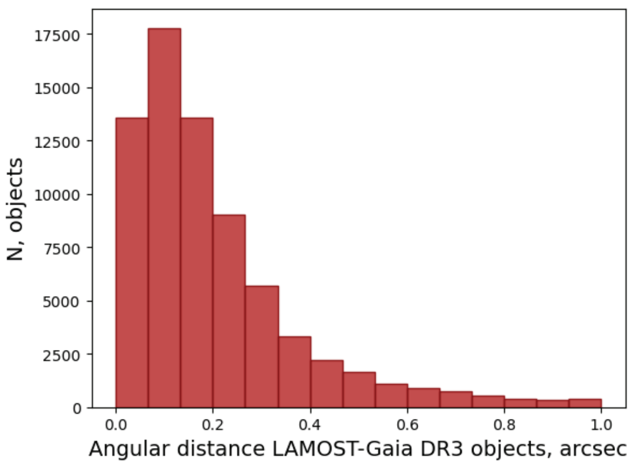

Figure 2. Angular distance between Gaia DR3 and LAMOST objects in the selected areas.

2.2. Estimation of Total Galactic Extinction

The process for obtaining the a_0 and β parameters is thoroughly explained in [13]. Here, we provide a brief overview, along with the modifications made for this specific task. The parameters were derived by minimizing the difference between the set of (d, A_V) values in each region and the function described in (1). The minimization was performed using the lmfit Python package [29]. An example of the results of a_0 and β determination for three selected regions is shown in Figure 3; the red line if the function (1) calculated with obtained a_0 and β. We are primarily interested in the result at large distances, so we can ignore some discrepancy for nearby stars.

As noted in [13], degeneracy often arises during the calculation of a_0 and β. However, A_{gal} is typically well-defined and not subject to such degeneracy. For the purposes of this study, we derived A_{gal} and β instead of a_0 and β, which allows for a more accurate determination of the total Galactic extinction. The results of the approximation are presented in Table 1.

Table 1. Galactic extinction.

No	SN	l	b	N	A_{gal}	σA_{gal}	A_X	SFD98	SF11	E_{B-V}	G23
1	1992bi	63.26	47.24	76	0.054	0.007	0.03	0.032	0.027	0.019	0.182
2	1994F	258.61	68.13	65	0.070	0.014	0.11	0.118	0.094	0.022	0.150
3	1994G	162.89	52.78	89	0.044	0.080	0.03	0.026	0.022	0.02	0.116
4	1994H	173.06	−1.52	22	0.116	0.018	0.1	0.104	0.087	0.025	0.082
5	1994al	163.16	−1.82	27	0.427	0.024	0.42	0.449	0.369	0.132	0.526
6	1994am	173.10	−1.56	23	0.107	0.015	0.1	0.101	0.084	0.025	0.108
7	1994an	69.41	−1.08	115	0.245	0.010	0.21	0.218	0.18	0.055	0.300
8	1995aq	113.34	−1.60	34	0.134	0.012	0.07	0.072	0.059	0.029	0.247
9	1995ar	127.66	−1.47	166	0.108	0.005	0.07	0.071	0.059	0.028	0.131
10	1995as	127.76	−1.34	162	0.116	0.005	0.07	0.068	0.057	0.028	0.123
11	1995at	129.27	−1.14	145	0.107	0.005	0.07	0.063	0.053	0.028	0.213
12	1995aw	165.47	−1.08	284	0.098	0.004	0.12	0.132	0.11	0.03	0.186
13	1995ax	166.06	−1.91	278	0.090	0.080	0.11	0.11	0.091	0.029	0.158
14	1995ay	176.87	−1.45	116	0.270	0.012	0.35	0.378	0.31	0.047	0.428
15	1995az	202.11	−1.50	44	0.295	0.082	0.61	0.6	0.521	0.034	0.532
16	1995ba	215.99	22.98	273	0.100	0.007	0.06	0.059	0.048	0.024	0.110
17	1996cf	250.45	50.01	135	0.101	0.008	0.13	0.133	0.111	0.027	0.173
18	1996cg	220.77	22.15	148	0.111	0.019	0.11	0.116	0.096	0.027	0.181
19	1996ci	333.11	62.08	88	0.065	0.007	0.09	0.091	0.075	0.027	0.149
20	1996ck	301.41	62.10	33	0.059	0.011	0.13	0.106	0.088	0.022	0.224
21	1996cl	256.57	48.67	157	0.095	0.008	0.18	0.118	0.097	0.028	0.123
22	1996cm	10.89	46.74	107	0.120	0.009	0.15	0.155	0.127	0.031	0.236
23	1996cn	334.31	61.81	91	0.073	0.080	0.08	0.084	0.069	0.027	0.170
24	1997F	204.47	−1.45	1			0.13	0.133	0.112	0.037	0.234
25	1997G	202.33	−1.51	35	0.176	0.022	0.2	0.143	0.116	0.039	0.214
26	1997H	202.37	−1.21	31	0.200	0.029	0.16	0.169	0.138	0.04	0.220
27	1997I	202.37	−1.21	31	0.200	0.029	0.16	0.17	0.138	0.04	0.220
28	1997J	209.92	15.37	84	0.116	0.010	0.13	0.128	0.105	0.034	0.165
29	1997K	216.35	16.08	163	0.091	0.005	0.07	0.068	0.058	0.032	0.125
30	1997L	220.03	21.88	172	0.078	0.017	0.08	0.082	0.07	0.026	0.141
31	1997N	220.66	22.10	153	0.096	0.022	0.1	0.102	0.087	0.027	0.171
32	1997O	220.07	22.45	172	0.108	0.013	0.09	0.095	0.08	0.026	0.139
33	1997P	256.58	48.25	137	0.089	0.080	0.1	0.111	0.091	0.028	0.191
34	1997Q	256.88	48.38	139	0.093	0.008	0.09	0.099	0.081	0.028	0.168
35	1997R	256.95	48.50	142	0.094	0.009	0.11	0.099	0.08	0.028	0.140
36	1997S	256.96	48.70	146	0.092	0.008	0.11	0.109	0.089	0.028	0.178
37	1997ac	220.01	22.49	171	0.111	0.014	0.09	0.091	0.077	0.026	0.139
38	1997af	220.03	22.42	169	0.112	0.015	0.09	0.094	0.078	0.026	0.112
39	1997ai	249.96	50.36	141	0.107	0.007	0.14	0.15	0.123	0.027	0.133
40	1997aj	256.60	48.22	133	0.086	0.080	0.11	0.11	0.089	0.028	0.164
41	1997am	256.34	49.06	168	0.097	0.008	0.11	0.119	0.098	0.028	0.167
42	1997ap	333.65	61.90	95	0.071	0.006	0.13	0.087	0.071	0.027	0.105

Content of the table: SN designation, galactic coordinates, number of stars in the area (N), galactic extinction in mag: A_{gal} with uncertainty, A_X [24], A_V(SFD98) [20], A_V(SF11) [21], reddening E_{B-V} [9], A_V(G23) [7].

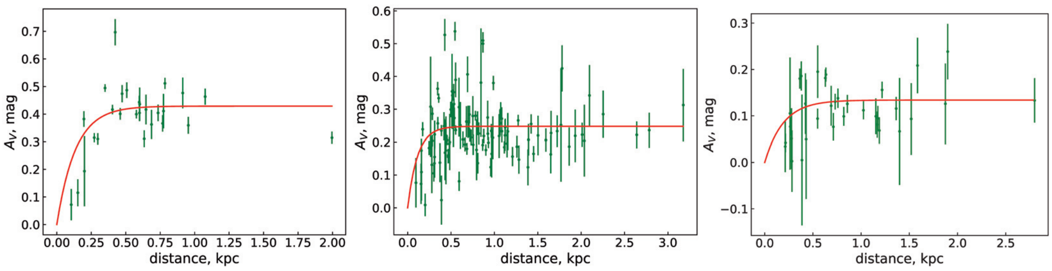

Figure 3. Examples of approximation of $A_V(d)$ dependence (red curves) in areas l,b = 163,−1 (**left**), l,b = 69,−1 (**middle**), and l,b = 111,−1 (**right**). Green points are stars in the area, with observational errors.

2.3. Error Budget

For each area, we estimated the effect of temperature measurement error on A_{gal} as follows. The effective temperature value for the objects in each area was modified by adding Gaussian noise. Specifically, each area was assigned a set of 1000 datasets whose temperature distribution for each object is a normal distribution with a standard deviation σ equal to the temperature measurement error of that object in the LAMOST survey. For the 1000 datasets, we then calculated A_{gal} values, which we characterize by the median Q_2, as well as upper (Q_3) and lower (Q_1) quartiles.

In the vast majority of cases (see Figure 4), the distribution turned out to be quite symmetrical;

$$|(Q_3 - Q_2) - (Q_2 - Q_1)| < 0.^m002, \tag{4}$$

therefore, a value equal to half of the interquartile range IQR was used as dispersion in the following: IQR/2 = $(Q_3 - Q_1)/2$.

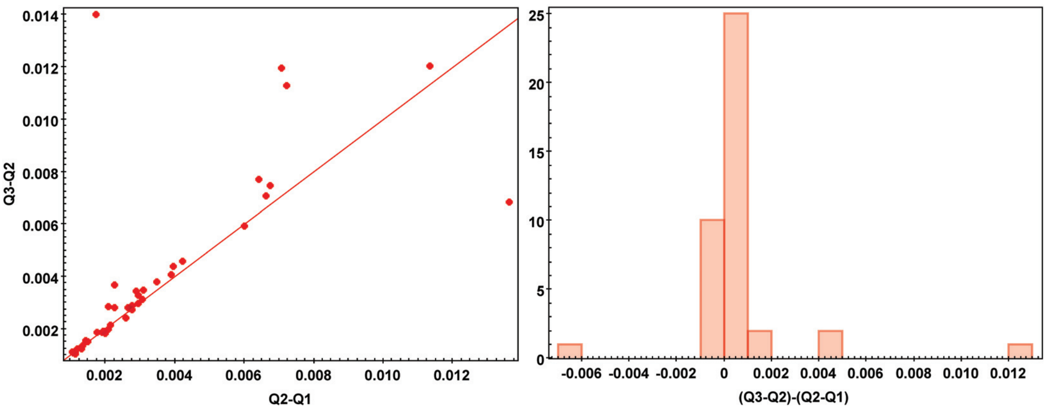

Figure 4. Quartile values for the areas. Median (Q_2), upper (Q_3) and lower (Q_1) quartiles. The one-to-one relation is shown for reference (**left** panel).

In addition, for each area, the χ^2 minimization algorithm (minimize with the lmfit package) calculates the standard deviation (SD). In the lmfit package, the standard deviation of parameters (parameter errors) is calculated based on the covariance matrix, which is obtained after the minimization procedure. The covariance matrix is the result of a linear approximation method and contains information about how the model parameters change relative to each other.

At five areas, SD could not be calculated. Sometimes the minimization method fails to calculate the standard deviations of the parameters due to poor conditioning of the covariance matrix, incorrect initial values, insufficient data, or high noise. We associate these problems with poor data quality. In these cases, we adopted a value of 0.08 mag as SD, slightly higher than the maximum of the calculated values.

As can be seen from Figure 5, in most areas, IQR values were comparable to SD. Therefore, for all areas, the error of the obtained value A_{gal} was assumed to be equal to

$$\sigma = \sqrt{SD^2 + (IQR/2)^2}. \quad (5)$$

It is the value that is used hereafter for comparison with data from other authors.

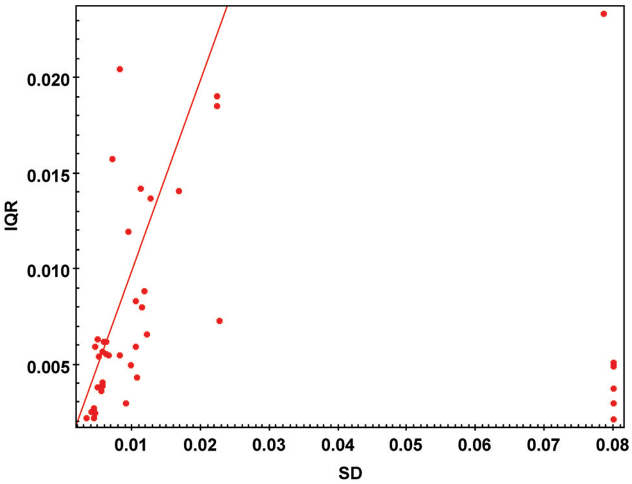

Figure 5. Standard deviation SD and interquartile range IQR for the areas. The one-to-one relation is shown for reference.

3. Comparison of A_{gal} with Other Maps

3.1. Area Centres

First of all, it should be noted that the stars are not uniformly distributed in the test areas. The mean coordinates of all the stars of the area (the "centers of gravity" of the areas) are slightly different from the coordinates of the SN (i.e., the geometric centers of the areas). Figure 6 shows the difference of these coordinates for all areas, as well as the number of stars in the areas. It can be seen that, as expected, the coordinate difference decreases as the number of stars increases. But even in the most "sparsely populated" sites, the "centers of gravity" is usually no further than 0.8 degrees from the geometric center. We believe that for such high latitudes, this is too insignificant a value to noticeably affect the resulting A_{gal}.

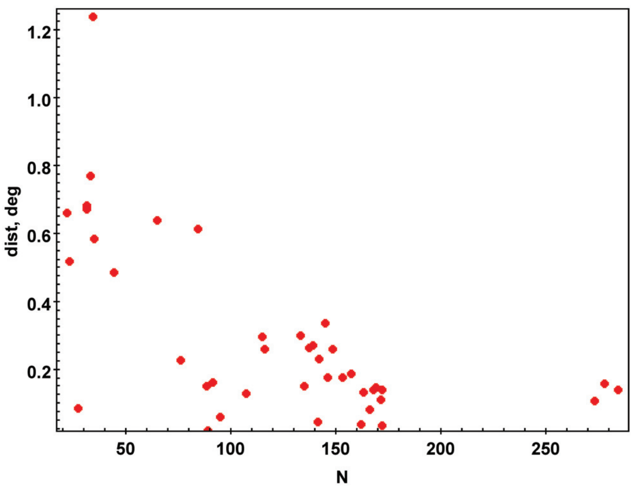

Figure 6. Difference between the mean coordinates of all stars of the area and the coordinates of SN, in degrees vs. the number of stars in the area. See text for details.

3.2. 2D Maps of Galactic Extinction

The A_{gal} values obtained in the previous paragraph can be compared with the A_x values taken from Table 1 of the paper [24], since these latter cases (as seen in Figure 7) are taken, with a few exceptions, from SFD98 [20].

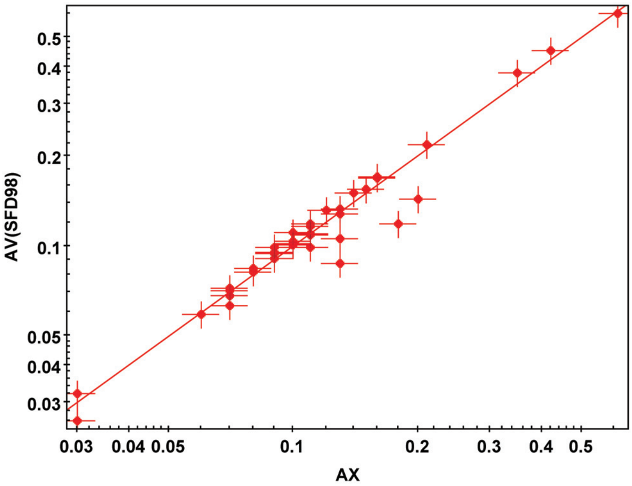

Figure 7. A_x ([24], Table 1) vs. A_V ([20]). According to [24], uncertainty of 10% is assumed. The one-to-one relation is shown for reference.

The results of comparing A_{gal} and A_x [24] are shown in Figure 8. It can be seen that good agreement is achieved for most of the areas.

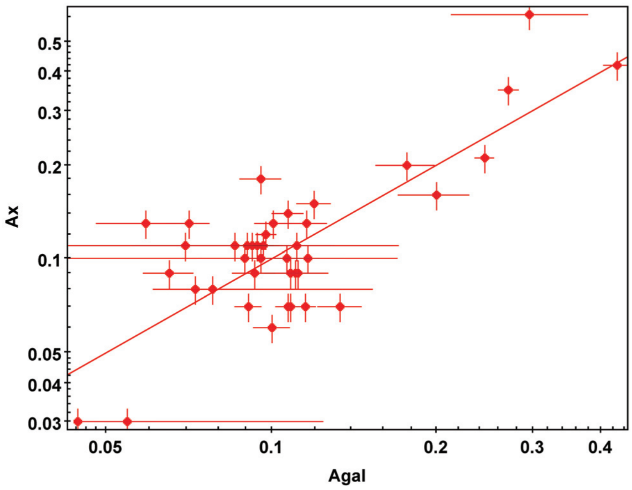

Figure 8. A_{gal} vs. A_x [24]. The one-to-one relation is shown for reference.

However, a comparison of A_{gal} with the more recent map $A(SF11)$ [21] (Figure 9) shows that the values of A_{gal} are systematically overestimated. The values of A_V(SF11) have decreased linearly compared to A_{gal} (and hence to A_x [24] and A_V(SFD98)). It can be roughly estimated that, on average, for the areas studied, A_V(SF11) = 0.8 A_V(SFD98). It can be estimated that the value of the distance to an extragalactic object increases by 3% when the absorption decreases by $0.^m06$.

The difference in results between Schlafly et al. [21,30] and Schlegel et al. [20] arises primarily from the reddening law used and calibration issues in the SFD map. Specifically, Schlafly et al. [21,30] applied a Fitzpatrick reddening law with R_V = 3.1 [31], which better fits their measurements, while the SFD98 map overestimates reddening, using O'Donnell [32] reddening law. They found that the SFD98 overpredicts reddening by factors of 1.4 in u-g, 1.0 in g-r, 1.2 in r-i, and 1.4 in i-z, likely due to the less precise reddening law. Moreover, temperature correction issues also contribute to the inconsistencies, leading to an observed 15% normalization difference between the galactic north and south, attributed to dust temperature errors.

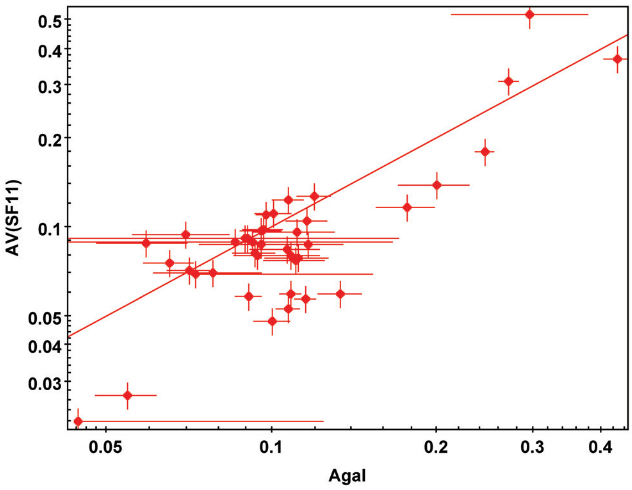

Figure 9. A_{gal} vs. $A(SF11)$ [21]. The one-to-one relation is shown for reference.

3.3. STILISM Service

Figure 10 shows a comparison of our results with data from the STILISM [9]. It should be noted that STILISM provides a 3D-map of interstellar extinction (i.e., the distance dependence of reddening $E_{B-V}(d)$ in different directions up to fixed distances). One would therefore expect that the STILISM values would not exceed the A_{gal} values. Within observational errors, this is the case.

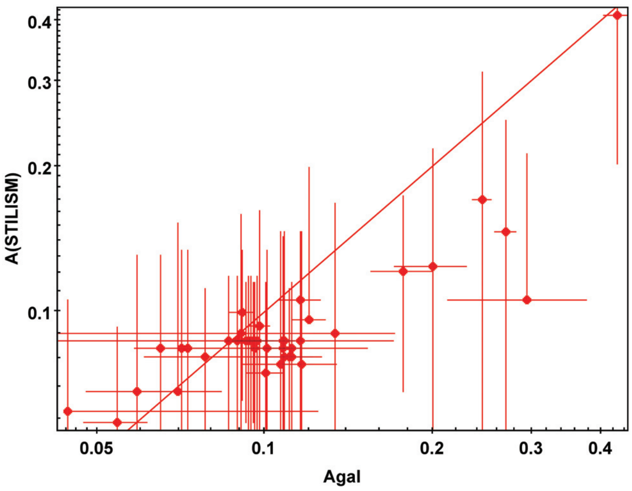

Figure 10. A_{gal} vs. $A(STILISM)$ [9]. The one-to-one relation is shown for reference.

3.4. G23 Map

Finally, we compared our results with the recently published G23 map [7] (see Figure 11). For most areas, the values of $A(G23)$ exceed the values of A_{gal} by $0.^{m}1$, which implies a 5% decrease in the value of distance to the extragalactic object estimation.

Note that the value of galactic extinction according to G23 can reach several magnitudes at mid-latitudes, despite the fact that the limiting distance does not exceed 2 kpc (see Figure 12).

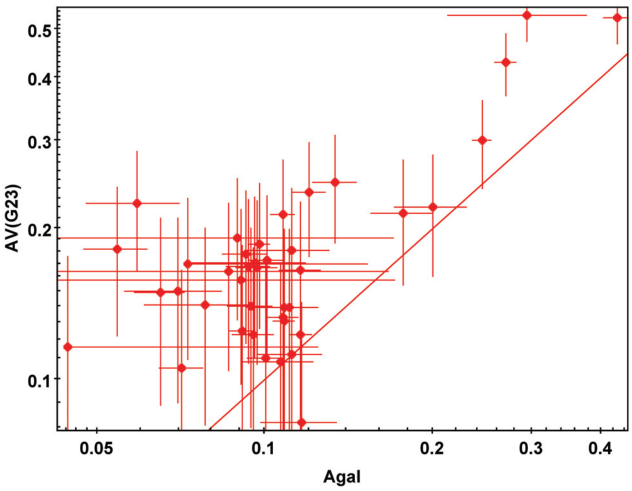

Figure 11. A_{gal} vs. $A(G23)$ [7]. According to Gontcharov (private communication), uncertainty of $0.^{m}06$ for $A(G23)$ is assumed. The one-to-one relation is shown for reference.

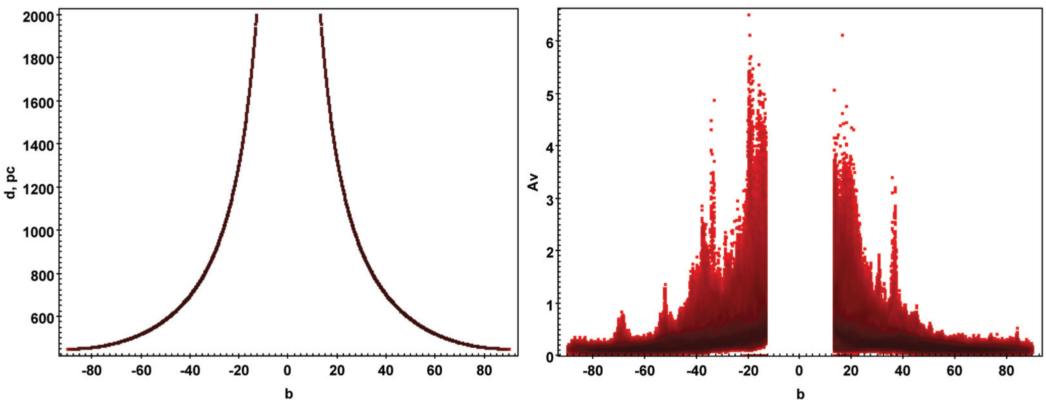

Figure 12. Limiting distance d, pc (**left**) and galactic extinction A_V, mag (**right**) as functions of galactic latitude b in G23 [7].

4. Conclusions

We estimated the galactic extinction value for 42 areas of the northern celestial hemisphere with high galactic latitude (SNe from [24]). Our estimations are based on stellar distances and reddening, inferred from Gaia parallaxes and photometry, and LAMOST atmospheric parameters. We chose this set because [24] is the now classic work that allowed the establishment of the accelerated expansion of the universe. This fact was subsequently confirmed by more abundant and accurate [33–35] data, and we may use these data in the future to further refine our procedure. We should report that our estimates agree well, within observation errors, with those of [24] and [20] (SFD98).

Comparison with other maps shows systematic differences that can cause the distance to the extragalactic object to change by ±3–5%. Apparently, in order to be able to rely on these dust distributions, it is necessary to extend the maps beyond the current limits of a few kiloparsecs, particularly in the inner galaxy. One way of achieving this will be the incorporation of deeper near-infrared photometry, allowing us to see stars through far greater dust column densities.

Author Contributions: The authors made equal contribution to this work; original draft prepared by O.M. All authors have read and agreed to the published version of the manuscript.

Funding: This research was funded by the Ministry of Science and Higher Education of the Russian Federation, according to the research project 13.2251.21.0177 (075-15-2022-1228).

Data Availability Statement: The data presented in this study are available on request from the corresponding author.

Acknowledgments: We warmly thank James Wicker for his great help in preparing the manuscript. The authors thank Maria Pruzhinskaya, Kefeng Tan, and Jingkun Zhao for the valuable remarks and suggestions. We also thank our reviewers, whose constructive comments helped us significantly improve the paper. This research has made use of NASA's Astrophysics Data System, of the SIMBAD database, operated at CDS (Strasbourg, France), of TOPCAT, an interactive graphical viewer and editor for tabular data [36]. The acknowledgements were compiled using the Astronomy Acknowledgement Generator.

Conflicts of Interest: The authors declare no conflicts of interest.

References

1. Parenago, P.P. On interstellar extinction of light. *Astron. Zh.* **1940**, *13*, 3.
2. Fitzgerald, M.P. The Distribution of Interstellar Reddening Material. *Astron. J.* **1968**, *73*, 983. [CrossRef]
3. Neckel, T.; Klare, G. The spatial distribution of the interstellar extinction. *Astron. Astrophys. Suppl. Ser.* **1980**, *42*, 251.
4. Pandey, A.K.; Mahra, H.S. Interstellar extinction and Galactic structure. *Mon. Not. R. Astron. Soc.* **1987**, *226*, 635–643. [CrossRef]
5. Arenou, F.; Grenon, M.; Gomez, A. A tridimensional model of the galactic interstellar extinction. *Astron. Astrophys.* **1992**, *258*, 104–111.
6. Gontcharov, G.A. Influence of the Gould belt on interstellar extinction. *Astron. Lett.* **2009**, *35*, 780–790. [CrossRef]
7. Gontcharov, G.A.; Marchuk, A.A.; Khovrichev, M.Y.; Mosenkov, A.V.; Savchenko, S.S.; Il'in, V.B.; Poliakov, D.M.; Smirnov, A.A. New Interstellar Extinction Maps Based on Gaia and Other Sky Surveys. *Astron. Lett.* **2023**, *49*, 673–696. [CrossRef]
8. Sale, S.E.; Drew, J.E.; Barentsen, G.; Farnhill, H.J.; Raddi, R.; Barlow, M.J.; Eislöffel, J.; Vink, J.S.; Rodríguez-Gil, P.; Wright, N.J. A 3D extinction map of the northern Galactic plane based on IPHAS photometry. *Mon. Not. R. Astron. Soc.* **2014**, *443*, 2907–2922. [CrossRef]
9. Lallement, R.; Capitanio, L.; Ruiz-Dern, L.; Danielski, C.; Babusiaux, C.; Vergely, L.; Elyajouri, M.; Arenou, F.; Leclerc, N. Three-dimensional maps of interstellar dust in the Local Arm: Using Gaia, 2MASS, and APOGEE-DR14. *Astron. Astrophys.* **2018**, *616*, A132. [CrossRef]
10. Green, G.M.; Schlafly, E.; Zucker, C.; Speagle, J.S.; Finkbeiner, D. A 3D Dust Map Based on Gaia, Pan-STARRS 1, and 2MASS. *Astrophys. J.* **2019**, *887*, 93. [CrossRef]
11. Chen, B.Q.; Huang, Y.; Yuan, H.B.; Wang, C.; Fan, D.W.; Xiang, M.S.; Zhang, H.W.; Tian, Z.J.; Liu, X.W. Three-dimensional interstellar dust reddening maps of the Galactic plane. *Mon. Not. R. Astron. Soc.* **2019**, *483*, 4277–4289. [CrossRef]
12. Leike, R.H.; Glatzle, M.; Enßlin, T.A. Resolving nearby dust clouds. *Astron. Astrophys.* **2020**, *639*, A138. [CrossRef]
13. Nekrasov, A.; Grishin, K.; Kovaleva, D.; Malkov, O. Approximate analytical description of the high latitude extinction. *Eur. Phys. J. Spec. Top.* **2021**, *230*, 2193–2205. [CrossRef]
14. Brown, A.G.A. et al. [Gaia Collaboration] Gaia Early Data Release 3. Summary of the contents and survey properties. *Astron. Astrophys.* **2021**, *649*, A1. [CrossRef]
15. Luo, A.L.; Zhao, Y.H.; Zhao, G.; Deng, L.C.; Liu, X.W.; Jing, Y.P.; Wang, G.; Zhang, H.T.; Shi, J.R.; Cui, X.Q.; et al. The first data release (DR1) of the LAMOST regular survey. *Res. Astron. Astrophys.* **2015**, *15*, 1095. [CrossRef]
16. Luo, A.L.; Zhao, Y.H.; Zhao, G. VizieR Online Data Catalog: LAMOST DR5 catalogs (Luo+, 2019). In *VizieR Online Data Catalog*; NASA: Washington, DC, USA, 2019; p. V-164.
17. Avdeeva, A.; Kovaleva, D.; Malkov, O.; Nekrasov, A. Fitting procedure for estimating interstellar extinction at high galactic latitudes. *Open Astron.* **2021**, *30*, 168–175. [CrossRef]
18. Steinmetz, M. et al. [RAVE Collaboration] The Sixth Data Release of the Radial Velocity Experiment (RAVE). II. Stellar Atmospheric Parameters, Chemical Abundances, and Distances. *Astron. J.* **2020**, *160*, 83. [CrossRef]
19. Burstein, D.; Heiles, C. Reddenings derived from H I and galaxy counts: Accuracy and maps. *Astron. J.* **1982**, *87*, 1165–1189. [CrossRef]
20. Schlegel, D.J.; Finkbeiner, D.P.; Davis, M. Maps of Dust Infrared Emission for Use in Estimation of Reddening and Cosmic Microwave Background Radiation Foregrounds. *Astrophys. J.* **1998**, *500*, 525–553. [CrossRef]
21. Schlafly, E.F.; Finkbeiner, D.P. Measuring Reddening with Sloan Digital Sky Survey Stellar Spectra and Recalibrating SFD. *Astrophys. J.* **2011**, *737*, 103. [CrossRef]
22. Vallenari, A. et al. [Gaia Collaboration] Gaia Data Release 3. Summary of the content and survey properties. *Astron. Astrophys.* **2023**, *674*, A1. [CrossRef]
23. Bailer-Jones, C.A.L.; Rybizki, J.; Fouesneau, M.; Mantelet, G.; Andrae, R. Estimating Distance from Parallaxes. IV. Distances to 1.33 Billion Stars in Gaia Data Release 2. *Astron. J.* **2018**, *156*, 58. [CrossRef]
24. Perlmutter, S.; Aldering, G.; Goldhaber, G.; Knop, R.A.; Nugent, P.; Castro, P.G.; Deustua, S.; Fabbro, S.; Goobar, A.; Groom, D.E.; et al. Measurements of Ω and Λ from 42 High-Redshift Supernovae. *Astrophys. J.* **1999**, *517*, 565–586. [CrossRef]

25. Bono, G.; Iannicola, G.; Braga, V.F.; Ferraro, I.; Stetson, P.B.; Magurno, D.; Matsunaga, N.; Beaton, R.L.; Buonanno, R.; Chaboyer, B.; et al. On a New Method to Estimate the Distance, Reddening, and Metallicity of RR Lyrae Stars Using Optical/Near-infrared (B, V, I, J, H, K) Mean Magnitudes: ω Centauri as a First Test Case. *Astrophys. J.* **2019**, *870*, 115. [CrossRef]
26. Cardelli, J.A.; Clayton, G.C.; Mathis, J.S. The Relationship between Infrared, Optical, and Ultraviolet Extinction. *Astrophys. J.* **1989**, *345*, 245. [CrossRef]
27. Jordi, C.; Gebran, M.; Carrasco, J.M.; de Bruijne, J.; Voss, H.; Fabricius, C.; Knude, J.; Vallenari, A.; Kohley, R.; Mora, A. Gaia broad band photometry. *Astron. Astrophys.* **2010**, *523*, A48. [CrossRef]
28. Pecaut, M.J.; Mamajek, E.E. Intrinsic Colors, Temperatures, and Bolometric Corrections of Pre-main-sequence Stars. *Astrophys. J. Suppl. Ser.* **2013**, *208*, 9. [CrossRef]
29. Newville, M.; Stensitzki, T.; Allen, D.B.; Ingargiola, A. *LMFIT: Non-Linear Least-Square Minimization and Curve-Fitting for Python*; Zenodo: Geneve, Switzerland, 2014. [CrossRef]
30. Schlafly, E.F.; Finkbeiner, D.P.; Schlegel, D.J.; Jurić, M.; Ivezić, Ž.; Gibson, R.R.; Knapp, G.R.; Weaver, B.A. The Blue Tip of the Stellar Locus: Measuring Reddening with the Sloan Digital Sky Survey. *Astrophys. J.* **2010**, *725*, 1175–1191. [CrossRef]
31. Fitzpatrick, E.L. Correcting for the Effects of Interstellar Extinction. *Publ. Astron. Soc. Pac.* **1999**, *111*, 63–75. [CrossRef]
32. O'Donnell, J.E. R v-dependent Optical and Near-Ultraviolet Extinction. *Astrophys. J.* **1994**, *422*, 158. [CrossRef]
33. Betoule, M.; Kessler, R.; Guy, J.; Mosher, J.; Hardin, D.; Biswas, R.; Astier, P.; El-Hage, P.; Konig, M.; Kuhlmann, S.; et al. Improved cosmological constraints from a joint analysis of the SDSS-II and SNLS supernova samples. *Astron. Astrophys.* **2014**, *568*, A22. [CrossRef]
34. Scolnic, D.M.; Jones, D.O.; Rest, A.; Pan, Y.C.; Chornock, R.; Foley, R.J.; Huber, M.E.; Kessler, R.; Narayan, G.; Riess, A.G.; et al. The Complete Light-curve Sample of Spectroscopically Confirmed SNe Ia from Pan-STARRS1 and Cosmological Constraints from the Combined Pantheon Sample. *Astrophys. J.* **2018**, *859*, 101. [CrossRef]
35. Brout, D.; Scolnic, D.; Popovic, B.; Riess, A.G.; Carr, A.; Zuntz, J.; Kessler, R.; Davis, T.M.; Hinton, S.; Jones, D.; et al. The Pantheon+ Analysis: Cosmological Constraints. *Astrophys. J.* **2022**, *938*, 110. [CrossRef]
36. Taylor, M.B. TOPCAT STIL: Starlink Table/VOTable Processing Software. In *Astronomical Society of the Pacific Conference Series, Proceedings of the Astronomical Data Analysis Software and Systems XIV, Pasadena, CA, USA, 24–27 October 2004*; Shopbell, P., Britton, M., Ebert, R., Eds.; Astronomical Society of the Pacific: San Francisco, CA, USA, 2005; Volume 347, p. 29.

galaxies

MDPI

Article

Looking for Signs of Unresolved Binarity in the Continuum of LAMOST Stellar Spectra

Mikhail Prokhorov [1,*], Kefeng Tan [2], Nikolay Samus [1,3], Ali Luo [2], Dana Kovaleva [3], Jingkun Zhao [2], Yujuan Liu [2], Pavel Kaygorodov [3], Oleg Malkov [3], Yihan Song [2], Sergey Sichevskij [3], Lev Yungelson [3] and Gang Zhao [2]

1 Sternberg Astronomical Institute, Moscow State University, 13 Universitetsky pr., Moscow 119991, Russia; samus@sai.msu.ru
2 National Astronomical Observatories, Chinese Academy of Sciences, Beijing 100101, China; tan@nao.cas.cn (K.T.); lal@nao.cas.cn (A.L.); zjk@nao.cas.cn (J.Z.); lyj@nao.cas.cn (Y.L.); yhsong@nao.cas.cn (Y.S.); gzhao@nao.cas.cn (G.Z.)
3 Institute of Astronomy, Russian Academy of Sciences, Pyatnitskaya 48, Moscow 119017, Russia; dana@inasan.ru (D.K.); pasha@inasan.ru (P.K.); malkov@inasan.ru (O.M.); s.sichevskij@gmail.com (S.S.); lev.yungelson@gmail.com (L.Y.)
* Correspondence: mike.prokhorov@gmail.com

Abstract: We describe an attempt to derive the binarity rate of samples of 166 A-, F-, G-, and K-type stars from LAMOST DR5 and 1000 randomly selected presumably single stars from Gaia DR3 catalogs. To this end, we compared continua of the observed spectra with the continua of synthetic spectra from within $3700 < \lambda < 9097$ Å. The latter spectra were reduced to the LAMOST set of wavelengths, while the former ones were smoothed. Next, we searched for every observed star of the nearest synthetic spectrum using a four-parameter representation—$T_{\rm eff}$, $\log g$, [Fe/H], and a range of interstellar absorption values. However, rms deviations of observed spectra from synthetic ones appeared to be not sufficient to claim that any of the stars is a binary. We conclude that comparison of the intensity of pairs of spectral lines remains the best way to detect binarity.

Keywords: stars; binaries; general; surveys

1. Introduction

Binary stars are very numerous, and binarity rate estimates increase from ≃(20–30)% for M-dwarfs to ≃(60–70)% for A-type ones, while extreme ones for O stars reach (94 ± 14)% [1] [1–4]. The importance of correct estimation of binarity rate is due to the role of binaries in formation of many extreme astrophysical objects, e.g., Supernovae, X-ray sources, gravitational wave sources, as well as formation of populations of stars of certain types, for instance, cataclysmic variables. No less important is the significance of the estimates of binarity rate for understanding star formation, dynamics of stellar aggregates, etc. (see, e.g., [5–10]).

Extensive sets of observational data for the stellar population of the Galaxy became available recently, as a result of several surveys. Among the most notable ones are the astrometric survey Gaia [11,12], multi-band survey SDSS [13], and spectroscopic surveys (see below). One may expect that a large proportion of the objects in these surveys are unresolved binary stars.

There are a number of approaches for resolving hidden binaries and assessing their characteristics, which employ different samples of observable characteristics and differ in the scope of physical and observable parameters of unresolved binaries that they may recover.

For the Gaia sources, the methods of detecting probable unresolved binaries based on Gaia supplementary information about astrometric solutions are proposed [14,15]. The methods based solely on photometric information [16,17] require a combined multicolor photometry. A variety of methods use a combination of photometric information and trigonometric parallaxes [18–20]. A combination of the data from several surveys may also be helpful for finding unresolved binaries. Each of these methods is able to reveal a certain fraction of the population of unresolved binary stars using the multidimensional space of observational parameters. Unfortunately, no one of them is universal, so they may be considered as intercomplementary.

Along with astrometric and photometric surveys, spectroscopic surveys, such as LAMOST [21], RAVE [22], GALAH [23], APOGEE [24,25], and GES [26,27], are an invaluable provider of information about unresolved binary systems. Spectroscopic binaries are, on the one hand, a fairly representative observational class of objects, and on the other hand, the parameters obtained from solving the spectroscopic orbit include almost all the orbital elements and the astrophysical parameters of the components. Compared with visual binaries, spectroscopic binaries have relatively short orbital periods. With this property, it is easier to construct their full orbital solutions by observing two stars orbiting each other multiple times. Spectroscopic searches make it possible to apprehend how unresolved binarity affects spectra of the sources [8,28,29].

Spectroscopic surveys have greatly enlarged the number of spectroscopic binaries by providing millions of spectra. For instance, Birko et al. [30] identified 3838 SB1 candidates using RAVE and Gaia DR2 data and estimated the most probable orbital parameters of main-sequence dwarf candidates. Price-Whelan et al. [31] discovered 19,635 APOGEE-SB1s and gave multiple possible orbital solutions for each system. Traven et al. [32] presented 12,760 binaries detected as SB2s in GALAH. Merle et al. [33] found 641 FGK SB1 candidates at the 5σ level in GES.

LAMOST is a special quasi-meridian reflecting Schmidt telescope with an effective aperture of 4 m and a field of view of 20 deg^2. The unique design of LAMOST enables it to acquire 4000 spectra in a single exposure [34,35]. Up until now it has obtained more than 11 million low-resolution ($R = 1800$) spectra and more than 13 million medium-resolution ($R = 7500$) spectra.

LAMOST is an invaluable provider of data on new spectral binary systems. Numerous and consistently successful attempts have been made to detect unresolved binaries in the LAMOST medium-resolution spectroscopic survey. Ref. [19] presented a data-driven method to estimate absolute magnitudes for O- and B-type stars from the LAMOST spectra. The inferred spectroscopic K_s-band magnitudes $M_{K\mathrm{s}}$ were compared with the geometric $M_{K\mathrm{s}}$ magnitudes derived from Gaia parallaxes to identify binaries. Ref. [19] identified 1597 of the 16,002 LAMOST OB stars as binaries. Li et al. [36] examined radial velocities of over 1.3 million LAMOST DR7 medium-resolution blue-arm spectra and found 3133 spectroscopic binaries (SB) and 132 spectroscopic candidate triples (ST). An overwhelming majority of these stars are new discoveries. Ref. [37] investigated the binarity of 9382 stars measuring the equivalent widths of several spectral lines in the LAMOST medium-resolution spectra. The binary fraction found by them ranges from $68 \pm 8\%$ for O- to B4-type stars to $44 \pm 6\%$ for B8 to A stars. At the same time, the results of searches for unresolved binaries in the low-resolution LAMOST survey are rather scarce [38,39].

Thus, LAMOST is the largest spectroscopic survey in terms of the volume of data obtained and the widest in terms of coverage of the sky. The low-resolution LAMOST spectra collection is no less representative than the medium-resolution one. There are not enough large spectroscopic surveys now to ignore this set of spectra. Additionally, LAMOST low-resolution spectroscopy has accumulated data for nearly nine years; thus, there are multiple observations for a significant number of sources. Examination of these sources may increase the number of known binary systems and give us additional information about the ensemble of binary stars in the Galaxy. In the present study we aim to investigate the options to discover the population of unresolved binaries using low-resolution spectra from LAMOST using synthetic spectra.

If the stellar spectrum is the main information about the star, then, in order to infer that the star is a binary, one needs to find the deviation of its spectrum from that of a single star—an excess due to the light from the second, fainter component.

The methods of obtaining stellar parameters from low-resolution stellar spectra were developed and widely applied to a substantial number of spectra in recent wide-scale spectroscopic surveys [40–42].

In parallel to these methods, other ones, based on multi-color photometric data, were developed and widely used. The reason for the popularity of the latter, despite their accuracy in determining the physical parameters of stars not being high, is that photometry, as accurate as spectrophotometry, can be obtained with much smaller telescopes.

The main trend in the development of stellar spectra analysis is improvement in the accuracy of determination of stellar physical parameters (for example, it is possible to derive the effective temperature of a star, $T_{\rm eff}$, with an uncertainty of several Kelvins). Therefore, the methods based on the analysis of the continuum are now out of use: they do not provide stellar parameters with adequate precision. However, in this paper we will test the effectiveness of the method for detecting unresolved binary stars by comparing their observed continuum (in the LAMOST project) with synthetic spectra of single stars.

In Sections 2 and 3, we discuss cross-identification of data of Gaia DR3 and LAMOST with selected lists of close binaries and presumably single stars. Section 4 describes modeling of spectra of unresolved binaries. Section 5 discusses results of testing approaches for distinguishing between single and unresolved binaries, comparing LAMOST spectra with sets of synthetic theoretical spectra of single stars, prepared in advance. Section 6 presents our conclusions.

2. Data: LAMOST Spectra

We use the LAMOST DR5 [43] catalog of A-, F-, G- and K-type stars, which contains stellar parameters ($T_{\rm eff}$, $\log g$, and [Fe/H]) for more than 5 million low-resolution ($R = 1800$ at 5500 Å) stellar spectra. The wavelength range of the spectra is about 3690–9100 Å. The signal-to-noise ratio (SNR) is larger than 6 (in the g-band) for the spectra obtained during dark nights, and it is larger than 15 for the spectra obtained during bright nights. The acquisition of spectra and processing of LAMOST data are described in detail in a number of papers (see [44] and references therein). We will not repeat them in this paper.

Currently, the most frequently used methods for determining the parameters of stars are those based on the analysis of the ratios of the depth of spectral line pairs (see, e.g., [45–47]). The lines of the pair should have sufficiently close wavelengths in order to eliminate the effects of interstellar extinction to the greatest possible extent. Different line pairs are used for different spectral types. The "classical" line set is presented in [48] (Table 15.3).

Line pairs analysis requires high-resolution spectra, but this is not the case for LAMOST spectra. Luo et al. [21] developed a different method for them. It is based on minimizing the squared difference between the observational and model spectra. This method is used both for the spectral classification of stars in the catalog and for the determination of the values of $T_{\rm eff}$, $\log g$, and [Fe/H].

It should be noted that while determining physical parameters from stellar spectra we attempted to achieve the best accuracy, but we can be satisfied with a rather rough parameter determination, only to be able to detect excess radiation from the binary's second star. Thus, in principle, all of the above methods are suitable for us.

The quality of calibration of LAMOST spectra is important for solving our problem. For the LAMOST flux calibration, the LAMOST 2D pipeline picks out several high-S/N standards in the temperature range of 5750–7250 K and then obtains the spectrograph response curve (SRC) by comparing the observed spectra with synthetic spectra (using the corresponding parameters from the Castelli–Kurucz spectral library [49]). As a result, the dereddening uncertainties of standards have an impact on the SRC derivation. This introduces uncertainties to all spectra of the spectrograph for one plate. For a few spectra (∼2%), flux calibrations are completed using the average response curve of each spectrograph (ASPSRC) method [50]. This method has some uncertainties caused by variations in the shape of individual SRCs, which introduces uncertainties to the calibrated spectra. The statistical analysis presented in Du et al. [50] revealed that the total uncertainties caused by the LAMOST flux calibration in the spectra are less than 10%.

The rest of the present paper deals with the method of detecting unresolved binary stars in the LAMOST catalog by the analysis of the spectral continuum.

3. Data: Known Single and Binary Stars

To investigate the possibility of distinguishing between single and unresolved binary stars from LAMOST spectra, we need to know what might be systematic differences between actual LAMOST spectra of single and binary stars. For this purpose, we compiled two data sets of LAMOST spectra. The first one contains sources identified with known close binary stars, which cannot be resolved by LAMOST (the fiber diameter of LAMOST is about 3.3 arcsec). Another set contains presumably single stars identified by cross-matching the LAMOST DR5 source catalog with selected catalogs, as described below.

3.1. Reliable Unresolved Binary Stars

For the stars to be included in the test list of binaries for modeling, we required them to be definitely binary and to have known spectral types of components. No multiple systems were accepted. These requirements are met by the objects from the ninth catalog of Spectroscopic Binary Orbits, SB9 [2]. This catalog continues the series of compilations of spectroscopic orbits carried out over 35 years by A. Batten and his collaborators and is continuously updated. As of 2023, the catalog contains about 5000 orbits for about 4000 systems. Note that SB9 binary stars usually contain two similar components, i.e., with mass ratio $m_2/m_1 \simeq 1$. There are 10 stars common to the LAMOST DR5 catalog. Two observations were found in the catalog for one of these stars; thus, in total, we possess 11 spectra.

3.2. Reliable Single Stars

We selected from several catalogs single stars that were highly reliably not binary or multiple. These catalogs are listed below with brief comments:

- Compilation of spectra of single stars, mostly Praesepe and M67 spectral standards [52]. There is N_{ov} = 1 star overlapping with the LAMOST DR5 catalog.
- ELODIE.3.1—an updated release of the library published in Prugniel et al. [53]. N_{ov} = 15.
- The Indo-US Library of Coudé Feed Stellar Spectra [54] containing spectra of 1273 stars obtained using the 0.9 m Coudé feed telescope at Kitt Peak National Observatory. N_{ov} = 30.
- LCO-SL, the Las Campanas Observatory Stellar Library [3], which is the most comprehensive near-infrared spectral library with 1300+ spectra obtained between 2013 and

2017 using the Folded-port InfraRed Echellette (FIRE) spectrograph operated using the 6.5 m Magellan Baade telescope. N_{ov} = 12.

- MILES—the library of spectra obtained by the 2.5 m Isaac Newton Telescope used, in particular, for stellar population synthesis [55]. N_{ov} = 25.
- Hubble's Next-Generation Spectral Library (NGSL) containing ∼1000 spectra of 380 stars of assorted temperature, gravity, and metallicity. Each spectrum covers the wavelength range 0.18–1.03 μ [56] [4]. N_{ov} = 6.
- The Tian Shan (Alma-Ata) Sternberg Astronomical Institute photometric $WBVR$ catalog of 13,586 bright northern-sky stars [57]. The catalog contains both single stars and double (multiple) systems. For single stars, $N_{ov} = 102$.
- The latest issue of the astrometric fundamental star catalog, FK6 [58], a combination of results from ground-based observations and from the Hipparcos project of space astrometry. $N_{ov} = 1$.

After exclusion of overlapping objects, the list contains 166 stars. For these stars, we find 278 observations (spectra) in the LAMOST DR5 catalog. Hereafter, we will refer to this sample as the main list of single stars, Main_Single.

3.3. Presumably Single and Unresolved Binary Stars

The number of reliable single stars identified with LAMOST DR5 objects was too low to provide a representative sample, so we added a number of stars that we presumed to be single and to be unresolved binaries, employing the data from Gaia DR3.

3.3.1. Presumably Single Stars

For this purpose, we cross-matched the LAMOST DR5 A-, F-, G-, and K-type star catalog [43] with Gaia DR3, using a standard X-Match CDS procedure with a radius of matching 1″, under the condition that there was no other Gaia source within the radius of 4″ from the LAMOST star, to avoid doubtful matches. We selected only Gaia DR3 sources with five-parametric solutions without "duplicate source" and "variable source" flags, which, by Gaia DR3 classification, have zero probability of being a galaxy or a quasar ($classprob\_dsc\_combmod\_quasar = 0$ and $classprob\_dsc\_combmod\_galaxy = 0$) and are most probably single stars ($classprob\_dsc\_combmod\_star > 0.99$) [59]. Further, we used photometry data to filter out probable mismatches based on comparison of photometric magnitude measurements. This filter is tentative, as the data on LAMOST sources after automatic processing of their spectra may contain several photometric magnitudes in different bands and not all of them are obligatorily presented. So, we filtered out stars with one of the LAMOST stellar magnitudes differing from Gaia G-magnitude by more than 3 rms in the entire sample of matched LAMOST–Gaia stars.

Next, we have filtered out the stars matching with Gaia sources with any indication of being non-single, astrometrically, photometrically, or spectroscopically. We have selected stars in close vicinity of the Sun (having parallax $\varpi \geq 5$, e.g., approximately within 200 pc) to make possibly unresolved components discoverable. It was required that the matched sources in Gaia had Renormalized Unit Weight Error $ruwe < 1.4$ [60] and corrected flux excess factors indicating no inconsistency between BP, RP, and G fluxes [61], since it was demonstrated that these factors may indicate duplicity of the source (see, e.g., [62]). Finally, we have checked that the remaining dataset did not contain stars marked as Gaia unresolved non-single sources [63].

The resulting list of presumably single Gaia sources cross-identified with LAMOST contains 6220 stars. Hereafter, we will name this sample Gaia list of single stars Gaia_Single.

3.4. Gaia Non-Single Stars

To increase the number of unresolved binary stars identified with LAMOST DR5 objects, we added a number of stars that are marked as presumably unresolved binary stars in the Gaia DR3 non-single star (NSS) catalogs [63]. These catalogs include sources revealing signs of periodical changes in astrometric, photometric, and/or spectroscopic Gaia data, which are interpreted as their binarity or multiplicity.

For this purpose, we cross-matched the LAMOST DR5 A-, F-, G-, and K-type star catalog [43] with Gaia DR3 NSS sources, using a standard X-Match CDS procedure with a radius of matching of $1''$ on the condition that there was no other Gaia source within a radius of $4''$ from the LAMOST star, to avoid doubtful matches. Further, we used photometry data to filter out probable mismatches based on comparison of photometric magnitude measurements. This filter is tentative, as the data on LAMOST sources after automatic processing of their spectra may contain several photometric magnitudes in different bands and not all of them are obligatorily presented. So, we filtered out stars with some of the LAMOST stellar magnitudes differing from Gaia G-magnitudes by more than 3 rms in the entire sample of matched LAMOST–Gaia stars. Next, we selected the stars matching with Gaia sources in close vicinity of the Sun (having parallax $\varpi \geq 5$, e.g., approximately within 200 pc).

The resulting list of presumably unresolved Gaia sources cross-identified with LAMOST contains 2278 stars.

4. The Method for Comparing Model Spectra with the LAMOST Spectrum in the Terms of Their Continua

4.1. Description of the Method in General

Among the astronomical software, there are a number of well-established programs for working with spectra, such as ULySS [64,65], SME [66–68], FERRE [69], The Payne [70], and RVSpecFit [71]. It might be possible to solve our problem using the FERRE package, which is unnecessary for our purposes. So, we applied our own code in Python v. 3.11.

LAMOST spectra and synthetic spectra are defined for different wavelength sets and normalized differently. In order to compare spectra, the former should be recomputed for the same set of wavelengths and presented with the same normalization. At this stage, the defects that are sometimes present at the edges of the LAMOST spectra can be detected and removed.

The criterion for two spectra to be considered similar is their mutual rms deviation. Among the synthetic spectra, we search for the one closest to the studied LAMOST spectrum according to the above criterion, with an account of interstellar reddening, within the limits acceptable for the star under study. We call such a reddened synthetic spectrum "optimal".

If divergence of the observed LAMOST spectrum and the optimal one is not large, the star under study is either a single star or a binary with a faint component that cannot be distinguished at the background of the companion. This category also includes the case of double stars with almost identical components whose spectra differ only slightly. Such a star will have a luminosity exceeding that of the more massive component of the binary, but the luminosity increase will not be recognized by us. If the spectra differ strongly, the LAMOST star can be peculiar (single or binary). A similar effect can be also caused by a strong defect in the LAMOST spectrum.

For an unresolved binary, the variance of the observed spectrum and the closest synthetic spectrum can look different in the following two cases. If one of the components is considerably brighter than the second one, the synthetic spectrum will be close to that of the bright component. An increase in the brightness difference of components hampers the discovery of unresolved binarity.

The second case corresponds to the occurrence when the radiation fluxes from components of an unresolved binary in the LAMOST working range are approximately the same, while the spectral types of them differ considerably. The synthetic spectrum consists of a component with one maximum, while the binary spectrum is the sum of two such components. The difference of observed and synthetic spectra will have a "wave-like" shape. This case is much more favorable for the detection of binarity.

Let us check if the suggested method is productive in the clearly expressed latter case. Simultaneously, we will be able to evaluate the upper limit for the mutual deviations of spectra between the binary and optimal single synthetic stars. For this purpose, we selected real A1V- and M6-type stars from the LAMOST DR5 catalog. Such stars are the most different in the catalog. For more information on them, see Table 1. The maximum of the continuum in the spectrum of the A1V star is located in the short-wavelength region, while in the spectrum of the M6 star it is at long wavelengths (see Figure 1). The sum of the spectra of such a pair will differ from the spectrum of a star of any spectral type. However, the latter difference will be not large, if the radiation flux of one of the stars is much lower than that from the companion. The difference is at the maximum, if the fluxes are equal. In order to illuminate the latter case, the fluxes were "equalized" by multiplication of one of the spectra by an appropriate factor. The spectra of both stars and the combined spectrum of the artificial binary are shown in the upper panel of Figure 1. The combined spectrum has two maxima situated at the edges of the LAMOST spectrograph's working range.

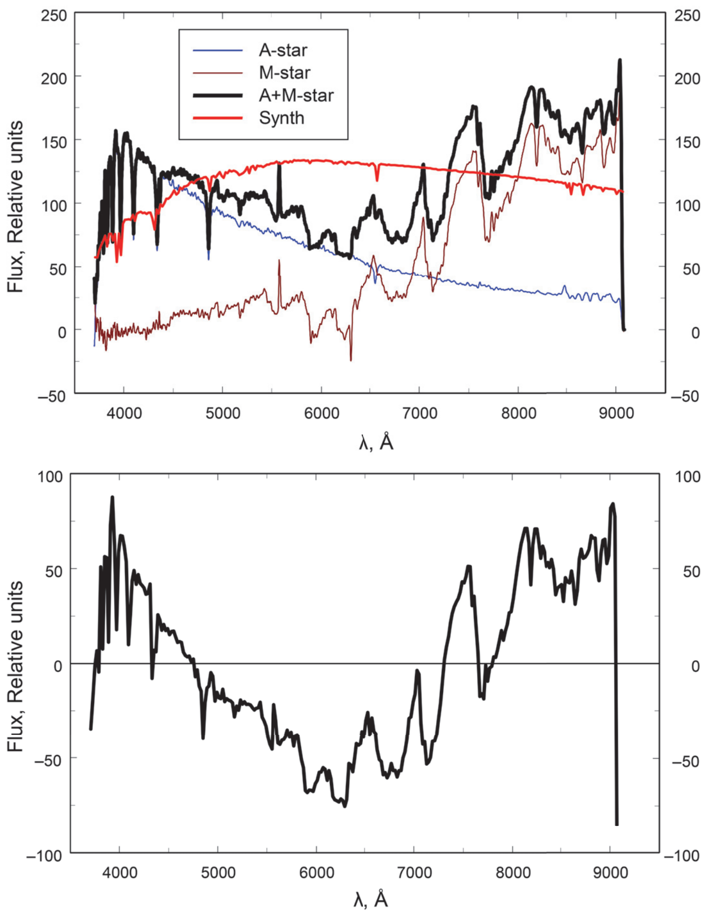

Figure 1. Upper panel—the combination of spectra of stars belonging to A1V and M6 spectral types from the LAMOST catalog as a spectrum of an unresolved binary with equal radiation fluxes from both components and the closest synthetic spectrum from the Castelli–Kurucz library (CKL). Lower panel—the difference between the spectrum of the unresolved binary with A1V and M6 components shown in the upper panel and the closest synthetic spectrum from CKL.

Table 1. Stars from the LAMOST DR5 catalog.

Obs_ID	Designation	α	δ	Sp.
404058	J004541.11 + 405100.1	11.421	40.850	A1V
113226	J221422.57 + 005400.8	333.594	0.900	M6

We searched for the optimal synthetic spectrum for all possible combinations of the parameters T_{eff}, $\log g$, and [Fe/H] available in the New Grids library of ATLAS9 Model Atmospheres [49] (hereafter the Castelli–Kurucz library (CKL); see Section 4.2 below). Interstellar extinction was incrementally increased by $\Delta A_v = 0.1$ from 0 to 1. The spectrum with the following parameters was found optimal:

$$T_{\mathrm{eff}} = 5500\ \mathrm{K}, \log g = 2.5, [\mathrm{Fe/H}] = -1.5, A_v = 1.0.$$

It is also shown in the upper panel of Figure 1. Naturally, this spectrum has a single maximum located between the maxima of the "binary's" combined spectrum, near the middle of the working range of the LAMOST survey.

The difference between the combined spectrum of the "binary" and the optimal synthetic spectrum (lower panel of Figure 1) has a "wave-like" shape with a rather large amplitude: the rms deviation for a point of the synthetic spectrum is as large as 37% of the mean signal level. This value, close to rms, may be accepted as an estimate of the upper limit for the possible deviation between the spectra in our approach. Figure 1 suggests that, in principle, the applied method may be used to search for stellar duplicity.

To establish a threshold between low and high levels of deviations between spectra, a statistical analysis is needed. For this purpose, we selected two special star samples from the LAMOST catalog, so it was known for the first of them from *a priori* information that the stars were single and for the second of them that the stars were binary.

4.2. The Library of Synthetic Spectra

The spectra in the CKL were computed for 1221 wavelengths between 9.09 nm and 160 μm. The main parameters of stellar atmospheres in the library vary within the following limits:

- T_{eff} takes 76 values from 3500 K to 50,000 K. The increment in T_{eff} is not uniform: it increases from $\Delta T = 250$ K for low temperatures to $\Delta T = 1000$ K for high temperatures;
- $\log g$ takes 11 values, from 0 to 5, with the uniform increment $\Delta \log g = 0.5$;
- Not every combination of these two parameters is possible; the allowed combinations form a triangle in the T_{eff}—$\log g$ plane. See Castelli and Kurucz [49] for details;
- [Fe/H] takes values from -1.5 to $+0.5$, with a uniform increment $\Delta[\mathrm{Fe/H}] = 0.5$.

We use only a part of a particular synthetic spectrum within the LAMOST sensitivity range 3700 Å $< \lambda <$ 9097 Å. This interval contains 270 points of the synthetic spectra from the CKL library with wavelengths 3710 Å $\lesssim \lambda \lesssim$ 9090 Å.

4.3. Removal of the Outliers at the Edges of LAMOST Spectra

Each LAMOST spectrum contains 3908 data points in the 3699.9863 Å $< \lambda <$ 9097.04 Å range. We use complete spectra.

Rather frequent defects of the LAMOST spectra are outliers at the long-wavelength edge of the spectrum. Among several hundred randomly selected spectra from the LAMOST archive that we viewed, outliers were present in ∼25–30% of the images. Synthetic spectra of stars with similar parameters in this region do not show any peculiarities in the behavior of the continuum. These outliers can be positive or negative and vary in width. An example of a spectrum with outliers is displayed in Figure 2, while one without outliers is shown in Figure 3 [5]. The reason for the occurrence of these emissions is unknown.

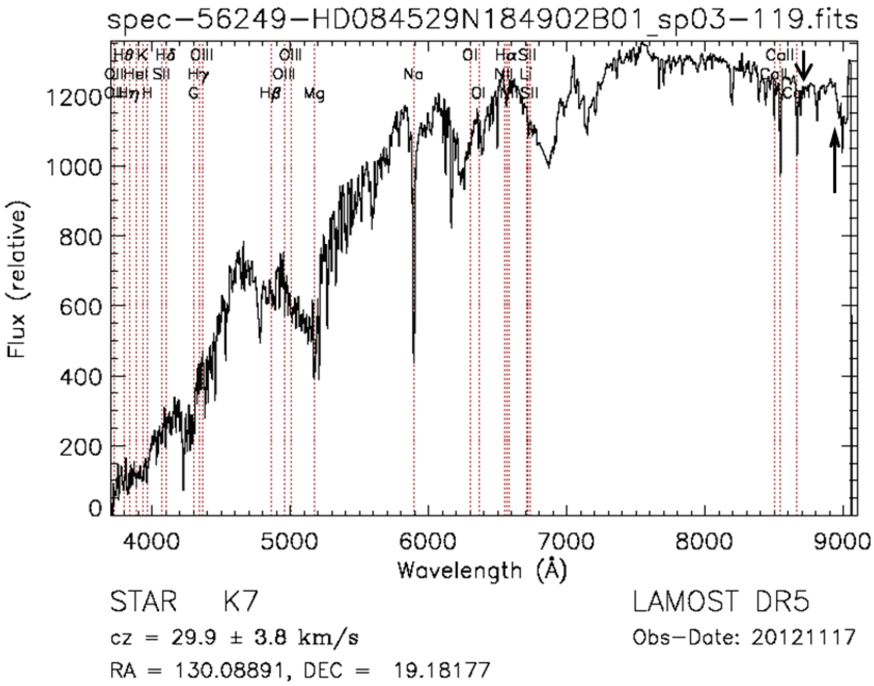

Figure 2. A LAMOST spectrum with outliers. Vertical dotted lines in this and the next figure mark the wavelengths of several spectral lines. The down arrow indicates the short-wave boundary of the region at the edge of the spectrum in which outliers are sought. The up arrow is the short-wave edge of the outlier in the presented spectrum.

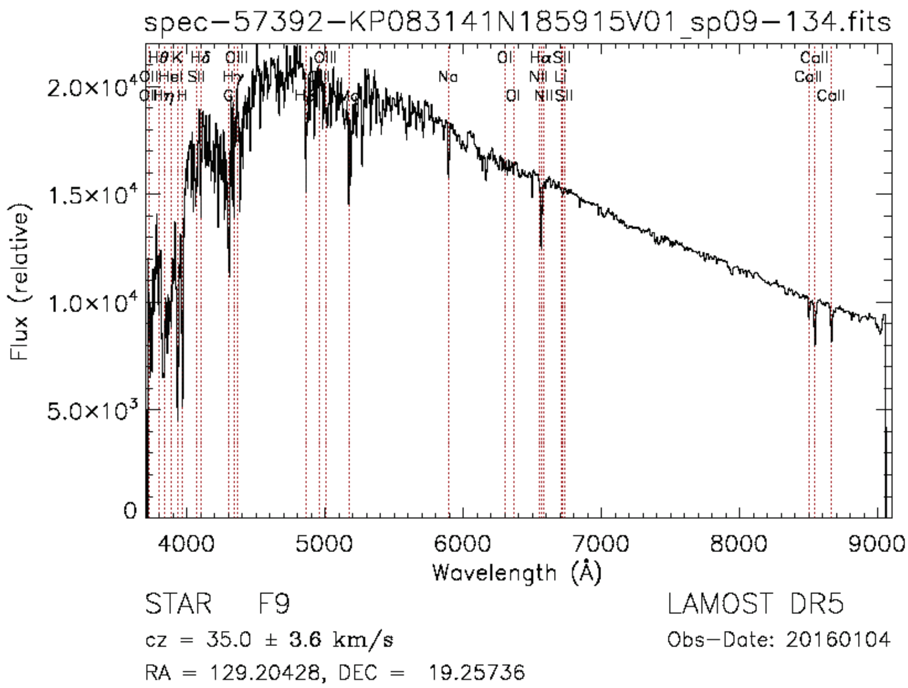

Figure 3. A LAMOST spectrum without outliers.

We detect the presence of an outlier in the following way:

- We check whether there is an outlier in the $\lambda > \lambda_{\rm right} = 8700$ Å range. This value is chosen based on the results of visual analysis of the spectra.
- We search a data point λ_R in the spectrum, closest to $\lambda_{\rm right}$ at longer λ. For most LAMOST spectra, the corresponding wavelength is $\lambda_R = 8701.62$ Å. The flux at this λ is $F_R = F(\lambda_R)$.

- If at any point of the LAMOST spectrum with $\lambda_i > \lambda_R$, the deviation of the flux from F_R exceeds the pre-selected value, ε, i.e., $\mathrm{mod}(F(\lambda_i)/F_R - 1)) > \varepsilon$, we assume that an outlier is present. In this study, we accept $\varepsilon = 0.2$.

If an outlier is detected, we reject the part of the spectrum with $\lambda > \lambda_R$, since there are no strong stellar lines in the 8700 Å $< \lambda <$ 9100 Å range of stellar spectra.

4.4. Interpolation and Normalization of the Spectra

LAMOST spectra and synthetic spectra in the CKL are defined for different wavelength sets. In addition, the set of λs in the LAMOST spectra is more than ten times larger than in the CKL synthetic spectra. Therefore, we interpolate the latter to the LAMOST set of wavelengths. Next, we smooth the LAMOST spectra in order to reduce the discrepancies in spectral comparisons. We use smoothing because the LAMOST spectra are quite noisy (see Figures 2 and 3). We apply a moving average using a triangular profile of weights according to the formula

$$\langle F_i \rangle = \frac{\sum\limits_{j=i-s}^{i+s} \left(1 - \frac{|i-j|}{s}\right) F_j}{2s+1}. \qquad (1)$$

Here, i, j are the numbers of data points in the spectrum; s is the smoothing width, taken as a parameter. We compute the smoothed spectrum for the same wavelengths as those in the initial LAMOST spectrum. A side effect of this procedure is removal of narrow and not very intense lines from the LAMOST spectra.

At the edges of the LAMOST spectra, at $i < i_{\mathrm{min}}^{(\mathrm{LAMOST})} + s$ or $i > i_{\mathrm{max}}^{(\mathrm{LAMOST})} - s$, no smoothing was applied.

We tried the smoothing parameters $s = 0$ (no smoothing), $s = 3$, and $s = 10$ and found that without smoothing the discrepancy in the comparison of spectra is noticeably larger, while with $s = 3$ and $s = 10$ the results are comparable. Further calculations were carried out with $s = 3$.

At the next stage, we interpolated the smoothed spectra to the set of wavelengths of the synthetic spectra within the LAMOST sensitivity range. Piecewise linear interpolation was used. We designate fluxes in the interpolated spectrum as $\tilde{F}_{i^{(\mathrm{CKL})}}$.

When comparing the spectra, we had to not only reduce them to a common set of wavelengths but also perform their normalization. We left the fluxes in the interpolated LAMOST spectra $F_i^{(\mathrm{CKL})}$ without changes. The values of fluxes in the synthetic spectrum were multiplied by the coefficient:

$$C = \frac{\sum_{j=i_{\mathrm{min}}^{(\mathrm{CKL})}}^{i_{\mathrm{max}}^{(\mathrm{CKL})}-1} F_j^{(\mathrm{CKL})}}{\sum_{j=i_{\mathrm{min}}^{(\mathrm{CKL})}}^{i_{\mathrm{max}}^{(\mathrm{CKL})}-1} \tilde{F}_j^{(\mathrm{CKL})}}. \qquad (2)$$

4.5. Four-Parameter Representation of Stellar Synthetic Spectra Taking into Account Interstellar Reddening

We did not vary additional parameters that influenced appearance of the spectra less than T_{eff}, $\log g$, and [Fe/H]. The ranges and increments of these parameters in the CKL library are described in Section 4.2. For the value of turbulent velocity in the photosphere, we assumed v_{turb} = 2.0 km/s. Stellar axial rotation was not taken into account.

The observed spectrum of a star can differ from the synthetic one because of interstellar extinction; its amount, described by the parameter A_V, is the fourth parameter in the total representation of stellar spectra.

To take into account interstellar reddening, we used the law suggested by Cardelli et al. [72]. In the LAMOST sensitivity range, it is described by the following relations:

$$
\begin{aligned}
&x = 1/\lambda_{\mu}, \\
&y = -1.82, \\
&a(x) = 1 + 0.17699y - 0.50447y^2 - 0.02427y^3 + 0.72085y^4 \\
&\qquad\quad +0.01979y^5 - 0.77530y^6 + 0.32999y^7, \\
&b(x) = 1.41338y + 2.28305y^2 + 1.07233y^3 - 5.38434y^4 \\
&\qquad\quad -0.62251y^5 + 5.30260y^6 - 2.09002y^7, \\
&\frac{A(\lambda)}{A_V} = a(x) + \frac{b(x)}{R_V}, \\
&R_V \equiv \frac{A_V}{E_{B-V}}.
\end{aligned}
\tag{3}
$$

We applied the standard assumption that the ratio R_V was constant, namely, $R_V = 3.1$. For the wavelength corresponding to the V band, we assumed $\lambda_V = 550$ nm. The four-parameter (4D) set of spectra was computed for all spectra of the CKL library in the following way:

1. For every star, we subdivided the range of possible values of interstellar absorption $[A_{V,\min}, A_{V,\max}]$ into $n(A_V) = 20$ intervals, and for every input synthetic spectrum from the CKL library we computed 21 spectra with different values of A_V.
2. Next, we formed the relative absorption line, i.e., for all 270 wavelengths of CKL spectra that were within the LAMOST range (see Section 4.2) we computed $A(\lambda)$ using Equation (3) with $A_V = 1$.
3. For a particular star, we found the acceptable range of interstellar absorption, $[A_{V,\min}, A_{V,\max}]$. The edges of this interval depended on stellar coordinates α, δ, which were well known and presented in the LAMOST catalog, and on the distance to the star d absent in the catalog.
   To determine the distance d, we used several approaches:
   (a) The majority of stars from the LAMOST catalog could be identified with the stars from the Gaia DR3 catalog [12,73] that currently contains the most accurate stellar parallaxes $\varpi^{(G)}$ and their uncertainties $\sigma_{\varpi}^{(G)}$. Using them, we computed possible limits for the distance to the star:
   $$d_{\min} = \frac{1}{\varpi^{(G)} + 3\sigma_{\varpi}^{(G)}}, \qquad d_{\max} = \frac{1}{\varpi^{(G)} - 3\sigma_{\varpi}^{(G)}}. \tag{4}$$
   If the computed $d_{\min}$ turned out to be negative, we set $d_{\min} = 0$.
   (b) If a LAMOST star had no identification in the Gaia DR3 catalog, then, for some single stars, we took information on the distance or interstellar absorption directly from the original catalogs (see Section 3.2).
   (c) If identification of a LAMOST star with the Gaia DR3 catalog and any information on the distance to it were lacking, we assumed $d_{\min} = 0, d_{\max} = 5$ Kpc.
4. The values of $d_{\min}$ and $d_{\max}$ together with the stellar coordinates α and δ were uploaded to the site http://stilism.obspm.fr (accessed on 5 December 2024), where an interactive procedure permitting us to determine the interstellar reddening E_{B-V} from a 3D map of interstellar absorption described in Lallement et al. [74], Capitanio et al. [75], Lallement et al. [76] is possible. This procedure returns the limits of interstellar reddening, $E_{B-V,\min}$, $E_{B-V,\max}$, possible for the star, with corresponding distances $d_{\min}$ and $d_{\max}$ and the limiting distance d_{stil} covered by the interactive interstellar

absorption map on the site. When $d_{\max} > d_{stil}$, we assumed $d_{\max} = 2 \times d_{stil}$, having in mind that factor 2 results in the maximum possible absorption for barometric dependence of the latter on the z-coordinate.

5. We recomputed the derived limits of the interstellar reddening E_{B-V} into the limits of the interstellar absorption $A_{V,\min} = R_V E_{B-V,\min}$ and $A_{V,\max} = R_V E_{B-V,\max}$.
6. For every spectrum from the CKL library defined by the parameters $T_{\rm eff}$, $\log g$, and [Fe/H], and for all wavelengths in the sensitivity range of the LAMOST survey, we computed reddened spectra for the following values of interstellar absorption:

$$A_{V,i} = A_{V,\min} + i\frac{A_{V,\max} - A_{V,\min}}{n(A_V)}\,, \tag{5}$$

where the index i takes the values $i = 0 \ldots n(A_V)$ and where $n(A_V) = 20$ is the number of intervals into which the range of interstellar absorption is split. To compute the intensity of light for the reddened synthetic spectrum, we used the Pogson [77] formula $I(A_{V,i}, \lambda) = 10^{-0.4A(\lambda)A_{V,i}} i_{CKL}(\lambda)$, where $i_{CKL}(\lambda)$ are intensities of stellar light given in the CKL library without account of the interstellar absorption.

Above, we described the part of the procedure we developed where we estimated the limits of interstellar absorption for a particular star using data not contained in the LAMOST catalog itself.

Certainly, uncertainties and systematic trends in the LAMOST flux calibration may also affect the results we obtain. Taking them into account is very important. However, we do not have the necessary initial data to study this influence. We assumed that the standard calibrations of the spectra in the LAMOST project were carried out with the highest quality.

4.6. The Search for Optimal Synthetic Spectrum in the Four-Parameter Set of the Reddened Synthetic Spectra

The procedure of the search for the optimal synthetic spectrum in the 4-parameter set of the reddened synthetic spectra has two steps.

First, in the synthetic set generated for a particular LAMOST star (see Section 4.5), we search for the spectrum with minimum deviation from the observed spectrum. Second, we attempt to improve parameters of the synthetic spectrum by interpolation among the spectra of the 4-parameter set with the most similar parameters. Let us consider these steps one by one.

4.6.1. The Search for a Spectrum with the Lowest Rms Deviations in the 4-Parameter Set of Synthetic Spectra

We searched for the spectrum with lowest rms deviations from the observed LAMOST spectrum in the 4-parameter set of reddened synthetic spectra using two different techniques described below, along with their advantages and drawbacks.

First, we applied the discrete descent method. Implementation of this method has several steps:

1. For a selected LAMOST spectrum, we found in the CKL library a spectrum with the parameters $T_{\rm eff,0}$, $\log g_0$, and $[\rm Fe/H]_0$, closest to the catalog parameters $T_{\rm eff}^{\rm (LAMOST)}$, $\log g^{\rm (LAMOST)}$, and $[\rm Fe/H]^{\rm (LAMOST)}$. For the initial value of interstellar absorption $A_{V,0}$, we selected the value from the sequence of acceptable values provided by Formula (5) that was either the closest to the interstellar absorption corresponding to the star's mean parallax ϖ (if the star was identified with the Gaia catalog) or the closest to the mean interstellar absorption known from the other sources (see Section 4.5).

2. The so-called "current spectrum", containing intermediate optimization results, is introduced. We designate parameters of the current spectrum as $T_{\text{eff},i}$, $\log g_i$, $[\text{Fe/H}]_i$, and $A_{V,i}$ for the spectrum used at the first step of the optimization procedure $i = 0$.
3. The deviation σ_C is computed for the current spectrum: $\sigma_C = \sigma(T_{\text{eff,i}}, \log g_i, [\text{Fe/H}]_i, A_{V,i})$.
4. We compute deviations for eight adjacent spectra, σ_{near8}, that differ from the current spectrum by their value of one of the parameters in the 4-parameter set of synthetic spectra. For example, $\sigma_{T+} = \sigma(T_{\text{eff},i+1}, \log g_i, [\text{Fe/H}]_i, A_{V,i})$ is the deviation for the spectrum with $\log g_i$, $[\text{Fe/H}]_i$, and $A_{V,i}$ similar to those of the current spectrum, but T_{eff} is the closest one, exceeding $T_{\text{eff},i}$. If the parameters of the current spectrum are at the edge of the 4D set, i.e., are at the maximum or minimum possible level, then the current spectrum will have only one neighbor in this direction.
5. If the deviation for one of these neighbor spectra is lower than that for the current spectrum, $\min(\sigma_{near8}) < \sigma_C$, then the spectrum with the lowest deviation is chosen as the current spectrum, and the minimization procedure returns to step 3.
6. If $\sigma_C \leq \min(\sigma_{near8})$, we additionally calculate deviations for 72 adjacent spectra, σ_{near72}, so that these spectra simultaneously have from 2 to 4 parameters differing from the current spectrum by one step. Similarly to calculating deviations σ_{near8}, if the current point is at the edge of the 4D distribution of the parameters, it will have less than 72 additional neighbors. If the deviation for one of adjacent spectra of the additional set is lower than that for the current spectrum, $\min(\sigma_{near72}) < \sigma_C$, then we select the spectrum with the lowest deviation as the current spectrum. The minimization procedure returns to step 3.
7. If $\sigma_C \leq \min(\sigma_{near72})$, the procedure of the search for the spectrum with the minimum rms deviation in the 4-parameter set is completed, and the desired spectrum $F^{(opt)}$ is contained in the current spectrum.

Second, we applied the method of exhaustive search, by which we computed deviations for all reddened spectra of the 4-parameter set and selected the one with the lowest deviation.

4.6.2. Comparison of the Methods

The discrete descent method is faster than the method of exhaustive search by almost three orders of magnitude. Performing the exhaustive search is, from a computational point of view, the most effort-consuming part of the technique we applied.

The exhaustive search is guaranteed to find the global extremum of the multi-dimensional deviation function $\sigma(T_{\text{eff}}, \log g, [\text{Fe/H}], A_V)$ at a discreet and limited parameter grid, no matter how many local extrema there are.

The discrete descent method is able to find the global extremum in two cases. First, if the deviation function is monotonous, i.e., if it possesses a single extremum in its domain, the result of optimization will not depend on the choice of the initial spectrum. Second, if the deviation function possesses several local minima and one of them, namely, the deepest one, is the global minimum, we will find the global extremum only if the parameters of the starting spectrum happen to be on the slopes of the global extremum.

It turns out that the methods of discrete descent and exhaustive search give different results in approximately 10 to 15% of all cases, when the deviation function has several extrema and the starting spectra are different. Unfortunately, we had to reject the discrete descent method and apply the much more effort-taking, but guaranteed successful, exhaustive search.

4.7. Improving the Optimal Spectrum by Interpolation Between Adjacent Spectra

At the previous stage, we used the optimization procedure to find in the 4-parameter set of reddened synthetic spectra the spectrum with the lowest deviation from that of the program star in the LAMOST catalog. However, we can try to improve this "optimal" spectrum by means of interpolation between the selected spectrum and its neighbors with the closest parameters.

We used an iteration procedure for finding the optimal combination of two adjacent reddened synthetic spectra by one of their four parameters, to obtain the minimum deviation. The interpolation was performed using the piecewise linear technique:

$$F(\alpha, i, \lambda, \mathbf{P}) = \frac{(1-\alpha)F(P_i^{(opt)\pm 1}) - \alpha F(P_i^{(opt)})}{P_i^{(opt)\pm 1} - P_i^{(opt)}}\,, \tag{6}$$

where α is the interpolation parameter $(0 \leq \alpha \leq 1)$; $\mathbf{P}$ are the four parameters describing reddened synthetic spectra; i is the number of the parameter used to perform interpolation (1—$T_{\rm eff}$, 2—$\log g$, 3—[Fe/H], 4—A_V), and $(opt) \pm 1$ means that the interpolation can be performed toward the larger optimal parameter, "$+$", as well as toward the smaller parameter, "$-$".

However, our modeling shows that linear interpolation of this kind does not give any considerable reduction in the deviation. Probably, this is the result of rather large fluctuations of real stellar spectra compared to their computed synthetic analogs.

In this work, the refinement of the optimal spectrum by interpolation between adjacent spectra was not used.

5. Presentation of Results of Comparison Between Synthetic and LAMOST Spectra for Single and Binary Stars

For a quantitative evaluation of results of comparison between observed and optimized synthetic spectra, we applied the following proximity criterion:

$$\sigma = \frac{\sqrt{\frac{1}{N}\sum\limits_{i=1}^{N}\left(F(\lambda_i)^{(opt)} - F(\lambda_i)^{(LAMOST)}\right)^2}}{\frac{1}{N}\sum\limits_{i=1}^{N} F(\lambda_i)^{(LAMOST)}}\,. \tag{7}$$

The value of σ is the dimensionless ratio of the rms deviation and its mean value. To make the discussion more transparent, we express σ in percent. The algorithm we developed was applied to the compiled test lists of stars. The upper panel of Figure 4 shows the histogram of the distribution of 278 spectra of 166 single stars from the Main_Single list (see Section 3.2) over rms deviations between the observed LAMOST spectrum and the corresponding optimal synthetic spectrum.

The interval of rms $<$ 15%, displayed in Figure 4, contains 255 spectra of single stars. In addition, there are 23 spectra with rms $>$ 15% not shown in the figure. Partially, large deviations are due to the technical flaws of these spectra (lacking observations for a part of the recorded LAMOST wavelength range, outliers, etc.), and partially, they are due to the individual peculiarities of stellar spectra. The right edge of the diagram (rms = 15%) was selected for clear demonstration of the distribution.

Since, according to the method we developed, binary stars should have significantly larger rms deviations compared to single stars, we marked in the histogram two characteristic levels of rms deviations: rms = 5.5% and 6.5%. In the main list of single stars, 46 spectra out of 278 (17%) have rms $<$ 5.5%; 96 spectra of 278 (35%) have rms $<$ 6.5%.

The middle panel of Figure 4 displays the histogram for the same single stars as in the upper panel and the histogram for bona fide binary stars from the SB9 catalog. The latter were processed in the same way as the LAMOST stars. For a more clear presentation, we artificially increased the actual height of the histogram columns for binaries by a factor of five.

For all binaries, rms $<$ 15%, so, they are visible in the diagram. The distribution of binary stars over the rms deviations is more compact than for single stars. In the list of binary stars from the SB9 catalog, rms $<$ 5.5% have 8 spectra out of 11 (73%), and rms $<$ 6.5% have 10 spectra out of 11 (91%). Thus, the rms deviations for binary stars from the SB9 catalog do not stand out by their rms deviations compared to the single stars from the main list of objects from the LAMOST catalog.

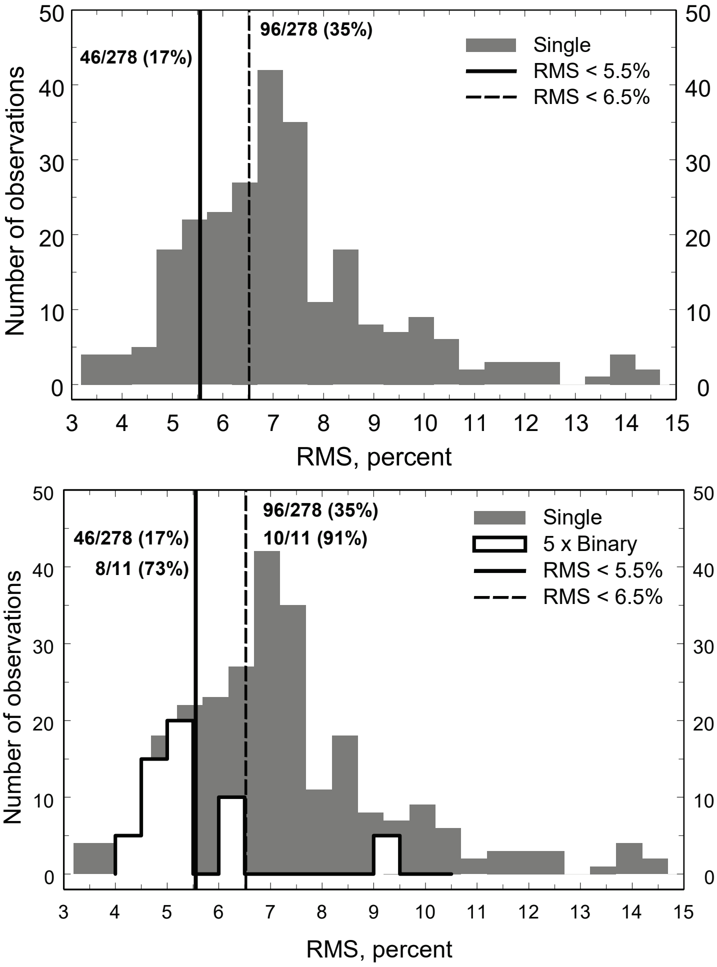

Figure 4. Upper panel—distribution of 278 observations of 166 single stars from the Main_Single list over rms residual deviations. Vertical lines indicate characteristic levels of rms = 5.5% and 6.5%.

We additionally process the LAMOST spectra for two lists of stars identified in the Gaia DR3 catalog. The first list, Gaia_Single, contains stars that have no indications of unresolved binarity in their astrometric and photometric characteristics in Gaia DR3 according to [60], and they are most likely single stars. The procedure for obtaining this list of stars is presented in Section 3.3.1. The Gaia_Single list contains 6220 stars.

The second list, Gaia_Binary, contains stars that do not have significant indications of unresolved binarity according to the Gaia DR3 catalog. The procedure for obtaining this list of stars is given in Section 3.4 above. The Gaia_Binary list contains 2278 stars. The stars in this list are most likely unresolved binaries.

Figure 5 shows histograms of rms distributions of stars from the Gaia_Single and Gaia_Binary lists. For each histogram, 1000 stars from each list were randomly selected. The histogram bin width is 0.25. The distributions are almost identical: the average values are $\langle rms_{Singl} \rangle = 6.3$ and $\langle rms_{Bin} \rangle = 6.2$. The distribution of unresolved binary stars is slightly wider: standard deviations are $\sigma_{Singl} = 3.4$ and $\sigma_{Bin} = 4.2$. Beyond the right edge of the figure ($rms > 10.0$) there are 60 single and 63 unresolved binary stars out of 1000.

Thus, the binary and single stars from the Gaia DR3 catalog differ only slightly and do not stand out in their rms against the background of the Main_Single stars considered above.

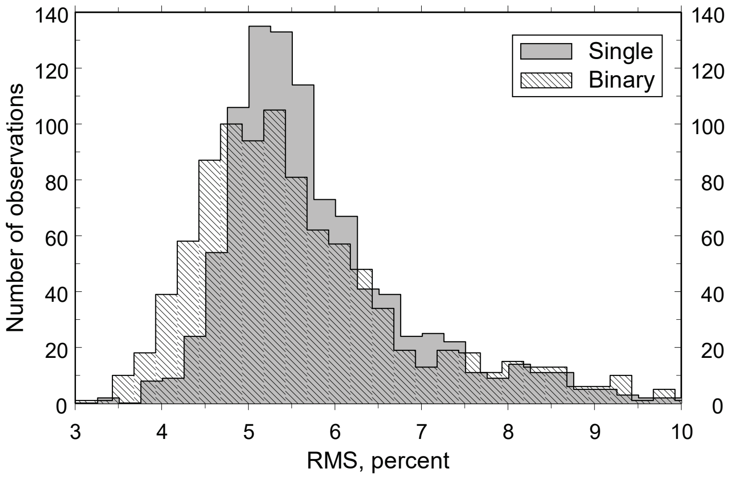

Figure 5. Distribution of 1000 putative single stars (gray histogram) and 1000 putative unresolved binaries (shaded histogram) from the Gaia DR3 catalog. Bin width 0.25.

6. Conclusions

We have suggested a method to find binary stars among LAMOST sources, based on the comparison between the continuum of the stellar spectrum of the LAMOST catalog and a synthetic spectrum, with interstellar reddening taken into account. It has been demonstrated that this method is not effective enough in its version described above and is apparently not able to distinguish between single and binary stars in the LAMOST catalog.

The possible directions of further studies are as follows:

1. Compilation of a special version of the CKL synthetic spectra library, with wavelengths exactly coinciding with those in the LAMOST spectra. Using such spectra would eliminate procedures of smoothing and interpolation, leading to lower rms deviations between the observed and synthetic spectra and to better sensitivity of the method. However, computation of stellar spectra library is a stand-alone problem.
2. Switching to a method based on a comparison of intensities for pairs of spectral lines or intensities for individual lines. The first of these methods is currently the most widely used approach for high-accuracy spectral classification of stars. The second approach is used for spectral classification of stars in the LAMOST project proper. However, the LAMOST survey provides low-resolution stellar spectra, and such methods can also turn out to be not sensitive to stellar binarity.

Author Contributions: Conceptualization, N.S., K.T., O.M. and G.Z.; methodology, K.T., S.S., A.L., D.K. and G.Z.; software, P.K. and S.S.; validation, M.P.; investigation, L.Y.; resources, A.L., J.Z., Y.L., Y.S. and G.Z.; data curation, K.T., A.L., J.Z., Y.L., Y.S. and G.Z.; writing-original draft preparation, N.S.; writing—review and editing, M.P., K.T., N.S., A.L., D.K., J.Z., Y.L., P.K., O.M., Y.S., S.S., L.Y. and G.Z.; visualization, S.S., P.K. and K.T.; supervision, M.P. and K.T.; project administration, M.P. All authors have read and agreed to the published version of the manuscript.

Funding: G.Z. is supported by the National Natural Science Foundation of China (NSFC) under grant No. 11988101 and by the National Key R&D Program of China No. 2024YFA1611900. K.T. is supported by the NSFC under grant Nos. 12261141689, 12090044, and 12090040. Y.L. is supported by the NSFC under grant No. 12073044. O.M. thanks the CAS President's International Fellowship Initiative (PIFI).

Guoshoujing Telescope (the Large Sky Area Multi-Object Fiber Spectroscopic Telescope LAMOST) is a National Major Scientific Project built by the Chinese Academy of Sciences. Funding for the project has been provided by the National Development and Reform Commission. LAMOST is operated and managed by the National Astronomical Observatories, Chinese Academy of Sciences. The study was conducted under the state assignment of Lomonosov Moscow State University.

Data Availability Statement: No new data were created or analyzed in this study. Data sharing is not applicable to this article.

Acknowledgments: This research has made use of the VizieR catalog access tool, CDS, Strasbourg, France. This work has made use of data from the European Space Agency (ESA) mission Gaia (https://www.cosmos.esa.int/gaia, accessed on 24 July 2025), processed by the Gaia Data Processing and Analysis Consortium (DPAC, https://www.cosmos.esa.int/web/gaia/dpac/consortium, accessed on 24 July 2025). Funding for the DPAC has been provided by national institutions, in particular the institutions participating in the Gaia Multilateral Agreement. The use of TOPCAT, an interactive graphical viewer and editor for tabular data [78], is acknowledged. We are grateful to our anonymous reviewers whose constructive comments greatly helped us to improve the paper.

Conflicts of Interest: The authors declare no conflicts of interest.

Notes

1 An estimate exceeding 100% means that binaries are components of triples.
2 Ref. [51] (http://sb9.astro.ulb.ac.be, accessed on 24 July 2025).
3 https://sl.voxastro.org/ (accessed on 24 July 2025)
4 http://archive.stsci.edu/prepds/stisngsl/ (accessed on 24 July 2025).
5 Both spectra are taken from the LAMOST DR5 site.

References

1. Duchêne, G.; Kraus, A. Stellar Multiplicity. *Annu. Rev. Astron. Astrophys.* **2013**, *51*, 269–310. [CrossRef]
2. Moe, M.; Di Stefano, R. Mind Your Ps and Qs: The Interrelation between Period (P) and Mass-ratio (Q) Distributions of Binary Stars. *Astrophys. J. Suppl. Ser.* **2017**, *230*, 15. [CrossRef]
3. Merle, T. Dancing with the Stars: A Review on Stellar Multiplicity. *Bull. Soc. R. Sci. Liege* **2024**, *93*, 170–214. [CrossRef]
4. Cifuentes, C.; Caballero, J.A.; González-Payo, J.; Amado, P.J.; Béjar, V.J.S.; Burgasser, A.J.; Cortés-Contreras, M.; Lodieu, N.; Montes, D.; Quirrenbach, A.; et al. CARMENES input catalogue of M dwarfs: IX. Multiplicity from close spectroscopic binaries to ultra-wide systems. *Astron. Astrophys.* **2025**, *693*, A228. [CrossRef]
5. Tutukov, A.V.; Yungelson, L.R. Evolutionary Scenario for Close Binary Systems of Low and Moderate Masses. *Nauchnye Informatsii* **1981**, *49*, 3.
6. Kroupa, P.; Tout, C.A.; Gilmore, G. The effects of unresolved binary stars on the determination of the stellar mass function. *Mon. Not. RAS* **1991**, *251*, 293–302. [CrossRef]
7. Kroupa, P. On the variation of the initial mass function. *Mon. Not. RAS* **2001**, *322*, 231–246. [CrossRef]
8. El-Badry, K.; Rix, H.W.; Ting, Y.S.; Weisz, D.R.; Bergemann, M.; Cargile, P.; Conroy, C.; Eilers, A.C. Signatures of unresolved binaries in stellar spectra: Implications for spectral fitting. *Mon. Not. RAS* **2018**, *473*, 5043–5049. [CrossRef]
9. Borodina, O.I.; Seleznev, A.F.; Carraro, G.; Danilov, V.M. Unresolved Binaries and Galactic Clusters' Mass Estimates. *Astrophys. J.* **2019**, *874*, 127. [CrossRef]
10. Sullivan, K.; Kraus, A.L. Undetected Binary Stars Cause an Observed Mass-dependent Age Gradient in Upper Scorpius. *Astrophys. J.* **2021**, *912*, 137. [CrossRef]
11. Prusti, T. et al. [Gaia Collaboration] The Gaia mission. *Astron. Astrophys.* **2016**, *595*, A1. [CrossRef]
12. Vallenari, A. et al. [Gaia Collaboration] Gaia Data Release 3. Summary of the content and survey properties. *Astron. Astrophys.* **2023**, *674*, A1. [CrossRef]
13. Almeida, A.; Anderson, S.F.; Argudo-Fernández, M.; Badenes, C.; Barger, K.; Barrera-Ballesteros, J.K.; Bender, C.F.; Benitez, E.; Besser, F.; Bird, J.C.; et al. The Eighteenth Data Release of the Sloan Digital Sky Surveys: Targeting and First Spectra from SDSS-V. *Astrophys. J. Suppl. Ser.* **2023**, *267*, 44. [CrossRef]
14. Castro-Ginard, A.; Penoyre, Z.; Casey, A.R.; Brown, A.G.A.; Belokurov, V.; Cantat-Gaudin, T.; Drimmel, R.; Fouesneau, M.; Khanna, S.; Kurbatov, E.P.; et al. Gaia DR3 detectability of unresolved binary systems. *arXiv* **2024**. [CrossRef]

15. Penoyre, Z.; Belokurov, V.; Evans, N.W. Astrometric identification of nearby binary stars—II. Astrometric binaries in the Gaia Catalogue of Nearby Stars. *Mon. Not. RAS* **2022**, *513*, 5270–5289. [CrossRef]
16. Malofeeva, A.A.; Mikhnevich, V.O.; Carraro, G.; Seleznev, A.F. Unresolved Binaries and Multiples in the Intermediate Mass Range in Open Clusters: Pleiades, Alpha Per, Praesepe, and NGC 1039. *Astron. J.* **2023**, *165*, 45. [CrossRef]
17. Chulkov, D.; Prokhorov, M.; Malkov, O.; Sichevskij, S.; Krussanova, N.; Mironov, A.; Zakharov, A.; Kniazev, A. Detection of unresolved binaries with multicolor photometry. *Balt. Astron.* **2015**, *24*, 137–143. [CrossRef]
18. Wallace, A.L. Photometric determination of main-sequence binaries with Gaia. *Mon. Not. RAS* **2024**, *527*, 8718–8726. [CrossRef]
19. Xiang, M.; Rix, H.W.; Ting, Y.S.; Zari, E.; El-Badry, K.; Yuan, H.B.; Cui, W.Y. Data-driven Spectroscopic Estimates of Absolute Magnitude, Distance, and Binarity: Method and Catalog of 16,002 O- and B-type Stars from LAMOST. *Astrophys. J. Suppl. Ser.* **2021**, *253*, 22. [CrossRef]
20. Kovaleva, D.A.; Malkov, O.Y. On the possible multiplicity of the components of some low-mass systems. *Astron. Rep.* **1999**, *43*, 80–88.
21. Luo, A.L.; Zhao, Y.H.; Zhao, G.; Deng, L.C.; Liu, X.W.; Jing, Y.P.; Wang, G.; Zhang, H.T.; Shi, J.R.; Cui, X.Q.; et al. The first data release (DR1) of the LAMOST regular survey. *Res. Astron. Astrophys.* **2015**, *15*, 1095. [CrossRef]
22. McMillan, P. BDASP Catalogue. 2020. Available online: https://doi.org/10.17876/RAVE/DR.6/008 (accessed on 24 July 2025). [CrossRef]
23. Buder, S.; Sharma, S.; Kos, J.; Amarsi, A.M.; Nordlander, T.; Lind, K.; Martell, S.L.; Asplund, M.; Bland-Hawthorn, J.; Casey, A.R.; et al. The GALAH+ survey: Third data release. *Mon. Not. RAS* **2021**, *506*, 150–201. [CrossRef]
24. Jönsson, H.; Holtzman, J.A.; Prieto, C.A.; Cunha, K.; García-Hernández, D.A.; Hasselquist, S.; Masseron, T.; Osorio, Y.; Shetrone, M.; Smith, V.; et al. APOGEE Data and Spectral Analysis from SDSS Data Release 16: Seven Years of Observations Including First Results from APOGEE-South. *Astron. J.* **2020**, *160*, 120. [CrossRef]
25. Abdurro'uf; Accetta, K.; Aerts, C.; Silva Aguirre, V.; Ahumada, R.; Ajgaonkar, N.; Filiz Ak, N.; Alam, S.; Allende Prieto, C.; Almeida, A.; et al. The Seventeenth Data Release of the Sloan Digital Sky Surveys: Complete Release of MaNGA, MaStar, and APOGEE-2 Data. *Astrophys. J. Suppl. Ser.* **2022**, *259*, 35. [CrossRef]
26. Gilmore, G.; Randich, S.; Asplund, M.; Binney, J.; Bonifacio, P.; Drew, J.; Feltzing, S.; Ferguson, A.; Jeffries, R.; Micela, G.; et al. The Gaia-ESO Public Spectroscopic Survey. *Messenger* **2012**, *147*, 25–31.
27. Randich, S.; Gilmore, G.; Gaia-ESO Consortium. The Gaia-ESO Large Public Spectroscopic Survey. *Messenger* **2013**, *154*, 47–49.
28. Li, J.; Ting, Y.S.; Rix, H.W.; Green, G.M.; Hogg, D.W.; Ren, J.J.; Müller-Horn, J.; Seeburger, R. Identification of 30,000 White Dwarf-Main Sequence binaries candidates from Gaia DR3 BP/RP(XP) low-resolution spectra. *arXiv* **2025**. [CrossRef]
29. Seeburger, R.; Rix, H.W.; El-Badry, K.; Xiang, M.; Fouesneau, M. Autonomous disentangling for spectroscopic surveys. *Mon. Not. RAS* **2024**, *530*, 1935–1955. [CrossRef]
30. Birko, D.; Zwitter, T.; Grebel, E.K.; Parker, Q.A.; Kordopatis, G.; Bland-Hawthorn, J.; Freeman, K.; Guiglion, G.; Gibson, B.K.; Navarro, J.; et al. Single-lined Spectroscopic Binary Star Candidates from a Combination of the RAVE and Gaia DR2 Surveys. *Astron. J.* **2019**, *158*, 155. [CrossRef]
31. Price-Whelan, A.M.; Hogg, D.W.; Rix, H.W.; Beaton, R.L.; Lewis, H.M.; Nidever, D.L.; Almeida, A.; Badenes, C.; Barba, R.; Beers, T.C.; et al. Close Binary Companions to APOGEE DR16 Stars: 20,000 Binary-star Systems Across the Color-Magnitude Diagram. *Astrophys. J.* **2020**, *895*, 2. [CrossRef]
32. Traven, G.; Feltzing, S.; Merle, T.; Van der Swaelmen, M.; Čotar, K.; Church, R.; Zwitter, T.; Ting, Y.S.; Sahlholdt, C.; Asplund, M.; et al. The GALAH survey: Multiple stars and our Galaxy. I. A comprehensive method for deriving properties of FGK binary stars. *Astron. Astrophys.* **2020**, *638*, A145. [CrossRef]
33. Merle, T.; Van der Swaelmen, M.; Van Eck, S.; Jorissen, A.; Jackson, R.J.; Traven, G.; Zwitter, T.; Pourbaix, D.; Klutsch, A.; Sacco, G.; et al. The Gaia-ESO Survey: Detection and characterisation of single-line spectroscopic binaries. *Astron. Astrophys.* **2020**, *635*, A155. [CrossRef]
34. Cui, X.Q.; Zhao, Y.H.; Chu, Y.Q.; Li, G.P.; Li, Q.; Zhang, L.P.; Su, H.J.; Yao, Z.Q.; Wang, Y.N.; Xing, X.Z.; et al. The Large Sky Area Multi-Object Fiber Spectroscopic Telescope (LAMOST). *Res. Astron. Astrophys.* **2012**, *12*, 1197–1242. [CrossRef]
35. Zhao, G.; Zhao, Y.H.; Chu, Y.Q.; Jing, Y.P.; Deng, L.C. LAMOST spectral survey—An overview. *Res. Astron. Astrophys.* **2012**, *12*, 723–734. [CrossRef]
36. Li, C.q.; Shi, J.r.; Yan, H.l.; Fu, J.N.; Li, J.d.; Hou, Y.H. Double- and Triple-line Spectroscopic Candidates in the LAMOST Medium-Resolution Spectroscopic Survey. *Astrophys. J. Suppl. Ser.* **2021**, *256*, 31. [CrossRef]
37. Guo, Y.; Li, J.; Xiong, J.; Li, J.; Wang, L.; Xiong, H.; Luo, F.; Hou, Y.; Liu, C.; Han, Z.; et al. The Binarity of Early-type Stars from LAMOST medium-resolution Spectroscopic Survey. *Res. Astron. Astrophys.* **2022**, *22*, 025009. [CrossRef]
38. Qian, S.B.; Shi, X.D.; Zhu, L.Y.; Li, L.J.; Zhang, J.; Zhao, E.G.; Han, Z.T.; Zhou, X.; Fang, X.H.; Liao, W.P. More than two hundred and fifty thousand spectroscopic binary or variable star candidates discovered by LAMOST. *Res. Astron. Astrophys.* **2019**, *19*, 064. [CrossRef]

39. Chen, Y.; Xia, F.; Wang, X.; Fu, Y.; Yuan, Y. New SB1s with Spectroscopic Orbits from LAMOST-LRS. *Astrophys. J. Suppl. Ser.* **2023**, *269*, 41. [CrossRef]
40. Liu, C.; Bailer-Jones, C.A.L.; Sordo, R.; Vallenari, A.; Borrachero, R.; Luri, X.; Sartoretti, P. The expected performance of stellar parametrization with Gaia spectrophotometry. *Mon. Not. RAS* **2012**, *426*, 2463–2482. [CrossRef]
41. Ting, Y.S.; Conroy, C.; Rix, H.W.; Cargile, P. Prospects for Measuring Abundances of >20 Elements with Low-resolution Stellar Spectra. *Astrophys. J.* **2017**, *843*, 32. [CrossRef]
42. Li, J.; Wong, K.W.K.; Hogg, D.W.; Rix, H.W.; Chandra, V. AspGap: Augmented Stellar Parameters and Abundances for 37 Million Red Giant Branch Stars from Gaia XP Low-resolution Spectra. *Astrophys. J. Suppl. Ser.* **2024**, *272*, 2. [CrossRef]
43. Luo, A.L.; Zhao, Y.H.; Zhao, G.; Deng, L.-C.; Liu, X.-W.; Jing, Y.-P.; Wang, G.; Zhang, H.-T.; Shi, J.-R.; Cui, X.-Q.; et al. VizieR Online Data Catalog: LAMOST DR5 catalogs (Luo+, 2019). *VizieR Online Data Catalog* **2019**, V/164.
44. Bai, Z.R.; Zhang, H.T.; Yuan, H.L.; Fan, D.W.; He, B.L.; Lei, Y.J.; Dong, Y.Q.; Yu, S.C.; Zhao, Y.H.; Zhang, Y.; et al. The first data release of LAMOST low-resolution single-epoch spectra. *Res. Astron. Astrophys.* **2021**, *21*, 249. [CrossRef]
45. Pavlovski, K.; Hensberge, H. Reconstruction and Analysis of Component Spectra of Binary and Multiple Stars. In Proceedings of the Binaries—Key to Comprehension of the Universe, Brno, Czech Republic, 8–12 June 2009; Prša, A., Zejda, M., Eds.; Astronomical Society of the Pacific Conference Series; Astronomical Society of the Pacific: San Francisco, CA, USA, 2010; Volume 435, p. 207. [CrossRef]
46. Hełminiak, K.G.; Tokovinin, A.; Niemczura, E.; Pawłaszek, R.; Yanagisawa, K.; Brahm, R.; Espinoza, N.; Ukita, N.; Kambe, E.; Ratajczak, M.; et al. Orbital and physical parameters of eclipsing binaries from the All-Sky Automated Survey catalogue. X. Three high-contrast systems with secondaries detected with IR spectroscopy. *Astron. Astrophys.* **2019**, *622*, A114. [CrossRef]
47. Furlan, E.; Howell, S.B. Unresolved Binary Exoplanet Host Stars Fit as Single Stars: Effects on the Stellar Parameters. *Astrophys. J.* **2020**, *898*, 47. [CrossRef]
48. Cox, A.N. *Allen's Astrophysical Quantities*; Springer: New York, NY, USA, 2000.
49. Castelli, F.; Kurucz, R.L. New Grids of ATLAS9 Model Atmospheres. In *Modelling of Stellar Atmospheres*; Piskunov, N., Weiss, W.W., Gray, D.F., Eds.; Uppsala University: Uppsala, Sweden, 2003; Volume 210, p. A20. [CrossRef]
50. Du, B.; Luo, A.L.; Kong, X.; Zhang, J.N.; Guo, Y.X.; Cook, N.J.; Hou, W.; Yang, H.F.; Li, Y.B.; Song, Y.H.; et al. LAMOST Spectrograph Response Curves: Stability and Application to Flux Calibration. *Astrophys. J. Suppl. Ser.* **2016**, *227*, 27. [CrossRef]
51. Pourbaix, D.; Tokovinin, A.A.; Batten, A.H.; Fekel, F.C.; Hartkopf, W.I.; Levato, H.; Morrell, N.I.; Torres, G.; Udry, S. S_{B^9}: The ninth catalogue of spectroscopic binary orbits. *Astron. Astrophys.* **2004**, *424*, 727–732. [CrossRef]
52. Allen, L.E.; Strom, K.M. Moderate-Resolution Spectral Standards From lambda5600 to lambda9000 angstrom. *Astron. J.* **1995**, *109*, 1379. [CrossRef]
53. Prugniel, P.; Soubiran, C.; Koleva, M.; Le Borgne, D. New release of the ELODIE library: Version 3.1. *arXiv* **2007**. [CrossRef]
54. Valdes, F.; Gupta, R.; Rose, J.A.; Singh, H.P.; Bell, D.J. The Indo-US Library of Coudé Feed Stellar Spectra. *Astrophys. J. Suppl. Ser.* **2004**, *152*, 251–259. [CrossRef]
55. Falcón-Barroso, J.; Sánchez-Blázquez, P.; Vazdekis, A.; Ricciardelli, E.; Cardiel, N.; Cenarro, A.J.; Gorgas, J.; Peletier, R.F. An updated MILES stellar library and stellar population models. *Astron. Astrophys.* **2011**, *532*, A95. [CrossRef]
56. Heap, S.R.; Lindler, D.J. Hubble's Next Generation Spectral Library (NGSL). In *From Stars to Galaxies: Building the Pieces to Build Up the Universe*; Vallenari, A., Tantalo, R., Portinari, L., Moretti, A., Eds.; Astronomical Society of the Pacific Conference Series; Astronomical Society of the Pacific: San Francisco, CA, USA, 2007; Volume 374, p. 409.
57. Kornilov, V.; Mironov, A.; Zakharov, A. The WBVR Photometry of Bright Northern Stars. *Balt. Astron.* **1996**, *5*, 379–390. [CrossRef]
58. Wielen, R.; Schwan, H.; Dettbarn, C.; Lenhardt, H.; Jahreiß, H.; Jährling, R. Sixth Catalogue of Fundamental Stars (FK6). Part I. Basic fundamental stars with direct solutions. *Veroeffentlichungen Astron. Rechen-Instituts Heidelb.* **1999**, *35*, 1.
59. Fouesneau, M.; Frémat, Y.; Andrae, R.; Korn, A.J.; Soubiran, C.; Kordopatis, G.; Vallenari, A.; Heiter, U.; Creevey, O.L.; Sarro, L.M.; et al. Gaia Data Release 3. Apsis. II. Stellar parameters. *Astron. Astrophys.* **2023**, *674*, A28. [CrossRef]
60. Lindegren, L.; Klioner, S.A.; Hernández, J.; Bombrun, A.; Ramos-Lerate, M.; Steidelmüller, H.; Bastian, U.; Biermann, M.; de Torres, A.; Gerlach, E.; et al. Gaia Early Data Release 3. The astrometric solution. *Astron. Astrophys.* **2021**, *649*, A2. [CrossRef]
61. Riello, M.; De Angeli, F.; Evans, D.W.; Montegriffo, P.; Carrasco, J.M.; Busso, G.; Palaversa, L.; Burgess, P.W.; Diener, C.; Davidson, M.; et al. Gaia Early Data Release 3. Photometric content and validation. *Astron. Astrophys.* **2021**, *649*, A3. [CrossRef]
62. Belokurov, V.; Penoyre, Z.; Oh, S.; Iorio, G.; Hodgkin, S.; Evans, N.W.; Everall, A.; Koposov, S.E.; Tout, C.A.; Izzard, R.; et al. Unresolved stellar companions with Gaia DR2 astrometry. *Mon. Not. RAS* **2020**, *496*, 1922–1940. [CrossRef]
63. Gaia Collaboration; Arenou, F.; Babusiaux, C.; Barstow, M.A.; Faigler, S.; Jorissen, A.; Kervella, P.; Mazeh, T.; Mowlavi, N.; Panuzzo, P.; et al. Gaia Data Release 3. Stellar multiplicity, a teaser for the hidden treasure. *Astron. Astrophys.* **2023**, *674*, A34. [CrossRef]
64. Koleva, M.; Prugniel, P.; Bouchard, A.; Wu, Y. ULySS: A full spectrum fitting package. *Astron. Astrophys.* **2009**, *501*, 1269–1279. [CrossRef]

65. Sharma, K.; Prugniel, P.; Singh, H.P.; Koleva, M. Analysis of stellar spectra using ULySS. In *Astronomical Society of India Conference Series*; Prugniel, P., Singh, H.P., Eds.; Astronomical Society of India: Hyderabad, India, 2012; Volume 6, p. 257.
66. Hebb, L.; Cargile, P. SME@XSEDE: An automated spectral synthesis tool for stellar characterization. In *American Astronomical Society Meeting Abstracts #225*; American Astronomical Society: Washington, DC, USA, 2015; Volume 225, p. 138.13.
67. Rosario Franco, M.; Cargile, P.; Hebb, L.; Johnson, J.A. vis.SME—Building a Visualization Tool to Analyze and Share Spectral Synthesis Stellar Characterization. In *American Astronomical Society Meeting Abstracts #223*; American Astronomical Society: Washington, DC, USA, 2014; Volume 223, p. 347.36.
68. Piskunov, N. Deriving stellar parameters with the SME software package. In Proceedings of the Second BRITE-Constellation Science Conference: Small Satellites—Big Science, Innsbruck, Austria, 22–26 August 2016; Zwintz, K., Poretti, E., Eds.; Polish Astronomical Society: Warsaw, Poland, 2017; Volume 5, pp. 209–213.
69. Allende-Prieto, C.; Apogee Team. FERRE: A Code for Spectroscopic Analysis. In *American Astronomical Society Meeting Abstracts #225*; American Astronomical Society: Washington, DC, USA, 2015; Volume 225, p. 422.07.
70. Ting, Y.S.; Conroy, C.; Rix, H.W.; Cargile, P. The Payne: Self-consistent ab initio Fitting of Stellar Spectra. *Astrophys. J.* **2019**, *879*, 69. [CrossRef]
71. Koposov, S.E. RVSpecFit: Radial velocity and stellar atmospheric parameter fitting. In *Astrophysics Source Code Library, Record ascl:1907.013*; 2019. Available online: https://ascl.net/1907.013 (accessed on 24 July 2025).
72. Cardelli, J.A.; Clayton, G.C.; Mathis, J.S. The Relationship between Infrared, Optical, and Ultraviolet Extinction. *Astrophys. J.* **1989**, *345*, 245. [CrossRef]
73. Gaia Collaboration; Brown, A.G.A.; Vallenari, A.; Prusti, T.; de Bruijne, J.H.J.; Babusiaux, C.; Biermann, M.; Creevey, O.L.; Evans, D.W.; Eyer, L.; et al. Gaia Early Data Release 3. Summary of the contents and survey properties. *Astron. Astrophys.* **2021**, *649*, A1. [CrossRef]
74. Lallement, R.; Vergely, J.L.; Valette, B.; Puspitarini, L.; Eyer, L.; Casagrande, L. 3D maps of the local ISM from inversion of individual color excess measurements. *Astron. Astrophys.* **2014**, *561*, A91. [CrossRef]
75. Capitanio, L.; Lallement, R.; Vergely, J.L.; Elyajouri, M.; Monreal-Ibero, A. Three-dimensional mapping of the local interstellar medium with composite data. *Astron. Astrophys.* **2017**, *606*, A65. [CrossRef]
76. Lallement, R.; Capitanio, L.; Ruiz-Dern, L.; Danielski, C.; Babusiaux, C.; Vergely, L.; Elyajouri, M.; Arenou, F.; Leclerc, N. Three-dimensional maps of interstellar dust in the Local Arm: Using Gaia, 2MASS, and APOGEE-DR14. *Astron. Astrophys.* **2018**, *616*, A132. [CrossRef]
77. Pogson, N. Magnitudes of Thirty-six of the Minor Planets for the first day of each month of the year 1857. *Mon. Not. RAS* **1856**, *17*, 12–15. [CrossRef]
78. Taylor, M.B. TOPCAT & STIL: Starlink Table/VOTable Processing Software. In *Astronomical Data Analysis Software and Systems XIV*; Astronomical Society of the Pacific Conference Series; Shopbell, P., Britton, M., Ebert, R., Eds.; Astronomical Society of the Pacific: San Francisco, CA, USA, 2005; Volume 347, p. 29.

galaxies

Article

A New Activity Cycle of V1413 Aql

Anna Tatarnikova, Andrey Tatarnikov *, Nataliia Maslennikova, Alexander Dodin, Marina Burlak, Natalia Ikonnikova, Alexander Belinski and Georgy Nikishev

Sternberg Astronomical Institute, Lomonosov Moscow State University, Universitetskii Prospekt, 13, Moscow 119234, Russia; anna.2005@mail.ru (A.T.); maslennikova.na16@physics.msu.ru (N.M.); dodin_nv@mail.ru (A.D.); mburlak@sai.msu.ru (M.B.); ikonnikova@gmail.com (N.I.); aleks@sai.msu.ru (A.B.); nikishevge@my.msu.ru (G.N.)
* Correspondence: andrew@sai.msu.ru

Abstract: V1413 Aql is an anomalous classical symbiotic star that has remained in an active state almost continuously. After failing to return to quiescence following the 2020 outburst, it underwent a new flare in 2025. We present an analysis of new photometric and spectroscopic observations, which provide estimates for the binary components at different stages of activity: $L_{\rm cool} = 1700\,\rm L_\odot$, $R_{\rm cool} = 130\,\rm R_\odot$; $L_{\rm hot} = 800\,\rm L_\odot$, $R_{\rm hot} = 28\,\rm R_\odot$ during minimum; $L_{\rm hot} = 7000\,\rm L_\odot$, $R_{\rm hot} = 64\,\rm R_\odot$ at the 2025 maximum. The significant increase in the luminosity of the hot component during the 2025 outburst deviates from the typical behavior observed in classical symbiotic stars, where outbursts are generally attributed to a redistribution of spectral energy rather than intrinsic changes in luminosity.

Keywords: symbiotic stars; observations; spectroscopy; variable stars; V1413 Aql

1. Introduction

V1413 Aql (≡AS 338) was discovered on objective-prism plates obtained by [1]. A distinctive feature of its spectrum at that time was the presence of strong Hα emission. In [2], it was suspected that the star could be a symbiotic star. However, it was not until 1978 that Allen obtained a detailed spectrum of V1413 Aql, revealing its symbiotic nature. This spectrum showed not only bright emission lines—including those from ions with high ionization potentials, such as He II—but also molecular absorption bands. As a result, the star was included in the first catalog of symbiotic stars [3]: interacting binary systems composed of a cool giant (or supergiant) and a hot companion, surrounded by a nebula of gas and dust.

Further spectral observations carried out between 1981 and 2025, as reported by several authors ([4] and references therein), showed that the spectrum obtained by Allen corresponded to a rare quiescent state of V1413 Aql. Spectra of a similar appearance were recorded only in 1993 [5] and 2017 [4]. Notably, each quiescent state lasted no more than six months—although never less than three months. The difference between the spectra of the quiescent and active states of V1413 Aql is striking, yet it remains typical for classical symbiotic stars (SySts). In quiescence, the SED can be fitted using the standard three-component model [6]: a hot component with a temperature of $T \approx 10^5$ K (well visible in the UV range, though its contribution in the optical is not detectable against the general background), a cool giant, and a nebula. In classical SySts, the transition to an active state—associated with the expansion of the burning shell—leads to a significant brightening of the hot component, making it the dominant source of optical radiation. Its SED resembles that of an A-F type star [7]. There is also observational evidence suggesting that this hot component has a disk-like structure (see, for example, [8], who analyzed eclipses of the flared hot component in the classical SySt CI Cyg).

The oldest photometric observations of V1413 Aql were compiled by [9]. Notably, the smooth light curve typical of classical SySts in quiescence was revealed only after folding sparse data from 1962 to 1967. In subsequent years, narrow and sharp minima appeared in the light curve—features characteristic of classical eclipses of the hot component by the red giant (see, for example, [10]). Based on V-band photometry obtained between 1982 and 1988, four such eclipse events were detected and the orbital period of the system was determined to be 434 d [11]. Spectral observations by [12] confirmed that the object was in an active state in 1983: high-ionization emission lines had disappeared from the spectrum, while molecular absorption bands of the cool component were overwhelmed by the radiation of the flaring hot component.

It should be noted that outbursts of classical SySts generally follow a fairly consistent scenario [7]: a rapid brightening over several months, a slower decline lasting multiple orbital periods, and long quiescent intervals between successive outbursts—typically ten years or more. In this context, V1413 Aql represents an anomalous case. Throughout the period of dense photometric monitoring since 1982, the star has entered a short-lived quiescent state only twice. Moreover, new outbursts may commence before the hot component has fully returned to quiescence—as was observed in 2009 [13]. A similar pattern has emerged during the current phase of increasing activity, which is the focus of the present study.

The distance to V1413 Aql was estimated at $D = 6$ kpc by [14]. We note that the Gaia parallax distance for the system is $8.8^{+2.2}_{-1.7}$ kpc [15]; however, the large value of the RUWE = 2.46 suggests that the distance estimate from [14] is more reliable. For both distance estimates, the map of interstellar reddening [16] yields a color excess of $E(B-V) = 0.56 \pm 0.04$. This value is consistent within the error bars with the color excess $E(B-V) = 0.50 \pm 0.05$ derived by [14] from the He II $\lambda1640/\lambda4686$ emission-line flux ratio. In the following, we adopt a distance of 6 kpc and a color excess of $E(B-V) = 0.50$. The impact of uncertainties in these values will be discussed in the conclusion.

This study presents an analysis of photometric and spectroscopic observations carried out between 2023 and 2025, covering the transition of V1413 Aql from a low-activity state—which did not fully resemble a classical quiescent phase—to its current rise in brightness, marking the onset of a new outburst.

2. Observations

Photometric observations of V1413 Aql were conducted from 2019 to 2025 using the 60 cm ASA RC600 telescope (ASA DDM160 mount, Astro Systeme Austria (ASA), Lieboch, Austria) of CMO of the Sternberg Astronomical Institute. The observations were carried out with an Andor iKon-L DZ936N-BV camera (Photonic Science Limited, East Sussex, UK). The image scale in the focal plane is $\sim 0.7''$ per pixel. A detailed description of the telescope can be found in [17]. Brightness measurements were performed using differential aperture photometry, with TYC 1585-1513-1 selected as the primary comparison star. The following magnitudes were adopted for this star: $U = 14.15 \pm 0.02$, $B = 12.99 \pm 0.01$, $V = 11.69 \pm 0.02$, $Rc = 10.97 \pm 0.01$ and $Ic = 10.31 \pm 0.01$.

Spectroscopic observations were carried out from 2020 to 2025 using the TDS [18], mounted on the 2.5 m telescope of CMO. A slit width of $1''$ was used. Spectra were recorded simultaneously in the B-channel (wavelength range 360–577 nm, spectral resolving power R = 1300) and the R-channel (wavelength range 567–746 nm, spectral resolving power R = 2500). The log of observations is presented in Table 1.

Table 1. Log of spectroscopic observations of V1413 Aql.

Date, yyyy-mm-dd	t_{exp}, s (Channel)	SNR (at 5500 Å)	V, mag	Phase
2020-09-02	400 (B), 150 (R)	250	10.53	0.65
2023-05-04	600 (B), 1600 (R)	140	12.73	0.89
2023-06-11	1200 (B), 600 (R)	44	14.61	0.99
2023-08-18	1200 (B), 600 (R)	150	12.69	0.14
2025-05-07	1200 (B), 600 (R)	340	10.55	0.58

3. Photometric Analysis

Figure 1 shows the V-band light curve of V1413 Aql, based on our new observations (Table 1) and previously published data [14,19–21]. During this period, we recorded four outbursts, with brightness maxima occurring in 1995, 2010, 2020, and 2025. No intermediate outbursts were detected between 1995 and 2010—a gap confirmed by photometric data from the AAVSO database.

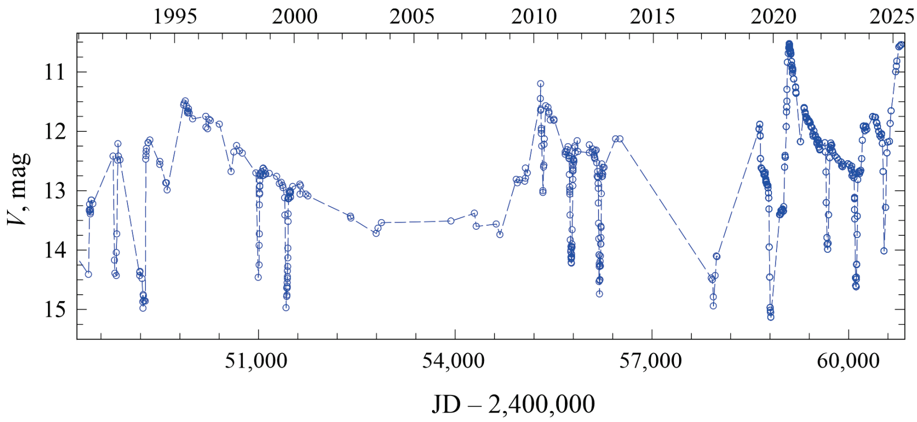

Figure 1. The V-band light curve of V1413 Aql (1991–2025).

During the 1995 and 2010 outbursts, the star reached a maximum brightness of approximately 11.5 mag, whereas the 2020 and 2025 outbursts were about one magnitude brighter at peak. In addition to difference in amplitude, these events also exhibited distinct light curve morphologies. The rise to maximum brightness in 1995 and 2010 was smooth and gradual, while the 2020 and 2025 outbursts showed a much more rapid brightening. The decline phases likewise differed: after the 1995 outburst, the brightness decreased by ~ 2 mag over approximately 8 years, whereas a similar 2 mag drop occurred within just 2.5 years following the 2020 outburst.

Over the 34 years of our photometric monitoring, we were able to observe 12 events in sufficient detail to reliably determine the time of minimum brightness for each. These measurements allowed us to refine the ephemeris of the binary system. For this purpose, we calculated the $(O - C)$ values for the observed times of eclipse minima. By varying the orbital period and the initial epoch, we then determined the values that minimized the sum of $(O - C)^2$:

$$JD_{\min} = 2,448,819.50_{\pm 1.5} + 434.45_{\pm 0.27} E, \quad (1)$$

where the primary minimum at phase $\varphi = 0$ corresponds to the eclipse of the hot component.

Figure 2 shows the $UBVRcIc$-band light curves of V1413 Aql, together with the evolution of the $B - V$ and $V - Ic$ color indice over the period 2019–2025. This interval is densely covered by our multi-color photometric observations and includes two major outbursts—in 2020 and 2025. Although these outbursts were similar in peak brightness, they differ significantly in their rise rates: in 2020, the brightening rate was

$\Delta V/\Delta t = 0.042$ mag/d and $\Delta Ic/\Delta t = 0.026$ mag/d, whereas in 2025, the rise was about three times slower. The variability amplitude in the *Ic* band was generally smaller, which is attributed to the fact that all observed events originate from the hot component, which contributes less flux in the red spectral region than in the blue.

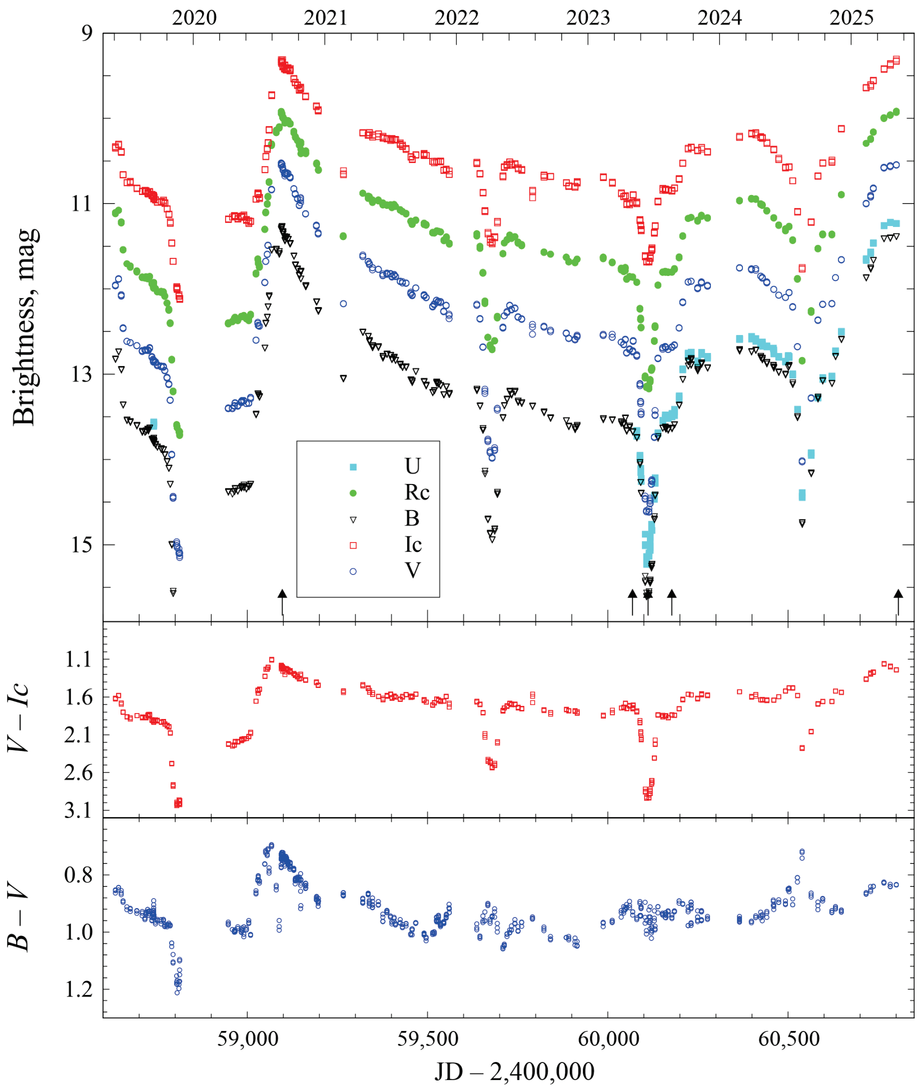

Figure 2. The U, B, V, Rc and Ic-band light and $B - V$, $V - Ic$ color curves of V1413 Aql (2019–2025). The arrows indicate the epochs of low-resolution spectra discussed in the paper.

In [21], a photometric criterion for quiescence was established based on a comparison of spectral and photometric data across different activity phases of V1413 Aql. According to this criterion, the hot component is considered to be in a quiescent state when $B - V \leq 0.68$. As shown in Figure 2, the $B - V$ color index approached this threshold value twice since 2019. Notably, one such episode occurred during the peak of the 2020 outburst. It is also worth noting that, despite the large brightness variations observed in the V band—with a total amplitude reaching nearly 5 mag—the $B - V$ color index remained relatively stable, varying only between 0.7 and 1.2. Moreover, the average $B - V$ value after 2021 remained at 0.94 ± 0.05, even during the 2025 outburst. This suggests that the system did not return to a true quiescent state after the 2020 outburst but rather transitioned directly into a new active phase.

Three primary eclipses occurred during the decline of the 2020 outburst, when the hot component was occulted by the cool giant. We focus on the 2023 minimum. Figure 3 shows the $UBVRcIc$ light and $U - B, B - V, Rc - Ic$ color curves over the phase interval ± 0.15 relative to the brightness minimum.

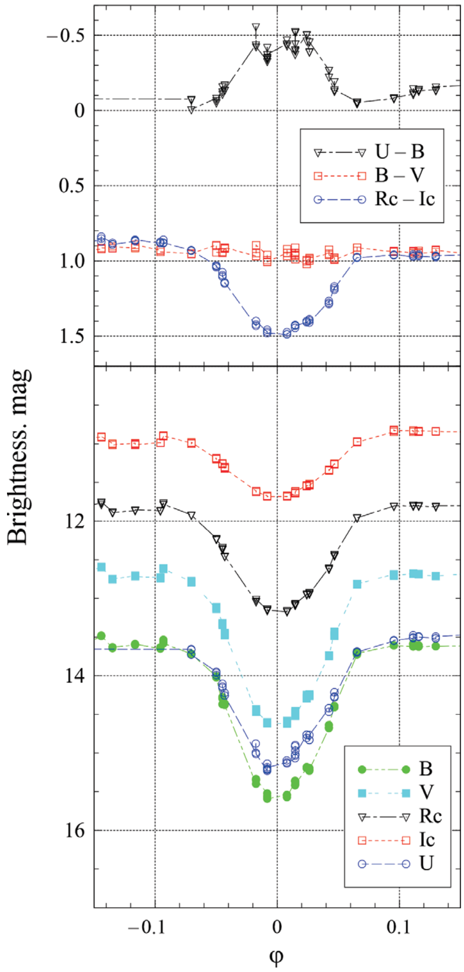

Figure 3. Phase-folded light and color curves of V1413 Aql during the 2023 minimum.

The depth of the 2023 minimum was measured as $\Delta U = 1.66 \pm 0.15$, $\Delta B = 1.97 \pm 0.03$, $\Delta V = 1.90 \pm 0.02$, $\Delta Rc = 1.35 \pm 0.02$, and $\Delta Ic = 0.84 \pm 0.04$. Taking into account the interstellar reddening of $E(B - V) = 0.50$, the dereddened magnitudes at minimum are $U_0 = 12.77$, $B_0 = 13.47$, $V_0 = 13.01$, $Rc_0 = 11.86$, $Ic_0 = 10.72$. The observed color indices during the eclipse differ significantly from those expected for a single red giant (see also the discussion below on the SED during the eclipse). This discrepancy suggests either a significant contribution from the nebular continuum or that the eclipse was not total. Furthermore, the light curve shape near minimum does not support a full eclipse of the hot component—no flat-bottomed minimum is observed, which would indicate a constant brightness level during totality. Using the extinction-corrected brightness of the star at minimum and the eclipse amplitude, we calculated the color indices of the eclipsed component to be $B - V = 0.40 \pm 0.05$, $V - Rc = 0.44 \pm 0.04$, $V - Ic = 0.77 \pm 0.06$. The $U - B$ color index is not considered diagnostic due to strong nebular emission in the blue spectral range. These values are consistent with a spectral type of F4–F7 for the hot component. However, the actual spectral type of the eclipsed component may be later due to the unaccounted contribution of emission lines (see discussion below).

The color behavior shown in Figure 3 is typical of V1413 Aql in its active state [22]. During eclipse, the object becomes bluer in the $U - B$ color index. This is because the flaring, eclipsed hot component contributes relatively redder emission in this spectral range compared to the nebular continuum. The $B - V$ color index remains nearly unchanged relative to the out-of-eclipse level, despite a photometric amplitude of almost 2 mag in the V band. In contrast, the star reddens in $Rc - Ic$, indicating that during eclipse, the red part of the spectrum is dominated by emission from the M5–M6 giant companion.

Assuming a total eclipse duration of $\Delta\varphi = 0.15$ and considering the eclipse to be central, the sum of the component radii in units of the semi-major axis a is $R_{\rm giant} + R_{\rm hot} = 0.47a$, which is consistent with the estimate obtained by [22].

4. Spectroscopic Analysis

The epochs of the spectra discussed below are indicated in Figure 2. Two spectra were obtained at the maxima of the 2020 and 2025 outbursts; two were taken before and after the primary eclipse minimum in 2023; and one was recorded during the eclipse itself. All spectra were normalized so that their convolution with the V passband matched the photometric measurements shown in Figure 2. The spectra were then corrected for interstellar reddening using a color excess of $E(B - V) = 0.50$. Unless otherwise noted, all subsequent analyses—except those presented in Table 2—are based on these calibrated data.

For each spectrum, we measured fluxes in the selected emission lines and blends (see Table 2). The uncertainties in the flux measurements of weak lines—such as Fe II in the spectrum obtained during the eclipse—can reach up to 30%, primarily due to uncertainties in the continuum placement. For strong lines, the measurement errors do not exceed 10%. The relative contribution of emission lines to certain blends varies with orbital phase. During eclipse, forbidden nebular lines may become detectable in some blends, whereas they are usually overwhelmed by the emission from the hot component outside of eclipse.

During the 2023 eclipse minimum, V1413 Aql exhibited a local activity minimum, although the object had not fully returned to its quiescent state. At that time, the emission-line spectrum was dominated by Balmer hydrogen lines, with relatively strong He I features, as well as forbidden lines such as [O III], [Ne III], and others (see Table 2). Notably, the He II 4686 Å line—a spectral feature indicative of the quiescent state according to [21]—was not detected in any of our spectra.

The hydrogen lines show a clear phase dependence. Their fluxes during the minimum are nearly half of those measured outside eclipse. The dereddened Hα/Hβ flux ratio ranges from 3.8 (post-eclipse) to 4.4 (during eclipse). These values deviate significantly from the Case B recombination value ($\approx$2.8 [23]), even when accounting for the small contribution of [N II] lines to the Hα flux—in contrast to the rest of the Balmer decrement. Assuming optically thin emission, the Hβ flux allows us to estimate the emission measure of the corresponding region as $EM = 1.6 \times 10^{59} (D[\text{kpc}]/6[\text{kpc}])^2\,\text{cm}^{-3}$ (for the spectrum obtained on 4 May 2023 and adopting $T_e = 10,000$ K).

The fluxes of He I lines also drop significantly during the eclipse. The HeI flux ratios are entirely inconsistent with the standard Case B recombination values. These ratios cannot be reproduced by commonly used photoionization codes such as CLOUDY under any physically reasonable assumptions. This discrepancy is not unique to V1413 Aql but is a well-known issue across the entire class of symbiotic stars (see the comprehensive review by [24]). Notably, over the course of our observations of V1413 Aql, the He I $\lambda7065/\lambda5876$ flux ratio has varied by an order of magnitude ([4] and references therein). However, the pre- and post-eclipse He I fluxes observed in 2023 formally match the model by [24], assuming nebular parameters of $T_e = 20,000$ K, $n_e = 10^{12}\,\text{cm}^{-3}$, $\tau(\lambda3889) = 1$, and hot component properties of $T_{\rm hot} = 10^5$ K and $R_{\rm hot} = 0.1\,R_\odot$. These parameters are roughly consistent with those observed for V1413 Aql in its quiescent state [4]. However, according to [24], even an order-of-magnitude change in the number of ionizing photons affects the predicted He I flux ratios by only about 15%. We also note that the He I flux ratios observed during the eclipse correspond to lower electron densities of $n_e = 10^{10}\,\mathrm{cm}^{-3}$, which appears reasonable from a geometrical perspective of the eclipse configuration.

Table 2. Emission-line fluxes in units of $10^{-14}\,\mathrm{erg\,cm^{-2}\,s^{-1}}$ for V1413 Aql. A dash indicates that the line is absent from the spectrum, while the symbol "Y" denotes a weak feature for which a reliable flux measurement is not possible.

Lines	2023-05-04	2023-06-11	2023-08-18	2025-05-07
[Ne III] 3869	7.64	8.52	7.88	–
HI 3889	9.00	6.38	10.33	Y
H I 3970	4.60	7.67 (+[Ne III])	7.02 (+[Ne III])	Y
He I 4026	3.09	1.63	3.25	–
[S II] 4069, 4076	2.83	–	3.22	–
H I 4102	18.2	9.0	19.0	Y
H I 4340	33.0	14.4	30.5	192
Fe II 4352	–	0.75	–	Y
[O III] 4363	5.91	5.22	4.94	–
He I 4388	3.20	–	–	–
Fe II 4417	–	2.03	3.57	Y
He I 4471	6.81	3.55	7.23	–
Fe II 4489	–	1.33	3.29	Y
Fe II 4583	–	1.32	–	Y
Fe II 4631	–	1.48	3.08	Y
C III+N III+Fe II 4640	–	7.51	15.7	52.8
H I 4861	90.7	47.2	93.3	356
He I 4922 + Fe II 4924	5.14	2.42	5.11	78.8
[O III] 4959 + [Fe II] 4958	13.67	11.75	9.56	–
[O III] 5007	48.1	41.1	36.2	–
He I 5016 + Fe II 5018	9.61	5.05	9.84	104
[Fe II] 5044	3.07	–	–	–
Fe II 5173	–	–	–	145
Fe II 5201	–	–	–	54.5
Fe II 5317	3.57	2.50	4.67	72.6
Fe II 5535	2.08	–	–	Y
[N II] 5755	1.30	1.07	1.40	–
He I 5876	45.5	17.5	35.0	91
Fe II 5991	2.70	–	3.11	122
Fe II 6148	–	–	–	24.6
Fe II 6238	–	0.69	2.84	>10.2
Fe II 6248	–	0.87	2.14	>14.0
[O I] 6300	2.35	1.77	2.58	–
Fe II 6319	3.03	–	3.55	Y
Fe II 6384	3.26	0.87	3.23	Y
Fe II 6433, 6434	3.06	0.91	3.58	17.8
Fe II 6456	–	1.25	3.06	19.1
Fe II 6516, 6517	4.04	1.20	4.82	13.1
H I 6563 + [N II]	686	372	635	1771
He I 6677	20.1	5.22	16.2	–
He I 7065	28.8	13.8	22.0	–

Phase variations are also observed in the Fe II and [O I] lines, which are likely formed in the region near the hemisphere of the red giant illuminated by the hot component. However, the absence of radial velocity curves for individual emission lines in V1413 Aql hinders the development of a robust kinematic model of the nebular structure.

In contrast to the previously discussed lines, the nebular [O III] and [Ne III] lines show no phase dependence, indicating that they originate from a different region within the inhomogeneous nebula. The fluxes of these lines are consistent with the nebular parameters of T_e = 10,000–11,000 K and $n_e = 10^6\,\mathrm{cm}^{-3}$ [25], under the assumption of cosmic elemental abundances.

During the 2025 outburst maximum, the emission-line spectrum of V1413 Aql underwent dramatic changes compared to the relatively low-activity state observed in 2023—although that period was not fully quiescent. Not only had the forbidden [O III] and [Ne III] lines disappeared, but for the first time in our observational history, the He I lines were nearly undetectable against the continuum (except for the broad, blended He I 5876Å line, which is affected by the Na I doublet). The spectrum clearly showed hydrogen Balmer lines and a forest of Fe II features, all exhibiting complex, multi-component profiles. Figure 4 shows the Hα line profile, where a narrow emission component—possibly with a P Cygni-type shape—is superimposed on the broad bell-shaped base with a FWHM of approximately 1450 km/s. This narrow feature closely resembles the Hα line observed in 2023. Notably, a similar spectral appearance was previously reported for the symbiotic star V407 Cyg during its recurrent nova-like outburst [26], although the broad components of the lines in that case were about twice as wide as those seen in V1413 Aql. A certain resemblance in the Hα profile is also observed in the classical symbiotic star BF Cyg during its latest outburst [27], which the authors attribute to jet formation.

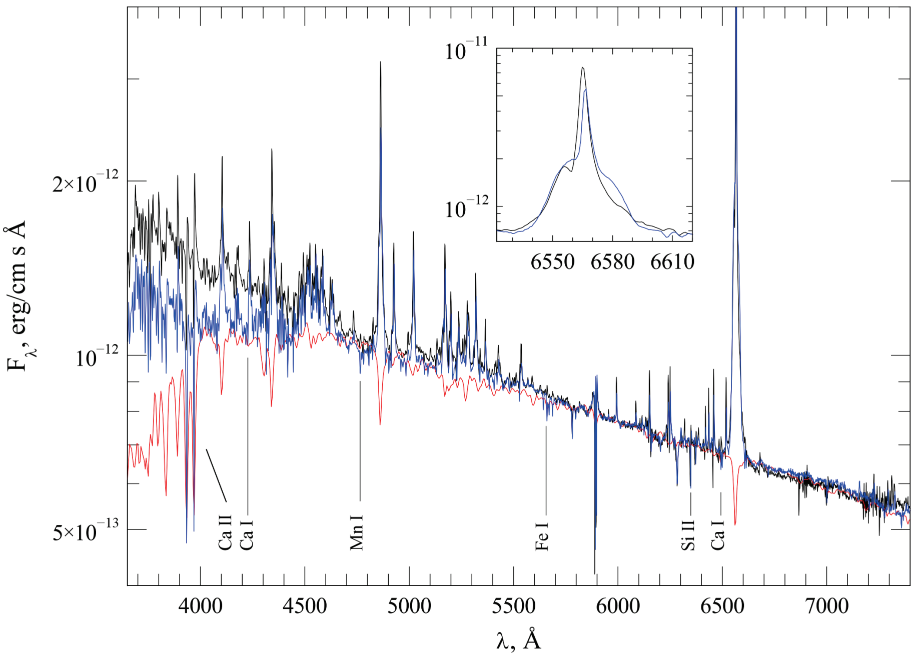

Figure 4. Dereddened spectra of V1413 Aql obtained during the maxima of the 2020 (2 September 2020, black line) and 2025 (7 May 2025, blue line) outbursts, compared to the spectrum of an F5 III star from [28] (red line).

The absorption features observed in the spectra of V1413 Aql can be divided into three groups. The first group consists of TiO absorption bands belonging to the spectrum of the cool component—an M5-M6 red giant. These bands are most clearly seen in the spectrum obtained on 11 June 2023, during the eclipse minimum (see the bottom spectrum in Figure 5). In contrast, in the spectra taken before and after this minimum (4 May and 18 August), the contribution of the red giant is barely detectable even in the red part of the spectrum—only the longest-wavelength TiO bands remain visible. During the outburst maximum (spectrum of 7 May 2025), molecular bands are almost entirely overwhelmed by the enhanced emission from the flaring hot component (see Figure 4).

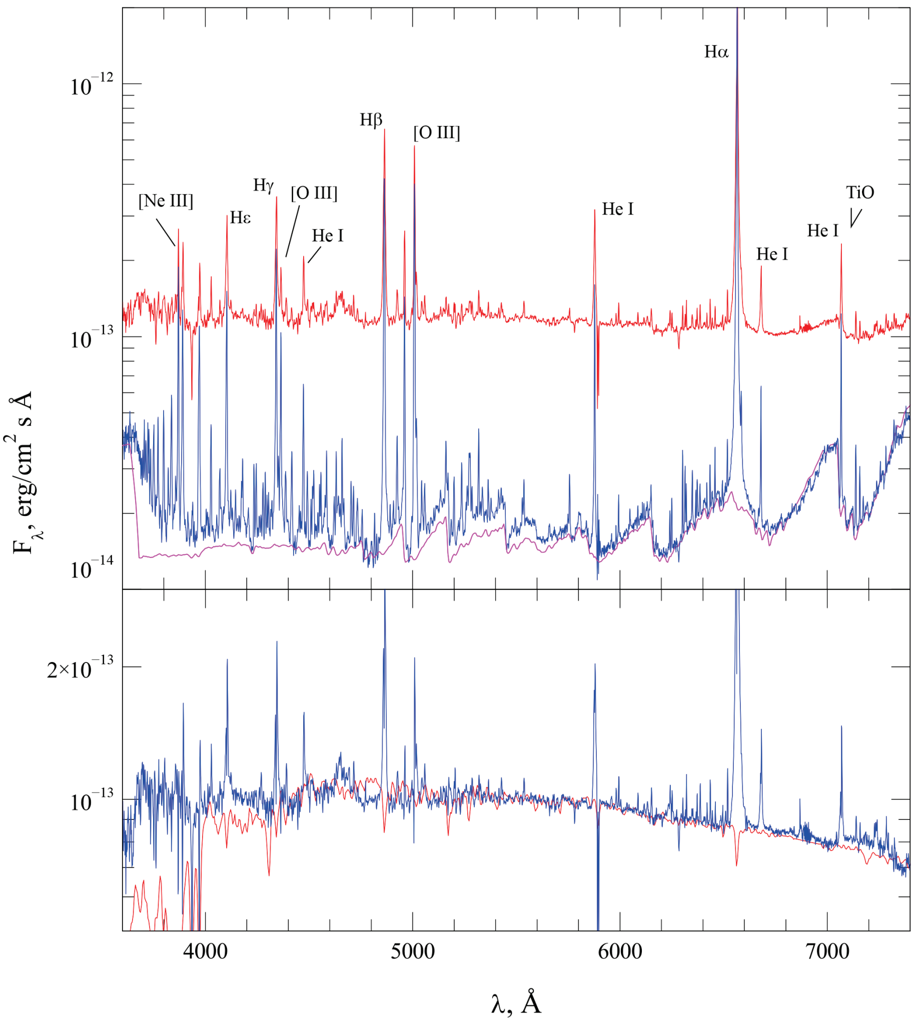

Figure 5. Upper panel: Dereddened spectra of V1413 Aql obtained on 4 May 2023 (red line, $\varphi = 0.89$) and 11 June 2023 (blue line, $\varphi \approx 0$). The magenta line represents the model continuum, composed of emission from a nebula with $T_e = 10,000$ K, an M6 III red giant, and a blackbody with $T_{\rm eff} = 8000$ K. Lower panel: The difference between the dereddened spectra of V1413 Aql obtained before the eclipse at $\varphi = 0.89$ and at minimum light (blue line). The red line shows the spectrum of a G0 III star from [28].

The second group consists of the absorption features associated with the interstellar medium. These features are not overwhelmed by the emission from the hot component and remain unaffected by either eclipses or changes in the activity state of the hot star. For example, the diffuse interstellar band at 6282 Å shows an equivalent width of $\geq$0.6 Å in all our spectra. According to [29], this result supports our adopted value of the color excess, $E(B-V) = 0.5$. We note that the Na I doublet lines likely have a complex structure, composed of both interstellar components and features related to the flaring hot component. The latter are significantly weakened during eclipse and may even show weak emission components. Since the Na I D1 and D2 lines lie within the wing of the He I 5876 Å line, they reduce the observed flux in this feature (this effect is accounted for in Table 2).

The third group consists of absorption features associated with the flaring hot component. These features are significantly weakened during the eclipse of the hot star. For example, the Ca II K line was clearly visible in absorption before and after the 2023 eclipse but nearly disappeared during the eclipse itself. The Ca II H line is not seen in absorption, likely due to blending with nearby emission features such as [Ne III] 3968 Å and H I 3970 Å. During the 2025 outburst, absorption lines typical of an F-type giant became clearly visible in the spectrum. Notably, the Si II lines at 6347 and 6371 Å exhibited P Cygni-type profiles.

Additional features included Ca I lines at 6494 and 6500 Å, among others (Figure 4). The hydrogen and Fe II absorption lines, which are typically prominent in the spectra of F-type stars, are veiled in our case by the nebular emission lines.

The spectra obtained at the maxima of the 2020 and 2025 outbursts are shown in Figure 4. They are nearly identical at wavelengths longer than 4500 Å. The SED in this range is well represented by the spectrum of an F5 III star [28]. Assuming that the hot component retains a similar spectral shape into the infrared, its luminosity can be estimated as $\sim$7000 $L_\odot$, with a characteristic radius $\lesssim$ 65 $R_\odot$.

The spectra of V1413 Aql obtained between outbursts show significant differences from those presented above. The red line in Figure 5 corresponds to the spectrum taken during the decline of activity prior to the 2023 eclipse (the post-eclipse spectrum from August 2023 is nearly identical and is not considered separately). Unfortunately, we lack coverage in the ultraviolet and infrared ranges, which limits our ability to estimate the luminosities of the system's components during this phase.

The spectrum obtained during the eclipse minimum at phase $\varphi = 0.99$ clearly shows the contribution of the cool component in the red part of the spectrum and nebular emission in the blue region. However, spectral modeling reveals that an additional source of continuum radiation is required to achieve a good match with the observed spectrum. In Figure 5, the blue line represents the observed spectrum during eclipse, while the magenta line shows its model approximation. The continuum emission of the model, which includes three components—an M6 III-type giant, a nebula with T_e =10,000–12,000 K, and an additional blackbody-like component with $T_{\rm eff}$ = 8000–10,000 K—differs from the observed SED corrected for interstellar extinction by no more than 20%. The luminosity of the cool component is $L_{\rm cool} = 1700\,L_\odot$, with a radius $R_{\rm cool} = 130\,R_\odot$. The blackbody component has a luminosity of $L_{\rm BB} = 70\,L_\odot$. It is worth noting that during the subsequent eclipse in 2024, discussed in detail by [30], a similar blackbody component was also detected but with a lower effective temperature of $T_{\rm eff} = 6000$ K.

The difference between the spectra shown in Figure 5 allows us to isolate the spectrum of the eclipsed hot component and, thus, estimate its parameters. The lower panel of Figure 5 presents this spectral difference together with the G0 III star template from [28]. The discrepancies between the spectra do not exceed 10% for all wavelengths longer than 4000 Å. Assuming that in the redder part of the spectrum the hot component resembles a G0 III star, we integrate the template spectrum to derive its bolometric flux. For a distance of 6 kpc, the luminosity of the hot component is estimated to be $L_{\rm hot} \approx 800\,L_\odot$, with a radius of $R_{\rm hot} \approx 28\,R_\odot$. The derived spectral class of the hot component differs from the above estimate based on photometric data. This discrepancy is due to the significant contribution of nebular emission to the observed spectra.

5. Conclusions

The long duration of our homogeneous observations and the large number of well-defined eclipse minima (see Figure 1) allow us to refine the ephemeris for the eclipses of the hot component in V1413 Aql: $JD_{\rm min} = 2,448,819.5 + 434.45E$. Despite the significant depth of the 2023 minimum ($\sim$2 mag in the V band), the eclipse appears to be partial. This is indicated by the absence of a plateau in the light curve at minimum and by the presence of an additional hot source in the SED.

According to the photometric criterion introduced by [21], V1413 Aql remained in an active state throughout our entire observational period. That is, between the two major outbursts in 2020 and 2025, the hot component of the system did not return to quiescence. This conclusion is further supported by the absence of He II lines in the spectrum. It is worth noting that other classical SySts have also been observed to remain in an active state for extended periods following outbursts. For example, BF Cyg has been in a permanent active phase since 2006 [31].

We determined the parameters of the system components during the 2023 activity minimum. The system consists of an M6 III red giant ($L_{\rm cool} = 1700(D[{\rm kpc}]/6[{\rm kpc}])^2\,{\rm L}_\odot$, $R_{\rm cool} = 130(D[{\rm kpc}]/6[{\rm kpc}])\,{\rm R}_\odot$), a 'hot' component of spectral type G0 III ($L_{\rm hot} = 800(D[{\rm kpc}]/6[{\rm kpc}])^2\,{\rm L}_\odot$, $R_{\rm hot} = 28(D[{\rm kpc}]/6[{\rm kpc}])\,{\rm R}_\odot$), and a nebula with an electron temperature of $T_e \approx 10^4$ K. Assuming reasonable mass ratios, the red giant appears to fill its Roche lobe. A secondary minimum detected in the infrared light curves by [21] was attributed to ellipsoidal variations caused by the distorted shape of the cool component.

It is worth noting that G0 III is not the latest spectral type assigned to the hot component of V1413 Aql during its active phases. In 2012, during an outburst, the hot component was classified as K2 III [13]. Note that a relatively cool 'hot' component has also been observed in the well-known classical SySt CI Cyg, where its temperature was estimated at 4000 K [8]. This is also a high-inclination system, and it is possible that in both CI Cyg and V1413 Aql, the disk is viewed nearly edge-on, with the observed emission originating from its outer, cooler layers. Such a 'hot' component does not emit sufficient Lyman-continuum photons to sustain the observed level of nebular emission. A possible explanation for this discrepancy lies in the assumption of a non-spherical geometry of the active 'hot' component. In this scenario, the actual ionizing source is a hot subdwarf-type star with $T \lesssim 10^5$ K, embedded within a disk-like envelope. Its direct radiation was detected only in an IUE spectrum obtained during quiescence on 10 June 1993 [14]. The similarity in Hβ fluxes observed in June 1993 and in 2023 implies a nearly constant emission measure of the nebula throughout this period.

The nature of the 'hot' component in V1413 Aql is most likely associated with an accretion disk. This hypothesis is further supported by the fact that the cool component fills its Roche lobe. The detection of flickering—a characteristic feature of accretion disks—could serve as a decisive argument in determining the nature of the 'hot' component. However, repeated attempts by the authors to detect such variability in V1413 Aql were unsuccessful. This may be due to the high orbital inclination of the system, which could obscure such phenomena from view.

The nature of the additional radiation component observed during minimum light—a blackbody with $T_{\rm eff} \approx 10,000$ K—remains unclear. The significant difference in size between the eclipsed component (28R$_\odot$) and the cool giant ($\approx$130 R$_\odot$), combined with the absence of a plateau in the light curve at minimum, suggests that the eclipse is not central. As a result, part of the 'hot' component may remain visible during eclipse. In the case of a disk-like geometry, this exposed region could be hotter than the star. An orbital inclination angle of $i \approx 70^\circ$ to the line of sight would be consistent with these observations. This value is in good agreement with the result reported by [30].

As noted in the Introduction, there is some uncertainty regarding the value of the color excess for V1413 Aql. All component parameters presented in this study were derived using $E(B-V) = 0.50$. If we adopt the higher reddening estimate of $E(B-V) = 0.56$, based on the 3D dust maps of [16], this would result in changes to the color indices (e.g., $B-V$ would decrease by 0.06,mag) and fluxes (by 10–25% in the $BVRcIc$ bands). The luminosity of the hot component at the 2025 outburst maximum would increase by approximately 20%, and its spectral type would shift to F3–F4. The color indices of the eclipsed component would also change, leading to a revised spectral type estimate—from F5–F7 to F3–F6. Other parameters are similarly affected: the emission measure derived from the spectrum obtained on 6 June 2023 would increase by about 40%, the luminosity of the additional continuum source observed during the 2023 minimum would rise by $\approx$20%, and the luminosity of the cool component would increase by approximately 4%.

In classical SySts, ordinary outbursts are typically events involving a redistribution of energy, with little or no change in the intrinsic luminosity of the hot component. However, the last two outbursts of V1413 Aql deviate from this behavior. The luminosity of the flaring hot component reached $7000(D[\mathrm{kpc}]/6[\mathrm{kpc}])^2\,\mathrm{L}_\odot$, nearly four times higher than its quiescent-state luminosity [14]. It is worth noting that similar luminosity increases—up to a factor of ten—have been observed in other symbiotic systems such as AG Dra [32], AG Peg [33], Gaia18aen [34], and V4141 Sgr [35]. However, in the first two systems, the outbursts did not involve the A-F supergiant stage.

Author Contributions: Conceptualization, A.T. (Anna Tatarnikova); investigation, N.I., M.B., A.B. and G.N.; software, A.D. and N.M.; formal analysis, A.T. (Andrey Tatarnikov) and M.B.; data curation, N.M., N.I., M.B. and A.B.; writing—original draft preparation, A.T. (Anna Tatarnikova) and A.T. (Andrey Tatarnikov); writing—review and editing, A.T. (Andrey Tatarnikov) and M.B. All authors have read and agreed to the published version of the manuscript.

Funding: The work of A.D. (preliminary processing and calibration of low-resolution spectra) and N.M. (catalog data handling, spectral data reduction, and result analysis) was supported by the Russian Science Foundation (grant 23-12-00092).

Data Availability Statement: Photometric data and original spectra reported in this study are available on request to the Andrey T. via email at andrew@sai.msu.ru.

Acknowledgments: This work was carried out using equipment purchased with support from the Development Program of the Lomonosov Moscow State University. The research makes use of the SIMBAD database (CDS, Strasbourg, France) and NASA's Astrophysics Data System (ADS). N. Maslennikova acknowledges support from Theoretical Physics and Mathematics Advancement Foundation "BASIS" (grant 22-2-10-21-1).

Conflicts of Interest: The authors declare no conflicts of interest.

Abbreviations

The following abbreviations are used in this manuscript:

CMO	Caucasian Mountain Observatory
SySt	Symbiotic Star
TDS	Transient Double-beam Spectrograph
SED	Spectral Energy Distribution

References

1. Merrill, P.W.; Burwell, C.G. Additional Stars whose Spectra have a Bright H α Line. *Astrophys. J.* **1950**, *112*, 72. [CrossRef]
2. Allen, D.A. Infrared observations of northern emission-line stars. *Mon. Not. R. Astron. Soc.* **1974**, *168*, 1. [CrossRef]
3. Allen, D.A. A catalogue of symbiotic stars. *Publ. Astron. Soc. Aust.* **1984**, *5*, 369–421. [CrossRef]
4. Tatarnikova, A.A.; Tatarnikov, A.M.; Tarasova, T.N. Determining the Physical Parameters of the System V1413 Aql in Its Quiescent and Active States in 2012–2017. *Astron. Lett.* **2020**, *46*, 24–37. [CrossRef]
5. Munari, U.; Yudin, B.F.; Sostero, G.; Lepardo, A. V1413 Aquilae. *IAU Circ.* **1993**, *5884*, 2.
6. Boyarchuk, A.A. The Binary Nature of Z Andromedae. *Sov. Astron.* **1968**, *11*, 818.
7. Kenyon, S.J.; Webbink, R.F. The nature of symbiotic stars. *Astrophys. J.* **1984**, *279*, 252–283. [CrossRef]
8. Mikolajewska, J.; Mikolajewski, M. A spectrophotometric study of CI Cygni during the 1980 eclipse. *Acta Astroomica* **1983**, *33*, 403–429.
9. Munari, U. Studies of symbiotic stars. VI. The eclipsing symbiotic nova AS 338. *Astron. Astrophys.* **1992**, *257*, 163–176.
10. Siviero, A.; Munari, U.; Moretti, S.; Graziani, M.; Tomaselli, S.; Gualdoni, C. Absolute Dimensions of the Outbursting WD in the Symbiotic Nova as 338 from Mapping of the 2005 Eclipse. *Balt. Astron.* **2007**, *16*, 55–58.
11. Wakuda, M. Photographic observations of eclipsing of AS 338. *Var. Star Bull.* **1988**, *5*, 17–18.
12. Schulte-Ladbeck, R. AS 338 in Outburst, or how i Found my "PET Symbiotic". *Messenger* **1985**, *39*, 3.

13. Esipov, V.F.; Tarasova, T.N.; Tatarnikov, A.M.; Tatarnikova, A.A. Spectral evolution of the classical symbiotic star V1413 Aql during a new activity cycle. *Astron. Lett.* **2013**, *39*, 458–473. [CrossRef]
14. Esipov, V.F.; Kolotilov, E.A.; Mikolajewska, J.; Munari, U.; Tatarnikova, A.A.; Tatarnikov, A.M.; Tomov, T.; Yudin, B.F. Evolution of the Symbiotic Star AS338 after Its Strong Outburst in 1983. *Astron. Lett.* **2000**, *26*, 162–176. [CrossRef]
15. Bailer-Jones, C.A.L.; Rybizki, J.; Fouesneau, M.; Demleitner, M.; Andrae, R. Estimating Distances from Parallaxes. V. Geometric and Photogeometric Distances to 1.47 Billion Stars in Gaia Early Data Release 3. *Astron. J.* **2021**, *161*, 147. [CrossRef]
16. Green, G.M. A 3D Dust Map Based on Gaia, Pan-STARRS 1, and 2MASS. *Astrophys. J.* **2019**, *887*, 27. [CrossRef]
17. Berdnikov, L.N.; Belinskii, A.A.; Shatskii, N.I.; Burlak, M.A.; Ikonnikova, N.P.; Mishin, E.O.; Cheryasov, D.V.; Zhuiko, S.V. BVI_c Observations and Search for Evolutionary Variations in the Cepheid V811 Oph Period. *Astron. Rep.* **2020**, *64*, 310–318. [CrossRef]
18. Potanin, S.A.; Belinski, A.A.; Dodin, A.V.; Zheltoukhov, S.G.; Lander, V.Y.; Postnov, K.A.; Savvin, A.D.; Tatarnikov, A.M.; Cherepashchuk, A.M.; Cheryasov, D.V.; et al. Transient Double-Beam Spectrograph for the 2.5-m Telescope of the Caucasus Mountain Observatory of SAI MSU. *Astron. Lett.* **2020**, *46*, 836–854. [CrossRef]
19. Kolotilov, E.A.; Mikolajewska, J.; Marrese, P.M.; Munari, U.; Shugarov, S.Y.; Yudin, B.F. Minimum on the Light Curve of the Classical Symbiotic Star AS 338 in 1999. *Astron. Lett.* **2001**, *27*, 51–57. [CrossRef]
20. Kolotilov, E.A.; Komissarova, G.V.; Tatarnikova, A.A.; Tatarnikov, A.M.; Shenavrin, V.I. New activity cycle of the classical symbiotic star V1413 Aql. *Astron. Lett.* **2012**, *38*, 468–473. [CrossRef]
21. Tatarnikova, A.A.; Tatarnikov, A.M.; Kolotilov, E.A.; Shenavrin, V.I.; Komissarova, G.V. Quiescent and Active States of V1413 Aql I: Photometric Activity Criterion and the Detection of a Secondary Minimum. *Astron. Lett.* **2018**, *44*, 803–810. [CrossRef]
22. Esipov, V.F.; Kolotilov, E.A.; Komissarova, G.V.; Shenavrin, V.I.; Shugarov, S.Y.; Tarasova, T.N.; Tatarnikov, A.M.; Tatarnikova, A.A. Spectral and photometric monitoring of the classical symbiotic star V1413 Aql in 2008–2013. *Contrib. Astron. Obs. Skaln. Pleso* **2014**, *43*, 485–486.
23. Baker, J.G.; Menzel, D.H. Physical Processes in Gaseous Nebulae. III. The Balmer Decrement. *Astrophys. J.* **1938**, *88*, 52. [CrossRef]
24. Proga, D.; Mikolajewska, J.; Kenyon, S.J. Hei Emission Lines in Symbiotic Stars. *Mon. Not. R. Astron. Soc.* **1994**, *268*, 213. [CrossRef]
25. Mikolajewska, J.; Kenyon, S.J.; Mikolajewski, M. On the Nature of the Symbiotic Star BF Cygni. *Astron. J.* **1989**, *98*, 1427. [CrossRef]
26. Munari, U.; Joshi, V.H.; Ashok, N.M.; Banerjee, D.P.K.; Valisa, P.; Milani, A.; Siviero, A.; Dallaporta, S.; Castellani, F. The 2010 nova outburst of the symbiotic Mira V407 Cyg. *Mon. Not. R. Astron. Soc.* **2011**, *410*, L52–L56. [CrossRef]
27. Skopal, A.; Tomov, N.A.; Tomova, M.T. Discovery of collimated ejection from the symbiotic binary BF Cygni. *Astron. Astrophys.* **2013**, *551*, L10. [CrossRef]
28. Pickles, A.J. A Stellar Spectral Flux Library: 1150–25000 Å. *Publ. Astron. Soc. Pacific* **1998**, *110*, 863–878. [CrossRef]
29. Friedman, S.D.; York, D.G.; McCall, B.J.; Dahlstrom, J.; Sonnentrucker, P.; Welty, D.E.; Drosback, M.M.; Hobbs, L.M.; Rachford, B.L.; Snow, T.P. Studies of Diffuse Interstellar Bands V. Pairwise Correlations of Eight Strong DIBs and Neutral Hydrogen, Molecular Hydrogen, and Color Excess. *Astrophys. J.* **2011**, *727*, 33. [CrossRef]
30. Boyd, D.; Cejudo, D.; Foster, J.; Sims, F.; Walker, G. Photometry and Spectroscopy of the Symbiotic Binary V1413 Aquilae during the 2024 Eclipse. *arXiv* **2025**, arXiv:2504.01465. [CrossRef]
31. Tomova, M. A look into the behaviour of BF Cygni after 2009. *Contrib. Astron. Obs. Skaln. Pleso* **2025**, *55*, 112–116. [CrossRef]
32. Mikolajewska, J.; Kenyon, S.J.; Mikolajewski, M.; Garcia, M.R.; Polidan, R.S. Evolution of the Symbiotic Binary System AG Draconis. *Astron. J.* **1995**, *109*, 1289. [CrossRef]
33. Skopal, A.; Shugarov, S.Y.; Sekeráš, M.; Wolf, M.; Tarasova, T.N.; Teyssier, F.; Fujii, M.; Guarro, J.; Garde, O.; Graham, K.; et al. New outburst of the symbiotic nova AG Pegasi after 165 yr. *Astron. Astrophys.* **2017**, *604*, A48. [CrossRef]
34. Merc, J.; Mikołajewska, J.; Gromadzki, M.; Gałan, C.; Iłkiewicz, K.; Skowron, J.; Wyrzykowski, Ł.; Hodgkin, S.T.; Rybicki, K.A.; Zieliński, P.; et al. Gaia18aen: First symbiotic star discovered by Gaia. *Astron. Astrophys.* **2020**, *644*, A49. [CrossRef]
35. Merc, J.; Mikołajewska, J.; Petit, T.; Monard, B.; Charbonnel, S.; Garde, O.; Le Dû, P.; Mulato, L.; Kojima, T. V4141 Sgr: Outflows and repeated outbursts. *Astron. Astrophys.* **2025**, *698*, L4. [CrossRef]

galaxies

MDPI

Article

On the Probability of the Astrometric Resolution of Spectroscopic Binaries into Components

Dugasa Belay Zeleke [1,2,*], Alexey Yu. Sytov [3,†], Seblu Humne Negu [1,†], Arseniy M. Sachkov [3,4,†], Solomon Belay Tessema [1,2,†] and Oleg Yu. Malkov [3,†]

1 Astronomy and Astrophysics Department, Space Science and Geospatial Institute (SSGI), Entoto Observatory and Research Center (EORC), Menilik II Ave., Addis Ababa 33679, Ethiopia; seblu1557@gmail.com (S.H.N.); tessemabelay@gmail.com (S.B.T.)
2 Kilo Campus, Addis Ababa University (AAU), King George VI St., Addis Ababa P.O. Box 1176, Ethiopia
3 Institute of Astronomy, 48 Pyatnitskaya St., Moscow 119017, Russia; sytov@inasan.ru (A.Y.S.); asachkov2003@yandex.ru (A.M.S.); malkov@inasan.ru (O.Y.M.)
4 Faculty of Physics, Moscow State University, 1 Kolmogorova St., Moscow 119234, Russia
* Correspondence: dugasa32@gmail.com
† These authors contributed equally to this work.

Abstract: Resolved spectroscopic binaries (RSBs) are an extremely valuable class of objects, being the only (apart from trigonometric) supplier of dynamical stellar parallaxes. This circumstance, as well as the comparative paucity of studied RSBs, makes the problem of identifying binary systems potentially capable of being added to the list of known RSBs extremely urgent. In this paper, we propose a methodology for estimating the probability of a spectroscopic binary system to be resolved into components, perform the first step of its application to the SB9 catalogue, and present preliminary results, in particular, a list of the most promising RSB candidates.

Keywords: binaries: spectroscopic; binaries: visual; binaries: catalogues; stars: parameters; parallaxes

1. Introduction

A significant fraction of stars in the Milky Way are binary or multiple stars. The studies conducted in [1–5] allow us to conclude that F-G-K-M stars may have an observed binary fraction of 20–40%, while that of O- and B-type stars may reach 100%.

A very interesting observational class of binary systems is resolved spectroscopic binaries (RSBs). Like some other observational classes (for example, double-lined eclipsing binaries, DLEBs), they are suppliers of dynamic stellar masses and other component parameters, but, most importantly, they provide us with the only way (apart from trigonometric parallax) to directly determine (rather than estimate) the distances to stars. Ref. [6] was one of the first to draw attention to this fact and compiled a list of about forty RSB systems. Later, Refs. [7–10] presented more representative lists, and, finally, Ref. [11] recently published a catalogue containing presumably all RSB systems studied to date. The catalogue in [11] is the most comprehensive list of RSBs to date, and it contains orbital elements (the orbital period P (yr), time of periastron $T0$ (JD), eccentricity e, inclination of the orbital plane i (deg), position angle of the ascending node Ω (deg), periastron longitude ω (deg), semi-major axis a (mas), and semi-major axis a (AU)), masses, orbital and trigonometric parallaxes, spectral classification, multicolour photometry, and reddening for 173 objects.

The exceptional importance of this class of binary systems makes the task of discovering new RSBs extremely urgent. One of the possibilities of replenishing the list of known

RSBs is an astrometric study of the most "promising" (primarily the widest) spectroscopic binaries with lines of both components in the spectrum (so-called SB2). The results of such a study were presented, for example, in [12].

Currently, the most complete and constantly updated catalogue of spectroscopic binaries is presented in [13] (hereafter, SB9). In this paper, we focus on estimating the probability of the astrometric resolution of spectroscopic binaries into components. We develop an original methodology for estimating this probability and conduct a pilot application of it to the SB9 catalogue. This paper is structured as follows: The methodology for estimating the resolution probability function of spectroscopic binary stars is described in Section 2. Results are presented and discussed in Section 3. Finally, in Section 4, we draw our conclusions.

2. Methodology for Estimating the Resolution Probability Function of Spectroscopic Binary Stars

Suppose that, in order for an unresolved spectroscopic binary star (SB) to be spatially resolved (RSB), it must have parameter values characteristic of other resolved spectroscopic binaries, i.e., be close to them in some parameter space. We also assume that the parameter space, for which the first assumption is correct, is formed by the observational parameters of the spectroscopic binaries, defined in the Catalogue of Resolved Spectroscopic Binaries [14] (hereafter, RSBcat) and the SB9 catalogue [13], which can be found in Table 1. The subset of SB9 objects identified with [14] is denoted by SB9R (SB9R = SB9 ∩ RSBcat), and the subset not identified with [14] (i.e., unresolved) is denoted by SB9U. Note that SB9R ≠ RSBcat, as 24 of the 173 RSBcat objects are not included in the SB9 catalogue. Accordingly, the set of all catalogue objects is SB9A (SB9A = SB9R ∪ SB9U). Note also that we consider only double-lined spectroscopic binary (SB2) systems from the SB9 catalogue, as only those systems can be fully solved for the orbital parameters (and thus the orbital parallax).

The essence of the proposed method is extremely simple: to use multidimensional distances in the space of observational parameters given a unified scale to estimate the proximity of spectroscopic binaries from SB9U and SB9R and, on the basis of the value of the obtained parametric distances, to estimate the prospectivity of the observations of objects from SB9U in terms of the probability of being resolved. We denote by $\vec{x} = \{x_k\}_{k=1}^{N_\mathrm{k}}$ the ordered set of SB9R object parameters, and we denote by $\vec{y} = \{y_k\}_{k=1}^{N_\mathrm{k}}$ the same set of SB9U object parameters. From the parameters given in Table 1, we choose the following $N_\mathrm{k} = 15$ values to estimate the parametric distances: $\{x_k\}, \{y_k\} = (\log P, e, \omega, \varpi_\mathrm{trig}, F_\mathrm{B}, F_\mathrm{V}, F_\mathrm{G}, F_\mathrm{J}, F_\mathrm{H}, F_\mathrm{K}, K_1, K_2, \gamma, V_1, V_2)$. Hereafter, k is the number of the parameter (component of the parametric vector).

Here, we use the vector notation to illustrate the idea of the method, but, of course, the quantities compiled in this way are not true vectors. Since all observational parameters have distinct scales of values, it is first necessary to renormalise all components x_k, y_k to the domain of values of the corresponding parameters for all SB9A objects and bring them to a unit value interval to equilibrate all parameters with each other. For the purpose of demonstrating the method, we assume that all N_k parameters are equally important and have the same weight while realising that this assumption can be false in some other cases, and the unequal weighting of the parameters can be easily accounted for by normalising the components differently. In order to renormalise x_k and y_k, at first, we have to calculate the bounding box in the parameter space that would contain both SB9U and SB9R sets of objects. Hereafter, we imply that every i-th object in SB9R and every j-th object in SB9U have their own $x_{k,i}$ and $y_{k,j}$ values , so omitting i and j object indices means that the expression is applicable for all objects.

Table 1. Parameters of spectroscopic binary stars in the RSBcat and SB9 catalogues. (*) The values of these parameters were added from the SIMBAD database for stars in the RSBcat and SB9 catalogues.

Parameter	Designation	Unit of Measurement	Availability in RSBcat	Availability in SB9
Orbit semi-major axis	a	mas	✓	
Orbital inclination	i	deg	✓	
Orbital parallax	ϖ_{orb}	mas	✓	
Longitude of node	Ω	deg	✓	
Mass of primary	m_1	$M_\odot$	✓	
Mass of secondary	m_2	$M_\odot$	✓	
Coordinates	α, δ	deg	✓	✓
Period	P	yr	✓	✓
Periastron time	T_0	JD	✓	✓
Orbital eccentricity	e	–	✓	✓
Argument of periastron	ω	deg	✓	✓
Trigonometric parallax (*)	ϖ_{trig}	mas	✓	✓
B-flux (*)	F_{B}	mag	✓	✓
V-flux (*)	F_{V}	mag	✓	✓
G-flux (*)	F_{G}	mag	✓	✓
J-flux (*)	F_{J}	mag	✓	✓
H-flux (*)	F_{H}	mag	✓	✓
K-flux (*)	F_{K}	mag	✓	✓
Velocity amplitude of primary	K_1	km/s		✓
Velocity amplitude of secondary	K_2	km/s		✓
Systematic velocity	γ	km/s		✓
Magnitude of component 1	V_1	mag		✓
Magnitude of component 2	V_2	mag		✓

The lower bound s_k is determined by the expression

$$s_k = \min\left(\min_{i=1}^{N_{\mathrm{SB9R}}}(x_{k,i}), \min_{j=1}^{N_{\mathrm{SB9U}}}(y_{k,j})\right) \tag{1}$$

where i is the number of the object in the SB9R set, and j is the number of the object in the SB9U set. The upper bound u_k is determined accordingly by the expression

$$u_k = \max\left(\max_{i=1}^{N_{\mathrm{SB9R}}}(x_{k,i}), \max_{j=1}^{N_{\mathrm{SB9U}}}(y_{k,j})\right) \tag{2}$$

Given that $r_k = u_k - s_k$ is the range of values of the k-th parameter, we finally obtain the expression for the renormalised parameters:

$$\tilde{x}_k = \frac{x_k - s_k}{r_k}, \qquad \tilde{y}_k = \frac{y_k - s_k}{r_k} \tag{3}$$

In the following, we omit the notation of the dimensionless value ($\tilde{}$) and assume that all components of vectors $\vec{x}$ and $\vec{y}$ are already renormalised.

The mean values of $\langle\vec{x}\rangle$ and $\langle\vec{y}\rangle$ point to the centres of the sets of objects SB9R and SB9U, respectively, in the observation parameter space. The vector $\langle\vec{z}\rangle = \langle\vec{y}\rangle - \langle\vec{x}\rangle$ defines the principal direction in the parameter space between the SB9U and SB9R sets.

When calculating the mean vectors $\langle\vec{x}\rangle$ and $\langle\vec{y}\rangle$, one has to take into account that, for every k-th parameter, there may be different numbers of objects for whom this parameter is measured and known from SB9cat. Therefore, the definition of the mean vectors can be written as follows:

$$\langle\vec{x}\rangle = \{\langle x_k\rangle\}_{k=1}^{N_k}, \qquad \langle\vec{y}\rangle = \{\langle y_k\rangle\}_{k=1}^{N_k} \tag{4}$$

$$\langle x_k \rangle = \frac{1}{n_{k,i}} \sum_{i=1}^{N_{\text{SB9R}}} \begin{cases} x_{k,i}, \text{if } x_{k,i} \text{ is defined} \\ 0, \text{otherwise} \end{cases} \qquad n_{k,i} = \sum_{i=1}^{N_{\text{SB9R}}} \begin{cases} 1, \text{if } x_{k,i} \text{ is defined} \\ 0, \text{otherwise} \end{cases} \tag{5}$$

$$\langle y_k \rangle = \frac{1}{n_{k,j}} \sum_{j=1}^{N_{\text{SB9U}}} \begin{cases} y_{k,j}, \text{if } y_{k,j} \text{ is defined} \\ 0, \text{otherwise} \end{cases} \qquad n_{k,j} = \sum_{j=1}^{N_{\text{SB9U}}} \begin{cases} 1, \text{if } y_{k,j} \text{ is defined} \\ 0, \text{otherwise} \end{cases} \tag{6}$$

Also, for the principal direction vector $\langle \vec{z} \rangle$, we have

$$\langle \vec{z} \rangle = \langle \vec{y} \rangle - \langle \vec{x} \rangle, \quad \langle \vec{z} \rangle = \{\langle z_k \rangle\}_{k=1}^{N_\text{k}}, \quad \langle z_k \rangle = \langle y_k \rangle - \langle x_k \rangle, \tag{7}$$

and normalising this vector gives the weights indicating the significance of the parameters with regard to the difference between the SB9U and SB9R sets.

$$\langle \vec{\bar{z}} \rangle = \frac{\langle \vec{z} \rangle}{|\langle \vec{z} \rangle|} = \left\{ \frac{\langle z_k \rangle}{\sqrt{\sum_{k=1}^{N_\text{k}} \langle z_k \rangle^2}} \right\}_{k=1}^{N_\text{k}} \tag{8}$$

Values for the principal direction vector components are provided in Table 2 in the "SB9U-SB9R mean diff." and "Normalised mean diff." columns.

Table 2. Properties of the parameter distributions of spectroscopic binary stars from SB9R and SB9U sets.

	SB9U				**SB9R**				**SB9U-SB9R**	**Normalised**
x_k, y_k	**Min**	**Max**	**Mean**	**Stddev**	**Min**	**Max**	**Mean**	**Stddev**	**Mean Diff.**	**Mean Diff.**
$\log P$	−1.273	4.972	3.332	2.131	−0.056	5.056	4.440	2.527	−1.107	−0.203
e	0	0.972	0.423	0.315	0	0.975	0.739	0.457	−0.316	−0.376
ω	−134.3	360.0	248.1	171.5	0	357.1	331.1	198.7	−83.04	−0.268
ϖ_{trig}	0.001	379.2	18.99	17.90	0.538	742.1	72.33	74.69	−53.34	−0.083
F_B	−1.460	23.40	18.10	9.485	0.720	13.26	13.10	6.882	5.004	0.233
F_V	−1.460	22.77	17.10	9.028	0.010	11.52	11.84	6.228	5.267	0.252
F_G	2.089	20.94	17.32	9.204	1.714	9.934	12.08	6.223	5.237	0.316
F_J	−2.300	18.63	14.84	7.990	−1.454	7.563	9.761	5.109	5.085	0.282
F_H	−3.220	17.68	14.19	7.696	−1.886	7.209	9.218	4.848	4.979	0.276
F_K	−3.510	17.49	13.95	7.584	−2.008	7.121	9.049	4.764	4.906	0.271
K_1	0.000	593.0	87.09	69.15	1.870	135.6	61.16	39.01	25.92	0.051
K_2	0.000	457.0	219.4	139.9	2.960	201.0	75.29	48.52	144.1	0.366
γ	−460.0	617.0	−6.448	47.30	−88.27	55.67	1.435	24.51	−7.883	−0.001
V_1	−1.470	22.50	17.24	9.096	−0.010	11.48	12.02	6.303	5.221	0.253
V_2	2.260	19.70	19.82	10.34	1.330	9.832	15.03	7.845	4.794	0.303

The proximity of the SB9U object to the SB9R region is determined by the distance $l_\text{m} = |\vec{y} - \langle \vec{x} \rangle|$. The most interesting measure of parametric proximity is the distance to the nearest SB9R object, $l_\text{x} = \min_{i=1}^{N_{\text{SB9R}}} |\vec{y} - \vec{x}_i|$, since its evaluation allows us to directly generate a list of candidates from SB9U to RSB and point to specific comparison objects. The smaller the l_m and l_x of an object from SB9U, the higher the probability that it can be resolved. Thus, for each SB9U object, we have a proximity criterion for the whole SB9R set (l_m) and for an individual SB9R object (l_x).

When calculating the parametric distances l_m and l_x, it should be taken into account that, for angular components, their arithmetic difference will not be the minimum angle difference, required for distance estimation, and the corresponding summands in the norm calculation should be calculated as $\Delta_k = \min(|y_k - x_k|, |360°/r_k - |y_k - x_k||)$. In addition, it should be considered that, since the values of all parameters are not known simultaneously for all objects, for each object from SB9U or a pair of objects from SB9U and SB9R, when computing l_m and l_x, the expression for the norm vector will only include the n_k of the known parameter values out of the total number of N_k parameters. Hence, the resulting value of l_m and l_x is not distorted downward when $n_k < N_\mathrm{k}$ due to the use of fewer identically normalised components, i.e., so that the parametric distance between the objects does not become formally smaller just because fewer parameters are known about them from observations, and the values of l_m, l_x must be corrected by the factor $c_k = N_\mathrm{k}/n_k$.

With all these considerations, we can rewrite l_m and l_x in a more detailed form. First, we define an absolute minimum difference between the k-th components as the $\mu(y_k, x_k)$ function:

$$\mu(y_k, x_k) = \begin{cases} |y_k - x_k|, \text{if } y_k \text{ and } x_k \text{ are not angles} \\ \min\left(|y_k - x_k|, \left|\frac{360^\circ}{r_k} - |y_k - x_k|\right|\right), \text{if } y_k \text{ and } x_k \text{ are angles} \\ 0, \text{if either } y_k \text{ or } x_k \text{ is undefined} \end{cases} \quad (9)$$

Then, the parametric distance between two objects is just an Euclidean distance corrected for undefined quantities:

$$l(\vec{y}, \vec{x}) = \frac{N_\mathrm{k}}{n_k}\sqrt{\sum_{j=1}^{N_\mathrm{k}} (\mu(y_k, x_k))^2}, \quad n_k = \sum_{j=1}^{N_\mathrm{k}} \begin{cases} 1, \text{if both } y_k \text{ and } x_k \text{ are defined} \\ 0, \text{otherwise} \end{cases} \quad (10)$$

Then, the distance l_m to the SB9R set centre for the j-th SB9U object is simply

$$l_\mathrm{m}(j) = l(\vec{y}_j, \langle\vec{x}\rangle) \quad (11)$$

and the distance l_x to the nearest SB9R object for the j-th SB9U object is

$$l_\mathrm{x}(j) = l(\vec{y}_j, \vec{x}_m) \quad (12)$$

where m is the number of an SB9R object that has minimal distance l to the j-th SB9U object

$$m(j) : l(\vec{y}_j, \vec{x}_m) = \min_{i=1}^{N_\mathrm{SB9R}} (l(\vec{y}_j, \vec{x}_i)) \quad (13)$$

3. Results and Discussion

An analysis of the distribution of observational parameters for the SB9U and SB9R sets shows that SB9R includes, on average, brighter stars with a larger orbital period and eccentricity and, correspondingly, smaller amplitudes of radial velocities. The lowest contribution to the difference between SB9R and SB9U is given by the radial velocity of the system γ, and the difference in the mean parallaxes ϖ_trig and radial velocities K_1 of the primary component of the binary system is somewhat more significant, but the contribution of all other quantities is approximately the same. The properties of the distributions of the observational parameters are given in Table 2: the columns SB9R (min, max, mean, stddev) and SB9U (min, max, mean, stddev) are given for SB9R and SB9U, respectively, containing the parameter value interval boundaries, mean values, and their standard deviations; the column “SB9U-SB9R” contains components of the vector $\langle\vec{z}\rangle$, i.e., the difference between the mean values SB9U.mean-SB9R.mean; and the “Normalised mean diff.” column contains the values of the components of the normalised vector $\langle\vec{z}\rangle/|\langle\vec{z}\rangle|$ to estimate their relative contribution.

As a result of the above methodology, we obtained lists of SB9U objects ordered by the parametric distances l_m and l_x. The most promising objects for observation, corresponding to the smallest values of the parametric distances, are listed in Tables 3 and 4. Figure 1 (red points) shows the location of SB9U objects in (l_x, l_m) coordinates. For comparison, the figure also shows the position of SB9R objects (red crosses).

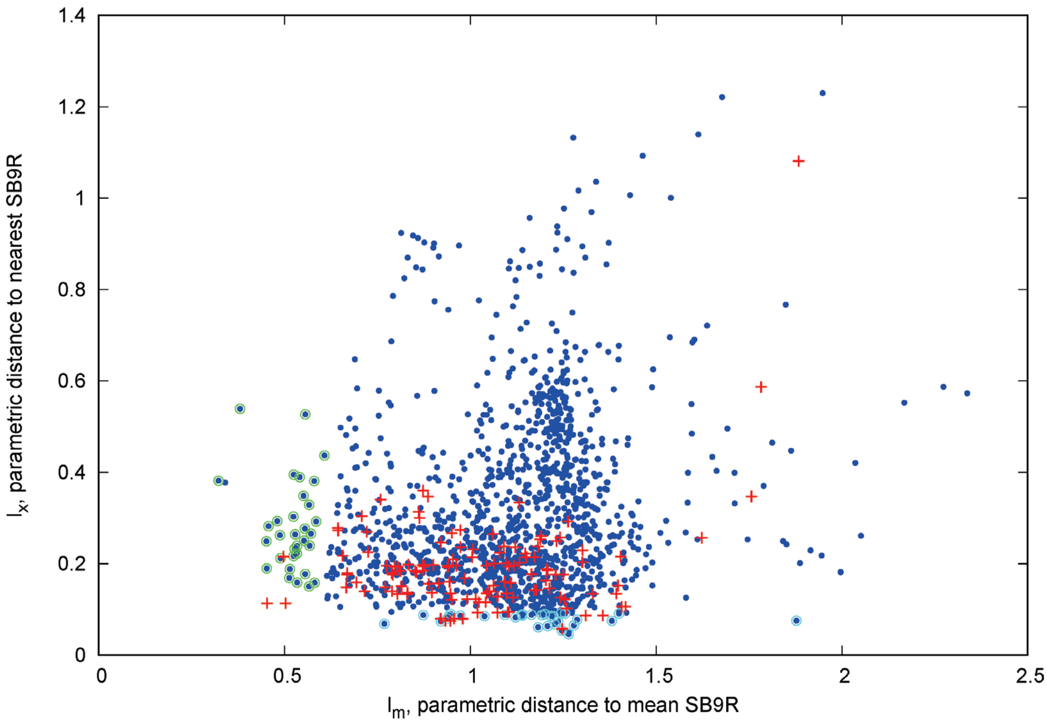

Figure 1. Parametric distances from the SB9U (blue points) and SB9R (red crosses) objects to the parametric centre (mean position) of the SB9R set (l_m) and to its nearest SB9R object (l_x). Circles mark the first 30 objects with the smallest l_m (green) and smallest l_x (cyan) distances.

A complete list of promising candidates is available upon request.

As one can see in Tables 3 and 4, the smallest l_x values are significantly lower than the smallest l_m values, and both tables have no common objects. At first glance, this looks like an inconsistency in the proposed methodology, as a solid result would have had a single list of objects, but, in fact, this indicates a more complex problem.

The value of l_m represents the distance to the SB9R population average, while the value of l_x represents the distance to the nearest neighbour in SB9R. Both of these measures are valuable but in different ways, and there is no fair reason to prefer one over the other. The distance l_x is more precise, as it reveals what SB9R object is the nearest neighbour to an SB9U object; additionally, since the smallest values of l_x are much lower than the l_m values, these particular SB9U and SB9R objects are parametrically closer than other objects in general, and, for that reason, both should probably be resolved. The distance l_m is a rough measure; the important thing here is not its value for a particular object but rather its range for all SB9R objects, as every SB9U object that falls within that range should probably be resolved. The basic idea behind the l_m values and Table 3 is that the closer to the centre of an SB9R cloud an SB9U object is, the higher the probability of its resolution should be; however, considering the SB9R mean position $\langle \vec{x} \rangle$ an optimal parameter combination in terms of binary resolvability is, of course, a gross oversimplification.

Table 3. The most promising SB9U systems in terms of parametric distance l_m to the mean value $\langle \vec{x} \rangle$ in the SB9R (to the centre of the SB9R object cloud). The RSBcat HIP column contains the Hipparcos number of the parametrically nearest (by l_x) SB9R object.

SB9 ID	RSBcat HIP	V, mag	SpType	P. day	ϖ, mas	l_m	l_x
CD -49 11403	103055	10.849		1318.2	1.1176 ± 0.0197	0.322	0.381
G 9-27	83064	12.050		1018.53	3.71 ± 0.1113	0.380	0.538
HIP 109767	102545	10.100	K0	650.19	11.0174 ± 0.1428	0.451	0.248
HIP 64787	77725	9.190	G0V	3751.0	8.6413 ± 0.055	0.480	0.293
HIP 70534	10952	8.610	K0	26,000.0	2.2475 ± 0.0402	0.514	0.188
BD +17 2603	77725	9.800	G6V	9278.0	7.6548 ± 0.0267	0.523	0.303
HIP 77122	83064	8.950		4290.0	9.8175 ± 0.0579	0.552	0.348
BD +51 2091	102545	9.580	G5	247.08	3.5091 ± 0.024	0.554	0.276
HIP 13498	83064	7.730	G1V?	18,794.0	11.9650 ± 0.3677	0.555	0.177
HIP 17102	77725	9.050	K2	183.113	25.4343 ± 0.0319	0.565	0.310
BD +22 2581	77725	9.590	G0V	15,000.0	6.9482 ± 0.4934	0.570	0.333
GAIADR2 45574 02515188596224	102545	11.020	F9	18.4359535	2.7714 ± 0.0135	0.579	0.380
HIP 56229	77725	9.750	M0	186.3	22.7378 ± 0.0511	0.580	0.278
HIP 56622	100287	8.320	G7V	1690.15	21.1416 ± 0.0165	0.615	0.165
HIP 11537	77725	9.450	G5V	1146.44	15.5178 ± 0.4379	0.616	0.129
HIP 101472	77725	9.380	G8V	354.88	11.3768 ± 0.0977	0.621	0.224
HIP 88639	102545	10.600	K7V	25.7631	24.694 ± 0.0225	0.625	0.236
HIP 105879	98416	7.180	F7V	2935.6	12.4373 ± 0.2139	0.626	0.203
Gl 220	117415	9.918G	M1.5V	721.0	47.7313 ± 0.5115	0.641	0.399
HIP 117666	77725	8.730	G5V	10,984.0	13.3973 ± 1.2719	0.643	0.231
2E 3709	102545	12.230	K7	35.95	5.9041 ± 0.3012	0.651	0.391
HIP 107731	117415	8.640	G1/G2V	469.92	14.9306 ± 0.2675	0.652	0.224
HIP 2563	19508	8.720		2127.82	17.315 ± 0.1009	0.660	0.245
BD +28 387	102545	11.000	G0	41.2013	3.6606 ± 0.2174	0.669	0.359
BD +29 2313	102545	10.140	G8V	17.778584	7.5141 ± 0.0185	0.669	0.325
HIP 79979	98416	6.820	F9V	1083.16	25.5345 ± 0.232	0.671	0.165
BD +29 2313	102545	10.140	G8V	17.7786	7.5141 ± 0.0185	0.673	0.325
HIP 28432	4889	7.940	Am	60.6378	5.7711 ± 0.0371	0.674	0.338
RX J0532.1-0732	102545	12.570	K2-K3	46.85	2.7331 ± 0.0131	0.674	0.517
HIP 91935	102545	8.310	F5	34.8634	8.0971 ± 0.0169	0.675	0.151
HIP 3428	102545	10.970	K7V	97.25	22.8103 ± 0.0695	0.677	0.303
GAIADR2 30174 02443157072768	34603	11.130	F9IV	118.34	3.5561 ± 0.0279	0.690	0.568
ADS 8861	77725	9.510	dM1.5	200.26	72.9733 ± 0.3217	0.690	0.262
GAIADR2 33168 44608086144128	77725	11.890		352.49	6.8078 ± 0.0557	0.690	0.515
HIP 105585	19508	8.100	G8V	87,658.0	30.24 ± 4.85	0.690	0.364
Cl* Melotte 111 AV 390	102545	12.400	K0III	94.4384	3.4746 ± 0.0166	0.695	0.583
HIP 61732	77725	9.180	G5	595.18	6.852 ± 0.3285	0.697	0.307
HIP 84129	100287	7.140	F5	556.213	14.3755 ± 0.0255	0.699	0.229

Table 3 shows that, for the smallest l_m values, the corresponding l_x values are comparable. This means that, nearer the centre of the SB9R cloud, the population density of SB9U and SB9R is about the same. In comparison, Table 4 shows pretty large l_m values corresponding to the smallest l_x values, and this means that the population density of SB9U is much higher at the edge of the SB9R cloud than at its centre. This difference in population density in the parameter space is the main reason why a single list of best candidate objects cannot be produced within this methodology (at least not now).

Table 4. The most promising SB9U systems in terms of the parametric distance l_x to the nearest SB9R object, whose HIP number is given in the RSBcat HIP column.

SB9 ID	RSBcat HIP	V, mag	SpType	P. day	ϖ, mas	l_m	l_x
HIP 89925	99404	5.630	A5m	5.5146126	17.9191 ± 0.0489	1.264	0.050
HIP 64478	20284	6.350	G0V	4.23345	23.1989 ± 0.0946	1.246	0.053
HIP 105660	46704	6.160	A2V	6.9463	5.5323 ± 0.0768	1.207	0.063
HIP 3572	52980	5.630	A1V	4.4672235	10.6528 ± 0.0511	1.278	0.065
HIP 4572	52980	5.968	A0III	6.82054	9.1239 ± 0.0375	1.227	0.067
HIP 61727	117186	7.590	F5	54.87864	10.1467 ± 0.0382	1.033	0.073
HIP 92117	52980	5.900	A2Vm	4.7653	10.8978 ± 0.0549	1.236	0.073
HIP 66438	16042	5.630	F6V	8.0714	27.99 ± 0.58	1.380	0.074
HIP 63143	52980	5.820	A5m	5.1259	11.54 ± 0.51	1.877	0.075
HIP 95176	57565	4.610	B8p+F2pe	137.9343	2.0869 ± 0.1716	1.287	0.077
HIP 42871	111170	6.543	F7V	700.3	13.3908 ± 0.0374	1.014	0.079
HIP 31850	52980	6.360	F8IV	5.6983	27.6925 ± 0.0393	1.223	0.084
HIP 107238	46704	6.220	Am	6.3702	8.9617 ± 0.0285	1.216	0.085
HIP 759	18277	7.170	G2V	23.49785	19.3683 ± 0.0238	0.972	0.086
HIP 68064	46704	6.790	F2V	4.9918	9.3946 ± 0.0234	1.192	0.087
HIP 10961	46704	6.880	F5	4.2220168	16.0685 ± 0.0202	1.200	0.089
HIP 29746	20284	6.360	F6V	2.184952	13.6168 ± 0.8743	1.254	0.091
HIP 48273	20284	6.230	F6V	3.05459836	21.1803 ± 0.1565	1.399	0.091
HIP 43496	52980	5.540	A4m	2.8952	7.3105 ± 0.1725	1.420	0.092
HIP 41564	52980	6.380	A5m	5.9771	13.41 ± 0.79	1.202	0.092
HIP 10285	46704	7.170	A7m	4.1212	7.4227 ± 0.0192	1.176	0.093
BD +45 172	111528	8.840	G0	5556.0000	11.1479 ± 0.252	0.787	0.094
HIP 113770	46704	7.390	F8	5.21465	15.1122 ± 0.0242	1.164	0.095
HIP 88581	46704	6.870	O6.5V	6.14	0.7893 ± 0.0297	1.135	0.095
HIP 25776	22407	6.190	A0V	8.569	8.0907 ± 0.0381	1.482	0.095
HIP 32067	46704	6.370	O6e	3.078098	0.7632 ± 0.0417	1.227	0.096
HIP 48218	20284	6.090	A8IV	4.1467465	5.22 ± 0.63	1.242	0.096
HIP 84586	20284	6.670	G5IV	1.6817	32.9511 ± 0.0184	1.264	0.097
HIP 115500	22407	6.660	F8	6.0499	15.0601 ± 0.0228	1.626	0.097
HIP 2888	20284	6.780	G3V	3.7418	22.5227 ± 0.0179	1.212	0.098
HIP 81305	99404	5.470	O9Ia	9.81475	0.7601 ± 0.0709	1.273	0.099

If we limit ourselves to a subset of SB9U objects that have $l_x \geq \min(l_m)$, then it is possible for common objects to appear in both tables, but this would be a bad choice since a huge number of better nearest neighbour candidates would drop out. Alternatively, we can explicitly merge tables and sort objects by the $\min(l_x, l_m)$ value or by the L_2 norm of these measures $l_* = \sqrt{l_x^2 + l_m^2}$; either way, such a result would not contain $l_x < \min(l_m)$ candidates.

Therefore, we propose to use Table 4 as the main list of candidates and Table 3 as a secondary guide and examine these spectroscopic binaries by other means.

It should be remembered that the SB9 catalogue contains orbital solutions rather than spectroscopic systems (multiple solutions are often given for a single spectroscopic system). In total, SB9 contains 5099 entries, of which 339 (7%) are SB9R and 4760 (93%) are SB9U. This means that the number of candidate stars is somewhat smaller than the number of candidate records. In addition, obviously, the probability of a spectroscopic binary to be resolved into components is also affected by other parameters: the angular distance between the components, the brightness of the system, the magnitude difference of the components, the orbit orientation, and so on. However, we believe that the values that we obtained can be used as rough estimates.

It should be added that another promising source of RSB candidates is the LAMOST survey [15,16]. Spectroscopic binary studies using LAMOST are being carried out quite intensively in [17–20]. This source also deserves the closest attention.

4. Conclusions

Resolved spectroscopic binaries (RSBs) are the only way (besides trigonometric parallax) to determine the dynamical, hypothesis-free distances to the stars of the Galaxy. Today, we know very few (less than two hundred) RSBs, so each new object makes a significant contribution to our knowledge of stellar distances.

We developed a method for estimating the probability of resolving the components of double-lined spectroscopic binaries (SB2), which depends on orbital element values and component parameters. The main points of this work are summarised as follows:

- The probability of the resolution of unresolved objects could be inferred from the similarity to resolved objects;
- Distances in the space of observational parameters could be used as a basic and straightforward measure of similarity;
- The highest similarity is achieved between individual objects, and it is loosely connected to the parameter space occupied by resolved objects.

The method was applied to the principal catalogue of spectroscopic binaries, SB9, and the results of this application are shown in Figure 1 and Table 1. A complete list of promising candidates is available upon request. Obviously, these results will be useful for organising astrometric/interferometric observations of spectroscopic binary systems in order to resolve them into components and add them to the list of resolved spectroscopic binaries.

Author Contributions: All authors contributed to the study conception and design. Material preparation, data collection, and analysis were performed by all authors. The first draft of the manuscript was written by D.B.Z., and all authors commented on previous versions of the manuscript. All authors have read and agreed to the published version of the manuscript.

Funding: A. Sachkov and O. Malkov thank the Foundation for the Advancement of Theoretical Physics and Mathematics "BASIS" for its support, grant No 25-1-1-34-1.

Data Availability Statement: Data are available on request from the authors.

Acknowledgments: We are grateful to the anonymous reviewers whose constructive comments greatly helped us to improve this paper. We warmly thank James Wicker for his invaluable assistance in preparing the manuscript. We thank Space Science and Geospatial Institute, Entoto Observatory and Research Center and Astronomy and Astrophysics Department for supporting this research. This research has made use of the SAO/NASA Astrophysics Data System and the SIMBAD database, operated at CDS, Strasbourg, France.

Conflicts of Interest: The authors have no relevant financial or non-financial interests to disclose.

References

1. Duchêne, G.; Kraus, A. Stellar Multiplicity. *Annu. Rev. Astron. Astrophys.* **2013**, *51*, 269–310. [CrossRef]
2. Duquennoy, A.; Mayor, M. Multiplicity among Solar Type Stars in the Solar Neighbourhood—Part Two—Distribution of the Orbital Elements in an Unbiased Sample. *Astron. Astrophys.* **1991**, *248*, 485.
3. Raghavan, D.; McAlister, H.A.; Henry, T.J.; Latham, D.W.; Marcy, G.W.; Mason, B.D.; Gies, D.R.; White, R.J.; ten Brummelaar, T.A. A Survey of Stellar Families: Multiplicity of Solar-type Stars. *Astrophys. J. Suppl. Ser.* **2010**, *190*, 1–42. [CrossRef]
4. Sheikhi, N.; Hasheminia, M.; Khalaj, P.; Haghi, H.; Zonoozi, A.H.; Baumgardt, H. The binary fraction and mass segregation in Alpha Persei open cluster. *Mon. Not. R. Astron. Soc.* **2016**, *457*, 1028–1036. [CrossRef]
5. Yuan, H.; Liu, X.; Xiang, M.; Huang, Y.; Chen, B.; Wu, Y.; Hou, Y.; Zhang, Y. Stellar Loci II. A Model-free Estimate of the Binary Fraction for Field FGK Stars. *Astrophys. J.* **2015**, *799*, 135. [CrossRef]

6. Pourbaix, D. Resolved double-lined spectroscopic binaries: A neglected source of hypothesis-free parallaxes and stellar masses. *Astron. Astrophys. Suppl. Ser.* **2000**, *145*, 215–222. [CrossRef]
7. Anguita-Aguero, J.; Mendez, R.A.; Claveria, R.M.; Costa, E. Orbital Elements and Individual Component Masses from Joint Spectroscopic and Astrometric Data of Double-line Spectroscopic Binaries. *Astron. J.* **2022**, *163*, 118. [CrossRef]
8. Gallenne, A.; Mér, A.; Kervella, P.; Graczyk, D.; Pietrzyński, G.; Gieren, W.; Pilecki, B. The Araucaria project: High-precision orbital parallaxes and masses of binary stars. I. VLTI/GRAVITY observations of ten double-lined spectroscopic binaries. *Astron. Astrophys.* **2023**, *672*, A119. [CrossRef]
9. Jancart, S.; Jorissen, A.; Babusiaux, C.; Pourbaix, D. Astrometric orbits of SB9 stars. *Astron. Astrophys.* **2005**, *442*, 365–380. [CrossRef]
10. Piccotti, L.; Docobo, J.Á; Carini, R.; Tamazian, V.S.; Brocato, E.; Andrade, M.; Campo, P.P. A study of the physical properties of SB2s with both the visual and spectroscopic orbits. *Mon. Not. R. Astron. Soc.* **2020**, *2*, 2709–2721. [CrossRef]
11. Zeleke, D.B.; Sachkov, A.M.; Malkov, O.Y.; Negu, S.H.; Tessema, S.B.; Grinenko, A.D. Resolved spectroscopic binaries: Orbital elements and parallaxes. *Astrophys. Space Sci.* **2025**, *370*, 1. [CrossRef]
12. Taylor, S.F.; Harvin, J.A.; McAlister, H.A. The CHARA Catalog of Orbital Elements of Spectroscopic Binary Stars. *Publ. Astron. Soc. Pac.* **2003**, *115*, 609–617. [CrossRef]
13. Pourbaix, D.; Tokovinin, A.A.; Batten, A.H.; Fekel, F.C.; Hartkopf, W.I.; Levato, H.; Morrell, N.I.; Torres, G.; Udry, S. The ninth catalogue of spectroscopic binary orbits. *Astron. Astrophys.* **2004**, *424*, 727–732. [CrossRef]
14. Zeleke, D.B.; Pakhomova, P.V.; Tessema, S.B.; Negu, S.H.; Malkov, O.Y. The Catalog of Resolved Spectroscopic Binaries: Development and Description. *Astron. Rep.* **2023**, *67*, 576–580. [CrossRef]
15. Luo, A.; Zhao, Y.; Zhao, G.; Deng, L.; Liu, X.; Jing, Y.; Wang, G.; Zhang, H.; Shi, J.; Cui, X.; et al. The first data release (DR1) of the LAMOST regular survey. *Res. Astron. Astrophys.* **2015**, *15*, 1095. [CrossRef]
16. Luo, A.L.; Zhao, Y.H.; Zhao, G. VizieR Online Data Catalog: LAMOST DR5 catalogs (Luo+, 2019). *Vizier Online Data Cat.* **2019**, *5165*, V/164.
17. Guo, S.; Kovalev, M.; Li, J.; Lü, G.; Jia, S.; Li, Z.; Li, J.; Xiong, J.; Yang, M.; Han, Z.; et al. Orbital Parameters of 665 Double-lined Spectroscopic Binaries in the LAMOST Medium-Resolution Survey. *arXiv* **2025**, arXiv:2504.11954. [CrossRef]
18. Jing, Y.; Mao, T.X.; Wang, J.; Liu, C.; Chen, X. Half a Million Binary Stars Identified from the Low-resolution Spectra of LAMOST. *Astrophys. J. Suppl. Ser.* **2025**, *277*, 15. [CrossRef]
19. Liu, J.; Zhang, B.; Wu, J.; Ting, Y.S. Double-lined Spectroscopic Binaries from the LAMOST Low-resolution Survey. *Astrophys. J. Suppl. Ser.*s **2024**, *275*, 40. [CrossRef]
20. Zhao, X.; Wang, S.; Liu, J. Searching for Accreting Compact Binary Systems from Spectroscopy and Photometry: Application to LAMOST Spectra. *Astrophys. J.* **2025**, *984*, 9. [CrossRef]

galaxies

Article

Abundance Analysis of the Spectroscopic Binary α Equulei

Anna Romanovskaya * and Sergey Zvyagintsev

Institute of Astronomy RAS, Moscow 119017, Russia; srgzvgntsv@gmail.com
* Correspondence: annarom@inasan.ru

Abstract: We present the results of a detailed spectroscopic analysis of the double-lined spectroscopic binary system α Equulei. High-resolution spectra obtained with the SOPHIE spectrograph at various orbital phases were used to disentangle the composite spectra into individual components using the spectral line deconvolution (SLD) iterative technique. The atmospheric parameters of each component were refined with the SME (spectroscopy made easy) package and further validated by following methods: SED (spectral energy distribution), the independence of the abundance of individual Fe I–II lines on the reduced equivalent width and ionisation potential, and fitting with the hydrogen line profiles. Our accurate abundance analysis uses a hybrid technique for spectrum synthesis. This is based on classical model atmospheres that are calculated under the assumption of local thermodynamic equilibrium (LTE), together with non-LTE (NLTE) line formation. This is used for 15 out of the 25 species from C to Nd that were investigated. The primary giant component (G7-type) exhibits a typical abundance pattern for normal stars, with elements from He to Fe matching solar values and neutron-capture elements showing overabundances up to 0.5 dex. In contrast, the secondary dwarf component displays characteristics of an early stage Am star. The observed abundance differences imply distinct diffusion processes in their atmospheres. Our results support the scenario in which chemical peculiarities in Am stars develop during the main sequence and may decrease as the stars evolve toward the subgiant branch.

Keywords: binary star; A star; Am star; α Equulei; high-resolution spectroscopy; composite spectra; spectral line deconvolution; abundances

1. Introduction

Am stars are characterized by the absence of a large-scale magnetic field and show an overabundance of metals. The question of the formation of chemical anomalies in the atmospheres of Am stars remains unclear. It is believed that the origin of anomalies is associated with the processes of atomic diffusion, according to which the diffusion of atoms and ions of an element occurs under the action of gravity directed towards the centre of the star and radiation pressure forces that push particles into the outer layers of the atmosphere [1]. To understand the mechanisms of formation of anomalies in chemical elements, it is necessary to determine accurately the abundances of elements from light CNO to rare earth elements (REE).

Observations [2] and theory [3] show that slow rotation (equatorial velocity below 120 km/s) favours the presence of chemical anomalies in A–B stars. There are two different atomic diffusion scenarios that attempt to explain the Am star phenomenon. Ref. [4] suggested that the separation of chemical elements occurs directly below the hydrogen convection zone, in the radiative zone (see, e.g., [5]), and it is assumed that a very small mass of a star has high abundance when the star is in the main sequence (MS) stage. Furthermore, when the star reaches the subgiant branch, there is a decrease in atmospheric abundances in the star's atmosphere. In another model proposed by [6], the separation of elements occurs much deeper in the star. Consequently, most of the mass has anomalous chemical abundances when the star is in the MS stage; furthermore, the anomalies presumably remain longer as the star evolves to the subgiant stage.

The majority of previous studies investigating the chemical composition of A-type and Am stars have been conducted under the assumption of local thermodynamic equilibrium (LTE) (e.g., [7,8]). However, deviations from LTE can have a significant impact on the accuracy of abundance determinations, which are essential for testing theories of atomic diffusion and for the correct interpretation of spectroscopic observations. The non-LTE (NLTE) approach accounts for these deviations by solving the equations of statistical equilibrium simultaneously with the radiative transfer equations, thereby providing more realistic level populations. Recent investigations have demonstrated that, in Am stars with effective temperatures exceeding 9300 K and surface gravities $\log g < 4.0$, elements such as calcium and scandium may appear overabundant relative to solar values when analysed in the non-LTE approach [9].

Of particular interest is the study of binary systems with chemically anomalous components at different stages of their evolution, which makes it possible to study the processes of creating chemical anomalies in stellar atmospheres in more detail. Binary star systems are formed from the same interstellar medium; thus, they should have similar chemical abundances. However, recent studies have suggested that the component stars in a binary system may have different chemical abundances (e.g., [10]), which means these differences are generated by processes during stellar evolution. Therefore, these studies may provide a clue to the understanding of the physical processes leading to the creation of anomalies in stellar atmospheres.

For this purpose, we chose the spectroscopic binary star α Equulei (HD 202447, HD 202448). Griffin and Griffin found that the primary component of the bright composite-spectrum binary α Equulei is a normal G7 giant, while the secondary is an Am star, classified as kA3hA4mA9 based on spectral disentangling [11] (hereafter, GG02). The system's well-determined visual orbit and high-resolution spectroscopy allowed for the precise measurement of the mass ratio (q = 1.15 ± 0.03) and component masses (2.3 $M_\odot$ for the giant primary and 2.0 $M_\odot$ for the dwarf secondary). Both stars fit a single 0.74 Gyr isochrone, with the primary on its first ascent of the red giant branch and the secondary evolving off the main sequence. α Equulei provides a rare opportunity to study the chemical composition and evolutionary status of an Am star in a well-characterised binary system.

The paper is organised as follows. Section 2 describes the observations and data sources used in this study. The spectral disentangling procedure is presented in Section 3. In Section 4, we detail the model atmospheres and methods applied to determine the stellar parameters of both components. The abundance analysis is discussed in Section 5. A comparison of our results with those from the literature is provided in Section 6. Finally, we present conclusions in Section 7.

2. Observations

We obtain high-resolution spectra from the SOPHIE spectrograph in HR mode ($R = \lambda/\Delta\lambda = 75.000$, spectral range 3872–6943 Å) in all ranges of phases of radial velocities; so, we are able to disentangle spectra and do spectral analysis. Observational data are provided in Table 1. Phases are calculated relative to $MJD_0 = 45{,}293.63$ (GG02). Additional spectra are available from other archives: UVES (with a resolving power of $R = 71.050$–107.200) and NARVAL ($R = 65.000$). In the case of

UVES, although the spectra cover a wide range of rotational phases, the signal-to-noise ratio is relatively low: approximately 50–170 for the 3282–4563 Å range, and 190–430 for the 4583–6686 Å range. In contrast, all NARVAL spectra are obtained during a single rotational phase, 0.491, when recalculated with respect to the MJD_0 value adopted in the study by GG02. Therefore, we select the SOPHIE spectra for spectral disentangling.

Table 1. Observed spectra from the SOPHIE spectrograph. Phases calculated from $MJD_0 = 45{,}293.63$.

Sequence Number	BJD	S/N	Phase
2345960_s1d	2458041.25604479	388	0.007
2253190_s1d	2457967.50131843	385	0.260
1872770_s1d	2457295.39394543	442	0.458
1877520_s1d	2457305.35730816	234	0.559
2007640_s1d	2457602.53160324	383	0.567
2016580_s1d	2457622.53572631	326	0.769
2023130_s1d	2457634.49218795	306	0.890

3. Spectral Disentangling

We used a new technique of spectral disentangling introduced in our previous paper [12]. It is based on the spectral line deconvolution (SLD) method, also developed by us, which consists of looking for the SLD function ν, which provides the observed spectrum R_λ after convolution with the theoretical profiles of individual spectral lines $p(\nu)$:

$$R_\lambda = \sum \alpha_\lambda \times (X(\nu)p(\nu)), \tag{1}$$

where α_λ is a set of multiplicative coefficients accounting for the fact that the profile of a blend is not necessarily a linear sum of the profiles of its individual components contributing to that blend. The SLD function is a normalised broadening profile that includes all global physical and instrumental effects that determine the spectral line shape: rotation, turbulence, and spectral resolution. Equation (1) can be generalised to spectroscopic double (SB2) and higher-order multiple systems. For SB2 systems in particular, two linear masks are used to identify two SLD functions, each of which corresponds to a different component of the binary system. Applying this to binary systems also involves introducing an additional free parameter: the flux ratio of two stars.

The disentangling process is characterised by an iterative approach, which can be described as follows: (I) theoretical line masks for both stars were calculated based on an initial set of atmospheric parameters. (II) Equation (1) was solved for the SLD functions. Subsequently, we optimised the flux ratios of the two stars using the golden section method to determine the radius ratio, and line strength corrections were performed by introducing a scale factor for each spectral line across all utilised spectra during the simultaneous disentangling. (III) The obtained SLD functions were convolved with improved line masks to produce disentangled spectra for the two components of the binary system. The convergence criterion in the search for the disentangled spectra was the simultaneous maximisation of the fit between the computed composite model spectra and the observed spectra across all phases. The resulting spectra, which were free from masking, were then analysed to refine the atmospheric parameters of the stars.

This entire process (steps I to III) is repeated until no significant changes are observed in the line strength corrections, flux ratios, and atmospheric parameters derived from the unmasked spectra.

The initial parameters were taken from the work of GG02. The radial velocities of the components were obtained using a two-dimensional mutual correlation method similar to that used in the TODCOR code [13]. This method was applied to the spectra used in the disentangling process.

For test purposes, we used artificial dual spectra mimicking the observed spectra. Synthetic spectra of each component, expressed in flux units, were folded to account for the shift in the wavelength scale according to the radial velocity of each component. These composite spectra were then convolved with an instrumental profile corresponding to $R = 75{,}000$, and noise was added to simulate the $S/N = 350$ ratio. Spectrum disentangling was performed under the perturbation of atmospheric parameters and showed insensitivity to their variations within the errors in the calculation of SLD masks. As for the disentangling of the real observed spectra, two iterations were sufficient to obtain the final results. Figure 1 shows the results of disentangling the observed spectra of the α Equulei system.

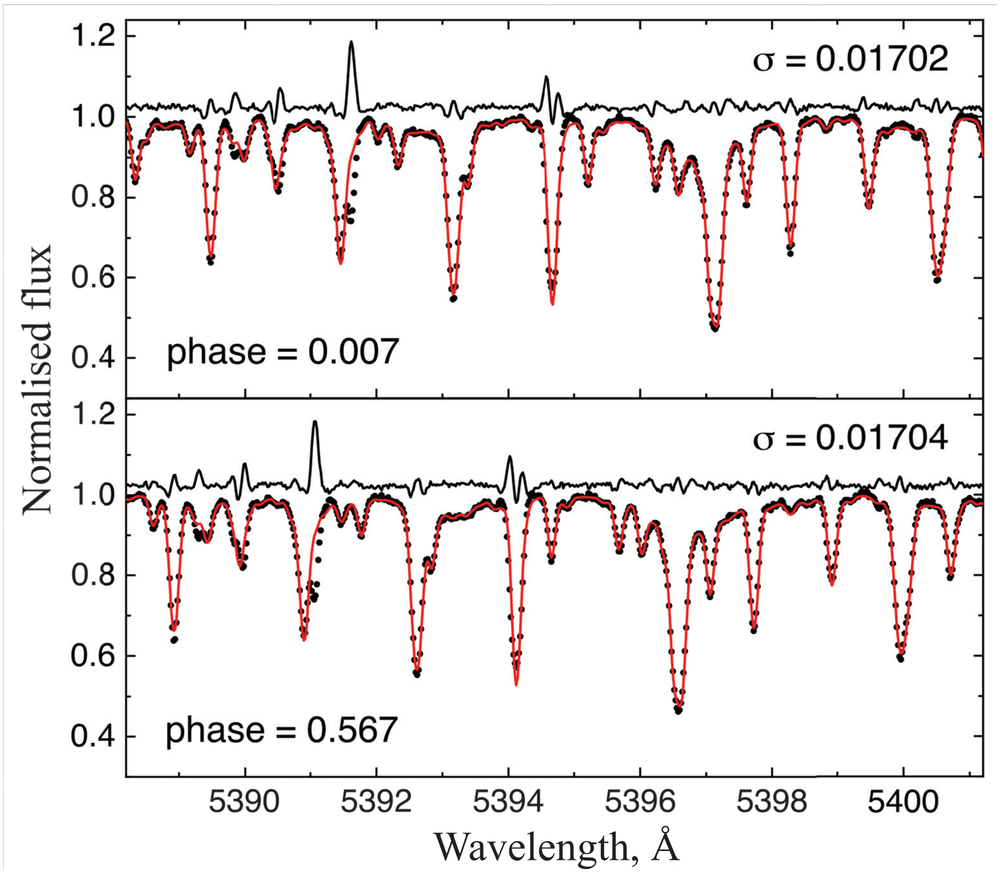

(**a**)

Figure 1. *Cont.*

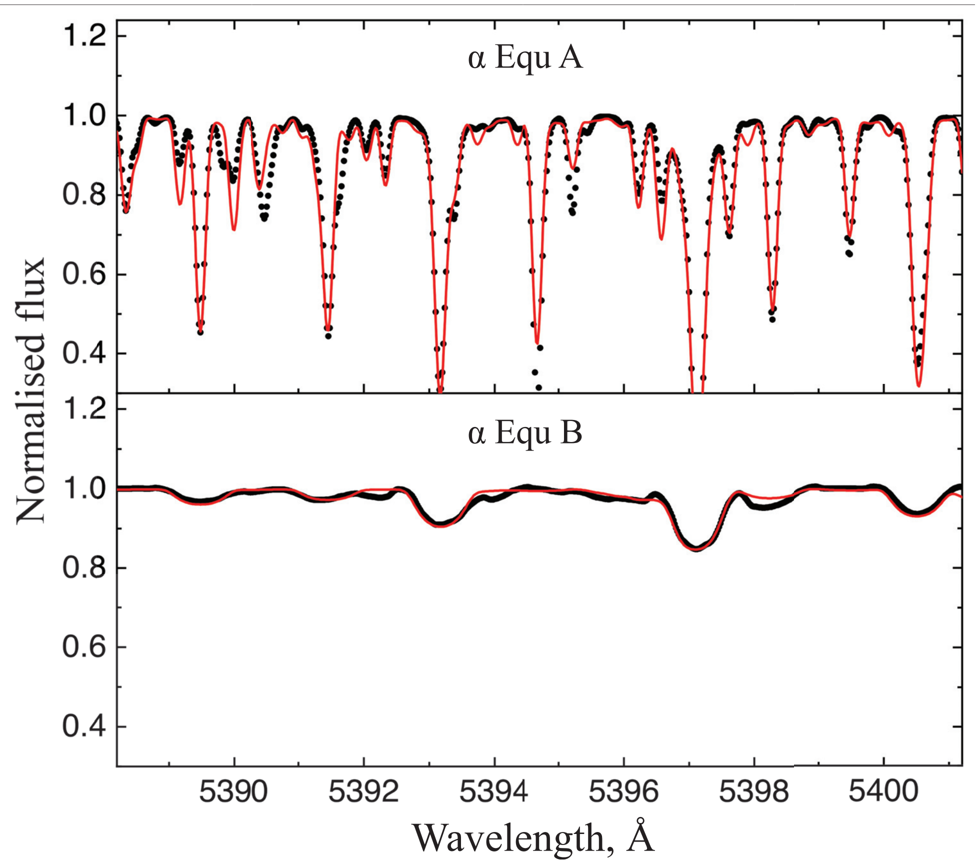

(**b**)

Figure 1. (**a**) The quality of the fit to observed spectra of α Equulei in two different orbital phases. The observations are indicated by black dots, the red line shows the best-fit composite profile, and the black line shows the residuals between the observations and the best-fit model. (**b**) Disentangled spectra of the components in the same spectral regions (black dots). The red lines show the fit of the synthetic spectra, which were calculated using the final atmospheric parameters, to the individual spectra of the components.

4. Stellar Fundamental Parameters

After each spectral disentangling into two component spectra, the atmospheric parameters of each component were determined using the spectroscopy made easy (SME) software package [14]. SME derives the effective temperature ($T_{\rm eff}$), surface gravity ($\log g$), metallicity ([M/H]), projected rotational velocity ($v_{\rm e} \sin i$), microturbulent velocity ($\xi_{\rm t}$), and macroturbulent velocity ($\zeta_{\rm RT}$). The code computes synthetic spectra using precomputed grids of stellar atmosphere models within selected spectral regions and performs a fitting procedure to the observed spectra to determine the best-fit values of the adjustable parameters. In our analysis, we employed the LLmodels grid [15]. Fitting was performed in the optical spectral range, including hydrogen lines that are particularly sensitive to variations in $T_{\rm eff}$, especially $\log g$.

The chosen spectral intervals contain approximately 300 Fe I and Fe II lines spanning a wide range of excitation potentials and equivalent widths (EWs) from 3 to 110 mÅ. These lines are crucial for constraining $T_{\rm eff}$ and $\log g$ by ensuring ionisation balance, i.e., agreement in elemental abundance derived from lines of different ionisation stages, as well as for determining $\xi_{\rm t}$. The microturbulent velocity was derived by requiring the consistency of the iron abundance obtained from individual lines of varying equivalent widths.

The results of the atmospheric parameter determination based on SME analysis of the observed spectra are presented in Table 2. We used two independent methods to estimate the uncertainties of the free parameters. The first is the classical approach based on the covariance matrix of the least-squares fit, which yields small internal errors that do not exceed 5 K for T_{eff} and 0.01 dex for the other parameters. Note that these uncertainties are not summarised in Table 2. The second method is based on the analysis of cumulative probability distributions (see, e.g., [14]), which accounts for observational noise, continuum normalisation, atomic data uncertainties, and other potential sources of systematic error. While the exact magnitude of these systematics is difficult to quantify, the true uncertainties likely lie between the estimates obtained from the two methods.

Table 2. Atmospheric parameters of both components.

Component	T_{eff}, K	$\log g$	[Fe/H]	$R/R_\odot$	ξ_t, km s^{-1}	ζ_{RT}, km s^{-1}	$v_e \sin i$, km s^{-1}
A	5160 ± 65	2.94 ± 0.28	0.11 ± 0.06	9.20 ± 0.01	1.13 ± 0.14	0.0	5.53 ± 0.14
B	8260 ± 218	3.62 ± 0.37	0.14 ± 0.16	2.60 ± 0.03	4.22 ± 1.15	0.0	25.88 ± 3.45

Note: T_{eff}, $\log g$, [Fe/H], ξ_t, ζ_{RT}, $v_e \sin i$ derived by SME and $R/R_\odot$ derived by SED for these parameters.

To check the adequacy of the chosen atmospheric model for the SME solution for the stars of the first and second components, we plotted the dependence of the abundance of individual Fe I–II lines on the reduced equivalent width $log(W_\lambda/\lambda)$ and ionisation potential E_i (Figure 2). In the first case, the absence of dependence confirms the correctness of the obtained microturbulent velocity ξ_t; in the second case, the parameters of the atmosphere T_{eff} and $\log g$. We also present the profiles of the H_α and H_β hydrogen lines with synthetic spectra calculated with the obtained from SME solution atmospheric models (Figure 3).

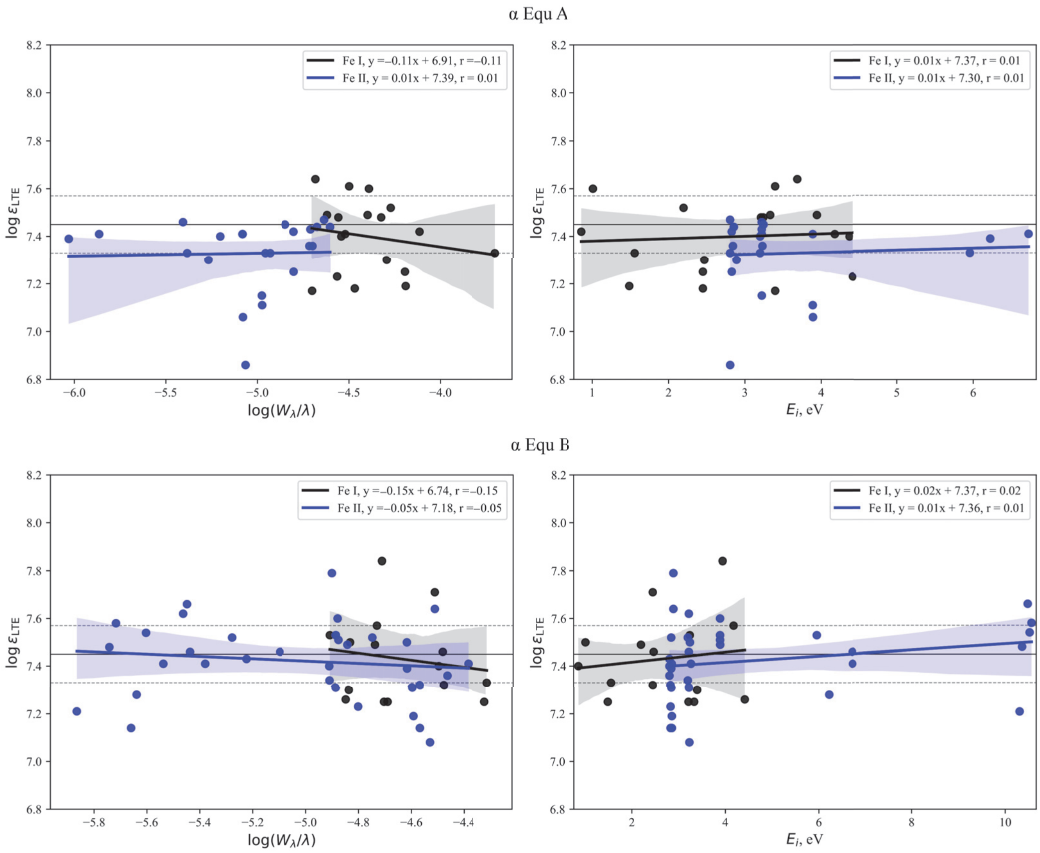

Figure 2. Fe I (black dots) and Fe I (blue dots) abundances relative to the reduced equivalent widths $log(W_\lambda/\lambda)$ and ionisation potential E_i for the α Equulei components. The solar Fe abundance is shown by the solid horizontal line. Dashed lines indicate differences of ± 0.12 from the solar abundance. The r value in the graphs is the Pearson correlation coefficient.

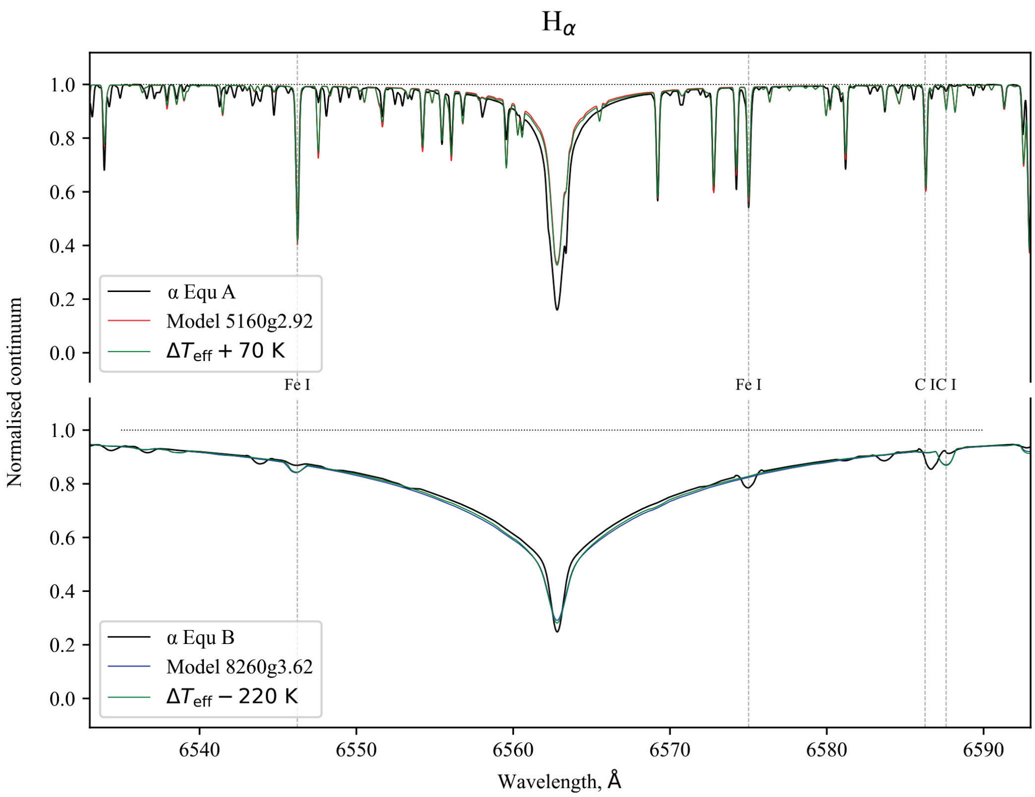

(**a**)

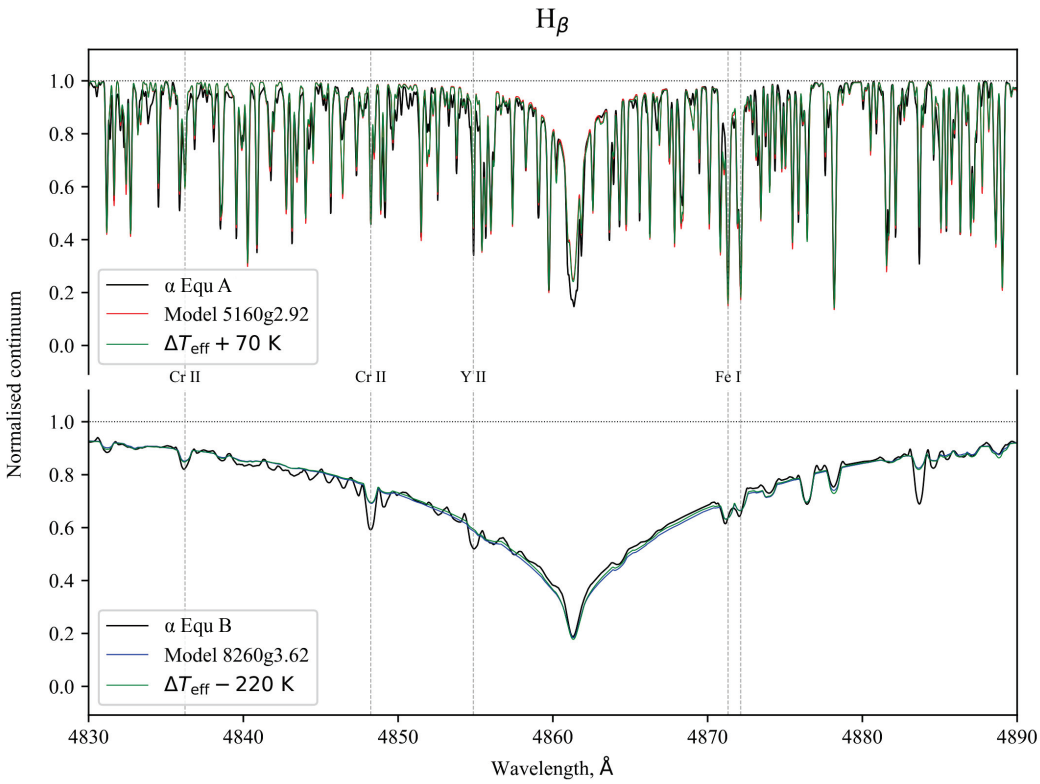

(**b**)

Figure 3. Hydrogen line profiles in the atmosphere of two components of α Equulei, (**a**)—H_α and (**b**)—H_β. Normalised continuum is indicated by a dashed line.

Another method for verifying the parameters is the spectral energy distribution (SED) fitting. This involves fitting a theoretical SED model to the observations by varying atmospheric parameters from an LLmodel grid, where absorption in each line is calculated taking into account the individual chemical composition. During the fitting process, parameters such as effective temperature ($T_{\rm eff}$), surface gravity ($\log g$), metallicity ([Fe/H]), and stellar radius ($R/R_\odot$) can be simultaneously adjusted. In this case, only the radius of each component in the binary star system was varied, as the other parameters were reasonably well determined using the SME method. The flux from each component was then calculated based on the radius contributions and compared to the observed data. The correction for interstellar reddening was applied according to the extinction curve from the paper [16] with the $A_v = 3.1 * E(B-V)$. $E(B-V)$ value was taken from the dust map from the EXPLORE (accessed on 21 July 2025) website[1] and for the distance 58 pc it equals 0.024.

As a result, we obtained $R_A = 9.20R_\odot$ and $R_B = 2.60R_\odot$, which is consistent with the results presented in the GG02 paper. The SED is shown in Figure 4.

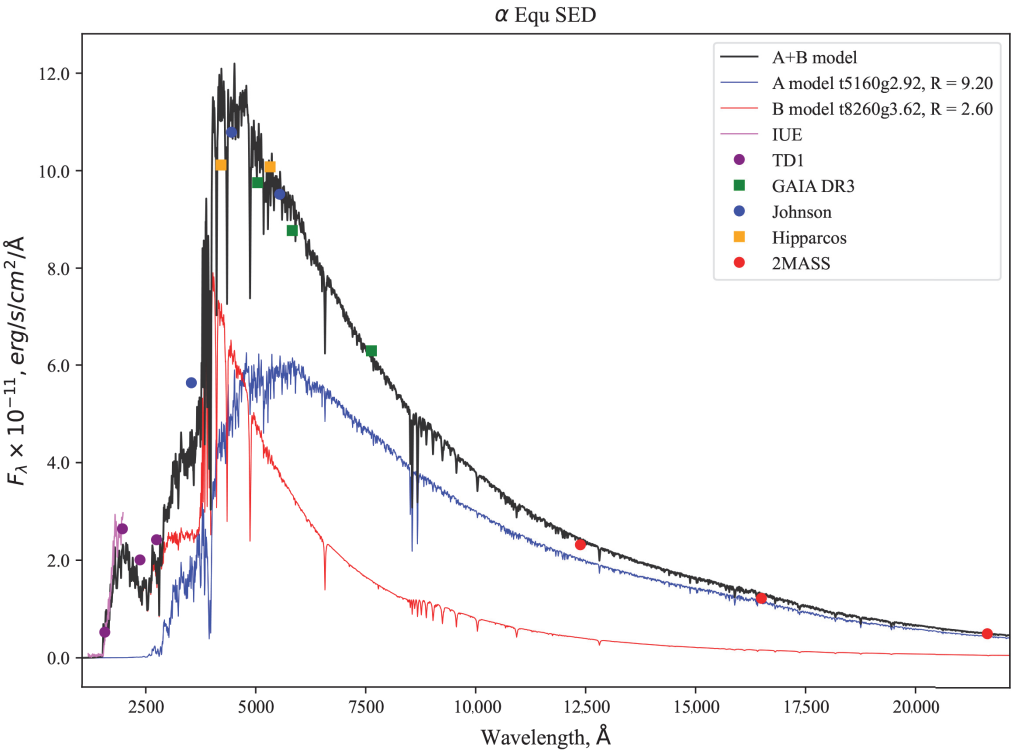

Figure 4. Spectral energy distributions for *α* Equulei. The black line represents the energy distribution obtained from calculations with the best-fit radius values of the primary and the secondary components; the red line represents the spectral energy distribution based on the SME solution for the primary component; the blue line refers to the secondary component. Radii are provided as the radius of the Sun.

5. Abundance Analysis

The determination of chemical abundances was carried out by fitting synthetic spectral line profiles to the observed ones using the BinMag6 code [17]. This program allows for variation of the elemental abundance, macroturbulent velocity, projected rotational velocity ($v_{\rm e} \sin i$), and radial velocity (V_r) of the star. We determined 25 abundances of elements from C to Nd. For elements up to barium, abundances were derived from lines of neutral atoms and first ions, while for the REEs, lines of first and second ions were used.

Synthetic spectra were computed with the SynthVb code [18], which enables the calculation of both LTE and non-LTE line profiles by incorporating b-factors (the ratio of atomic level populations in non-LTE to those in LTE), computed with the DETAIL code ([19–21]). Atomic data were taken from VALD3 [22,23].

Elemental abundances are provided on the standard logarithmic scale, $\log \epsilon = \log(N_{\rm el}/N_{\rm H}) + 12.04$, where $N_{\rm el}$ and $N_{\rm H}$ are the number densities of the element and hydrogen, respectively.

He, Al, S, V, Cr, Mn, Co, Ni, and REE abundances (La, Ce, and Nd) were derived in LTE. For C, O, Na, Mg, Si, K, Ca, Sc, Ti, Fe, Zn, Sr, Y, Zr, and Ba, we determined LTE and non-LTE abundances using model atoms. The model atoms and references to their detailed descriptions are summarized in Table 3. The derived abundances of α Equulei components are presented in Table 4 and shown in Figure 5.

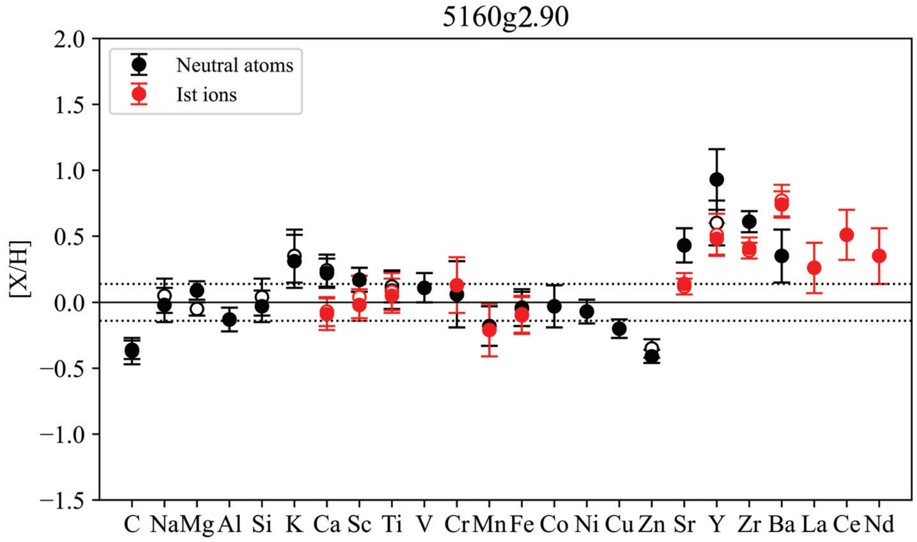

(**a**)

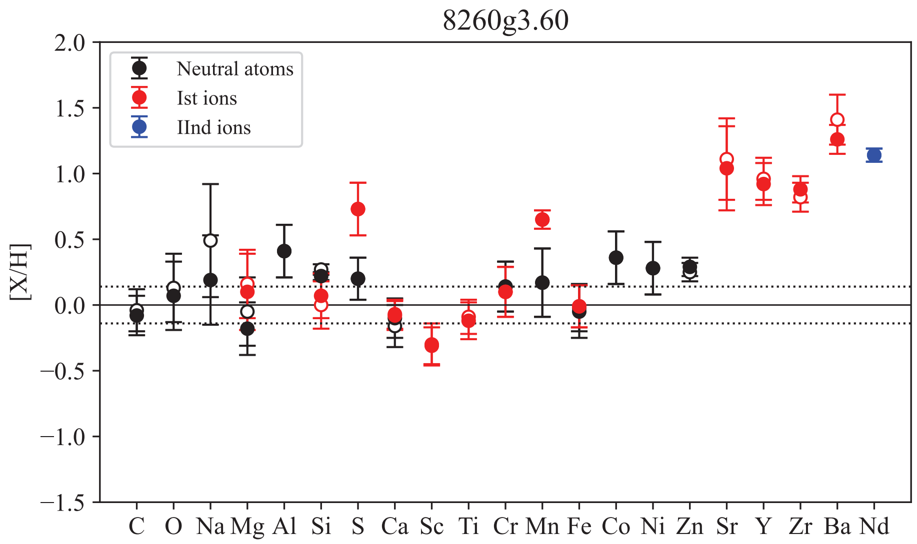

(**b**)

Figure 5. Abundance pattern in α Equulei relative to solar values, indicated by the solid line, with 3σ errors shown as dashed lines. (**a**) Abundances of α Equulei A with model 5160g3.90; (**b**) abundances of α Equulei B with model 8260g3.60. For elements where both LTE and non-LTE abundances are available, the corresponding LTE values are shown using open symbols.

In the spectrum of the primary component, the following elements are represented by a single line: K I 5108Å, Mn I 6205Å and Ba I 6110Å. The resonance line K I 7698Å was not observed in the SOPHIE spectrum because the necessary band was missing. In the secondary component, the elements Al I 5557Å, S I 5032Å, and Co I 5483Å are represented by a single line.

Table 3. Model atoms used for non-LTE calculations and corresponding references.

Element	Reference
C	Alexeeva, Ryabchikova, and Mashonkina [24]
O	Sitnova, Mashonkina, and Ryabchikova [25]
Na	Alexeeva, Pakhomov, and Mashonkina [26]
Mg	Alexeeva et al. [27]
Si	Mashonkina [28]
Ca	Sitnova, Mashonkina, and Ryabchikova [29]
K	Neretina et al. [30]
Sc	Mashonkina [31]
Ti	Sitnova et al. [32]
Fe	Sitnova et al. [33]
Zn	Sitnova et al. [34]
Sr, Zr, Ba	Mashonkina et al. [35]
Y	Romanovskaya et al. [36]

Table 4. Non-LT E and LTE abundances for atoms and ions in the atmosphere of both components of α Equulei (A: 5160g2.90 and B: 8260g3.60), scaled to $\log\epsilon = \log(N_{el}/N_H) + 12.04$.

		α Equulei A			**α Equulei B**			**Sun**
Element		**logϵ**	**[X/H]**	**n_l**	**logϵ**	**[X/H]**	**n_l**	
C I	L	8.11(07)	−0.36	2	8.43(16)	−0.04	5	8.47
	N	8.10(10)	−0.37		8.39(15)	−0.08		
O I	L				8.86(26)	0.13	9	8.73
	N				8.80(26)	0.07		
Na I	L	6.32(13)	0.05	4	6.76(43)	0.49	4	6.27
	N	6.25(13)	−0.02		6.46(34)	0.19		
Mg I	L	7.47(05)	−0.05	5	7.47(26)	−0.05	6	7.52
	N	7.61(07)	0.09		7.34(20)	−0.18		
Mg II	L				7.68(26)	0.16	4	
	N				7.62(29)	0.10		
$[Mg/H]_{mean}$	N		0.09(07)			−0.07(28)		
Al I	L	6.29(09)	−0.13	3	6.83(20)	0.41	1	6.42
Si I	L	7.55(14)	0.04	12	7.78(04)	0.27	5	7.51
	N	7.48(12)	−0.03		7.73(03)	0.22		
Si II	L				7.51(18)	0.00	5	
	N				7.58(17)	0.07		
$[Si/H]_{mean}$	N		−0.03(12)			0.15(15)		
S I	L				7.35(16)	0.20	4	7.15
S II	L				7.88(20)	0.73	1	
$[S/H]_{mean}$	L					0.31(26)		
K I	L	5.42(20)	0.35	1				5.07
	N	5.38(20)	0.31					
Ca I	L	6.51(12)	0.24	11	6.11(16)	−0.16	12	
	N	6.54(11)	0.27		6.17(15)	−0.10		
Ca II	L	6.20(11)	−0.07	3	6.20(11)	−0.07	5	
	N	6.18(12)	−0.09		6.19(11)	−0.08		
$[Ca/H]_{mean}$	N		0.20(19)			−0.10(14)		
Sc I	L	3.21(09)	0.17	11				3.04
Sc II	L	3.00(05)	0.04	7	2.74(16)	−0.30	6	
	N	3.02(12)	−0.02		2.73(14)	−0.31		
$[Sc/H]_{mean}$	L*		0.12(14)			−0.30(14)		
Ti I	L	5.02(12)	0.12	75				4.90
	N	4.99(14)	0.09					
Ti II	L	4.98(14)	0.08	37	4.81(13)	−0.09	36	
	N	4.95(13)	0.05		4.78(14)	−0.12		

Table 4. *Cont.*

Element		α Equulei A			α Equulei B			Sun
		logϵ	[X/H]	n_l	logϵ	[X/H]	n_l	
$[Ti/H]_{mean}$	N		0.08(14)			−0.12(14)		
V I	L	4.06(11)	0.11	24				3.95
	N							
Cr I	L	5.69(25)	0.06	9	5.77(19)	0.14	8	5.63
	N							
Cr II	L	5.74(20)	0.11	21	5.73(19)	0.10	28	
	N							
$[Cr/H]_{mean}$	L		0.10(22)			0.11(19)		
Mn I	L	5.29(15)	−0.18	6	5.64(26)	0.17	10	5.47
Mn II	L	5.26(20)	−0.21	1	6.12(07)	0.65	2	
$[Mn/H]_{mean}$	L		−0.18(14)			0.25(30)		
Fe I	L	7.41(14)	−0.04	24	7.43(18)	−0.02	19	7.45
	N	7.40(13)	−0.05		7.40(20)	−0.05		
Fe II	L	7.36(14)	−0.09	26	7.44(16)	−0.01	40	
	N	7.35(14)	−0.10		7.44(16)	−0.01		
$[Fe/H]_{mean}$	N		−0.08(14)			−0.02(18)		
Co I	L	4.83(16)	−0.03	13	5.22(20)	0.36	1	4.86
Ni I	L	6.13(09)	−0.07	13	6.48(20)	0.28	17	6.20
Cu I	L	4.04(07)	−0.14	3				4.24
Zn I	L	4.26(07)	−0.35	3	4.86(07)	0.25	3	4.61
	N	4.20(05)	−0.41		4.90(07)	0.29		
Sr I	L	3.31(13)	0.43	3				2.88
Sr II	L	3.00(06)	0.12	3	3.99(31)	1.11	3	
	N	3.02(08)	0.14		3.92(32)	1.04		
$[Sr/H]_{mean}$	L*		0.28(19)			1.11(31)		
Y I	L	2.75(17)	0.60	3				2.15
	N	3.08(23)	0.93					
Y II	L	2.66(16)	0.51	12	3.11(16)	0.96	15	
	N	2.63(17)	0.48		3.07(16)	0.92		
$[Y/H]_{mean}$	N		0.57(25)			0.92(16)		
Zr I	L	3.16(08)	0.61	2				2.55
Zr II	L	2.94(06)	0.39	3	3.37(11)	0.82	7	
	N	2.96(09)	0.41		3.43(10)	0.88		
$[Zr/H]_{mean}$	L*		0.48(13)			0.82(11)		
Ba I	L	2.52(20)	0.35	1				2.17
Ba II	L	2.94(12)	0.77	5	3.58(19)	1.41	5	
	N	2.91(10)	0.74		3.43(11)	1.26		
$[Ba/H]_{mean}$	L*		0.70(19)			1.41(19)		
La II	L	1.43(19)	1.43	4				1.17
Ce II	L	2.09(19)	0.51	11				1.58
Nd II	L	1.80(21)	0.35	15				1.45
Nd III	L				2.59(05)	1.14	3	

Note: L and N indicate LTE and non-LTE mean abundances. [X/H] indicates the abundance relative to solar abundance. n_l is the number of spectral lines used for abundance determination. The standard deviation is provided in parentheses and was assumed to be 0.2 dex when the abundance was obtained from a single line. 'Mean' in the lower index indicates an average abundance for both ionisation stages. The '*' symbol in the 'Mean' row denotes that the mean was calculated under LTE assumptions only, as non-LTE data are not available for both ionisation stages. The last column contains present-day solar system abundances taken from [37].

In the atmospheres of the investigated stars, the concentrations of Mg, Si, Ca, Sc, Ti, Cr, Mn, and Fe remain at equilibrium values. The abundances of heavy elements Zn, Sr, Y, Zr, and Ba in the primary component are represented by neutral atoms and ions. The non-LTE models of the atoms of the corresponding elements contain only the transitions of the once ionised element, and the non-LTE corrections do not exceed ±0.03 dex. Therefore, for neutral atoms, the non-LTE corrections are expected to be in approximately the same range. REEs are also observed in the primary component spectrum: La I, Ce I, and Nd I, where Ce I shows the maximum deviation from the solar values of 0.51 dex among the neighbouring elements.

In the spectrum of the secondary component, the non-LTE corrections of the heavy elements do not exceed ±0.06 dex and differ from the solar values in the range from 0.88 to 1.26, while the REEs are represented only by Nd III, which exceeds the solar value by 1.14 dex.

6. Discussion

The observed abundance pattern of chemical elements in the primary component is close to the solar values. The overall metallicity of the star is 0.09 ± 0.28, and the metallicity for elements from C to Cu is -0.02 ± 0.16. For the secondary component the metallicity are 0.35 ± 0.46 and for elements from C to Ni 0.09 ± 0.26, respectively.

Stars can be considered as normal if the abundance of the elements from He to Fe matches the solar values within 3σ error and the abundance of heavier elements can be correlated with the effective temperature, as we demonstrate in our previous paper [38]. The primary component of α Equulei has an almost solar abundance of elements from C to Cu, Zn show underabundance of 0.41 dex, and neutron-capture elements (n-capture) show overabundances from 0.41 dex for Zr I to 0.74 dex for Ba I. REEs are denoted by the elements Ce and Nd, and their relative abundances are estimated to be 0.35 and 0.51 dex greater than the solar values, respectively. Therefore, we conclude that the primary component of α Equulei is a normal star of the G spectral class.

Since the secondary component exhibits a higher metallicity than the primary component, we investigated the differences in abundance between low-rotation Am-type stars in different evolutionary stages. To make this comparison, we selected stars with close fundamental parameters: star HD 145788, which is in the early stages of becoming an Am star, with atmospheric parameters of $T_{\rm eff} = 9800$ and $\log g = 3.73$ [38], and the Am star o Peg with $T_{\rm eff} = 9600$ and $\log g = 3.81$ [36]. Both stars have well-determined LTE and non-LTE abundances, as well as reliably established atmospheric parameters. This makes them suitable benchmarks for comparison in Figure 6. The RMS of overall metallicity is -0.08 ± 0.29 between α Equulei B and HD 145788 and -0.21 ± 0.28 between α Equulei B and oPeg. The abundance pattern in the atmosphere of α Equulei B is close to that of HD 145788, despite the $T_{\rm eff}$ discrepancy of 1540 K.

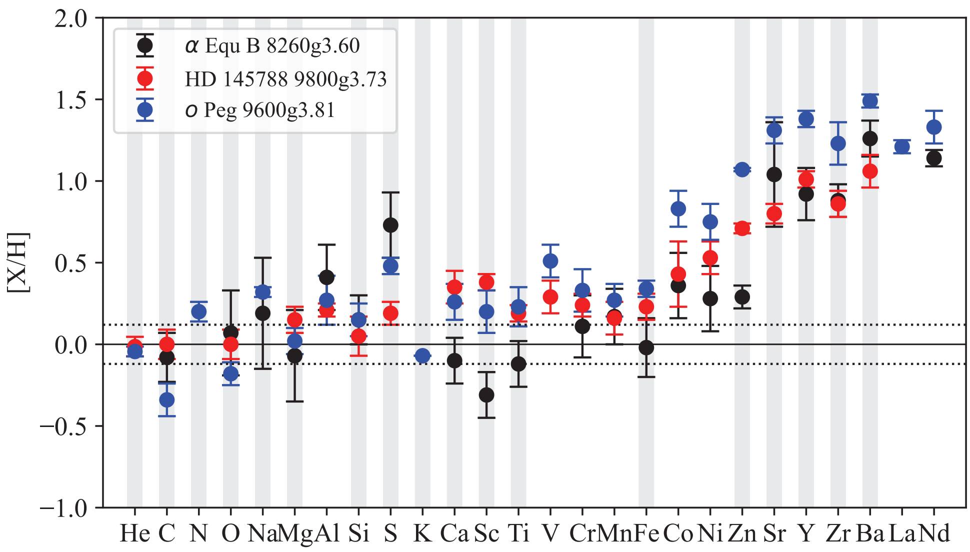

Figure 6. Abundance comparison of the secondary component of α Equulei B (black dots) to early Am star HD 145788 (red dots) and Am star o Peg (blue dots), relative to solar values, indicated by the solid line, with 3σ errors shown as dashed lines. Grey lines indicate non-LTE abundances.

The abundances of elements Al and S are higher than in Am stars, but note that the abundances of both elements were derived from a single line. The abundances of elements from Sc to Zn are lower than in an Am star; however, the abundances of heavy elements Sr, Y, Zr, and Ba are close to the values observed in HD 145788 within errors. Non-LTE calculations from [31] showed that in Am stars with $T_{\rm eff}$ < 9000 K and $\log g$ < 4 Ca and Sc have predominantly lower than solar abundances [9]. In the secondary component α Equulei, the Ca and Sc abundances do not contradict the conclusions of the above paper. Zn shows an abundance close to that of normal stars, where a Zn excess of up to 0.75 dex is observed in the 9500 K effective temperature range. Therefore, we conclude that α Equulei B is in the early stages of becoming an Am.

7. Conclusions

In this study, we performed, for the first time, a self-consistent chemical abundance analysis of the eclipsing spectroscopic binary α Equulei, covering elements from C to Nd. The fundamental stellar parameters were refined using spectral disentangling and the SME package. Additionally we validated the fundamental parameters by demonstrating that the abundance of individual Fe I–II lines does not depend on the reduced equivalent widths and ionisation potential, spectral energy distributions, or hydrogen line profile fitting. We determined the abundances of 25 chemical elements, applying non-LTE methods to 15 of them. The non-LTE abundances of C, O, Na, Mg, Si, K, Ca, Sc, Ti, Fe, Zn, Sr, Y, Zr, and Ba were obtained using the same non-LTE modelling approach as in [36].

The primary component (G7-type) exhibited a typical abundance pattern for normal stars: the elements from He to Fe matched the solar values, and neutron-captured elements showed an overabundance average of up to 0.5 dex, relative to solar values. Despite this, non-LTE effects for the primary prove negligible (<0.1 dex) and can be safely disregarded in abundance analysis.

In contrast, the secondary component shows Am star characteristics, requiring non-LTE corrections for elemental abundances. Our results support the spectral type classifications of both components proposed in GG02. However, based on our comparison of chemical abundances in Am stars at different evolutionary stages, we conclude that α Equulei B is an early stage Am star. We also detect Na, K, V, Cu, La, and Ce exclusively in the primary component, while S appears only in the secondary.

Since the atmospheric parameters we obtained match those in the GG02 paper, we also confirm the conclusion that these stars formed simultaneously. The observed differences in chemical abundance between the two components of the α Equulei binary system suggest different diffusion processes in their stellar atmospheres. Our results support the idea that chemical anomalies in Am stars emerge during the main sequence and may decrease as the stars evolve toward the subgiant branch due to the deepening of the convective zone.

Supplementary Materials: The following supporting information can be downloaded at: https://www.mdpi.com/article/10.3390/galaxies13040088/s1.

Author Contributions: Conceptualisation, A.R.; methodology, A.R. and S.Z.; software, A.R. and S.Z.; validation, A.R. and S.Z.; formal analysis, A.R. and S.Z.; investigation, A.R. and S.Z.; resources, A.R. and S.Z.; data curation, A.R.; writing original draft preparation, A.R.; writing review and editing, A.R. and S.Z.; visualisation, A.R. and S.Z.; supervision, A.R.; project administration, A.R.; funding acquisition, A.R. All authors have read and agreed to the published version of the manuscript.

Funding: This research received no external funding.

Data Availability Statement: Spectra of α Equulei normalised to the continuum level are provided as Supplementary Materials in the form of an ASCII file in CDS. The full table of used lines with $loggf$, excitation potentials E_i, LTE and non-LTE abundances, and references for oscillator strengths and hyperfine constants is available online.

Acknowledgments: The authors would like to express their gratitude to T. Sitnova for providing the results of non-LTE calculations for Fe, Ti, Y, and Zn and to L. Mashonkina for providing the results of non-LTE calculations for Sc II. The authors would also like to acknowledge T. Ryabchikova for her constructive feedback on the paper.

Conflicts of Interest: The authors declare no conflicts of interest.

Abbreviations

The following abbreviations are used in this manuscript:

SLD	Spectral Line Deconvolution
SME	Spectroscopy Made Easy
REE	Rare Earth Elements
MS	Main Sequence
LTE	Local Thermodynamic Equilibrium
SOPHIE	Spectrograph for the Observation of the Phenomena of Stellar Interiors and Exoplanets
HR mode	High-resolution Mode
UVES	Ultraviolet and Visual Echelle Spectrograph
LLmodels	Line-by-Line models
EWs	Equivalent Widths

Notes

[1] https://explore-platform.eu (accessed on 21 July 2025).

References

1. Michaud, G. Diffusion Processes in Peculiar a Stars. *Astrophys. J.* **1970**, *160*, 641. [CrossRef]
2. Preston, G.W. The chemically peculiar stars of the upper main sequence. *Annu. Rev. Astron. Astrophys.* **1974**, *12*, 257. [CrossRef]
3. Michaud, G. Meridional circulation versus diffusion in stellar envelopes. *Astrophys. J.* **1982**, *258*, 349. [CrossRef]
4. Watson, W.D. Particle Diffusion in Stars Having Shallow Convective Envelopes. *Astron. Astrophys.* **1971**, *13*, 263.
5. Alecian, G. Fm-Am stars in open clusters as a tool for stellar physics. *Astron. Astrophys.* **1996**, *310*, 872.
6. Richer, J.; Michaud, G.; Turcotte, S. The Evolution of AMFM Stars, Abundance Anomalies, and Turbulent Transport. *Astrophys. J.* **2000**, *529*, 338. [CrossRef]
7. Trust, O.; Jurua, E.; De Cat, P.; Joshi, S.; Lampens, P. HERMES spectroscopy of normal A and Am stars. *Mon. Not. R. Astron. Soc.* **2021**, *504*, 5528. [CrossRef]
8. Nasolo, Y.; Çalışkan, S. A search for chemical anomalies of seven A-type stars. *Mon. Not. R. Astron. Soc.* **2023**, *521*, 3699. [CrossRef]
9. Mashonkina, L.I.; Fadeyev, Y.A. Revision of the Calcium and Scandium Abundances in Am Stars Based on Non-LTE Calculations and Comparison with Diffusion Stellar Evolution Models. *Astron. Lett.* **2024**, *50*, 373. [CrossRef]
10. Paunzen, E.; Fedurco, M.; Hełminiak, K.G.; Pintado, O.I.; Hambsch, F.-J.; Hümmerich, S.; Niemczura, E.; Bernhard, K.; Konacki, M.; Hubrig, S.; et al. Orbital parameters and evolutionary status of the highly peculiar binary system HD 66051. *Astron. Astrophys.* **2018**, *615*, A36. [CrossRef]
11. Griffin, R.E.M.; Griffin, R.F. Composite spectra Paper 11: α Equulei, an astrometric binary with an Am secondary. *Mon. Not. R. Astron. Soc.* **2002**, *330*, 288. [CrossRef]
12. Ryabchikova, T.; Zvyagintsev, S.; Tkachenko, A.; Tsymbal, V.; Pakhomov, Y.; Semenko, E. Fundamental parameters and abundance analysis of the components in the SB2 system HD 60803. *Mon. Not. R. Astron. Soc.* **2022**, *509*, 202. [CrossRef]
13. Mazeh, T.; Zucker, S.; Smith, H. TODCOR: A New Two-Dimensional Correlation Technique to Analyze Stellar Spectra in Search for Faint Companions. *Am. Astron. Soc. Meet. Abstr.* **1993**, *25*, 1425
14. Piskunov, N.; Valenti, J.A. Spectroscopy Made Easy: Evolution. *Astron. Astrophys.* **2017**, *597*, A16. [CrossRef]
15. Shulyak, D.; Tsymbal, V.; Ryabchikova, T.; Stütz, C.; Weiss, W.W. Line-by-line opacity stellar model atmospheres. *Astron. Astrophys.* **2004**, *428*, 993. [CrossRef]
16. Fitzpatrick, E.L. Correcting for the Effects of Interstellar Extinction. *Publ. Astron. Soc. Pac.* **1999**, *111*, 63. [CrossRef]
17. Kochukhov, O. BinMag: Widget for Comparing Stellar Observed with Theoretical Spectra. Astrophysics Source Code Library. ascl:1805.015. 2018. Available online: https://ui.adsabs.harvard.edu/abs/2018ascl.soft05015K/abstract (accessed on 21 July 2025).
18. Tsymbal, V.; Ryabchikova, T.; Sitnova, T. Software for NLTE Spectrum Fitting. *Phys. Magn. Stars* **2019**, *518*, 247.

19. Giddings, J.R. Quantum Particles in Kerr-Newman Fields. Ph.D. Thesis, Moscow University, Moscow, Russia, 1981.
20. Butler, K. A Non-LTE Study of NIII in O Stars. Ph.D. Thesis, University College London, London, UK, 1984.
21. Przybilla, N.; Nieva, M.-F.; Butler, K. Testing common classical LTE and NLTE model atmosphere and line-formation codes for quantitative spectroscopy of early-type stars. *J. Phys. Conf. Ser.* **2011**, *328*, 012015. [CrossRef]
22. Piskunov, N.E.; Kupka, F.; Ryabchikova, T.A.; Weiss, W.W.; Jeffery, C.S. VALD: The Vienna Atomic Line Data Base. *Astron. Astrophys. Suppl. Ser.* **1995**, *112*, 525.
23. Pakhomov, Y.V.; Ryabchikova, T.A.; Piskunov, N.E. Hyperfine Splitting in the VALD Database of Spectral-line Parameters. *Astron. Rep.* **2019**, *63*, 1010. [CrossRef]
24. Alexeeva, S.A.; Ryabchikova, T.A.; Mashonkina, L.I. NLTE carbon abundance determination in selected A- and B-type stars and the interpretation of C I emission lines. *Mon. Not. R. Astron. Soc.* **2016**, *462*, 1123. [CrossRef]
25. Sitnova, T.M.; Mashonkina, L.I.; Ryabchikova, T.A. Influence of departures from LTE on oxygen abundance determination in the atmospheres of A-K stars. *Astron. Lett.* **2013**, *39*, 126. [CrossRef]
26. Alexeeva, S.A.; Pakhomov, Y.V.; Mashonkina, L.I. Non-LTE sodium abundance in galactic thick- and thin-disk red giants. *Astron. Lett.* **2014**, *40*, 406. [CrossRef]
27. Alexeeva, S.; Ryabchikova, T.; Mashonkina, L.; Hu, S. NLTE Line Formation for Mg I and Mg II in the Atmospheres of B-A-F-G-K Stars. *Astrophys. J.* **2018**, *866*, 153. [CrossRef]
28. Mashonkina, L. Non-local thermodynamic equilibrium line formation for Si I-II-III in A-B stars and the origin of Si II emission lines in ι Her. *Mon. Not. R. Astron. Soc.* **2020**, *493*, 6095. [CrossRef]
29. Sitnova, T.M.; Mashonkina, L.I.; Ryabchikova, T.A. A NLTE line formation for neutral and singly ionized calcium in model atmospheres of B-F stars. *Mon. Not. R. Astron. Soc.* **2018**, *477*, 3343. [CrossRef]
30. Neretina, M.D.; Mashonkina, L.I.; Sitnova, T.M.; Yakovleva, S.A.; Belyaev, A.K. Influence of Collisions with Hydrogen Atoms on Non-LTE Effects for K I and Ca II in Stellar Atmospheres. *Astron. Lett.* **2020**, *46*, 621. [CrossRef]
31. Mashonkina, L. Influence of departures from LTE on determinations of the scandium abundances in A-B-type stars. *Mon. Not. R. Astron. Soc.* **2024**, *527*, 8234. [CrossRef]
32. Sitnova, T.M.; Yakovleva, S.A.; Belyaev, A.K.; Mashonkina, L.I. Influence of Collisions with Hydrogen on Titanium Abundance Determinations in Cool Stars. *Astron. Lett.* **2020**, *46*, 120. [CrossRef]
33. Sitnova, T.; Ryabchikova, T.; Alexeeva, S.; Mashonkina, L. NLTE abundances of C, O, Ca, Ti, and Fe in the reference BAF-type stars. *Rediscovering Our Galaxy* **2018**, *334*, 360. [CrossRef]
34. Sitnova, T.M.; Yakovleva, S.A.; Belyaev, A.K.; Mashonkina, L.I. Non-LTE abundances of zinc in different spectral type stars and the Galactic [Zn/Fe] trend based on quantum-mechanical data on inelastic processes in zinc-hydrogen collisions. *Mon. Not. R. Astron. Soc.* **2022**, *515*, 1510. [CrossRef]
35. Mashonkina, L.; Ryabchikova, T.; Alexeeva, S.; Sitnova, T.; Zatsarinny, O. Chemical diversity among A-B stars with low rotational velocities: Non-LTE abundance analysis. *Mon. Not. R. Astron. Soc.* **2020**, *499*, 3706. [CrossRef]
36. Romanovskaya, A.M.; Ryabchikova, T.A.; Pakhomov, Y.V.; Korotin, S.A.; Sitnova, T.M. Non-LTE abundance analysis of A-B stars with low rotational velocities—II. Do A-B stars with normal abundances exist? *Mon. Not. R. Astron. Soc.* **2023**, *526*, 3386. [CrossRef]
37. Lodders, K. Relative Atomic Solar System Abundances, Mass Fractions, and Atomic Masses of the Elements and Their Isotopes, Composition of the Solar Photosphere, and Compositions of the Major Chondritic Meteorite Groups. *Space Sci. Rev.* **2021**, *217*, 44. [CrossRef]
38. Romanovskaya, A.M.; Ryabchikova, T.A.; Mashonkina, L.I.; Sitnova, T.M.; Serebryakova, N. Non-LTE Abundance Analysis of Main-Sequence A–B Stars. III. Normal-Star Criteria. *Astron. Lett.* **2025**, *51*, 1. [CrossRef]

galaxies

MDPI

Article

Long-Term Stability of Chemical Spots and Reasons for the Period Variations in Ap Star CU Vir

Ilya Potravnov [1,*], Tatiana Ryabchikova [1], Leonid Kitchatinov [2] and Yuri Pakhomov [1]

1 Institute of Astronomy of Russian Academy of Sciences, Pyatnitskaya Str., 48, 119017 Moscow, Russia; pakhomov@inasan.ru (Y.P.)
2 Institute of Solar-Terrestrial Physics, Siberian Branch of Russian Academy of Sciences, Lermontov Str. 126A, 664033 Irkutsk, Russia
* Correspondence: ilya.astro@gmail.com

Abstract

We present the results of Doppler Imaging of the Ap star CU Vir in the silicon lines over the 1985–2011 time span, as well as multi-element imaging in the 2009/2011 epoch. The surface distribution of silicon in CU Vir exhibits stability over the approximately 26 years studied: the number, shape, and mutual distribution of the overabundance spots have remained unchanged. The modelling of the light curve based on the surface elemental distribution obtained with DI did not reveal any significant changes in the shape of the light curve that could explain the photometric phase shift observed in CU Vir. Consequently, the phase shifts and changes in the photometric period of CU Vir are caused by the rigid longitudinal drift of the surface-abundance structures. We performed simulations of the Tayler instability of the background magnetic field of CU Vir, and discuss the possibility of explaining the period variations by the drift of surface instability modes.

Keywords: Ap star; Si star; CU Vir; high-resolution spectroscopy; Doppler Imaging; synthetic photometry; Tayler instability

1. Introduction

The star CU Vir (=HD124224) is one of the most extensively studied magnetic Ap/Bp stars. In key properties, it is a typical representative of its class; however, a number of unique features attract attention to this object.

CU Vir exhibits a peculiar A0p spectrum, typical of Ap/Bp stars, with a weakened intensity of helium and an enhanced intensity of silicon lines varying in antiphase with the period of axial rotation [1]. The star also hosts a global, large-scale magnetic field with a dominant dipole component, $B_p \sim$4 kG in strength [2]. Surface imaging of CU Vir revealed the inhomogeneous (spotty) surface distribution of Si, He, Fe, Cr, and Mg with abundance gradients up to +2 dex in logarithmic scale relative to the Sun [2–6]. Axial rotation of the spotted stellar surface leads to a modulation of the light variations of CU Vir, with an amplitude of about $\Delta V \sim$0.1 mag, in accordance with the so-called "oblique rotator model" [3,7,8].

Meanwhile, CU Vir has one of the shortest rotational periods, $P \approx 0.52$ d, among known Ap/Bp stars[1] and demonstrates extraordinary changes. A comparison between observations obtained at different epochs allowed the detection of significant phase shifts on the decadal timescale, both in line intensity and photometric variations [11], which can be indicative of apparent rotational period changes. Employing the distribution of the surface magnetic field recovered by Zeeman–Doppler Imaging [2], MacDonald et al. [12] showed that magnetic braking due to radiatively driven wind can lead to a spin-down time consistent with the observed increase in the CU Vir period in ∼1960–2010. However, this model does not resolve two contradictions. First, as Mikulášek et al. [13] noted, this spin-down timescale is ∼2 orders of magnitude less than the age of the star. Second, braking by the magnetised wind results in a period increase only, whereas observations show a more complex behavior. Apparently, another mechanism is responsible for both the decreases and increases in the CU Vir period.

Currently, published observations of CU Vir cover the interval from 1955 to 2017 and show unambiguous evidence of such an effect. It is noteworthy that CU Vir has also been detected as a variable radio source at 1.4 GHz [14–16]. Its radio emission also exhibits period variations resembling so-called "glitches" in pulsars. Period changes in CU Vir can be interpreted within the framework of two different data models. First, based on O-C analysis of critically selected observations, a model with three discrete (discontinuous) period changes in 1985, 1992, and 2012 was proposed [11,17–19]. Within the interval between successive glitches, the model suggests a constant period. The first two abrupt period changes correspond to a deceleration in the apparent stellar rotation, and the last one corresponds to an acceleration. Although these period changes do not exceed three seconds in magnitude, given the rapid rotation of the star, such changes lead to significant phase shifts. In turn, Mikulášek et al. [13] proposed, and later updated [20], a model of continuous period variations. The data were fitted by a cosine function as well as by a 5th-order polynomial, which yielded a cycle of ∼65 years. According to this model, a slowdown of rotation was observed from 1958 to 2005. After the local maximum of the period in 2005, the acceleration of rotation began.

It has now been established that CU Vir is not a unique object, but belongs to a small subgroup of Ap stars with variable periods, although its behavior is the most complex (e.g., [18,19]). The reasons for the period variations in CU Vir and other Ap stars are currently unclear. It was pointed out that the observed rates of period changes and their character are difficult to explain through evolutionary changes in angular momentum [13,21]. In non-magnetic peculiar HgMn stars, annual changes in spot structure have been recorded [22–24], which also lead to changes in their very low-amplitude photometric variability [25]. In Ap stars, the spot patterns are expected to be much more stable due to the stabilising role of the magnetic field. However, the fields themselves are affected by MHD instabilities, which can lead to internal changes or rigid longitudinal drift of magnetic and associated chemical structures [26–29]. In such cases, variations in surface distribution and abundance scale of elements like silicon, which grossly affect the emergent flux, may lead to variations in the photometric period. In the context of this idea, several models have been proposed to explain period variations in CU Vir and other Ap stars by Alfvén waves [27,28] or the Tayler instability [29]. On the other hand, an independent mechanism of the free-body precession of the magnetically distorted star, which affects the visibility of the spots, was proposed even earlier [30]. In the latter case, the phase shifts arise due to small variations in the shape of the light curve with a period of several decades. Indeed, changes in the shape of the CU Vir light curve between the 1993–94 and 1997–98 seasons have been suspected [19].

A direct method to discriminate between these two scenarios is to reconstruct the surface distributions of elements contributing to the light variability on a reliable timescale. CU Vir has been frequently targeted for Doppler Imaging (DI) [2,4–6]. Kochukhov et al. [2] compared their surface maps recovered from 2009–2011 data with the previous maps by Kuschnig et al. [6] based on 1995 observations and pointed out the fundamental similarity of the reconstructed surface structures. The remaining minor differences could be due to differences in the imaging techniques, adopted stellar parameters, and spectral line lists. Therefore, it is of interest to compare the spot structures in CU Vir reconstructed in a uniform way over an extended time interval over which noticeable changes in the photometric period occurred and to check its impact on the light curve. These are the aims of the present study.

2. Observational Data

2.1. Spectroscopy

We collected archival as well as previously unpublished original phase-resolved spectroscopic time series of CU Vir over the interval of 1985–2011. Namely, we collected the following:

(1) Observations in the Si II 6347 Å line obtained by A. Hatzes in February–March 1985 with the 3-m Shane telescope at Lick Obsevatory equipped with a Coudé-spectrograph and 800 × 800 px Texas Instruments CCD detector. The wavelength coverage of each spectrogram was 6332–6362 Å with a resolving power R ≈ 50,000. In total, 12 spectrograms were obtained with a uniform distribution over rotational phases. Surface silicon maps of CU Vir were published based on these data [4,5].

(2) Observations in the Si II 6347 Å line were made in April 1994 and February–June 1996 by V. Malanushenko at the Crimean Astrophysical Observatory using a Coudé-spectrograph and CCD detector attached to the 2.6-m Shajn telescope. The wavelength coverage of the observations was 6329–6358 Å with 0.2 Å resolution corresponding to R ≈ 32,000. In total, 39 spectrograms were obtained. We used 16 of them, covering rotational period of CU Vir with a step of $\Delta\varphi \approx 0.1$ in phase.

(3) Observations in the Si II 4128/4130 Å doublet, obtained in March 1995 with the 1.93-m telescope of Haute-Provence Observatory, equipped with the AURELLIE spectrograph. A total of 19 spectrograms with good phase coverage were obtained in the wavelength range 4060–4260 Å with a nominal resolution $R \approx 20,000$. The multi-element DI of CU Vir was published using these data [6].

(4) Echelle spectra of CU Vir observed with the 2m Bernard Lyot Telescope at Pic du Midi Observatory were retrieved from the PolarBase archive [31]. Observations were made in spectropolarimetric mode with the NARVAL spectrograph during several observational runs between 2009 and 2011. The wavelength coverage was 3700–10,500 Å with a resolving power $R \approx 65{,}000$. This material was used by Kochukhov et al. [2] to perform Zeeman–Doppler Imaging of CU Vir. In our study, we used 12 intensity spectra with a signal-to-noise ratio S/N ≈ 200–300.

The complete observational log is provided in Table 1. All spectra except those obtained with NARVAL were at our disposal in the already processed form and cover only short spectral region around Si II 6347 Å and 4128/4130 Å lines. Post-processing of these data involved only corrections of the continuum level. NARVAL spectra were retrieved in ASCII format automatically processed with the Libre-ESpRIT software package [32]. Data handling consisted of combining the individual exposures, merging the echelle orders, and normalising the continuum in the spectral intervals of interest using low-order spline fitting. Water-vapour telluric lines were removed from the target spectra using an appropriately scaled spectrum of the featureless, rapidly rotating star HR 1948 observed with NARVAL in similar instrumental setting. The heliocentric correction was applied to the wavelength scale, and the spectra were also corrected for a radial velocity of $RV = -3.7$ km s^{-1} estimated from the phase-averaged spectrum.

Table 1. Journal of spectroscopic observations of CU Vir used for DI. Rotational phases are given according to the Pyper and Adelman [18] model (P20) and the Mikulášek et al. [20] cosine model (M19).

HJD	Phase (P20)	Phase (M19)	HJD	Phase (P20)	Phase (M19)
	1985 (Lick)			1996 (CrAO)	
2446101.905	0.913	0.874	2449470.295	0.895	0.833
2446101.925	0.952	0.912	2449470.320	0.943	0.881
2446101.973	0.042	0.005	2449496.344	0.920	0.859
2446102.016	0.126	0.087	2450134.603	0.658	0.606
2446102.063	0.217	0.177	2450174.451	0.184	0.132
2446102.989	0.995	0.956	2450191.418	0.769	0.716
2446132.900	0.439	0.400	2450210.412	0.244	0.193
2446132.965	0.564	0.525	2450233.317	0.232	0.181
2446133.020	0.670	0.631	2450233.358	0.311	0.260
2446133.069	0.764	0.725	2450233.454	0.495	0.444
2446133.887	0.335	0.296	2450253.303	0.615	0.563
2446133.960	0.475	0.436	2450253.363	0.730	0.679
	1995 (OHP)		2450254.311	0.551	0.499
2449798.489	0.172	0.115	2450255.275	0.402	0.351
2449798.622	0.427	0.371	2450255.289	0.428	0.377
2449799.434	0.986	0.930	2450255.305	0.459	0.408
2449799.575	0.257	0.201		2009/11 (PdM)	
2449799.612	0.328	0.272	2454902.517	0.151	0.09
2449800.410	0.861	0.805	2454904.485	0.930	0.869
2449800.502	0.037	0.981	2454905.554	0.984	0.922
2449800.599	0.224	0.168	2454906.487	0.774	0.714
2449801.412	0.785	0.729	2454909.493	0.548	0.487
2449802.415	0.711	0.655	2454935.487	0.468	0.407
2449803.438	0.676	0.620	2454935.523	0.537	0.476
2449804.444	0.601	0.552	2454945.486	0.670	0.610
2449804.468	0.654	0.598	2455292.589	0.261	0.203
2449806.413	0.389	0.333	2455596.718	0.322	0.269
2449806.435	0.431	0.375	2455657.510	0.070	0.017
2449806.452	0.464	0.408	2455690.479	0.385	0.333
2449806.469	0.497	0.441			
2449806.484	0.525	0.469			
2449806.500	0.556	0.500			

2.2. Calculation of Rotational Phases

To calculate the rotational phases corresponding to the moments of spectroscopic observations, we explored both existing models of period changes in CU Vir: a model with discrete period glitches [18] and a model with continuous period variations [13,20]. In the framework of the former model, the star is assumed to experience three period changes: in 1985, 1993, and 2012, respectively. The following constant periods were adopted: (1) $P_1 = 0.5206775$ d for the interval 1958–1983; (2) $P_2 = 0.5206961$ d for the interval 1979–1992; (3) $P_3 = 0.5207140$ d for the interval 1993–2011; (4) $P_4 = 0.5206987$ d for the interval 2012–2017. As an alternative, we examined the cosine model of continuous period changes [20]. A more detailed discussion of these models will be presented in the forthcoming paper [33]. Here, we note that at the moments of spectroscopic observations, both models predict very close phases (as can be seen from Table 1), with a difference not exceeding $\Delta\phi \approx 0.06$.

In our study, we adopt the model Pyper and Adelman [18] for calculating the rotational phases, owing to the convenience of handling spectroscopic data obtained at different epochs. It should be noted that due to the temporal remoteness of the ephemeris zero point $T_0 = 2435256.755$, corresponding to the light minimum from the discussed epochs, the determination of rotational phases requires a recalculation of T_0 to the beginning of a new epoch after each period glitch.

The spectroscopic observations analysed in the present study were obtained at epochs (2) and (3). As demonstrated by our analysis of the line profiles and the Doppler maps reconstructed from them, the 1995, 1996, and 2009–2011 observations are coherently phased with the P_3 period, while the 1985 observations required the use of the P_2 period. Since the period is assumed to be constant within epoch (3), the addition of selected 1994 observations to the 1996 dataset, for better phase coverage, is justified. The same is true for the NARVAL data distributed over 2009–2011.

3. Doppler Imaging

3.1. Technique

The surface-abundance distribution in CU Vir was inversed using the Doppler Imaging technique implemented in the INVERS11 code [34], which is a non-magnetic version of the INVERS10 code. The idea of the method is to solve the inverse problem of reconstructing the surface distribution of element(s) based on a phase-resolved sequence of spectral line(s) profiles containing Doppler details arising from an inhomogeneous surface chemical composition and modulated by axial rotation [35,36]. The problem is solved by fitting the observed line profiles by theoretical spectrum. The stellar surface is divided into a grid where local line profiles are calculated by solving the non-magnetic radiative transfer equation. The elemental abundance is a free parameter determined by minimising discrepancies between the synthetic line profile integrated over the disc of the rotating star and the observations. The uniqueness of the solution of the inverse problem is achieved by using the Tikhonov regularisation method. As input parameters, the DI procedure requires (1) a series of observed line profiles with reliable coverage of the stellar rotation period; (2) a model of stellar atmosphere, an initial assumption about chemical composition, and atomic data for the examined spectroscopic transitions; and (3) stellar rotation parameters: $v \sin i$ and inclination angle i. The parameters that control the solution, i.e., the surface-abundance maps, are the grid density, which have to be matched to the achievable spatial resolution, and the regularisation parameter Λ.

As input parameters for the DI of CU Vir, we adopted the stellar atmosphere parameters from Kochukhov et al. [2]: an effective temperature $T_{\rm eff}$ = 12,750 K, and a surface gravity $\log g = 4.3$. The phase-averaged abundances of He, Si, Fe, Cr, and Mg were adopted from Kochukhov et al. [2], Kuschnig et al. [6]. Using these parameters and abundances, the LTE model of the CU Vir atmosphere was computed with the LLMODEL code [37], accounting for opacity distribution due to the specific chemical composition. This model was subsequently employed in the Doppler inversion. The atomic data for the lines used in DI were critically selected from the VALD3 database [38] and are listed in Table A1. The wavelengths and oscillator strengths of the transitions were verified and corrected, where necessary, using the high-resolution spectrum of the slowly rotating normal star π Cet as a benchmark.

Given the rapid axial rotation of CU Vir with $v \sin i$ = 145 km/s, the potentially achievable resolution of DI can be estimated as $\Delta l \approx 2.9$–9° at the equator, i.e., 36–120 elements, depending on the spectral resolution of the observations. We employed two surface grids to compute local profiles: with a total number of 1436 cells matching the moderate resolution of historical spectroscopic time series in 1985–2011 and another with 3764 cells to fully utilise the resolution of NARVAL data for multi-element imaging. The inclination angle of the rotation axis to the line of sight was adopted as $i = 47^\circ$ [2].

3.2. Silicon Spots in 1985–2011

Silicon surface maps of CU Vir at four observational seasons within the 1985–2011 time span are presented in Figure 1. The distribution of silicon over the stellar surface is strongly inhomogeneous. At phase $\phi = 0.0$, an extended region with near-solar Si abundance dominates. The areas of enhanced Si abundance are grouped in three patches. A highly contrast spot with an excess [Si/H] = $\log(N_{Si}/N_{tot}) - \log(N_{Si}/N_{tot})_{\odot} \approx +2$ dex is located south of the equator and is visible on the limb at phase $\phi = 0.25$. At phase $\phi = 0.75$, a butterfly-like structure consisting of two Si spots with abundance [Si/H] $\approx$ +1.5 dex is situated on the visible disc of the star, symmetrically relative to the equator. The difference in abundance scale among the 1985, 1996, and 2009/11 maps, which were inversed using Si II 6347 Å line, does not exceed 0.1 dex and is likely due to differences in data processing, primarily uncertainties in the continuum level of the original observational data. The Doppler map derived from the 1995 observations using the Si II 4128/4130 Å doublet shows a larger abundance contrast; its maximum value exceeds those obtained from the Si II 6347 Å line by ∼0.7 dex. Uncertainties in continuum placement (the silicon line is located in the wing of $H\delta$) and NLTE effects are possible reasons for this discrepancy. Nevertheless, the silicon spot pattern remains consistent across different seasons and aligns with previous DI results [2,6].

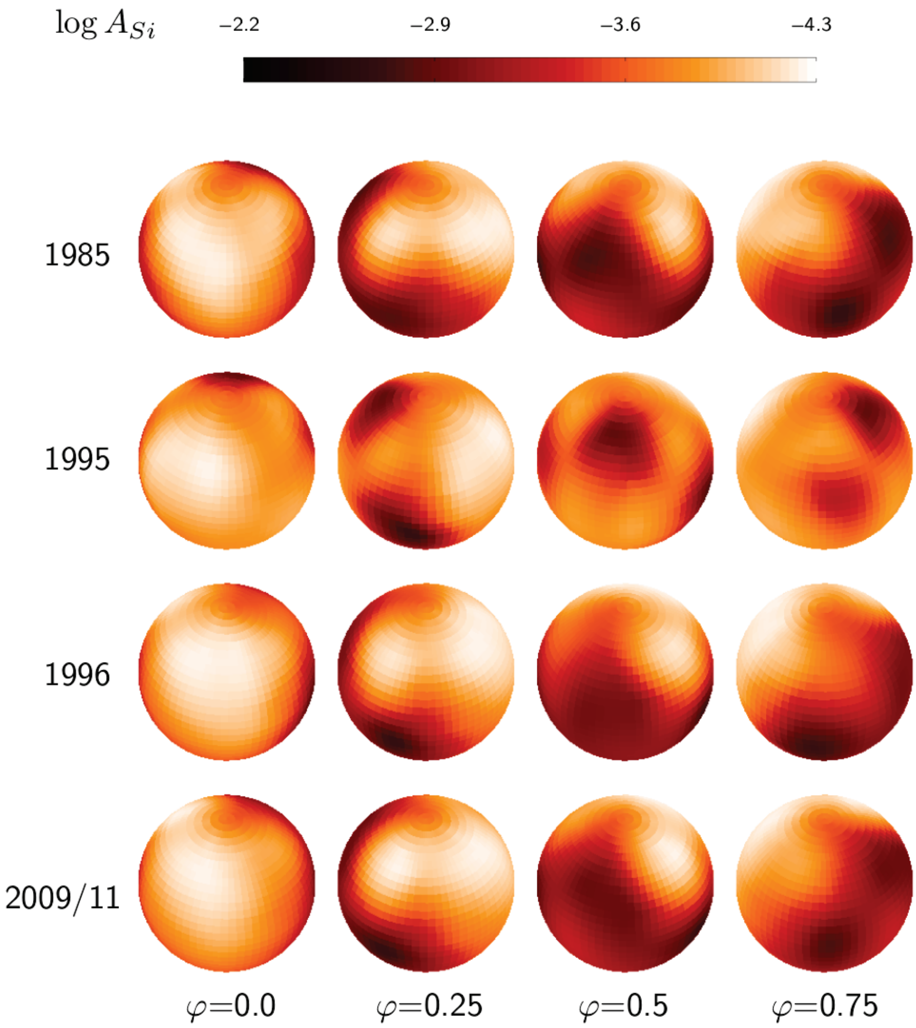

Figure 1. Silicon distribution over the surface of CU Vir during the period 1985—2011. Spherical maps are displayed for four equally spaced rotational phases. The abundance scale is provided at the top of the figure. Darker regions correspond to higher silicon abundances.

A comparison of the maps in Figure 1 reveals a clear stability of the spot pattern from season to season. The number of spots and their mutual position remained unchanged. The geometry of the main regions and the abundance scale (considering the higher contrast in the 1995 map due to employment of the Si II 4128/4130 Å doublet) are also preserved, even in the fine details. A characteristic example is the low-contrast "bridge" from the north pole to the spot at longitude $l \approx 100^\circ$, passing through the region of near-solar silicon abundance, which is clearly visible in the figure at phase $\phi = 0.25$ in all seasons. The maps also did not reveal any significant latitudinal changes in spot positions, which would be expected in the case of precession of the stellar rotational axis. Thus, the DI results demonstrate the stability of the silicon spot structure in CU Vir over the 1985–2011 interval, including at least one abrupt period change in 1992. The consistency between the maps derived from the 1985 dataset and those from subsequent years indicates that the period increase of about $+3.15$ s detected from photometry between 1983 and 1993 was caused by a rigid longitudinal shift of the spot pattern.

3.3. Light Curves in 1985–2011

To investigate whether the possible changes in the light curve shape reported by Pyper and Adelman [19] were caused by seasonal variations in the surface distribution of silicon, we calculated synthetic light curves based on the obtained Doppler images. The methodology and technique of these calculations are described in detail in Pakhomov et al. [39] and in a forthcoming paper by Pakhomov and et al. [33]. In general, the process involves computing local radiation intensities across the stellar surface, taking into account opacity due to the specific abundance distributions revealed by DI. This is followed by disc integration of the local intensities, taking into account the limb darkening, for all rotational phases. Convolution of the emergent flux with the passbands of the photometric filters yields synthetic light curves suitable for comparison with observations.

To calculate the synthetic light curves of CU Vir, we employed surface silicon distributions for the 1985, 1996, and 2009/11 seasons (the 1995 map was omitted because it was obtained from a different Si II 4128/4130 Å doublet). The distributions of helium, iron, and chromium, elements that also contribute to the emergent flux, were taken from multi-element imaging based on 2009/11 data. The results are shown in Figure 2 in comparison with the observational light curve in Strömgren v filter [17]. One can see that the shape of the light curves, acounting for the contribution of silicon alone, is reproduced perfectly from season to season, remaining well within the scatter in the observational data. The synthetic curves, which incorporate the silicon distribution as well as that of other considered elements, reproduce well both the amplitude and shape of the observed light curve. A more detailed discussion on the modelling of the light curves of CU Vir will be presented in a related paper [33].

3.4. Multi-Element DI

Taking advantage of the wavelength coverage and high resolution of NARVAL spectra, we performed multi-element DI with the aim of further light-curve modelling over a broad wavelength range. Since the lines in the spectrum of CU Vir are significantly broadened by rotation, the challenge was to select moderately blended lines suitable for imaging. We performed the selection procedure using the spectrum of the slowly rotating, chemically normal star π Cet as a reference, and the results are presented in Table A1. In general, the set of elements for which DI is feasible in CU Vir: He, Mg, Si, Fe, Cr is the same as used by Kochukhov et al. [2], Kuschnig et al. [6]. Since the lines of these elements were most often blended with iron lines, we made a special effort to select appropriate Fe lines. In subsequent Doppler inversion, we also added one or two reliable iron lines to the input dataset and performed simultaneous imaging of the element of interest and iron. The contribution of the variable iron blend was controlled by comparing the multi-element maps with those obtained using Fe lines only. The results of fitting the observed line profiles with theoretical ones are presented in Figure 3. The multi-element Doppler images are shown in Figure 4.

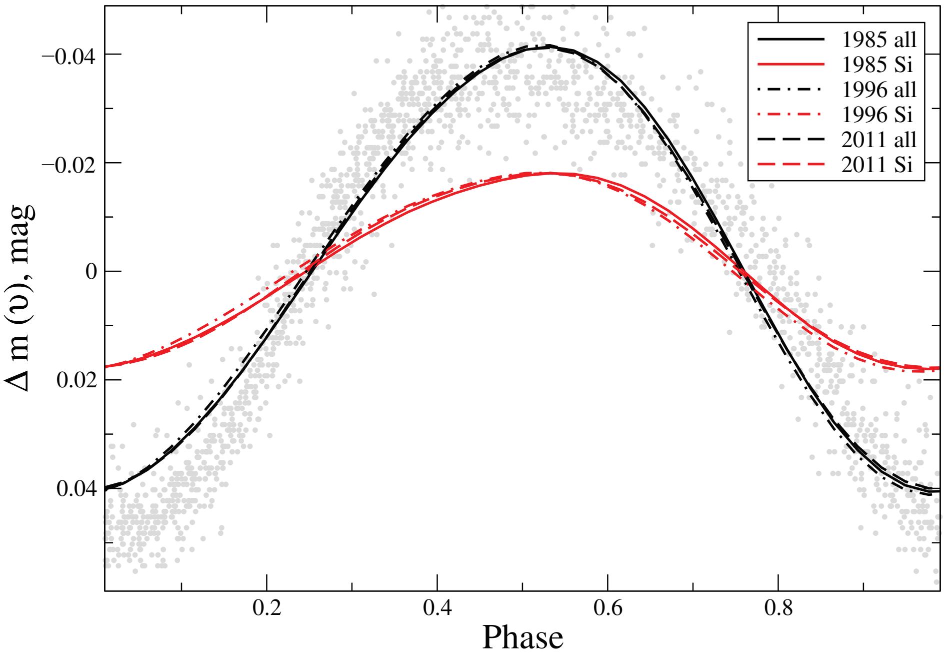

Figure 2. Synthetic light curves of CU Vir calculated using the surface Si maps for 1985, 1996, and 2009/11. Explanations of the line types are provided in the legend at the upper right. The light curves resulting from the inhomogeneous distribution of silicon alone are shown separately by red curves. Light curves calculated while also taking into account the He, Fe, and Cr are depicted by black lines. The dots represent observations in the Strömgren v band according to Pyper et al. [17]. The vertical scale is graded in magnitudes relative to the average brightness.

3.4.1. Helium

To reconstruct the surface helium distribution, we used two He I lines at 4471 and 5876 Å each consisting of several components. The phase-variable contribution of Fe and Ti to the He I blend at 4471 Å was taken into account. The final abundance map is shown in Figure 4. The average helium abundance over the surface of CU Vir appears to be depleted by ∼1–1.5 dex with respect to the Sun. The region of lowest He abundance (up to [He/H] ≈ −2 dex) forms a ring contribution 30° wide, inclined at ∼25° to the equator. At phase $\phi \approx 0$ a single spot with relatively enhanced helium abundance dominates between latitudes 0–30°. It should be noted that this spot exhibits an internal abundance gradient featuring a compact high-contrast centre and a more extended "penumbra". The artificial origin of this effect is doubtful, as the regularisation parameter was properly chosen. On average, the He abundance within the spot is near-solar.

3.4.2. Magnesium

We traced the surface distribution of magnesium in CU Vir using the single strong Mg II 4481 Å line which exhibits prominent variability. The surface map revealed an abundance gradient [Mg/H] ranged from +0.6 to −1.7 dex. The region of depleted Mg abundance also forms a ring resembling that observed in the helium distribution. Two spots with slightly oversolar abundance are visible at phases $\phi \approx 0$ and 0.5.

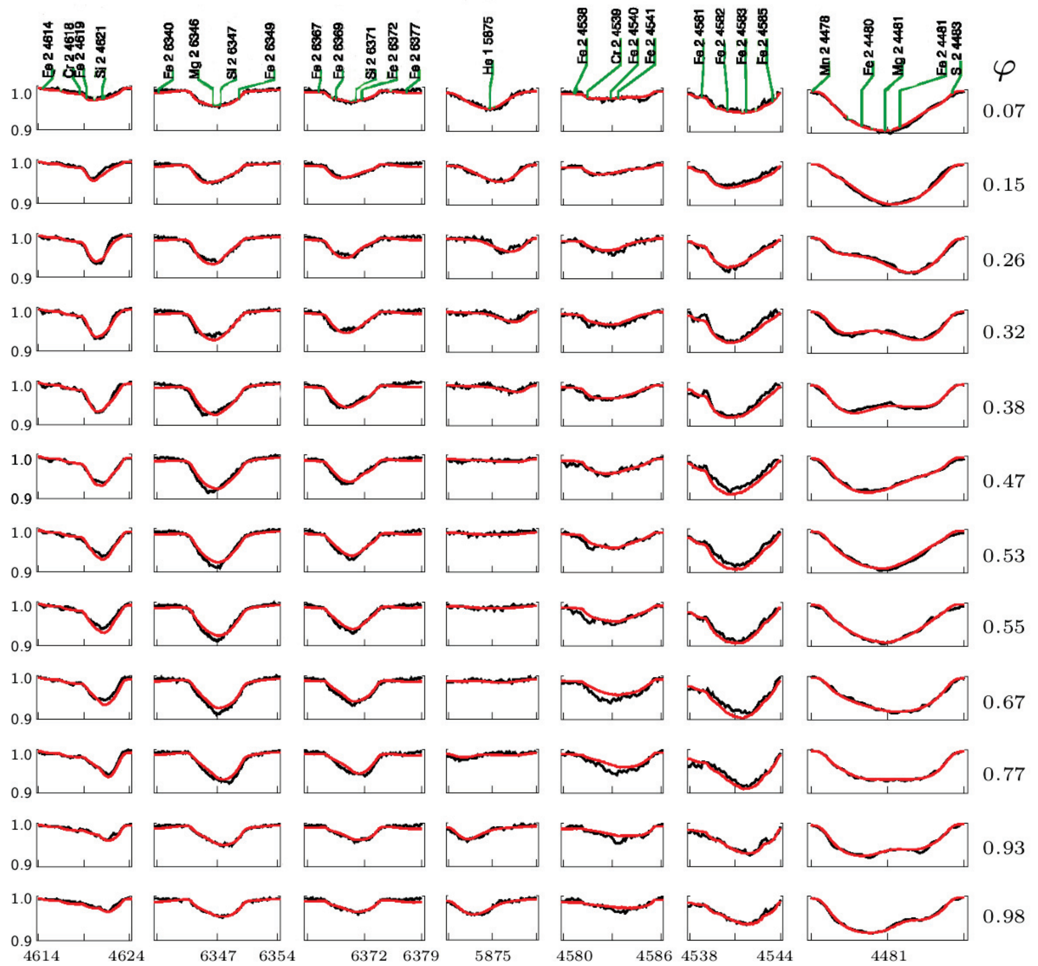

Figure 3. A comparison of the observed with NARVAL in 2009/11 selected Si II, He I, Cr II/Fe II blend, Fe II, Mg II profiles (from left to right, black curves) with the theoretical profiles (red curves) predicted by our DI. The profiles correspond to different rotational phases labelled to the right of the plot. Only the selected transitions contributing to the blends are labelled at top of the plot.

3.4.3. Silicon

The surface distribution of silicon was reconstructed using a set of Si II 4621, 5041, 5056, 6347, 6371 Å, lines which are formed at different depths in atmosphere and affected differently by non-LTE effects. Generally, the spot pattern obtained using these lines is similar to that described in Section 3.2. The surface distribution of silicon is remarkably anticorrelated with that of helium. However, the use of different silicon lines and their combinations for DI results in different abundance scales. All lines yield a minimum abundance of [Si/H] ≈ +0.4, slightly above the solar value. At the same time, DI using the set of Si II 4621, 5041, 5056 Å lines with energies E_{low} = 10–12 eV yields maximum abundances in the silicon spots that are ∼0.5 dex higher than those derived from the pair of Si II 6347, 6371 Å lines with energies $E_{low} = 8.2$ eV. NLTE calculations at the given effective temperature suggest negative corrections for these latter lines [40]. Roughly simulating this effect by applying a correction to the oscillator strengths $\Delta gf = -0.3$ we were able to converge the abundance scales and obtain a resonable good profiles fit to the profiles of various silicon lines. Previously, the line-to-line scatter and even changes in the shape of the lines' profiles with different excitation energies at the same phases were noted by Kochukhov et al. [2] and attributed to the effects of vertical element stratification in the atmosphere of CU Vir. We also admit this possibility and note a contrast difference between the two spots at phases φ = 0.25–0.5: from the full set of Si II lines, the northern spot appears more contrasted, whereas from only the Si II 6347, 6371 Å the southern spot shows greater contrast. This may either be an artificial effect or tentative indication for the different vertical stratification profiles across the different regions of the star.

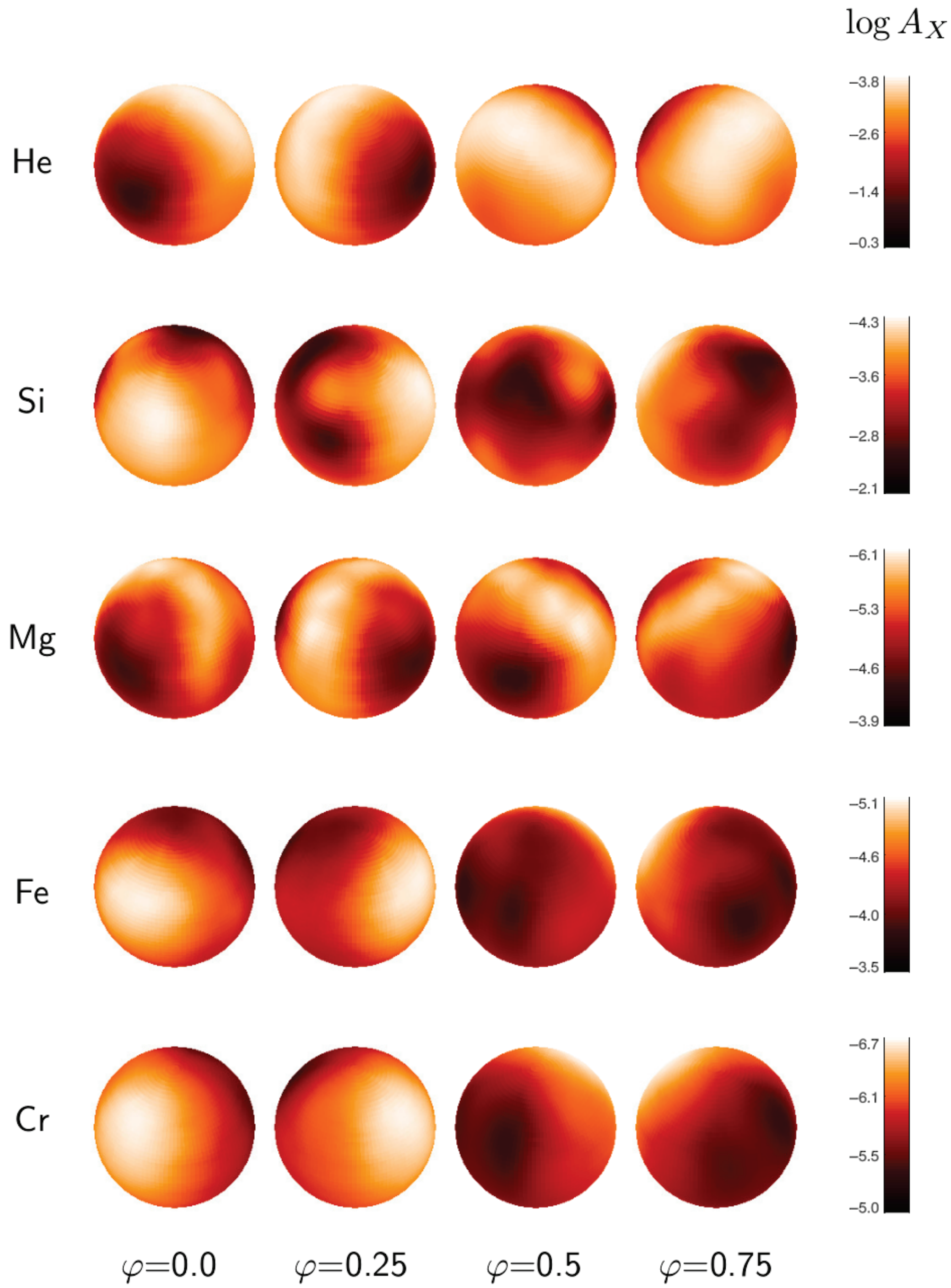

Figure 4. Surface-abundance distributions in CU Vir for different elements recovered from the 2009/11 NARVAL dataset. The abundance scales are shown to the right from the corresponding subplots.

3.4.4. Iron

For the inversion of the iron distribution, we fitted spectral regions 4512–4524, 4538–4544, and 4580–4586 Å dominated by iron blends with reliable atomic parameters available in VALD3 database. The surface distribution of Fe is characterised by an extended region at phase $\varphi = 0$ depleted by ≈ 0.6 dex relative to the Sun, and two distinctly separated compact spots at $\varphi = 0.6$, located between the equator and +30° latitude. The Fe overabundance in these spots is of the order of $+1$ dex. Although not exactly identical, the distribution of iron resembles that of silicon.

3.4.5. Chromium

The isolation of unblended chromium lines amidst such rotational broadening of profiles is a challenging task. We used blends containing the strongest chromium lines Cr II 4539, 4554, 4558 Å and fitted them simultaneously with the iron lines. The resulting chromium distribution is identical to that of iron, as expected due to the very similar energy configurations and term structures of these elements. We found ≈0.4 dex depletion of chromiun in a large region at phase $\varphi = 0$ and an overabundance reaching up to +1.5 dex in a double spot near phase $\varphi = 0.6$.

4. Tayler Instability of Magnetic Field in CU Vir

Previously, we proposed an explanation for the observed linear increase in the rotation period of another Ap star, 56 Ari, in terms of the Tayler instability of its magnetic field [29]. Here, we explore the possibility of applying this explanation to period changes in CU Vir.

The dominant component of the magnetic field in radiative stellar interiors is believed to be an axisymmetric toroidal field [41], which may currently be understood within a paradigm of a relic origin [42,43] and shaped by differential rotation, or as the product of stellar merging [44,45]. As demonstrated by Tayler [46] and Pitts and Tayler [47], such a field can be unstable to non-axisymmetric disturbances, producing longitude-dependent instability modes. These modes can shape the surface magnetic fields of Ap/Bp stars [48,49]. An important feature of these modes, relevant to the observed change in photometric periods, is their rigid longitudinal drift [50,51]. The magnetic field drags ions in surface chemical spots, causing them to drift, which results in an apparent change in the photometric period.

We performed computations of the Tayler instability of the CU Vir internal magnetic field using the model by Kitchatinov and Rüdiger [52] and Kitchatinov [53]. The basic equations and a discussion of application of the model to an Ap star with a variable period can be found in Potravnov and Kitchatinov [29]. We generally assume a simple toroidal axisymmetric configuration of the internal magnetic field, $B = \sqrt{4\pi\rho}\,\sin\vartheta r \Omega_A$, where r is the radius, ϑ is the co-latitude of the standard spherical coordinates, and Ω_A is the angular Alfvén frequency. We solve numerically the eigenvalue problem of the field stability to define the instability patterns and the corresponding eigenvalues in dependence on the background field strength. The dominant mode of the instability has an azimuthal wave number of $m = 1$ [54]. The dependence of the mode on the longitude ϕ can be combined with its exponential time-dependence, $\exp(\mathrm{i}\phi - \mathrm{i}\omega t)$. The complex eigenvalue, $\omega = \mathrm{i}\gamma + w$, includes the (real) growth rate γ and the frequency w. Any constant value of phase, $\phi - wt = const$, of an eigenmode drifts in longitude at a rate of $\dot{\phi} = w$. The frequency, w, is therefore the rate at which the eigenmode pattern drifts azimuthally. In the co-rotating reference frame, all drift rates are negative [51], meaning counter-rotational migration of the instability patterns.

Tayler instability can develop fine spatial structure in latitude [55]. Our model employs series expansion in the (associated) Legendre polynomials $P_l^m(\cos\vartheta)$ for latitudinal dependence of the eigenmodes. The expansion with maximum $l = 100$ ensured sufficient numerical resolution for sometimes emerging small-scale latitudinal structure.

The key parameter of the model is the background (internal) field strength normalized to the energy equipartition value, Ω_A/Ω. $\Omega_A/\Omega < 1$ means a relatively weak (sub-equipartition) field, where the magnetic energy density is smaller than the rotational kinetic energy; Ω is the angular velocity of the star. A reversed inequality, $\Omega_A/\Omega > 1$, indicates a strong (superequipartition) field. Another governing parameter is the normalized radial wavelength, $\hat{\lambda} = N/\Omega kr$, where N is the Brunt–Väisälä frequency and k is the radial wave number. The model also accounts for finite diffusion. A stellar structure model is needed to specify these parameters. For this purpose, we used the *MESA* evolutionary model of stellar internal structure [56]. For a star with $M = 3.06M_\odot$ and metallicity $Z = 0.015$ at the age of 1.64×10^7 y, *MESA* yields a radius $R = 1.974R_\odot$ and an effective temperature $T_{\rm eff}$ = 12,747 K close to the observed parameters of CU Vir. This model of internal structure is therefore was used in the computations for CU Vir.

Given the similarity of the 56 Ari and CU Vir parameters, we expectedly obtained quite similar results. Figure 5 shows the radial profiles of the N/Ω ratio and equipartition field strength $B_{eq} = \sqrt{\pi\rho}r\Omega$. Since the largest growth rate of the Tayler instability corresponds to $\hat{\lambda} \simeq 0.1$ [52], we took the stellar parameters at $r/R = 0.93$, which is approximately one radial wavelength below the surface. The computed growth and drift rates are shown in Figure 6 as a function of the background field strength.

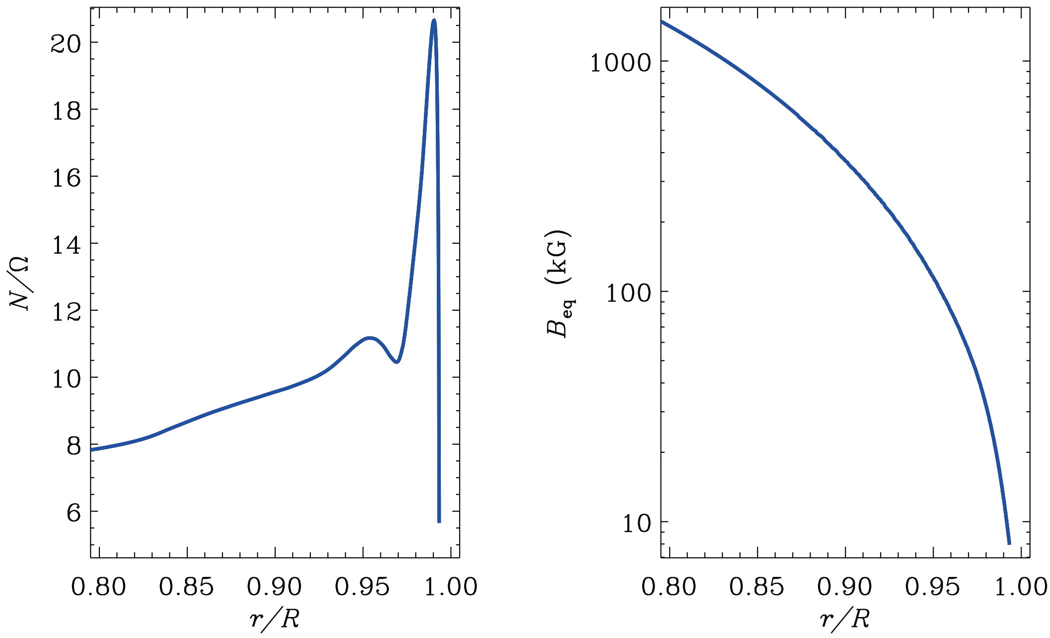

Figure 5. The frequency ratio N/Ω (left panel) and the equipartition field strength (right panel) as a function of radius.

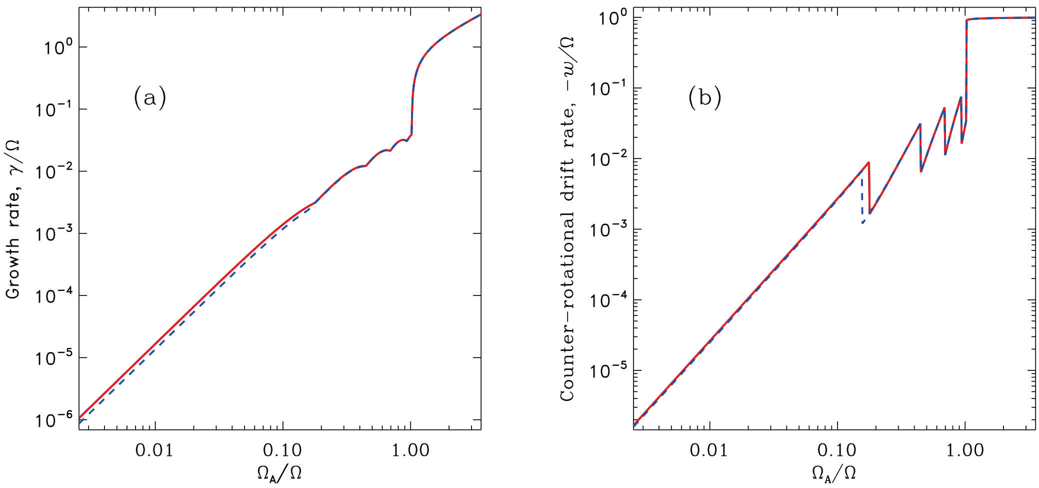

Figure 6. The growth rates (panel (**a**)) and drift rates (panel (**b**)) of the instability in the reference frame rotating with the star. The full and dashed lines correspond to modes symmetric and antisymmetric about the equator, respectively.

Our instability model is global in horizontal dimensions. It allows for two types of solution: symmetric and antisymmetric about the equator. The symmetric modes have somewhat larger growth rates, as can be seen in Figure 6a. The following discussion refers to this type of symmetry. The family of equator-symmetric modes also consists of a set of modes with different growth rates and spatial structures. The growth and drift rates of Figure 6 belong to the so-called dominant modes, which grow most rapidly. However, which particular mode is dominant depends on the background field strength. This is why the plot of Figure 6a for $\Omega_{\rm A} > 0.1\,\Omega$ is wavy. The kinks in the plot occur at field strengths where the maximum growth rate changes between eigenmodes of different shapes (cf. Figure 7). The growth rates depend continuously on the field strength. However, the drift rates differ between the modes that are dominant at different strengths of the background field. This explains the saw-like section of the plot of the Figure 6b.

Since oscillations in growth and drift rates are associated with changes in dominant (fastest growing) modes of instability, an important consequence is also a change in the spatial structure of the surface magnetic field. Figure 7 shows the patterns of the different dominant modes for several strengths of the background field. For $\Omega_A/\Omega \lesssim 0.7$ the equatorial dipole with obliquity $\beta \approx 90^\circ$ dominates, which is consistent with observed in CU Vir $\beta = 76^\circ$ [2]. As the field strength increases, new structures appear at high latitudes and, for $\Omega_A/\Omega > 1$, the dominant mode shifts to the poles.

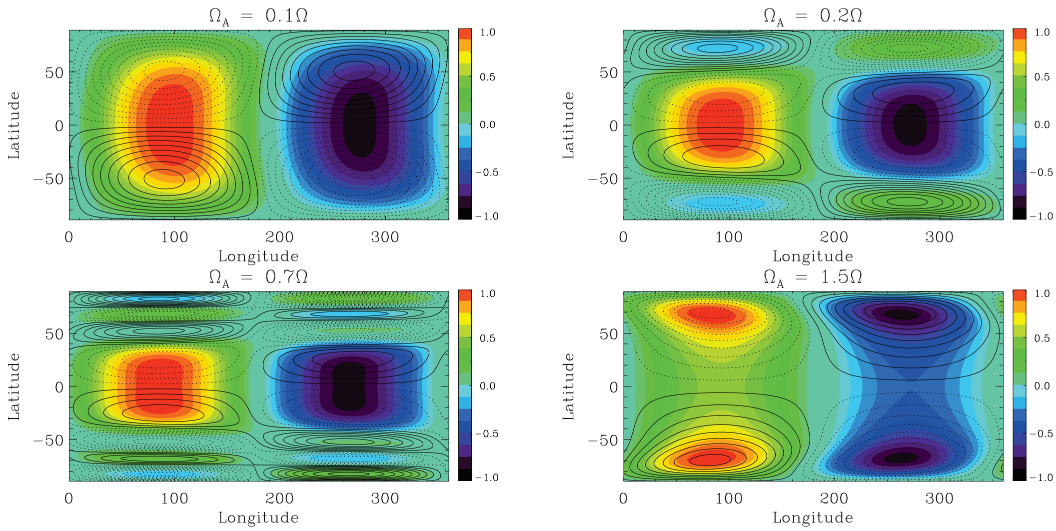

Figure 7. The structure of the magnetic field of the most rapidly growing mode of the instability for different values of Ω_A/Ω (labeled at the top of the plot panels). The color scale shows the normalized strength of the radial field. The solid (dashed) lines show the force lines of toroidal-field perturbations with clockwise (counterclockwise) circulation. The color scale is given in arbitrary units.

A comparison of Figure 5 with the observed strength of the surface magnetic field of CU Vir suggests that $\Omega_A/\Omega \approx 10^{-2}$. This indicates that CU Vir lies in the sub-equipartition region, where $w \propto \Omega_A^2$ in the plot of Figure 6b. Variations in the strength of the background field will produce smooth changes in drift velocity (and photometric period), like in the case of 56 Ari. However, a much stronger background field ($\Omega_A/\Omega \sim$0.1–1) is required for a transition to a regime in which abrupt changes in the drift velocity of the dominant instability mode occur.

5. Discussion

5.1. Surface-Abundance Distributions in CU Vir and Their Stability

With the DI technique we reconstructed the surface distribution of elements in the chemically peculiar star CU Vir. We obtained surface-abundance maps for five elements: Si, He, Fe, Cr, and Mg using the 2009/11 observations. For the first time, we reconstructed the silicon distribution in a uniform manner across four observing seasons spanning from 1985 to 2011, when the star exhibited notable changes in its photometric period.

Comparison of our DI results with previous studies allows us to validate abundance maps of CU Vir obtained using slightly different approaches and updated atomic data. In terms of spot geometry, the results show very good agreement with earlier imaging [2,5,6]. The abundance scales may differ to some extent depending on the line lists and the atomic data employed. A comparison of the maps (Figure 4) reveals very similar distribution patterns for silicon, iron, and chromium featuring a double spot near the negative magnetic pole (as inferred from the magnetic curve in Figure 6 by Kochukhov et al. [2]) and an extended region of decreased abundance near the positive pole. On the contrary, helium and magnesium in this latter region exhibit large overabundant spots, while areas of elemental deficiency form rings tilted relative to the equator of rotation.

A comparison of the surface distribution of silicon in 1985, 1995, 1996, and 2009/11 revealed them to be exactly identical. Over ≈26 years, within the accuracy of our maps, neither the shape nor the mutual location and the abundance scale of silicon spots has changed. Previously, we obtained the same result based on ∼30 years observations of another Ap star with a variable period-56 Ari [57]. In contrast to 56 Ari, which is observed equator-on, CU Vir is viewed at an intermediate inclination angle. This means that the DI solution is not affected by the mirror degeneration, and the latitudinal distribution of spots can be reconstructed reliably. Nevertheless, as in the case of 56 Ari, we could not detect latitudinal variations in spots distribution in CU Vir over the examined time span that might indicate a precession of its rotation axis. Synthetic light curves computed from our Doppler maps for different seasons did not show variations exceeding the dispersion of photometric observations. Thus, there are no decadal variations in the surface distribution of silicon, and these do not account for the previously reported changes in light-curve shape between different seasons. Since we traced the secular behavior of silicon only, it is possible that light-curve changes could be caused by variations in the surface distribution of other elements. Indeed, the model of atomic diffusion in Ap/Bp stars in the presence of electric currents [26] predicts the possibility of slow variations in the relative surface abundances of different elements. Therefore, it is of interest to obtain follow-up spectroscopic observations of CU Vir and to perform multi-element DI for comparison with the 2009/11 images.

However, the conventional treatment of selective atomic diffusion suggests a similar character for silicon and iron-peak elements. This is supported by our multi-element DI results for CU Vir using the 2009/11 observations. Therefore, based on the currently available data, we conclude that the spot pattern in CU Vir remained stable between 1985 and 2011. At the same time, variations in the photometric period of the star imply a rigid longitudinal drift of this pattern. Below, we discuss one of the possible explanations for such a drift.

5.2. Period Changes and Longitudinal Drift of Magnetic and Abundance Structures

We modelled the Tayler instability of the background magnetic field of CU Vir, which results in a longitudinal drift of surface magnetic patterns. We also propose that such a drift could be responsible for the observed change in the star's rotation period. A comparison between the global magnetic field strength (measured at the stellar surface) and our calculations shows that the instability operates in the sub-Alfvénic regime, leading to only a linear change in drift velocity. However, this is inconsistent with observations. A much stronger magnetic field is required for the instability to switch to the dominant mode, which leads oscillating changes in drift velocity.

Regarding this issue, we have two remarks. Firstly, the background field is the star's internal magnetic field, which can be much stronger than the field observed at the surface. Secondly, in our model, we normalise the field strength to B_{eq}. In turn, the equipartition field strength B_{eq} depends on depth and decreases towards the stellar surface. Therefore, an increase in the normalised field can occur when the magnetic field rises without a change in the strength of the magnetic structure under consideration.

Let us suppose that we have overcome the difficulties associated with the amplitude of the background magnetic field and deal with Tayler instability in a regime of changing dominant modes. Is it possible to explain the observed change in CU Vir rotation period with such a mechanism? The necessary changes in drift velocity also require temporal variations in the background field strengths. Moreover, the character of these changes depends on the interpretation of the observational data. Recall that two models—one with abrupt period changes [11,17–19] and another with quasi-sinusoidal variations [13,20]—have been considered for CU Vir. Within the framework of our model, it can be assumed that the abrupt changes in drift velocity are caused by a change of the instability mode when the normalised background field strength is $\Omega_A/\Omega \approx 0.4$–$0.5$. In this case, to reconcile with the observed direction of period change, it is necessary to assume a decrease in the normalised field over a historical period of CU Vir observations. Then, at the start of observations in 1950s, the star would be located somewhere on the second or third wave of the plot for drift velocity (Figure 6a), moving leftward. A step-like change in drift velocity corresponds to an increase in period (deceleration of the star) between 1983 and 2012, and a subsequent gradual acceleration after 2012 would return the background field value (and drift velocity) close to those at the beginning of the previous cycle.

The model with continuous period change permits a smaller field strength $\Omega_A/\Omega \approx 0.1$–$0.2$, but implies an increase in the field strength. Period changes occur near the first switching of the instability mode. Initially, an increase in the drift velocity took place, corresponding to a slowing of the apparent rotation until 2005; subsequently, the drift rate decreased, corresponding to an acceleration of the rotation. We can estimate the value of the period change ΔP predicted by the model as $\Delta P = P \cdot (\Delta w/\Omega)$. From the figure Figure 6a $\Delta w/\Omega \approx 0.007$ near $\Omega_A/\Omega \approx 0.2$ (the first change in the dominant instability mode). This corresponds to a period increase by $\Delta P \approx 300$ s, while the observed increase in the CU Vir period from 1958 to 2012 was much smaller, about $\Delta P_{obs} \approx 3$ s. The reason for this discrepancy may lie in the utilisation of a simplified magnetic field structure within our linear instability model. Additionally, the quasi-sinusoidal model of period change implies smooth variations over decadal timescales, whereas our model predicts abrupt changes in the dominant mode of the Tayler instability within a few ($\sim$10–20) rotational cycles.

Can the different directions of field changes, decrease and increase, have a physical interpretation? If we assume that the field consists of small-scale flux tubes undergoing double-diffusive rise [58,59], then both increases and decreases in the background field can be observed. It depends on where the field changes are monitored. If we are tracking an uplifting tube, then its normalised field strength decreases as $B/B_{eq} \propto \sqrt{\rho}$. However, if we observe the field strength at a fixed location, then both scenarios are possible. If at this location the field was weak or simply absent, then the arrival of a flux tube can increase the local field. Conversely, flux tubes with weaker fields can also rise.

To summarise, explaining the period changes in CU Vir via the Tayler instability of its magnetic field requires extensive speculation arising from the simplifying assumptions of our model and the lack of direct information on the structure and dynamics of the internal magnetic field. Currently, our model offers no clear advantages over other models that propose the effect of standing Alfvén waves on the azimuthal distribution of the magnetic field and chemical spots [27,28]. While the aforementioned models, with prescribed parameters for the radial field distribution, can reproduce quasi-sinusoidal oscillations of CU Vir period with a timescale of $\sim$65 yr, our model is more consistent with the abrupt period changes. While recent observations seem to support the gradual period variations, a definitive way to distinguish between these models will only become possible through further photometric monitoring of the star [33].

Our model has the potential for independent observational verification to justify its further development. Note that the change in the dominant mode is associated with a change in the spatial structure of the instability pattern and the emergence of high-latitude magnetic structures. This does not contradict observations, since results from ZDI [2] revealed deviations of the CU Vir magnetic field from a simple dipole structure (a combination of dipole plus quadrupole also does not fully describe the observed Stokes profiles). In our model, changes in the high-latitude structures occur rapidly, while the equatorial dipole remains the dominant structure, with its longitudinal drift responsible for the period changes. Therefore, ZDI monitoring of CU Vir may serve as a valuable test to search for rapid changes in the magnetic field structure associated with a shift in the dominant mode of Tayler instability.

6. Conclusions

We have analysed a unique series of spectroscopic observations of the Ap star CU Vir, spanning between 1985 and 2011, which includes both archival and original data. Over these 26 years, noticeable changes in the photometric period were observed, raising the question of whether these period variations were caused by changes in surface-abundance spots. Using DI technique, we reconstructed the surface distribution of silicon in CU Vir, which is one of the major contributors to photometric variability, at four epochs more or less evenly distributed across this timeframe. A comparison of silicon distribution in different seasons revealed the stability of the spot pattern: both the geometry and abundance scale remained unchanged from season to season, like in case of another recently studied Ap star with a variable period—56 Ari. Hence, the period changes in these stars may originate from the rigid longitudinal drift of the spot pattern. Such drift of surface inhomogeneous modes is a specific feature of Tayler instability of magnetic field.

To explore the relation of Tayler instability to period changes in CU Vir, we performed simulations of the instability of internal magnetic field of CU Vir. Our modelling indicates that the drift of surface azimuthally inhomogeneous instability modes can influence the photometric period on observable timescales. However, the observed surface magnetic field strength of CU Vir appears to be insufficient for the instability regime that would produce oscillating period variations. While there are possibilities to address this issue, they remain highly speculative, given the limitations of our simplified representation of the internal magnetic field and the lack of direct observational data on its characteristics. Currently, the proposed model does not offer clear advantages over other models discussed in the literature for explaining period variations of CU Vir, but it holds potential for further development. One of its predictions—rapid changes in surface magnetic field structure caused by a shift in the dominant instability mode—could be directly tested through spectropolarimetric monitoring.

Author Contributions: Conceptualisation, I.P. and T.R.; methodology, I.P., T.R., Y.P., L.K.; software, Y.P., L.K.; formal analysis, I.P., Y.P.; investigation, I.P., T.R., Y.P., L.K.; resources, T.R., Y.P.; data curation, T.R.; writing—original draft preparation, I.P.; writing—review and editing, I.P., T.R., Y.P. and L.K.; visualisation, Y.P., I.P.; supervision, I.P.; project administration, I.P., T.R. All authors have read and agreed to the published version of the manuscript.

Funding: This research was funded by the Ministry of Science and High Education of Russian Federation.

Data Availability Statement: Spectra of CU Vir and complete linelists are available upon reasonable request from the authors. NARVAL data are publicly available in the Polarbase.

Conflicts of Interest: The authors declare no conflicts of interest.

Abbreviations

The following abbreviations are used in this manuscript:

DI	Doppler Imaging
ZDI	Zeeman–Doppler Imaging
LTE	Local Thermodynamic Equilibrum

Appendix A. List of Elements and Lines Used for DI

Table A1. Spectral lines and their parameters used for DI.

Element	Line, Å	E_{low}, eV	$\log gf$	$\log \Gamma_4$	Comment
Si II	4621.4182	12.525	−0.540	−3.860	bl. Fe II, Cr II
	4621.6960	12.525	−1.680	−3.860	
	4621.7216	12.525	−0.380	−3.860	
	5041.0240	10.0664	0.150	−5.170	bl. Fe II, Ni II
	5055.9841	10.0739	0.512	−5.170	bl. Fe II, Ni II, atm. H_2O
	5056.3165	10.0739	−0.679	−5.170	
	6347.1087	8.1210	0.000	−5.680	bl. Fe II, Mg II, gf: −0.17 dex
	6347.1329	13.9351	−1.721	−2.810	gf: −0.3 dex
	6347.1973	13.9351	−1.567	−2.810	gf: −0.3 dex
	6371.3714	8.1210	−0.320	−5.680	bl. Fe II, gf: −0.3 dex
He I	4471.4690	20.9641	−2.198	−3.690	bl. Fe II, Ti II
	4471.4730	20.9641	−1.028	−3.690	
	4471.4730	20.9641	−0.278	−3.690	
	4471.4850	20.9641	−1.028	−3.690	
	4471.4880	20.9641	−0.548	−3.690	
	4471.6820	20.9642	−0.898	−3.690	
	5875.5990	20.9641	−1.511	−4.720	w.bl.atm. H_2O
	5875.6140	20.9641	−0.341	−4.720	
	5875.6150	20.9641	0.409	−4.720	
	5875.6250	20.9641	−0.341	−4.720	
	5875.6400	20.9641	0.139	−4.720	
	5875.9660	20.9642	−0.211	−4.720	
Fe II	4515.3330	2.8441	−2.537	−6.530	bl. Ca II
	4520.2180	2.8067	−2.600	−6.530	bl. Mn II
	4522.6276	2.8441	−2.189	−6.530	bl. S II
	4541.5156	2.8555	−2.927	−6.530	
	4582.8296	2.8441	−3.130	−6.530	
	4583.8292	2.8067	−1.940	−6.530	
	4583.9912	2.7043	−3.840	−6.540	
Cr II	4554.9880	4.0712	−1.282	−6.540	bl. Fe II, Ba II
	4558.6500	4.0734	−0.449	−6.540	bl. Fe II
	4558.7830	4.0735	−2.530	−6.540	
	4588.1990	4.0712	−0.826	−6.560	
	4589.9010	4.0722	−2.660	−6.560	
Mg II	4481.1260	8.8637	0.740	−4.70	bl. Fe II, Mn II, Al III
	4481.1500	8.8637	−0.560	−4.70	
	4481.3250	8.8637	0.590	−4.70	

Note

1 A couple of faster rotators among Ap/Bp stars were recently reported in Mikulášek et al. [9], Semenko et al. [10].

References

1. Deutsch, A.J. A New Spectrum Variable of Short Period, HD 124224. *Astrophys. J.* **1952**, *116*, 536. [CrossRef]
2. Kochukhov, O.; Lüftinger, T.; Neiner, C.; Alecian, E.; MiMeS Collaboration. Magnetic field topology of the unique chemically peculiar star CU Virginis. *Astron. Astrophys.* **2014**, *565*, A83. [CrossRef]
3. Krivoseina, A.A.; Ryabchikova, T.A.; Khokhlova, V.L. Distribution of SI on the Surface of the Silicon Ap-Star Cu-Virginis and Interpretation of the Lightcurves in the Vby Bands. *Nauchnye Informatsii* **1980**, *43*, 70.
4. Hatzes, A.P. Mapping the Surface Distribution of Elements on Ap-Stars Using the Maximum Entropy Method. In Proceedings of the IAU Colloq. 138: Peculiar versus Normal Phenomena in A-type and Related Stars, Trieste, Italy, 6–10 July 1993.
5. Hatzes, A.P. Doppler imaging of the silicon distribution on CUVir: Evidence for a decentred magnetic dipole? *Mon. Not. R. Astron. Soc.* **1997**, *288*, 153–160. [CrossRef]

6. Kuschnig, R.; Ryabchikova, T.A.; Piskunov, N.E.; Weiss, W.W.; Gelbmann, M.J. Multi element Doppler imaging of AP stars. I. He, Mg, Si, CR and Fe surface distribution for CU Virginis. *Astron. Astrophys.* **1999**, *348*, 924–932.
7. Krtička, J.; Mikulášek, Z.; Lüftinger, T.; Shulyak, D.; Zverko, J.; Žižňovský, J.; Sokolov, N.A. Modelling of the ultraviolet and visual SED variability in the hot magnetic Ap star CU Virginis. *Astron. Astrophys.* **2012**, *537*, A14. [CrossRef]
8. Krtička, J.; Mikulášek, Z.; Henry, G.W.; Janík, J.; Kochukhov, O.; Pigulski, A.; Leto, P.; Trigilio, C.; Krtičková, I.; Lüftinger, T.; et al. HST/STIS analysis of the first main sequence pulsar CU Virginis. *Astron. Astrophys.* **2019**, *625*, A34. [CrossRef]
9. Mikulášek, Z.; Semenko, E.; Paunzen, E.; Hümmerich, S.; North, P.L.; Bernhard, K.; Krtička, J.; Janík, J. HD 60431, the CP2 star with the shortest rotational period. Physical parameters and period analysis. *Astron. Astrophys.* **2022**, *668*, A159. [CrossRef]
10. Semenko, E.; Romanyuk, I.; Yakunin, I.; Kudryavtsev, D.; Moiseeva, A. Spectropolarimetry of magnetic Chemically Peculiar stars in the Orion OB1 association. *Mon. Not. R. Astron. Soc.* **2022**, *515*, 998–1011. [CrossRef]
11. Pyper, D.M.; Ryabchikova, T.; Malanushenko, V.; Kuschnig, R.; Plachinda, S.; Savanov, I. An abrupt decrease in the rotational period of the chemically peculiar magnetic star CU Virginis. *Astron. Astrophys.* **1998**, *339*, 822–830.
12. MacDonald, J.; Natan, T.; Petit, V.; Kochukhov, O.; Shultz, M.E. Using ZDI maps to determine magnetic forces and torques at the photospheres of early-type stars. *Mon. Not. R. Astron. Soc.* **2024**, *530*, 2840–2851. [CrossRef]
13. Mikulášek, Z.; Krtička, J.; Henry, G.W.; Janík, J.; Zverko, J.; Žižňovský, J.; Zejda, M.; Liška, J.; Zvěřina, P.; Kudrjavtsev, D.O.; et al. Surprising variations in the rotation of the chemically peculiar stars CU Virginis and V901 Orionis. *Astron. Astrophys.* **2011**, *534*, L5. [CrossRef]
14. Trigilio, C.; Leto, P.; Umana, G.; Leone, F.; Buemi, C.S. A three-dimensional model for the radio emission of magnetic chemically peculiar stars. *Astron. Astrophys.* **2004**, *418*, 593–605. [CrossRef]
15. Trigilio, C.; Leto, P.; Umana, G.; Buemi, C.S.; Leone, F. The radio lighthouse CU Virginis: The spin-down of a single main-sequence star. *Mon. Not. R. Astron. Soc.* **2008**, *384*, 1437–1443. [CrossRef]
16. Das, B.; Chandra, P. Ultra-wideband, Multiepoch Radio Study of the First Discovered "Main-sequence Radio Pulse Emitter" CU Vir. *Astrophys. J.* **2021**, *921*, 9. [CrossRef]
17. Pyper, D.M.; Stevens, I.R.; Adelman, S.J. An update on the rotational period of the magnetic chemically peculiar star CU Virginis. *Mon. Not. R. Astron. Soc.* **2013**, *431*, 2106–2110. [CrossRef]
18. Pyper, D.M.; Adelman, S.J. Newly Discovered Period Changes in Two mCP Stars and Updates for Previously Published Stars. *Publ. Astron. Soc. Pac.* **2020**, *132*, 024201. [CrossRef]
19. Pyper, D.M.; Adelman, S.J. Light Curve Changes and Possible Precession in mCP Stars. *Publ. Astron. Soc. Pac.* **2021**, *133*, 084203. [CrossRef]
20. Mikulášek, Z.; Krtička, J.; Henry, G.W.; Janík, J.; Pigulski, A. Towards Comprehension of the Variability of the mCP Star CU Virginis. *Phys. Magn. Stars* **2019**, *518*, 125. [CrossRef]
21. Stępień, K. On a mechanism of an abrupt change of period of CU Virginis. *Astron. Astrophys.* **1998**, *337*, 754–756.
22. Kochukhov, O.; Adelman, S.J.; Gulliver, A.F.; Piskunov, N. Weather in stellar atmosphere revealed by the dynamics of mercury clouds in α Andromedae. *Nat. Phys.* **2007**, *3*, 526–529. [CrossRef]
23. Hubrig, S.; Savanov, I.; Ilyin, I.; González, J.F.; Korhonen, H.; Lehmann, H.; Schöller, M.; Granzer, T.; Weber, M.; Strassmeier, K.G.; et al. The magnetic field and the evolution of element spots on the surface of the HgMn eclipsing binary ARAur. *Mon. Not. R. Astron. Soc.* **2010**, *408*, L61–L65. [CrossRef]
24. Korhonen, H.; González, J.F.; Briquet, M.; Flores Soriano, M.; Hubrig, S.; Savanov, I.; Hackman, T.; Ilyin, I.V.; Eulaers, E.; Pessemier, W. Chemical surface inhomogeneities in late B-type stars with Hg and Mn peculiarity. I. Spot evolution in HD 11753 on short and long time scales. *Astron. Astrophys.* **2013**, *553*, A27. [CrossRef]
25. Prvák, M.; Krtička, J.; Korhonen, H. The nature of the photometric variability of HgMn stars: A test of simulated light curves of φ Phe against the TESS data. *Mon. Not. R. Astron. Soc.* **2020**, *492*, 1834–1840. [CrossRef]
26. Urpin, V. Chemical spots and oscillatory diffusion modes in magnetic stars. *Astron. Nachrichten* **2016**, *337*, 633. [CrossRef]
27. Krtička, J.; Mikulášek, Z.; Henry, G.W.; Kurfürst, P.; Karlický, M. Torsional oscillations and observed rotational period variations in early-type stars. *Mon. Not. R. Astron. Soc.* **2017**, *464*, 933–939. [CrossRef]
28. Takahashi, K.; Langer, N. Standing torsional Alfvén waves as the source of the rotational period variation in magnetic early-type stars. *Astron. Astrophys.* **2025**, *696*, A129. [CrossRef]
29. Potravnov, I.S.; Kitchatinov, L.L. Tayler instability of magnetic field as the possible reason for the period changes in Ap star 56 Ari. *Astron. Rep.* **2025**, *69*, 500. [CrossRef]
30. Shore, S.N.; Adelman, S.J. Magnetic fields and diffusion processes in peculiar A stars. II. Precession and the oblique rotator model. *Astrophys. J.* **1976**, *209*, 816–820. [CrossRef]
31. Petit, P.; Louge, T.; Théado, S.; Paletou, F.; Manset, N.; Morin, J.; Marsden, S.C.; Jeffers, S.V. PolarBase: A Database of High-Resolution Spectropolarimetric Stellar Observations. *Publ. Astron. Soc. Pac.* **2014**, *126*, 469. [CrossRef]
32. Donati, J.F.; Semel, M.; Carter, B.D.; Rees, D.E.; Collier Cameron, A. Spectropolarimetric observations of active stars. *Mon. Not. R. Astron. Soc.* **1997**, *291*, 658–682. [CrossRef]

33. Pakhomov, Y.; Potravnov, I.; Ryabchikova, T. Light variability from UV to near-infrared in Ap star CU Vir induced by chemical spots. *Galaxies* **2025**, *13*, 97. [CrossRef]
34. Piskunov, N.; Kochukhov, O. Doppler Imaging of stellar magnetic fields. I. Techniques. *Astron. Astrophys.* **2002**, *381*, 736–756. [CrossRef]
35. Piskunov, N.E.; Rice, J.B. Techniques for Surface Imaging of Stars. *Publ. Astron. Soc. Pac.* **1993**, *105*, 1415. [CrossRef]
36. Piskunov, N. Doppler imaging. *Phys. Scr. Vol. T* **2008**, *133*, 014017. [CrossRef]
37. Shulyak, D.; Tsymbal, V.; Ryabchikova, T.; Stütz, C.; Weiss, W.W. Line-by-line opacity stellar model atmospheres. *Astron. Astrophys.* **2004**, *428*, 993–1000. [CrossRef]
38. Ryabchikova, T.; Piskunov, N.; Kurucz, R.L.; Stempels, H.C.; Heiter, U.; Pakhomov, Y.; Barklem, P.S. A major upgrade of the VALD database. *Phys. Scr.* **2015**, *90*, 054005. [CrossRef]
39. Pakhomov, Y.; Potravnov, I.; Romanovskaya, A.; Ryabchikova, T. Modeling the TESS Light Curve of Ap Si Star MX TrA. *Universe* **2024**, *10*, 341. [CrossRef]
40. Mashonkina, L. Non-local thermodynamic equilibrium line formation for Si I-II-III in A-B stars and the origin of Si II emission lines in ι Her. *Mon. Not. R. Astron. Soc.* **2020**, *493*, 6095–6108. [CrossRef]
41. Spruit, H.C. Differential rotation and magnetic fields in stellar interiors. *Astron. Astrophys.* **1999**, *349*, 189–202. [CrossRef]
42. Cowling, T.G. On the Sun's general magnetic field. *Mon. Not. R. Astron. Soc.* **1945**, *105*, 166. [CrossRef]
43. Moss, D. Magnetic Fields in the Ap and Bp Stars: A Theoretical Overview. *Magn. Fields Across-Hertzsprung-Russell Diagr.* **2001**, *248*, 305.
44. Bogomazov, A.I.; Tutukov, A.V. Merging of components in close binaries: Type Ia supernovae, massive white dwarfs, and Ap stars. *Astron. Rep.* **2009**, *53*, 214–222. [CrossRef]
45. Schneider, F.R.N.; Ohlmann, S.T.; Podsiadlowski, P.; Röpke, F.K.; Balbus, S.A.; Pakmor, R.; Springel, V. Stellar mergers as the origin of magnetic massive stars. *Nature* **2019**, *574*, 211–214. [CrossRef]
46. Tayler, R.J. The adiabatic stability of stars containing magnetic fields-I.Toroidal fields. *Mon. Not. R. Astron. Soc.* **1973**, *161*, 365. [CrossRef]
47. Pitts, E.; Tayler, R.J. The adiabatic stability of stars containing magnetic fields. IV - The influence of rotation. *Mon. Not. R. Astron. Soc.* **1985**, *216*, 139–154. [CrossRef]
48. Spruit, H.C. Dynamo action by differential rotation in a stably stratified stellar interior. *Astron. Astrophys.* **2002**, *381*, 923–932. [CrossRef]
49. Arlt, R.; Rüdiger, G. Magnetic fields of Ap stars as a result of the Tayler instability. *Astron. Nachrichten* **2011**, *332*, 70–76. [CrossRef]
50. Rüdiger, G.; Kitchatinov, L.L. The kink-type instability of toroidal stellar magnetic fields with thermal diffusion. *Geophys. Astrophys. Fluid Dyn.* **2010**, *104*, 273–285. [CrossRef]
51. Kitchatinov, L.L.; Potravnov, I.S.; Nepomnyashchikh, A.A. Longitudinal drift of Tayler instability eigenmodes as a possible explanation for super-slowly rotating Ap stars. *Astron. Astrophys.* **2020**, *638*, L9. [CrossRef]
52. Kitchatinov, L.; Rüdiger, G. Stability of toroidal magnetic fields in rotating stellar radiation zones. *Astron. Astrophys.* **2008**, *478*, 1–8. [CrossRef]
53. Kitchatinov, L.L. Stability of toroidal magnetic fields in the radiation zone of a star. *Astron. Rep.* **2008**, *52*, 247–255. [CrossRef]
54. Goossens, M.; Biront, D.; Tayler, R.J. Additional Results for Unstable Stratified Toroidal Magnetic Fields in Stars. *Astrophys. Space Sci.* **1981**, *75*, 521–526. [CrossRef]
55. Denissenkov, P.A.; Pinsonneault, M. A Revised Prescription for the Tayler-Spruit Dynamo: Magnetic Angular Momentum Transport in Stars. *Astrophys. J.* **2007**, *655*, 1157–1165. [CrossRef]
56. Paxton, B.; Bildsten, L.; Dotter, A.; Herwig, F.; Lesaffre, P.; Timmes, F. Modules for Experiments in Stellar Astrophysics (MESA). *Astrophys. J. Suppl.* **2011**, *192*, 3. [CrossRef]
57. Potravnov, I.; Piskunov, N.; Ryabchikova, T. Secular stability of surface abundance structures in the rapidly rotating Ap star 56 Ari. *Astron. Astrophys.* **2024**, *689*, A111. [CrossRef]
58. Parker, E.N. The Instability of a Horizontal Magnetic Field in an Atmosphere Stable Against Convection. *Astrophys. Space Sci.* **1979**, *62*, 135–142. [CrossRef]
59. Hughes, D.W.; Weiss, N.O. Double-diffusive convection with two stabilizing gradients: Strange consequences of magnetic buoyancy. *J. Fluid Mech.* **1995**, *301*, 383–406. [CrossRef]

galaxies

MDPI

Article

Unveiling the Variability and Chemical Composition of AL Col

Surath C. Ghosh [1,2,*], Santosh Joshi [1], Samrat Ghosh [1], Athul Dileep [1], Otto Trust [3,4], Mrinmoy Sarkar [1], Jaime Andrés Rosales Guzmán [5], Nicolás Esteban Castro-Toledo [5], Oleg Malkov [6], Harinder P. Singh [7], Kefeng Tan [8] and Sarabjeet S. Bedi [2]

[1] Aryabhatta Research Institute of Observational Sciences (ARIES), Nainital 263001, India
[2] Department of Computer Science and Information Technology, MJP Rohilkhand University, Bareilly 243006, India
[3] Department of Physics, Mbarara University of Science and Technology, Mbarara P.O. Box 1410, Uganda; otrust@must.ac.ug
[4] Department of Physics, Faculty of Science, Kyambogo University, Kyambogo P.O. Box 1, Uganda
[5] Departamento de Física, Universidad de Concepción (UdeC), Concepcion 4070412, Chile
[6] Institute of Astronomy of the Russian Academy of Sciences (INASAN), Moscow 119017, Russia; malkov@inasan.ru
[7] Department of Physics and Astrophysics, University of Delhi, Delhi 110007, India
[8] National Astronomical Observatories, Chinese Academy of Sciences (NAOC), Beijing 100101, China
* Correspondence: su5virat@gmail.com or surath@aries.res.in

Abstract: In this study, we present analysis of *TESS* photometry, spectral energy distribution (SED), high-resolution spectroscopy, and spot modeling of the α^2 CVn-type star AL Col (HD 46462). The primary objective is to determine its fundamental physical parameters and investigate its surface activity characteristics. Using *TESS* short-cadence (120 s) SAP flux, we identified a rotational frequency of 0.09655 d^{-1} ($P_{rot} = 10.35733$ d). Wavelet analysis reveals that while the amplitudes of the harmonic components vary over time, the strength of the primary rotational frequency remains stable. A SED analysis of multi-band photometric data yields an effective temperature (T_{eff}) of 11,750 K. High-resolution spectroscopic observations covering wavelengthrange 4500–7000 Å provide refined estimates of T_{eff} = 13,814 $\pm$ 400 K, $\log g = 4.09 \pm 0.08$ dex, and $v \sin i = 16 \pm 1$ km s^{-1}. Abundance analysis shows solar-like composition of O II, Mg II, S II, and Ca II, while helium is under-abundant by 0.62 dex. Rare earth elements (REEs) exhibit over-abundances of up to 5.2 dex, classifying the star as an Ap/Bp-type star. AL Col has a radius of $R = 3.74 \pm 0.48 R_\odot$, with its H–R diagram position estimating a mass of $M = 4.2 \pm 0.2 M_\odot$ and an age of 0.12 $\pm$ 0.01 Gyr, indicating that the star has slightly evolved from the main sequence. The *TESS* light curves were modeled using a three-evolving-spot configuration, suggesting the presence of differential rotation. This star is a promising candidate for future investigations of magnetic field diagnostics and the vertical stratification of chemical elements in its atmosphere.

Keywords: stars—chemically peculiar; He weak; techniques—TESS photometry; high resolution spectroscopy; abundance; individual—AL Col; variable—α^2CVn

1. Introduction

Chemically peculiar (CP) stars on the upper main sequence, ranging from early B to early F spectral types, exhibit significant deviations from solar surface abundances, with anomalies manifesting as localized chemical over- or under-abundances across their atmospheres [1,2]. These anomalies often involve light elements such as helium (He), which may be strongly depleted, and heavy elements like iron-peak and rare-earth species (e.g., Sr, Cr, Eu), which can exceed solar abundances by several dex. The distribution of these elements is frequently non-uniform, forming chemical spots, belts, or rings modulated by stellar rotation.

CP stars are traditionally grouped into four major subtypes based on their spectral characteristics and magnetic properties [3–6]: (i) CP1 stars, or Am/Fm stars, exhibit enhanced metallic lines but typically lack strong magnetic fields; (ii) CP2 stars, also known as Bp/Ap stars, are magnetic and chemically peculiar with pronounced Si, Sr, and Eu over-abundances; (iii) CP3 stars are HgMn stars, characterized by peculiar mercury and manganese lines; and (iv) CP4 stars, or He-weak stars, are defined by strong helium under-abundances.

The CP2 and CP4 subclasses, commonly referred to as magnetic chemically peculiar (mCP) stars, are distinguished by the presence of strong, globally organized magnetic fields, often with dipolar topology and field strengths ranging from a few hundred Gauss to several tens of kiloGauss [7–9]. These fields are believed to be of fossil origin, i.e., remnants from earlier evolutionary stages or star formation processes [10].

The surface abundance patterns observed in CP stars are explained primarily through atomic diffusion in radiative atmospheres [11,12]. In the absence of significant turbulent mixing or convection, and under the stabilizing influence of a magnetic field, radiative levitation can elevate certain elements to the photosphere, while gravitational settling pulls others downward. The efficiency of these processes depends sensitively on atomic properties, local temperature, and magnetic field geometry. The magnetic field suppresses convective motions and horizontal diffusion, leading to the formation of stable chemical spots aligned with magnetic field structures [13,14].

The observational consequences of this inhomogeneity are profound. As CP stars rotate, the chemical spots traverse the visible disk, producing rotational modulation in brightness, spectral line strengths, and longitudinal magnetic field measurements. This phenomenon is well explained by the oblique rotator model [15,16], wherein the magnetic axis is inclined to the rotational axis. Stars exhibiting such periodic variability are classified as α^2 *CanumVenaticorum* (ACV) variables. These variations are typically stable over long timescales, making ACV stars ideal targets for rotational studies and magnetic field mapping through Doppler imaging and Zeeman Doppler imaging techniques [17,18].

In addition to the rotational modulation, a set of mCP stars pulsates in high-overtones p-modes (6–24 min), offering unique asteroseismic insight into the stellar interiors [19–23]. The co-existence of rotation and pulsations allow for the investigation of various physical process, such as transport of the angular momentum. In the past, such candidates have been searched and studied through systematics surveys (e.g., [24]). In the context of the present work, one of the longest such ground-based surveys is the Nainital–Cape (N–C) Survey conducted between the Aryabhatta Research Institute of Observational Sciences (ARIES) and South African Astronomical Observatory (SAAO), South Africa, where several asteroseismic candidates were discovered [25–33].

Modern space-based observatories such as *Kepler*, *Transiting Exoplanet Survey Satellite* (*TESS*), and *BRITE* have revolutionized the study of CP stars by enabling high-precision, uninterrupted time-series photometry, uncovering new variability classes, rotational modulation, and pulsation signatures in hundreds of mCP candidates [34–36]. Combined with large-scale spectroscopic efforts and magnetic field surveys (e.g., ESPaDOnS, HARPSpol, MiMeS, and BinaMIcS), this has greatly improved statistical constraints on the incidence and properties of magnetic CP stars across different stellar environments and evolutionary stages [9,37,38].

In this study, we investigate the photometric and spectroscopic characteristics of AL Col. Despite limited previous attention, initial classifications suggest it may belong to the CP2 or CP4 subclass, motivating a more detailed analysis. Using new time-series photometry and high-resolution spectroscopy, we aim to characterize its variability, derive its atmospheric parameters and elemental abundances, and assess its position within the framework of mCP star phenomenology. Our goal is to contribute to the understanding of magnetic field-driven chemical stratification and variability in upper main-sequence stars and to place AL Col in the broader context of CP star evolution.

The structure of this paper is as follows. Section 2 outlines the selection of the target star. In Section 3, we present the analysis of *TESS* photometric data, including variability characterization through wavelet and autocorrelation methods. Section 4 details the derivation of fundamental stellar parameters and chemical abundances using high-resolution spectral synthesis. The evolutionary status of the star is discussed in Section 5. In Section 6, we analyze the spatial and temporal characteristics of surface chemical spots. Finally, Section 7 summarizes our main findings and discusses future directions for this study.

2. Sample Selection

Bernhard et al. [39] determined rotational parameters for more than 300 magnetic CP stars by utilizing ground-based archival photometry from surveys such as ASAS-3, KELT, and MASCARA. From this compilation, we selected a southern hemisphere target for which both the high-precision *TESS* light curves and high-resolution spectra with high signal-to-noise ratio (SNR) are available. Our selected target is the α^2 CVn-type variable star AL Col (HD 46462), classified as an ApSi star.

3. *TESS* Photometry

TESS was launched on 18 April 2018 with the primary goal of detecting exoplanets via the transit method. The mission observes nearly the entire sky, which is divided into 26 sectors, each covering a field of $24^\circ \times 96^\circ$. Each sector is continuously monitored for approximately 27.4 days using four wide-field cameras. Each camera hosts four 2K $\times$ 2K CCD detectors, enabling high-precision photometry over a large field of view.

AL Col was observed by *TESS* during the observation of sectors 6 and 7. The Python-based (3.13.6) `lightkurve` package [40] was employed to search, download, and analyze the *TESS* time-series data for these sectors. We utilized the short-cadence data (120 s) processed by the Science Processing Operations Center (SPOC) pipeline.

Although the Pre-search Data Conditioning Simple Aperture Photometry (PDCSAP) flux is generally preferred due to its correction for systematics and long-term instrumental drifts, in the case of AL Col, the raw Simple Aperture Photometry (SAP) flux was found to be of higher quality. Outliers were removed using a sigma-clipping algorithm where necessary. The *TESS* flux values (in $e^{-}\,s^{-1}$) were converted to magnitudes in the T-band using the following standard flux-to-magnitude relation:

$$I_{\text{mag}} = -2.5\log(\text{FLUX}) + 20.44. \tag{1}$$

To investigate the rotational modulation, the time-series data were phase-folded using the rotation period $P_{\text{rot}} = 10.35733$ d, following the ephemeris:

$$\phi_i = 2\pi\left(\frac{t_i - t_0}{P_{\text{rot}}} - \left\lfloor \frac{t_i - t_0}{P_{\text{rot}}} \right\rfloor\right), \tag{2}$$

where t_i is the Barycentric Julian Date (BJD) of each observation and t_0 = 2,458,471.6706 days is the reference epoch. Figure 1 shows the resulting phase-folded light curve, binned into 200 phase intervals. The observed light variation exhibits a clear non-sinusoidal shape with a double-peaked structure, indicative of surface brightness inhomogeneities caused by two dominant chemical spots on the stellar surface.

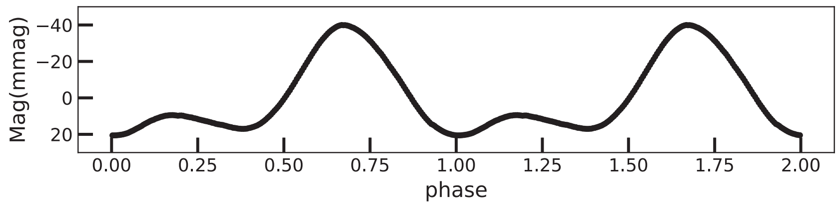

Figure 1. Phase-folded light curve of AL Col using a reference epoch of t_0 = 2,458,471.6706 days (time corresponding to minimum brightness) and a rotation period of 10.35733 d. The data have been binned into 200 phase intervals to improve clarity and reveal the rotational variability.

To identify the periodic components of the photometric variability, we performed a Discrete Fourier Transform (DFT) of the combined *TESS* light curve using the PERIOD04 software package [41], up to the Nyquist frequency ($\nu_{\rm nyq} \sim 360\,{\rm d}^{-1}$). Significant frequency peaks were identified using the SNR threshold of ≥5.2, as recommended by Baran and Koen [42]. The dominant frequencies were iteratively prewhitened, and the residuals were reanalysed until no significant frequencies remained.

Figure 2 presents the resulting amplitude spectrum of the combined data. The most prominent peak is found at $\nu = 0.09655\,{\rm d}^{-1}$, corresponding to a rotation period of $P_{\rm rot} = 10.35733$ d—consistent with the value reported by Bernhard et al. [39]. The detection of higher-order harmonics further supports the presence of non-uniform surface features modulating the light curve. The identified frequencies, amplitudes, phases, and SNRs are summarized in Table 1. To confirm the nature of the detected signals, we performed wavelet and autocorrelation analyses of the time-series data.

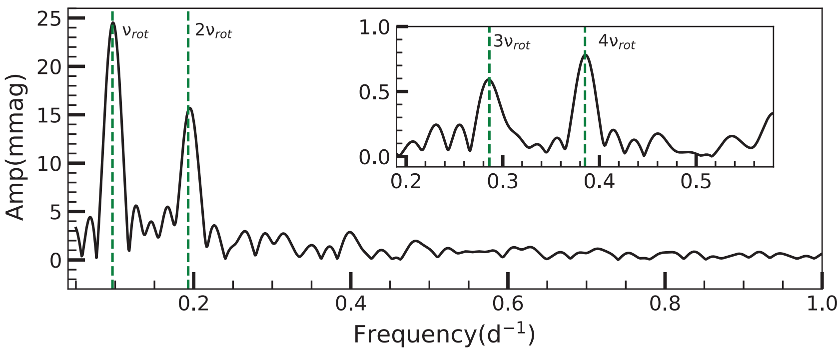

Figure 2. Amplitude spectrum of AL Col corresponding to the time-series data in Figure 1. The vertical green lines indicate the observed rotational frequency and its second harmonic. After removing the two dominant frequencies, the inset displays the third and fourth low-amplitude harmonics.

Table 1. Listed are the frequencies, amplitudes, phases, signal-to-noise ratios (SNRs), and identified combination frequencies derived from the Fourier Transform of the *TESS* light curve, constructed by combining time-series data from sectors 6 and 7.

Frequency (d^{-1})	Amplitude (mmag)	Phase	SNR	Combination Frequencies
0.09655	24.2324	0.9878	210.93	$\nu_{\rm rot}$
0.19296	14.6962	0.4103	137.74	$2\nu_{\rm rot}$
0.38499	0.8011	0.7481	8.34	$4\nu_{\rm rot}$
0.28611	0.6341	0.8373	6.28	$3\nu_{\rm rot}$

Wavelet and Autocorrelation Analysis

Low-amplitude variations in stellar brightness, such as those caused by eclipses or rotational modulation, occasionally remain undetected through conventional time-series analysis. To enhance the detection sensitivity and examine the temporal evolution of such modulations, advanced time–frequency analysis techniques such as wavelet transforms and autocorrelation functions (ACFs) are frequently employed. These methods are particularly effective in analyzing non-stationary signals and offer robustness against temporal evolution of active regions.

Wavelet analysis, in particular, is a powerful tool for detecting signatures of rotation, magnetic activity, and pulsations in stellar atmospheres [43]. For the present study, we utilized a wavelet analysis code jointly developed by Prof. Rafael Garcia and Prof. Savita Mathur. This code employs a Morlet wavelet, a complex sinusoidal function modulated by a Gaussian envelope, to perform convolution with the light curve. Figure 3 presents the resulting wavelet power spectrum alongside its corresponding Global Wavelet Power Spectrum (GWPS).

The local wavelet power spectrum captures the distribution of signal energy in both time and frequency domains, while the GWPS is obtained by integrating the local spectrum over time, thereby revealing the average amplitude as a function of frequency. From the GWPS, we identified two dominant periodicities at 10.1043 ± 1.6809 d and 5.0521 ± 0.8411 d. These values are close to those derived from the Fourier analysis (see Table 1 and Figure 2).

To independently validate these periodicities, we also applied the autocorrelation function (ACF) technique to the *TESS* light curve. This method, which evaluates the correlation of the signal with itself at varying time lags, is effective in identifying rotational modulation from co-rotating starspots. The resulting normalized ACF displays a series of quasi-periodic local maxima, indicative of persistent surface features. The first significant peak beyond zero lag yields a dominant autocorrelation period of $P_{\mathrm{ACF}} = 10.2118 \pm 1.3074$ d (see Figure 3), again in agreement with the results from both the wavelet and DFT analyses.

As seen in Figure 3, the GWPS exhibits two prominent peaks that persist over the full observation baseline. These are represented in the local wavelet power map by warm color gradients (yellow to red), with the dark black regions indicating the strongest power. The primary rotation period maintains a stable amplitude across the observation span, while the secondary period shows a transient behavior—intensifying and subsequently fading after approximately 30 days of observation.

This behavior is characteristic of surface inhomogeneities such as starspots. When two active longitudes are positioned roughly 180° apart on opposite hemispheres, the harmonic content of the light curve increases [44]. The dominant active region corresponds to the fundamental rotation period ($\sim$10.1581 d), while the secondary spot gives rise to the second harmonic, observed at $\sim$5.1471 d in both the ACF and GWPS. These findings reinforce the hypothesis that the photometric variability of AL Col is driven by rotational modulation due to two major surface chemical spots, which are diametrically opposite.

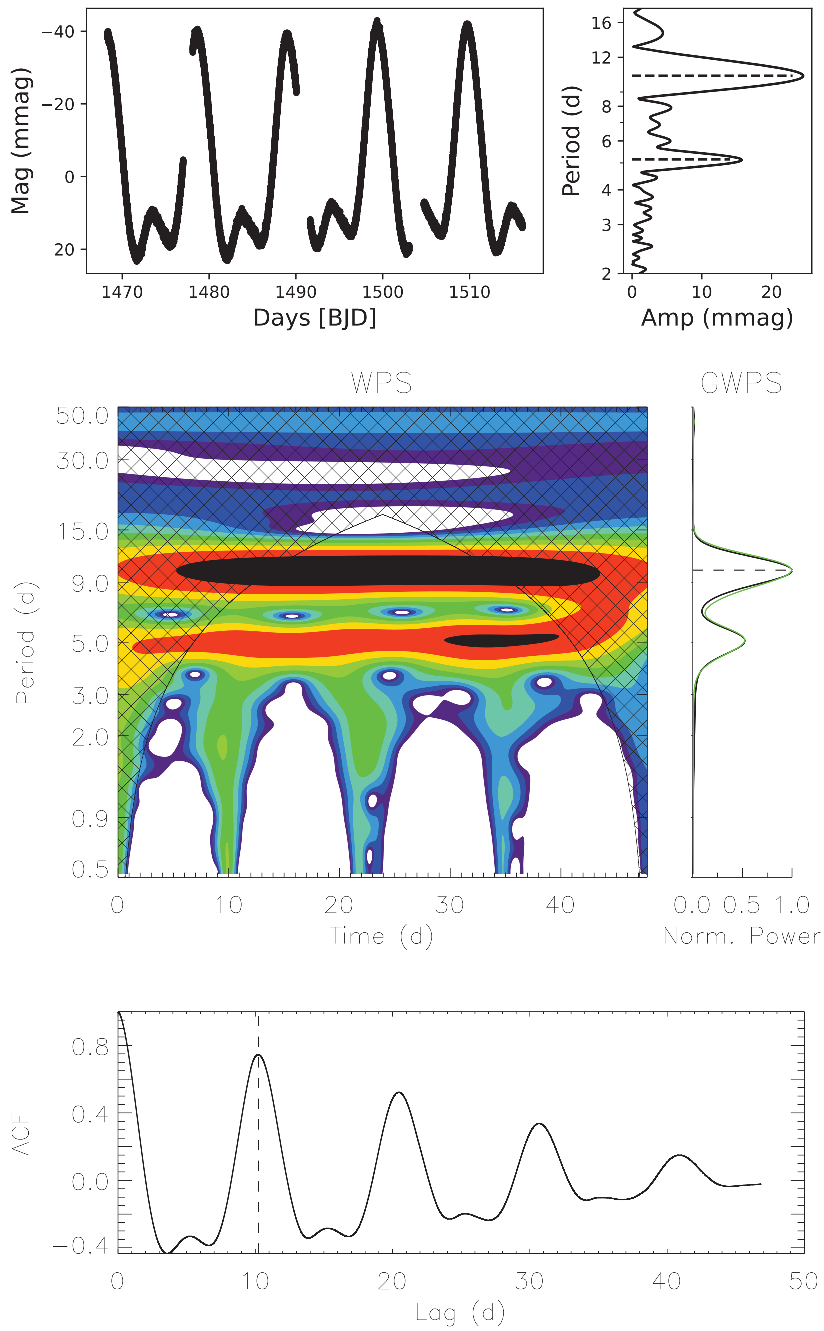

Figure 3. (**Top panels**): The left sub-panel displays the stellar light curve (time-series photometry), while the right sub-panel presents the corresponding Fourier amplitude spectrum, highlighting dominant periodicities. (**Middle panels**): The left sub-panel shows the wavelet power spectrum (WPS), where black indicates the highest power and blue represents weaker signals. The red and yellow regions trace strong periodicities, such as stellar rotation and its first harmonic. The shaded region marked by black crosses denotes the cone of influence, where edge effects render the wavelet results unreliable. The right sub-panel shows the Global Wavelet Power Spectrum (GWPS), derived by averaging the WPS over the full timespan of the data. (**Bottom panel**): The autocorrelation function (ACF) of the light curve is plotted for time lags between 0 and 50 days. Recurrent peaks in the ACF suggest the presence of quasi-periodic variability, often associated with stellar rotation.

4. High-Resolution Spectroscopy

A high-resolution spectrum of AL Col was obtained using the High Accuracy Radial Velocity Planet Searcher (HARPS), mounted on the ESO 3.6 m telescope at La Silla Observatory, Chile. The wavelength-calibrated spectra were retrieved from the European Southern

Observatory (ESO) Science Portal[1]. Two exposures, each with an integration time of 300 s, were acquired on 8 December 2007, yielding a resolving power of $R\sim$115,000 and covering the wavelength range 3780–6900 Å.

Continuum normalization was performed using a custom Python-based routine, which fits a Chebyshev polynomial to the local maxima representing the spectral upper envelope. To improve the signal-to-noise ratio (SNR), the two spectra were combined using a median-combination technique, resulting in a final SNR of 125.2 at 5500 Å.

4.1. Basic Physical Parameters

Accurate determination of fundamental stellar parameters—such as effective temperature ($T_{\rm eff}$), surface gravity ($\log g$), and global metallicity ([M/H]) —is essential for characterizing the star's atmospheric properties and for constraining asteroseismic and evolutionary models. Spectroscopic techniques remain among the most reliable tools for obtaining these parameters, though initial estimates are typically required to optimize convergence.

Preliminary estimates of the stellar parameters were derived by comparing the observed SED with synthetic photometric fluxes from theoretical models.

4.2. Spectral Energy Distribution

To estimate the effective temperature, we performed an SED analysis by assembling multi-wavelength photometric fluxes spanning the optical to infrared regimes. The observational SED was constructed using data from various photometric systems: the Strömgren–Crawford *uvby* system, Tycho-2, Johnson UBV, Hipparcos, Gaia DR3, CMC15, 2MASS, WISE, NEOWISE, and DENIS catalogues [45–54]. Data retrieval was facilitated through VizieR[2] and the Spanish Virtual Observatory (SVO)[3].

The observed fluxes were plotted as a function of their respective effective wavelengths, and a synthetic SED was generated by fitting theoretical flux distributions to the multi-band data using an iterative χ^2 minimization technique. The best-fitting model yields an effective temperature of $T_{\rm eff} = 11{,}750 \pm 125$ K (see Figure 4). The derived $T_{\rm eff}$ serves as initial inputs for the detailed spectroscopic analysis discussed in the next section.

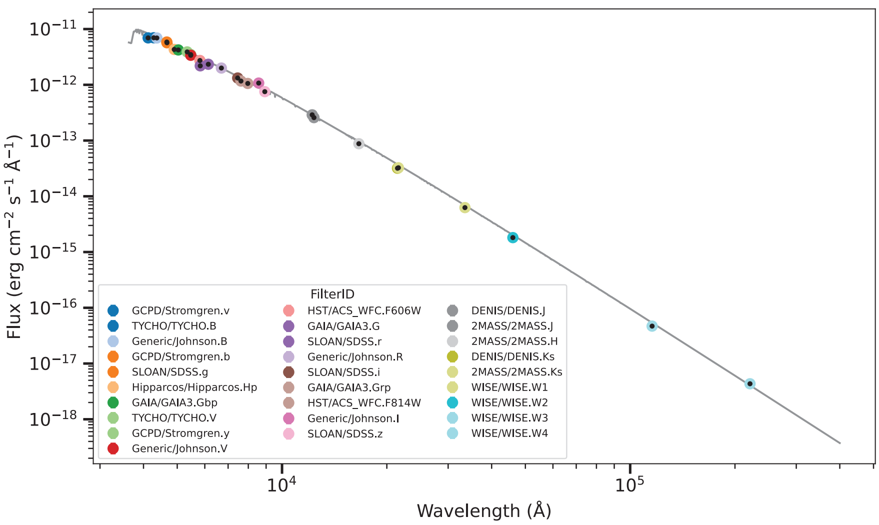

Figure 4. Spectral energy distribution (SED) spanning the optical to infrared wavelengths. Colored dots represent observed fluxes in different photometric bands, as indicated in the legend. The solid gray line corresponds to the best-fitting theoretical model ($T_{\rm eff} = 11{,}750 \pm 125$ K). Both the axes are plotted in logarithmic scale.

4.3. Spectral Synthesis with pySME

The atmospheric parameters derived from the SED analysis were used as initial inputs to compute synthetic spectra for detailed spectroscopic modeling. The estimated (T_{eff}) from SED, along with $\log g$ = 4.0 dex (assuming the target to be a main-sequence star), were adopted to extract the atomic and molecular line data from the VALD3 database [55], which includes isotopic and hyperfine structure components essential for high-resolution modeling.

To align the synthetic spectra with the observed HARPS data, a Doppler correction was applied, yielding a measured radial velocity of $v_{\text{rad}} = 28\,\text{km}\,\text{s}^{-1}$. Grids of synthetic spectra were generated using the Python-based package `pySME` [56], which implements the `Spectroscopy Made Easy` (SME) framework. This code adopts plane-parallel model atmospheres from ATLAS9 [57] under the assumption of local thermodynamic equilibrium (LTE). SME determines atmospheric parameters and chemical abundances by fitting synthetic spectra to selected regions of the observed spectrum. A χ^2 minimization approach is employed to iteratively adjust the parameters until the best match is achieved.

A line mask was constructed by selecting diagnostic lines that are sensitive to variations in different atmospheric parameters. The fitting process searched for the optimal combination of T_{eff}, $\log g$, and projected rotational velocity ($v \sin i$) by minimizing residuals between the synthetic and observed spectra.

For the iterative fitting procedure, the initial parameters were set as follows: T_{eff} from the SED analysis, $\log g$ was fixed at 4.0 (typical of main-sequence stars), solar metallicity ([M/H] = 0), $v_{mic} = 2\,\text{km}\,\text{s}^{-1}$, and $v \sin i$ was estimated by visually matching the width of metal lines. Since Balmer lines are particularly sensitive to T_{eff} and $\log g$, we refined these parameters by fitting synthetic profiles to the observed Hβ (4861 Å) and Hα (6563 Å) line profiles. The projected rotational velocity $v \sin i$ was determined by fitting the Mg I triplet region (5160–5187 Å). Figure 5 shows the comparison between the observed and best-fit synthetic spectra in the regions around the Hβ and Hα lines.

Parameter uncertainties were estimated from the standard deviation of the residuals between the observed and synthetic spectra within each fitted region. The final atmospheric parameters are T_{eff} = 13,814 ± 400 K, $\log g$ = 4.09 ± 0.08 dex, and $v \sin i$ = 16 ± 1 km s^{-1}.

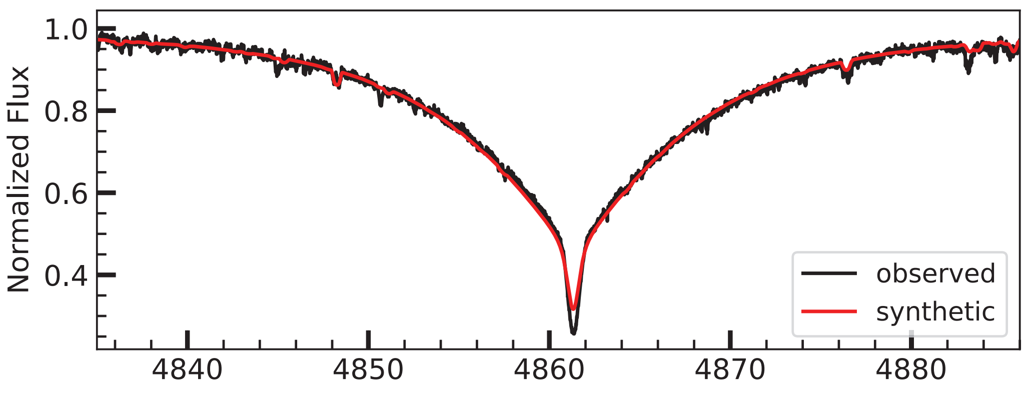

Figure 5. *Cont.*

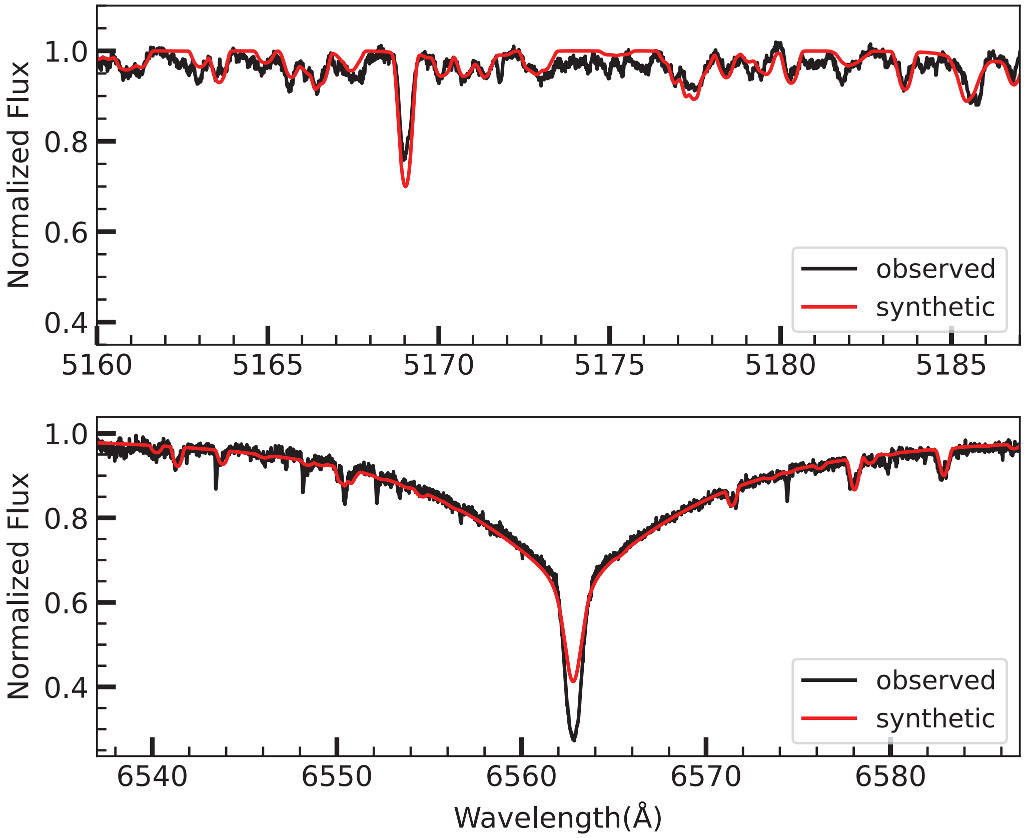

Figure 5. Comparison between the observed (black) and synthetic (red) spectra in three key regions: the Hβ (**top panel**), the Mg I triplet region (**middle panel**), and the Hα (**bottom panel**). The synthetic spectra were computed using the best-fitting atmospheric parameters.

4.4. Photospheric Chemical Abundance Analysis

Chemical abundances provide valuable insights into the patterns of elemental enhancement and depletion in stellar atmospheres, which in turn inform our understanding of stellar structure, evolution, and diffusion processes. We performed a detailed analysis of the photospheric composition of AL Col under the assumption of local thermodynamic equilibrium (LTE). Individual elemental abundances were derived by fitting synthetic line profiles to the observed HARPS spectrum using the `BinMag6` visualization tool[4] [58]. The atmospheric parameters determined in Section 4.3 ($T_{\rm eff}$, $\log g$, and $v \sin i$) were held fixed throughout the abundance analysis.

A total of 25 chemical elements, ranging from helium (He) to europium (Eu), were investigated. Both neutral and ionized species (first and second ions) were considered based on the presence of unblended or mildly blended absorption lines in the optical spectral range. The synthetic spectra used for fitting were interpolated from the model grid developed by Tkachenko [59], which includes 41,888 LTE models spanning a metallicity range of [M/H] = -0.8 to $+0.8$ dex (in steps of 0.1 dex) and assumes a fixed microturbulent velocity of $v_{\rm mic} = 2\,{\rm km\,s^{-1}}$. The grid offers high resolution in $T_{\rm eff}$ (100 K steps between 4500–10,000 K and 250 K steps between 10,000–22,000 K) and in $\log g$ (2.5–5.0 dex for low $T_{\rm eff}$, 3.0–5.0 dex for high $T_{\rm eff}$).

For AL Col, we selected the model atmosphere closest to the spectroscopically determined parameters. Atomic line data were extracted from the VALD3 database, and relevant absorption features were identified in the 4500–6850 Å wavelength range. For each element, spectral sub-regions containing suitable diagnostic lines were selected for abundance determination. Each sub-region yielded an independent abundance measurement, and the final elemental abundance was computed as the mean of the values derived from multiple segments.

The interface of `BinMag6` is displayed in Figure 6, illustrating the spectral window spanning approximately 4947–4953 Å. The shaded region indicates the active fitting area, where spectral lines corresponding to the elements present have been modeled. In this analysis, emphasis was placed on the strongest lines, particularly three Fe II transitions. Spectral features associated with Ni II and a weaker Fe II line within this interval exhibited an insufficient signal-to-noise ratio and were therefore excluded from the analysis. A notable feature is the presence of a central bump in the cores of the Fe II lines, a phenomenon commonly observed in metallic lines (Cr, Ni, Nd, Pr, Eu, etc.) of magnetic chemically peculiar (mCP) stars. Additionally, asymmetries—particularly bumps on line cores—are attributed to line profile variations induced by chemical spots on the stellar surface. Accurate modeling of such line profile variations necessitates time-series spectroscopic observations [60].

Elemental abundances are reported in the standard logarithmic notation:

$$\log \epsilon = \log\left(\frac{N_{\rm el}}{N_{\rm tot}}\right) + 12.04,$$

where $N_{\rm el}$ and $N_{\rm tot}$ represent the number densities of the element and the total number of atoms, respectively. The final abundances are summarized in Table 2 and visualized in Figure 7.

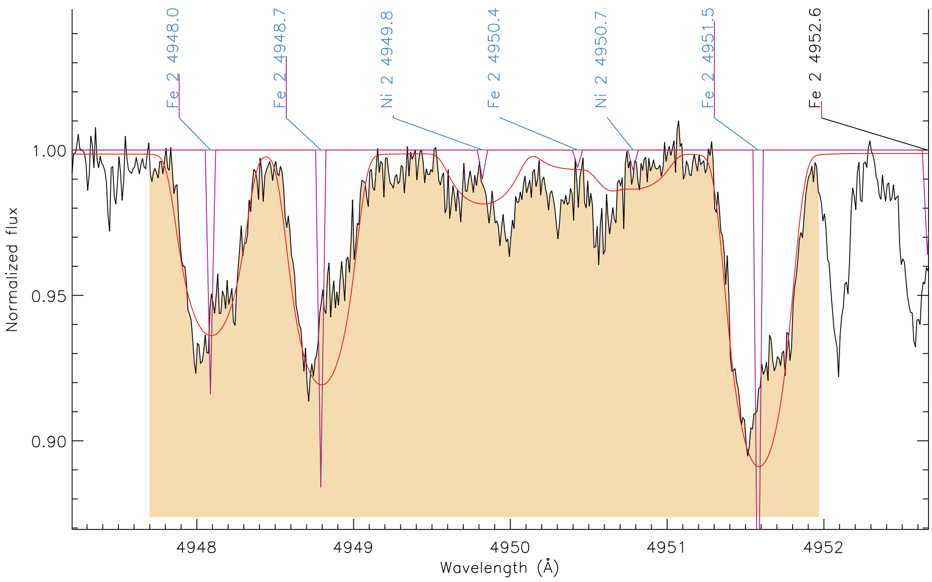

Figure 6. A selected piece of the spectrum in a narrow range if the wavelength range is 4943 Å–4953 Å for the clear visibility. Lines of various ions are marked using *BinMag6* interface. The observed and synthetic spectra are shown with black and red colors, respectively. The shaded region is the active region; i.e., only lines under that region are fitted (e.g., fitted Fe II lines).

Table 2. Chemical elements analyzed in AL Col, along with their atomic numbers, number of spectral lines used, and mean photospheric abundances. The standard errors of the mean abundances, calculated as the standard deviation of individual line measurements, are provided. Solar photospheric abundances adopted from Asplund et al. [61] are listed for comparison.

Element	Atomic No. Z	No. of Lines Used	log ϵ_{ALCol} (dex)	Error (dex)	log $\epsilon_{\odot}$ (dex)
He I	2	6	−1.71	0.39	−1.09
C II	6	5	−2.72	0.62	−3.54
N I	7	1	−3.04	–	−4.17
N II	7	5	−2.52	0.54	−4.17
O I	8	1	−2.46	–	−3.31
O II	8	3	−3.11	0.24	−3.31
Ne I	10	10	−3.23	0.30	−3.94
Na II	11	2	−3.80	0.21	−5.78
Mg I	12	1	−3.69	–	−4.45
Mg II	12	5	−4.63	0.91	−4.45
Al II	13	3	−4.47	0.60	−5.57
Si II	14	29	−3.78	0.63	−4.49
Si III	14	2	−2.55	0.45	−4.49
P II	15	6	−5.78	0.48	−6.59
S I	16	1	−3.48	–	−4.88
S II	16	20	−4.68	0.86	−4.88
Cl II	17	3	−4.14	0.90	−6.69
Ca II	20	2	−5.36	0.09	−5.70
Ti II	22	9	−5.89	0.62	−7.03
V II	23	1	−6.16	–	−8.10
Cr II	24	12	−5.53	0.78	−6.38
Mn II	25	2	−4.73	1.11	−6.58
Fe I	26	1	−1.77	–	−4.54
Fe II	26	133	−3.86	0.44	−4.54
Ni II	28	10	−4.77	0.42	−5.80
Zn I	30	1	−4.84	–	−7.44
Y II	39	4	−6.81	0.71	−9.79
Ce II	58	15	−5.27	0.55	−10.42
Ce III	58	1	−6.32	–	−10.42
Pr II	59	3	−6.36	0.36	−11.25
Pr III	59	26	−7.08	0.64	−11.25
Nd II	60	4	−5.38	0.76	−10.58
Nd III	60	28	−7.37	0.39	−10.58
Eu III	63	3	−6.35	0.45	−11.48

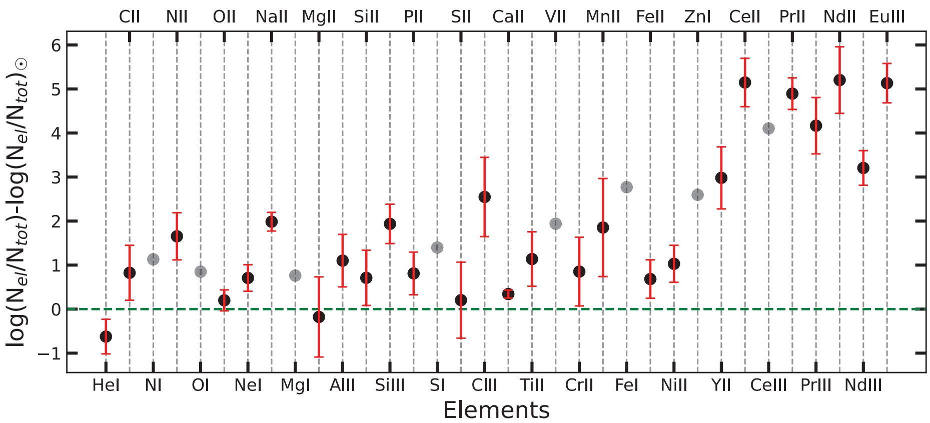

Figure 7. Graphical representation of the elemental abundances listed in Table 2. The horizontal green line indicates the solar abundances from Asplund et al. [61]. Black dots represent the mean abundances of elements for which multiple spectral lines were measured; the associated red error bars denote the standard deviation of these measurements. Gray dots indicate elements for which only a single line was available, and these values should be interpreted with caution.

The large discrepancies between abundances derived from successive ionization stages, in particular the 1.23 dex offset between Si II and Si III and the 2.09 dex offset between Fe I and Fe II, strongly point to departures from a simple LTE, homogeneous atmospheric model. In A- and B-type chemically peculiar stars, overionization of minority species under non-LTE conditions leads to weakened neutral-stage lines and hence to underestimated LTE abundances [62,63]. At the same time, vertical stratification of elements, observationally demonstrated in Ap stars, can concentrate both Fe and Si at different optical depths where Fe I, Fe II, Si II, and Si III lines form, amplifying ionization imbalances [64]. Indeed, Romanovskaya et al. (2024) find a $\approx$1.5 dex abundance jump between the layers where Fe II-III and Si II-III lines form in the Ap star BD +00° 1659, further underscoring the combined role of stratification and non-LTE effects [65]. Depth-dependent micro- and macro-turbulences further distort line profiles in opposite senses for neutral versus ionized species [66]. To reconcile these offsets and to derive a physically consistent abundance profile for AL Col, full non-LTE spectrum synthesis with a stratified abundance model is required (e.g., using TLUSTY/SYNSPEC [67] or DETAIL/SURFACE [68]), which will also shed light on the operation of diffusion and weak stellar winds in its atmosphere.

5. Evolutionary Status

Determining the evolutionary status of the target star is crucial for placing its physical and chemical properties in the broader context of stellar structure and evolution. It provides insight into the star's internal processes, surface composition, and variability mechanisms and is essential for accurately modeling its pulsations and rotational behavior.

To assess the evolutionary status of AL Col, we utilized the PAdova and TRieste Stellar Evolution Code (PARSEC; Bressan et al. [69]) to compute stellar evolutionary tracks and isochrones. The models were generated assuming a solar metallicity of $Z = 0.0152$ [70]. A grid of evolutionary tracks was computed for a range of stellar masses, and isochrones corresponding to various ages were overlaid on the $T_{\rm eff}$–$\log g$ diagram.

5.1. Luminosity Estimate

The stellar luminosity was calculated using the following relation:

$$\log\left(\frac{L}{\mathrm{L}_\odot}\right) = -0.4(M_\mathrm{V} + BC - M_{\mathrm{bol},\odot}), \tag{3}$$

where $M_{\mathrm{bol},\odot} = 4.74$ is the solar bolometric magnitude, and BC is the bolometric correction derived using the empirical relation from Torres [71]. The absolute magnitude M_V in the V band was computed using

$$M_\mathrm{V} = m_\mathrm{V} + 5 - 5\,\log(d) - A_\mathrm{V}, \tag{4}$$

where $m_\mathrm{V} = 7.56$ is the apparent visual magnitude, $d = 243$ pc is the distance estimated from *Gaia* DR3 parallax [72], and $A_\mathrm{V} = 1.61$ is the extinction in the V band, derived using the reddening value $E(\mathrm{B} - \mathrm{V}) = 0.52$ [73] and adopting $R_V = 3.1$.

Substituting the derived values into Equations (3) and (4) yields $\log(L/\mathrm{L}_\odot) = 2.69 \pm 0.09$, which corresponds to a mid-late B-type to early A-type main-sequence star, in excellent agreement with the spectroscopic classification presented in Section 4.3.

5.2. Radius, Mass, and Age

The stellar radius was estimated using the following relation:

$$\log\left(\frac{R}{\mathrm{R}_\odot}\right) = 0.5\log\left(\frac{L}{\mathrm{L}_\odot}\right) - 2\log\left(\frac{T}{\mathrm{T}_\odot}\right), \tag{5}$$

yielding a value of $R = 3.74 \pm 0.48\,R_\odot$ that is approximately a solar radius larger than the published value ($2.44\,R_\odot$) by Glagolevskij [74]. The underestimated stellar radius in previous studies can primarily be attributed to the use of Hipparcos-based parallaxes and the adoption of luminosities uncorrected for interstellar extinction [74]. By combining the stellar radius (R) and $v \sin i$ derived in our analysis, we infer an inclination angle of approximately 60°.

The location of the star in the Hertzsprung–Russell (H–R) diagram is illustrated in Figure 8, where evolutionary tracks corresponding to stellar masses ranging from 3.2 to $4.8\,M_\odot$, in increments of $0.4\,M_\odot$, are overplotted. The position of the target aligns closely with the evolutionary track of $4.2 \pm 0.2\,M_\odot$, consistent with the mass estimate of $M_\star = 3.9\,M_\odot$ reported by Glagolevskij [74].

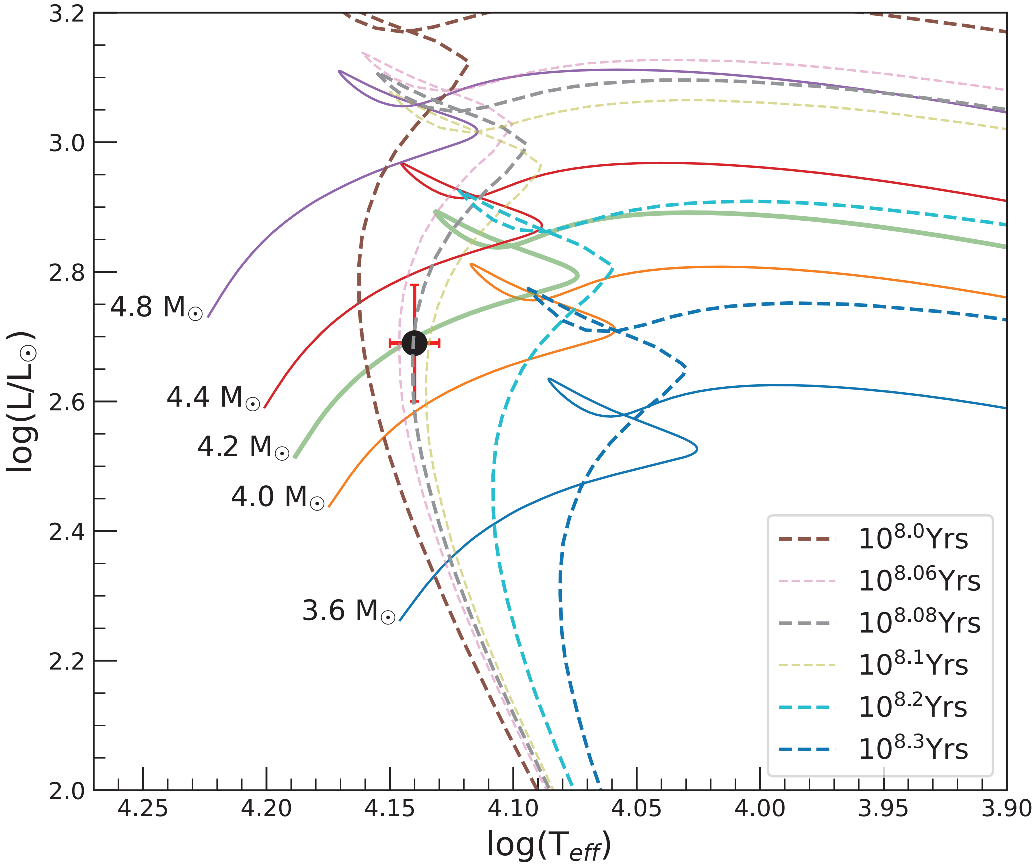

Figure 8. Location of AL Col in the Hertzsprung–Russell (H–R) diagram is marked with a filled black circle. Vertical and horizontal red lines are representing the errors in luminosity and temperature, respectively. Solid lines represent PARSEC evolutionary tracks for stellar masses ranging from 3.6 to $4.6\,M_\odot$, while dashed lines show PARSEC isochrones of different ages, as indicated in the legend.

By comparing the position of the star on the H–R diagram with theoretical isochrones, we estimate its age to be 0.120 ± 0.01 Gyr. This value is approximately twice that reported by Glagolevskij [74] (∼0.055 Gyr), likely due to an underestimation of stellar luminosity in their study. The diagram suggests that the star is situated at the middle of ZAMS and TAMS, slowly approaching the turn-off point, consistent with its derived physical parameters.

A summary of the fundamental parameters of HD 46462, including values obtained in this study and from the literature, is presented in Table 3.

Table 3. Basic parameters of AL Col compiled from both the literature and this study. The reference numbers correspond to the following sources: [1] (Borisov et al. [75]), [2] (Bernhard et al. [39]), [3] (Glagolevskij [74]), [4] (SIMBAD astronomical Database), [5] (McEvoy et al. [73]), [6] (Gaia Collaboration et al. [72]), [7] (van Leeuwen [76]).

Literature		Present Study	
Parameter	**Value**	**Parameter**	**Value**
$T_{\rm eff}$ (K) [1]	12,600 ± 126	$T_{\rm eff}$ (K) (Spectroscopy)	13,814 ± 400
		$T_{\rm eff}$ (K) (SED)	11,750 ± 125
$\log g$ (dex) [1]	3.99 ± 0.03	$\log g$ (dex)	4.09 ± 0.08
$v \sin i$ (km s^{-1}) [1]	19.49 ± 0.74	$v \sin i$ (km s^{-1})	16 ± 1
$P_{\rm rot}$ (d) [2]	10.363	$P_{\rm rot}$ (d)	10.35733
$\log(L/{\rm L}_\odot)$ [3]	2.336	$\log(L/{\rm L}_\odot)$	2.69 ± 0.09
$R/{\rm R}_\odot$ [3]	2.44	$R/{\rm R}_\odot$	3.74 ± 0.48
$M/{\rm M}_\odot$ [3]	3.9	$M/{\rm M}_\odot$	4.2 ± 0.2
Age (Gyrs) [3]	0.055	Age (Gyrs)	0.12 ± 0.01
$m_{\rm v}$ (mag) [4]	7.56		
B-V [4]	−0.1		
$E({\rm B}-{\rm V})$ [5]	0.52		
plx(mas) [6,7]	4.11 ± 0.38 (d = 243 pc)		
	2.93 ± 0.52 (d = 341 pc)		

6. Spot Modeling

Modeling a stellar surface provides crucial insights into surface dynamics and magnetic activity, as starspots co-rotate with the stellar surface and induce brightness modulations modulated by stellar rotation. We reconstructed the *TESS* light curves from sectors 6 and 7 using the BestrAndom StarSpots Model cAlculatioN (BASSMAN; [77])[5] program to perform inverse modeling of starspots and generate stellar surface maps. The required input parameters for BASSMAN include the star's rotation period, $T_{\rm eff}$, radius, and inclination angle (or $v \sin i$). Using a Markov Chain Monte Carlo (MCMC) approach, the program determines spot parameters such as amplitude, size, latitude, and longitude. A three-spot model was adopted, as it provided a better fit to the data than a two-spot configuration.

Once the input parameters are provided, BASSMAN proceeds by positioning the spots on the stellar surface and fitting a model light curve to the observed data. This is accomplished using optimization routines from the scipy library, which iteratively adjust the spot parameters to improve the match between the modeled and observed light curves. The fitting performance is evaluated using correlation coefficients or a reduced χ^2 statistic to determine the model's reliability. If the fit does not converge or yield satisfactory agreement, the algorithm samples a new set of spot parameters and restarts the fitting process. This approach allows BASSMAN to successfully model light curves affected by both magnetic and chemical spots, ultimately providing best-fit parameters that describe the observed brightness variations with high fidelity.

Our results indicate the presence of three cool surface regions. For Sectors 6 and 7, the model yielded a reduced χ^2 of 4.42 and 5.89, along with spot coverage of 1.49 + 1.99 + 1.00 = 4.48% and 1.00 + 2.49 + 1.39 = 4.88% which are consistent with analytically derived spot sizes 5.77% and 5.68%, respectively, using equations [78–80]:

$$T_{spot} = 0.751\, T_{\rm eff} - 3.58 \times 10^{-5} T_{\rm eff}^2 + 808 \tag{6}$$

and

$$\frac{A_{\rm spot}}{A_{\rm star}} = 100\% \times \frac{\Delta F}{F}\left[1 - \left(\frac{T_{\rm spot}}{T_{\rm eff}}\right)\right]^{-1}. \tag{7}$$

The spot configurations, including locations, sizes, and temperature contrasts, are shown in Aitoff projections in Figure 9, and the corresponding parameters are summarized in Table 4. The latitudes of the spots remain almost unchanged, indicating that the spot locations on the stellar surface do not vary significantly. The longitudes differ, as expected, due to the rotation of the object and mapping them at different rotational phases. Even the longitudinal distance between the spots changes noticeably from one sector to another, suggesting differential surface rotation. However, Figure 9 shows that spots 1 and 2 shift slightly towards lower latitudes, while spot 3 shifts towards higher latitudes ($\lesssim 7°$). The contrast of spot 1 changes from sector 6 to sector 7, while the contrasts of spots 2 and 3 remain nearly constant, as indicated by the color bar. These results support the findings from our wavelet analysis. The ∼10-d periodicity and associated harmonics observed in the wavelet maps primarily originate from spots 1 and 2. In contrast, the polar location of spot 3 has little impact on the light curve morphology. Although the individual spot sizes vary between the two sectors, the total spot coverage does not change significantly (approximately ∼0.4%). This signifies that spot modulation might be present. The value of $\chi^2 > 1$ suggests the presence of small-scale variations with timescales shorter than the stellar rotation period, resulting in features in the light curve that the model light curves do not fully capture. Nevertheless, the high signal-to-noise ratio (SNR) values confirm that the modeled light curve is robust and reliable, which is consistent with the quality of the TESS light curves.

In the wavelet diagram, persistent horizontal bands correspond to stable periodic signals, indicative of coherent stellar rotation. Variations in dominant periodicities or light curve morphology over time may reflect evolving spot distributions, longitudinal migration of active regions, or differential rotation. In this case, the light curve morphology remains relatively unchanged across sectors, consistent with modest changes in spot configuration and coverage, particularly in longitudinal positions.

In this modeling, BASSMAN assumes spots are spherical on the stellar surface. During the modeling of a single sector of TESS observations, spots are assumed to be static, i.e., they do not evolve in size, position, or contrast within that time frame. The only parameter that changes over time is the longitude, due to stellar rotation. Due to the degeneracy between spot contrast and size in single-band photometry, the model uses spot amplitude, i.e., the amount of flux blocked, rather than contrast. Spot amplitude is defined based on the range of flux variation; size is estimated based on the ingress and egress duration. Markov Chain Monte Carlo (MCMC) sampling is used to optimize the fit of the spot model to the observed light curve. So, small spot size with proper amplitude can generate significant variability in the light curve. Although this modeling approach does not convincingly establish that the small spots alone are responsible for the photometric modulation, and CP stars have been known to have larger spots, we have conducted a preliminary analysis of spot location on the stellar surface here. For example, if the contrast were lower for the spots, their size would increase, which could be the case for these CP stars. The 'size' in our tables refers to the area needed to reproduce the observed light curve modulation under a reasonable assumed contrast derived from empirical relations. We emphasize that while the individual spots may be relatively small, the total spotted area on the visible hemisphere, combined with high contrast and favorable geometries (i.e., near-equatorial spots and favorable inclination), is sufficient to produce the observed light curve modulations. Our modeling also reproduces the phase and shape of the modulation across multiple TESS sectors, reinforcing the credibility of the fit. We acknowledge that, due to the degeneracy between spot size and contrast in single-color data, alternative models with slightly larger, lower-contrast spots cannot be fully ruled out. However, the solutions presented represent the best-fit results of a Bayesian sampling process (via MCMC) within a physically motivated parameter space, constrained by the theoretical values (Equations (6) and (7)), observed flux variations, and stellar parameters.

It is important to note that modeling stellar surface features is inherently degenerate [81], as multiple spot configurations can produce light curves that are nearly indistinguishable. Therefore, any derived solution must be interpreted cautiously, with due consideration for uncertainties and degeneracies. While a single spot configuration may not fully capture the true surface geometry, consistent modeling across multiple light curves can reveal meaningful trends and correlations that reflect real physical processes on the stellar surface. Lastly, the BASSMAN code is typically employed for investigating surface spot distributions in late-type stars. In the present study, we extend its application to AL Col, a massive star. Given the fundamental differences in a spot's origin between late-type and massive stars, the results derived from this approach should be interpreted with due caution.

Table 4. Comprehensive spot model parameters and associated diagnostics for AL Col.

Sec. No.	Spot No.	Lat. (deg)	Long. (deg)	Spot Size (%)	Analytical Spot Size (%)	χ^2	SNR
6	1	49.09	−120.05	1.49	5.77	4.42	1657.84
	2	20.86	106.53	1.99			
	3	−65.32	−85.27	1.00			
7	1	42.98	−24.91	1.00	5.68	5.89	1455.62
	2	23.92	−157.87	2.49			
	3	−61.24	149.79	1.39			

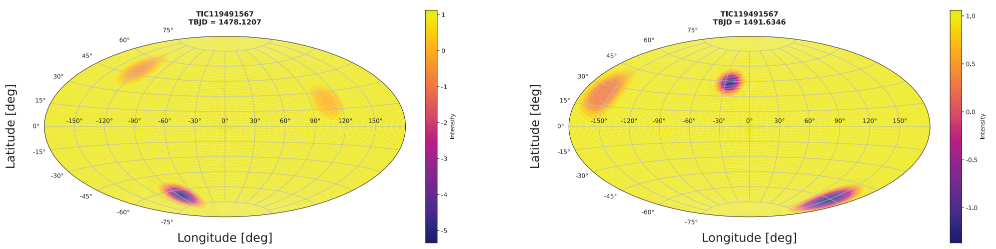

Figure 9. Spot locations, sizes, and contrasts are illustrated using Aitoff projections for sectors 6 (**left panel**) and 7 (**right panel**). Dark regions indicate the presence of spots, and the strength of the spots has been scaled by the color map shown in the figures.

7. Discussion and Conclusions

This study presents a comprehensive photometric and high-resolution spectroscopic analysis of the Ap/Bp star AL Col (HD 46462). Frequency analysis of the *TESS* light curve revealed a dominant peak at $\nu = 0.09655\,\mathrm{d}^{-1}$, corresponding to a rotational period of $P_{\mathrm{rot}} = 10.35733$ d, in close agreement with the value of $P_{\mathrm{rot}} = 10.363$ d reported by Bernhard et al. [39]. The phase-folded light curve exhibits a clear quasi-sinusoidal shape, characteristic of α^2 CVn-type variability commonly seen in Ap/Bp stars. Assuming rigid-body rotation and adopting a spectroscopically derived $v \sin i$ of $16\,\mathrm{km\,s^{-1}}$, we estimate an inclination angle of the stellar rotation axis of $i \approx 60^\circ$.

A notable discrepancy was noticed between the effective temperature derived from SED fitting ($T_{\mathrm{eff}} = 11{,}750$ K) and that obtained from high-resolution spectroscopic analysis using the SME tool ($T_{\mathrm{eff}} = 13{,}814 \pm 400$ K). This is common in CP stars because of flux redistribution in the presence of chemical spots. Flux are being absorbed (maximum in ultraviolet) by chemical elements present in the photosphere and getting emitted in a longer wavelength (generally in IR), which changes the shape of the SED [82]. This highlights the importance of detailed spectral synthesis for accurate atmospheric parameter determination in CP stars. The core of the strong lines like the Balmer regions and the Fe line in the Mg triplet region are not properly fitted. NLTE analysis is one of the possible solutions for fitting the core region of Balmer lines. Also, in the Hα region, the presence of telluric lines in the wings occasionally leads to poor agreement between the observed and synthetic spectra. However, for metal lines (e.g., Fe II in Figure 6), the line profile of the core region varies (spikes at the center) due to chemical spots. To model these line profile variations, time-series spectroscopy is essential.

Using synthetic spectrum fitting, we derived abundances for 25 chemical elements across various ionization stages. Our results show that O II, Mg II, S II, and Ca II have abundances close to solar, while He I is significantly underabundant by about 0.5 dex, possibly due to diffusion processes [83]. Rare earth elements (REEs), on the other hand, exhibit substantial overabundances up to 6 dex, consistent with the typical chemical peculiarities observed in Ap/Bp stars.

At $T_{\rm eff} = 13{,}814 \pm 400$ K and $\log g = 4.09 \pm 0.08$ dex, the atmosphere lies in a regime where departures from the LTE are expected. Nevertheless, all abundances reported here were derived strictly under LTE, and the formal uncertainties quoted in Table 2 do not include any allowance for NLTE offsets. Literature grids predict downward corrections of $\approx$0.10–0.15 dex for He I triplet lines and up to -0.20 dex for C II/N II/O II lines [84,85]. Mg II and Si II/III resonance lines are expected to shift upward by +0.05–0.10 dex, whereas Fe II and Cr II remain within $|\Delta \log \epsilon| \lesssim 0.05$ dex thanks to efficient collisional coupling [86–88]. For the observed rare-earth ions, Y II, Ce II/III, Pr II/III, Nd II/III, and Eu III, published NLTE studies suggest mainly negative corrections of 0.05–0.15 dex [89,90]. These potential systematic offsets will be explored in a future re-analysis employing full NLTE spectrum synthesis; until then, the LTE abundances and their errors should be regarded as lower-limit uncertainties.

Although magnetic measurements were not obtained in the present study, it is well established that magnetic fields in Ap/Bp stars suppress convective and turbulent motions, enabling the radiative accumulation of heavy elements like REEs in the photosphere. Future spectropolarimetric observations are essential to constrain the magnetic field geometry and understand its role in shaping the observed abundance anomalies.

A significant discrepancy was also noted between the abundances derived from Si II and Si III lines, consistent with the expected vertical stratification of chemical elements in magnetic atmospheres. In particular, Si III lines yield a considerably higher abundance than Si II, a common feature in magnetic chemically peculiar stars (e.g., [91]). This underscores the need for future non-LTE analyses and stratified atmospheric modeling to better understand the vertical abundance gradients.

By locating our target in the H–R diagram, we estimate the stellar mass to be $M = 4.0 \pm 0.4\,{\rm M}_{\odot}$ and the radius to be $R = 3.74 \pm 0.48\,{\rm R}_{\odot}$, indicating that the star has evolved slightly beyond the main sequence. The isochrone fitting suggests an age of 0.12 ± 0.01 Gyr.

To probe surface activity, we modeled starspots using *TESS* time-series photometry from sectors 6 and 7 via the BASSMAN code. The best-fit three-spot model revealed the presence of cool surface features at different longitudes and latitudes. Temporal evolution in spot sizes and contrasts, most notably an increase in the strength of one spot, suggests the presence of differential rotation and evolving surface magnetic activity. These findings are tentative though corroborated with our wavelet analysis, which detected persistent periodicities consistent with rotational modulation by surface spots.

Collectively, these results provide a coherent picture of AL Col as a moderately evolved magnetic Ap/Bp star exhibiting strong chemical peculiarities, rotational modulation due to starspots, and potential surface differential rotation. Follow-up spectropolarimetric and non-LTE spectroscopic analyses will be instrumental in refining our understanding of its magnetic topology and atmospheric structure.

Author Contributions: Conceptualization, S.C.G., S.J., A.D. and J.A.R.G.; Methodology, S.C.G., S.J., S.G. and M.S.; Software, S.C.G., S.G., A.D. and O.T.; Validation, S.C.G., S.J., O.M., H.P.S. and S.S.B.; Formal analysis, S.C.G., S.G., A.D., O.T., N.E.C.-T. and K.T.; Investigation, S.C.G., S.J., S.G., A.D., O.T., M.S., J.A.R.G., N.E.C.-T., H.P.S. and S.S.B.; Resources, S.C.G.; Writing—original draft, S.C.G., S.J., J.A.R.G. and O.M.; Writing—review & editing, S.C.G., S.J., S.G., A.D., O.T., M.S., J.A.R.G., N.E.C.-T., O.M., H.P.S., K.T. and S.S.B.; Visualization, S.C.G., S.J., O.T. and J.A.R.G.; Supervision, S.J. and S.S.B.; Project administration, S.J.; Funding acquisition, S.J., O.M. and K.T. All authors have read and agreed to the published version of the manuscript.

Funding: The authors acknowledge the financial support received from the BRICS grant under the project DST/ICD/BRICS/Call-5/SAPTARISI/2023 (G). J.A.R.G. acknowledges support by Vicerrectoría de Investigación y Desarrollo (VRID) Postdoctoral DICA N181/23. OT acknowledges financial support from the SEISMIC project, the Max Planck–Humboldt Research Unit in collaboration with the Max Planck Institutes for Astrophysics (MPA) and Solar System Research (MPS), and Kyambogo University, as well as from the International Science Programme (ISP) at Uppsala University. AD acknowledges the financial support received from the DST-INSPIRE Fellowship Programme (DST/INSPIRE Fellowship/2020/IF200245). KT acknowledges support by the National Natural Science Foundation of China (NSFC) under grant no. 12261141689.

Data Availability Statement: The data presented in this study are available on request from the corresponding author.

Acknowledgments: This study uses data from the TESS missions that are accessible at the Mikulski Archive for Space Telescopes (MAST) operated by NASA. The wavelet maps and autocorrelation function were created using the code provided by Rafel Garcia and Savita Mathur. The spectroscopic analysis for this study is based on the data available in the European Southern Observatory (ESO) Science Archive Facility under ESO Prog ID 080.C-0032(A).

Conflicts of Interest: The authors declare no conflicts of interest.

Notes

1. https://archive.eso.org/scienceportal/home, accessed on 8 December 2008.
2. http://cdsarc.u-strasbg.fr/viz-bin/Cat?II/168, accessed on 1 August 2025, https://cdsarc.unistra.fr/viz-bin/cat/I/327, accessed on 1 August 2025.
3. http://svo2.cab.inta-csic.es/vocats/cmc15/, accessed on 1 August 2025.
4. http://www.astro.uu.se/~oleg/binmag.html, accessed on 1 August 2025.
5. https://github.com/KBicz/BASSMAN, accessed on 1 August 2025.

References

1. Lueftinger, T.; Wade, G.A.; Weiss, W.W. Magnetic Fields in B, (peculiar) A, and F stars recent results from MuSiCoS Data. In *Proceedings of the EAS Publications Series*; Arnaud, J., Meunier, N., Eds.; EAS Publications Series; Cambridge University Press: Cambridge, UK, 2003; Volume 9, p. 249.
2. Lehmann, H.; Tkachenko, A.; Fraga, L.; Tsymbal, V.; Mkrtichian, D.E. The helium weak silicon star HR 7224. II. Doppler Imaging analysis. *Astron. Astrophys.* **2007**, *471*, 941–949. [CrossRef]
3. Preston, G.W. The chemically peculiar stars of the upper main sequence. *Annu. Rev. Astron. Astrophys.* **1974**, *12*, 257–277. [CrossRef]
4. Maitzen, H.M. A note on the relation between magnetic fields and the lambda 5200 feature in helium weak-stars. *Astron. Astrophys.* **1984**, *138*, 493–494.
5. Paunzen, E. The λ Bootis stars. In Proceedings of the A-Star Puzzle, IAU Symposium, Přerov, Czech Republic, 5–10 July 2004; Zverko, J., Ziznovsky, J., Adelman, S.J., Weiss, W.W., Eds.; Cambridge University Press: Cambridge, UK, 2004; Volume 224, pp. 443–450. [CrossRef]
6. Ghazaryan, S.; Alecian, G.; Hakobyan, A.A. Statistical Analysis of the New Catalogue of CP Stars. *Commun. Byurakan Astrophys. Obs.* **2018**, *65*, 223–227. [CrossRef]
7. Aurière, M.; Wade, G.A.; Silvester, J.; Lignières, F.; Bagnulo, S.; Bale, K.; Dintrans, B.; Donati, J.F.; Folsom, C.P.; Gruberbauer, M.; et al. Weak magnetic fields in Ap/Bp stars. Evidence for a dipole field lower limit and a tentative interpretation of the magnetic dichotomy. *Astron. Astrophys.* **2007**, *475*, 1053–1065. [CrossRef]

8. Kochukhov, O. The spots on Ap stars. In Proceedings of the Physics of Sun and Star Spots, IAU Symposium, La Palma, Spain, 22–26 August 2010; Prasad Choudhary, D., Strassmeier, K.G., Eds.; Cambridge University Press: Cambridge, UK, 2011; Volume 273, pp. 249–255. [CrossRef]
9. Shultz, M.; Wade, G.A.; Alecian, E.; Neiner, C.; Kholtygin, A.; Monin, D.; Sikora, J.; Landstreet, J.D.; Bohlender, D.; Bord, D.J.; et al. The incidence and properties of magnetic fields in early B-type stars. *Mon. Not. R. Astron. Soc.* **2019**, *490*, 274–296. [CrossRef]
10. Braithwaite, J.; Spruit, H.C. Fossil magnetic fields in stars: Origin and evolution. *Proc. Int. Astron. Union* **2014**, *302*, 338–347. [CrossRef]
11. Michaud, G. Diffusion Processes in Peculiar a Stars. *Astrophys. J.* **1970**, *160*, 641. [CrossRef]
12. Richer, J.; Michaud, G.; Turcotte, S. Implications of Diffusion for the Surface Composition of A and B Stars. *ApJ* **2005**, *625*, 548–556. [CrossRef]
13. Michaud, G.; Alecian, G.; Richer, J. *Atomic Diffusion in Stars*; Springer: Berlin/Heidelberg, Germany, 2015. [CrossRef]
14. Alecian, E.; Villebrun, F.; Grunhut, J.; Hussain, G.; Neiner, C.; Wade, G.A. Fossil magnetic fields in intermediate-mass and massive stars *EAS Publ. Ser.* **2019**, *82*, 345–335. [CrossRef]
15. Babcock, H.W. Stellar magnetic fields and rotation. *Observatory* **1949**, *69*, 191–192.
16. Stibbs, D.W.N. A Light Curve for the Magnetic Variable Star HD125248. *Nature* **1950**, *165*, 195. [CrossRef]
17. Shulyak, D.; Krtička, J.; Mikulášek, Z.; Kochukhov, O.; Lüftinger, T. Modelling the light variability of the Ap star ϵ Ursae Majoris. *Astron. Astrophys.* **2010**, *524*, A66. [CrossRef]
18. Kochukhov, O.; Wade, G.A.; Shulyak, D. Zeeman Doppler imaging of magnetic Ap stars: A practical approach. *Astron. Astrophys.* **2012**, *542*, A116. [CrossRef]
19. Kurtz, D.W.; Elkin, V.G.; Cunha, M.S.; Mathys, G.; Hubrig, S.; Wolff, B.; Savanov, I. The discovery of 8.0-min radial velocity variations in the strongly magnetic cool Ap star HD154708, a new roAp star. *Mon. Not. R. Astron. Soc.* **2006**, *372*, 286–292. [CrossRef]
20. Saio, H.; Gruberbauer, M.; Weiss, W.W.; Matthews, J.M.; Ryabchikova, T. Pulsation models for the roAp star HD 134214. *Mon. Not. R. Astron. Soc.* **2012**, *420*, 283–290. [CrossRef]
21. Joshi, S.; Joshi, Y.C. Asteroseismology of Pulsating Stars. *J. Astrophys. Astron.* **2015**, *36*, 33–80. [CrossRef]
22. Holdsworth, D.L.; Cunha, M.S.; Kurtz, D.W.; Antoci, V.; Hey, D.R.; Bowman, D.M.; Kobzar, O.; Buzasi, D.L.; Kochukhov, O.; Niemczura, E.; et al. TESS cycle 1 observations of roAp stars with 2-min cadence data. *Mon. Not. R. Astron. Soc.* **2021**, *506*, 1073–1110. [CrossRef]
23. Kurtz, D.W. Asteroseismology Across the Hertzsprung-Russell Diagram. *Annu. Rev. Astron. Astrophys.* **2022**, *60*, 31–71. [CrossRef]
24. Martinez, P.; Kurtz, D.W.; Kauffmann, G.M. The Cape rapidly oscillating star survey-I. First results. *Mon. Not. R. Astron. Soc.* **1991**, *250*, 666. [CrossRef]
25. Martinez, P.; Kurtz, D.W.; Ashoka, B.N.; Chaubey, U.S.; Girish, V.; Gupta, S.K.; Joshi, S.; Kasturirangan, K.; Sagar, R.; Seetha, S. The Naini Tal—Cape survey for pulsations in chemically peculiar A-type stars. I. Methods and preliminary results. *Astron. Astrophys.* **2001**, *371*, 1048–1055. [CrossRef]
26. Joshi, S.; Girish, V.; Sagar, R.; Kurtz, D.W.; Martinez, P.; Kumar, B.; Seetha, S.; Ashoka, B.N.; Zhou, A. Discovery of unusual pulsations in the cool, evolved Am stars HD 98851 and HD 102480. *Mon. Not. R. Astron. Soc.* **2003**, *344*, 431–438. [CrossRef]
27. Joshi, S.; Mary, D.L.; Martinez, P.; Kurtz, D.W.; Girish, V.; Seetha, S.; Sagar, R.; Ashoka, B.N. The Nainital-Cape Survey. II. Report for pulsation in five chemically peculiar A-type stars and presentation of 140 null results. *Astron. Astrophys.* **2006**, *455*, 303–313. [CrossRef]
28. Joshi, S.; Mary, D.L.; Chakradhari, N.K.; Tiwari, S.K.; Billaud, C. The Nainital-Cape Survey. III. A search for pulsational variability in chemically peculiar stars. *Astron. Astrophys.* **2009**, *507*, 1763–1784. [CrossRef]
29. Joshi, S.; Ryabchikova, T.; Kochukhov, O.; Sachkov, M.; Tiwari, S.K.; Chakradhari, N.K.; Piskunov, N. Time-resolved photometric and spectroscopic analysis of the luminous Ap star HD103498. *Mon. Not. R. Astron. Soc.* **2010**, *401*, 1299–1307. [CrossRef]
30. Joshi, S.; Semenko, E.; Martinez, P.; Sachkov, M.; Joshi, Y.C.; Seetha, S.; Chakradhari, N.K.; Mary, D.L.; Girish, V.; Ashoka, B.N. A spectroscopic analysis of the chemically peculiar star HD 207561. *Mon. Not. R. Astron. Soc.* **2012**, *424*, 2002–2008. [CrossRef]
31. Joshi, S.; Martinez, P.; Chowdhury, S.; Chakradhari, N.K.; Joshi, Y.C.; van Heerden, P.; Medupe, T.; Kumar, Y.B.; Kuhn, R.B. The Nainital-Cape Survey. IV. A search for pulsational variability in 108 chemically peculiar stars. *Astron. Astrophys.* **2016**, *590*, A116. [CrossRef]
32. Joshi, S.; Semenko, E.; Moiseeva, A.; Sharma, K.; Joshi, Y.C.; Sachkov, M.; Singh, H.P.; Yerra, B.K. High-resolution Spectroscopy and Spectropolarimetry of Selected δ-Sct Pulsating Variables. *Mon. Not. R. Astron. Soc.* **2017**, *467*, 633–645. [CrossRef]
33. Joshi, S.; Trust, O.; Semenko, E.; Williams, P.E.; Lampens, P.; De Cat, P.; Vermeylen, L.; Holdsworth, D.L.; García, R.A.; Mathur, S.; et al. Study of chemically peculiar stars–I. High-resolution spectroscopy and K2 photometry of Am stars in the region of M44. *Mon. Not. R. Astron. Soc.* **2022**, *510*, 5854. [CrossRef]
34. Buysschaert, B.; Neiner, C.; Martin, A.J.; Oksala, M.E.; Aerts, C.; Tkachenko, A.; Alecian, E.; MiMeS Collaboration. Magnetic characterization and variability study of the magnetic SPB star o Lupi. *Astron. Astrophys.* **2019**, *622*, A67. [CrossRef]

35. Holdsworth, D.L.; Cunha, M.S.; Lares-Martiz, M.; Kurtz, D.W.; Antoci, V.; Barceló Forteza, S.; De Cat, P.; Derekas, A.; Kayhan, C.; Ozuyar, D.; et al. TESS Cycle 2 observations of roAp stars with 2-min cadence data. *Mon. Not. R. Astron. Soc.* **2023**, *527*, 9548–9580. [CrossRef]
36. Bagnulo, S.; Landstreet, J.D.; Power, J.; Fossati, L.; Wade, G.A.; Donati, J.-F.; Grunhut, J.H.; Neiner, C.; Oksala, M.E.; Owocki, S.P.; et al. Magnetic chemically peculiar stars in the TESS era: Rotation and magnetic field from photometry and spectroscopy. *Astron. Astrophys.* **2023**, *671*, A154. [CrossRef]
37. Wade, G.A.; Alecian, E.; Grunhut, J.H.; Bohlender, D.A.; Bouret, J.-C.; Cohen, D.H.; David-Uraz, A.; Folsom, C.P.; Henrichs, H.F.; Kochukhov, O.; et al. The MiMeS survey of magnetism in massive stars: Introduction and overview. *Proc. Int. Astron. Union* **2014**, *302*, 265–270. [CrossRef]
38. Sikora, J.; Wade, G.A.; Power, J. Magnetism in Ap/Bp stars with rotational periods longer than 100 d. *Mon. Not. R. Astron. Soc.* **2020**, *499*, 5049–5068. [CrossRef]
39. Bernhard, K.; Hümmerich, S.; Paunzen, E. New and improved rotational periods of magnetic CP stars from ASAS-3, KELT, and MASCARA data. *Mon. Not. R. Astron. Soc.* **2020**, *493*, 3293–3330. [CrossRef]
40. Lightkurve Collaboration; Cardoso, J.; Hedges, C.; Gully-Santiago, M.; Saunders, N.; Cody, A.; Barclay, T.; Hall, O.; Sagear, S.; Turtelboom, E.; et al. *Lightkurve: Kepler and TESS Time Series Analysis in Python*; Astrophysics Source Code Library (ascl: 1812.013): Online, 2018.
41. Lenz, P.; Breger, M. Period04 User Guide. *CoAst* **2005**, *146*, 53–136. [CrossRef]
42. Baran, A.S.; Koen, C. A Detection Threshold in the Amplitude Spectra Calculated from TESS Time-Series Data. *Acta Astron.* **2021**, *71*, 113–121. [CrossRef]
43. Bravo, J.P.; Roque, S.; Estrela, R.; Leão, I.C.; De Medeiros, J.R. Wavelets: A powerful tool for studying rotation, activity, and pulsation in Kepler and CoRoT stellar light curves. *Astron. Astrophys.* **2014**, *568*, A34. [CrossRef]
44. Mathur, S.; García, R.A.; Ballot, J.; Ceillier, T.; Salabert, D.; Metcalfe, T.S.; Régulo, C.; Jiménez, A.; Bloemen, S. Magnetic activity of F stars observed by Kepler. *Astron. Astrophys.* **2014**, *562*, A124. [CrossRef]
45. Ochsenbein, F.; Bauer, P.; Marcout, J. The VizieR database of astronomical catalogues. *Astron. Astrophys. Suppl. Ser.* **2000**, *143*, 23–32. [CrossRef]
46. Paunzen, E. A new catalogue of Strömgren-Crawford uvbyβ photometry. *Astron. Astrophys.* **2015**, *580*, A23. [CrossRef]
47. Høg, E.; Fabricius, C.; Makarov, V.V.; Bastian, U.; Schwekendiek, P.; Wicenec, A.; Urban, S.; Corbin, T.; Wycoff, G. Construction and verification of the Tycho-2 Catalogue. *Astron. Astrophys.* **2000**, *357*, 367–386.
48. Gaia Collaboration; Montegriffo, P.; Bellazzini, M.; De Angeli, F.; Andrae, R.; Barstow, M.A.; Bossini, D.; Bragaglia, A.; Burgess, P.W.; Cacciari, C.; et al. Gaia Data Release 3: The Galaxy in your preferred colours. Synthetic photometry from Gaia low-resolution spectra. *arXiv* **2022**, arXiv:2206.06215.
49. Gaia Collaboration; Prusti, T.; de Bruijne, J.H.J.; Brown, A.G.A.; Vallenari, A.; Babusiaux, C.; Bailer-Jones, C.A.L.; Bastian, U.; Biermann, M.; Evans, D.W.; et al. The Gaia mission. *Astron. Astrophys.* **2016**, *595*, A1. [CrossRef]
50. Skrutskie, M.F.; Cutri, R.M.; Stiening, R.; Weinberg, M.D.; Schneider, S.; Carpenter, J.M.; Beichman, C.; Capps, R.; Chester, T.; Elias, J.; et al. The Two Micron All Sky Survey (2MASS). *Astron. J.* **2006**, *131*, 1163–1183. [CrossRef]
51. Wright, E.L.; Eisenhardt, P.R.M.; Mainzer, A.K.; Ressler, M.E.; Cutri, R.M.; Jarrett, T.; Kirkpatrick, J.D.; Padgett, D.; McMillan, R.S.; Skrutskie, M.; et al. The Wide-field Infrared Survey Explorer (WISE): Mission Description and Initial On-orbit Performance. *Astron. J.* **2010**, *140*, 1868–1881. [CrossRef]
52. Fouqué, P.; Chevallier, L.; Cohen, M.; Galliano, E.; Loup, C.; Alard, C.; de Batz, B.; Bertin, E.; Borsenberger, J.; Cioni, M.R.; et al. An absolute calibration of DENIS (deep near infrared southern sky survey). *Astron. Astrophys. Suppl. Ser.* **2000**, *141*, 313–317. [CrossRef]
53. Epchtein, N.; Deul, E.; Derriere, S.; Borsenberger, J.; Egret, D.; Simon, G.; Alard, C.; Balázs, L.G.; de Batz, B.; Cioni, M.R.; et al. A preliminary database of DENIS point sources. *Astron. Astrophys.* **1999**, *349*, 236–242.
54. Mainzer, A.; Bauer, J.; Cutri, R.M.; Grav, T.; Masiero, J.; Beck, R.; Clarkson, P.; Conrow, T.; Dailey, J.; Eisenhardt, P.; et al. Initial Performance of the NEOWISE Reactivation Mission. *Astrophys. J.* **2014**, *792*, 30. [CrossRef]
55. Pakhomov, Y.; Piskunov, N.; Ryabchikova, T. VALD3: Current developments. *arXiv* **2017**, arXiv:1710.10854. [CrossRef]
56. Wehrhahn, A.; Piskunov, N.; Ryabchikova, T. PySME: Spectroscopy Made Easier. *Astron. Astrophys.* **2023**, *671*, A171. [CrossRef]
57. Castelli, F.; Kurucz, R.L. New Grids of ATLAS9 Model Atmospheres. *arXiv* **2004**, arXiv:astro-ph/0405087. [CrossRef]
58. Kochukhov, O. *BinMag: Widget for Comparing Stellar Observed with Theoretical Spectra*; Astrophysics Source Code Library: Online, 2018; p. ascl-1805.
59. Tkachenko, A. Grid search in stellar parameters: A software for spectrum analysis of single stars and binary systems. *Astron. Astrophys.* **2015**, *581*, A129. [CrossRef]
60. Dileep, A.; Joshi, S.; Alexeeva, S.; Kochukhov, O.; Semenko, E.; De Cat, P.; Zúñiga-Fernández, S.; Trust, O.; Pollard, K.; Crause, L.; et al. Chemical abundances and doppler imaging of the Ap Si/He-wk star HD 100357. *Mon. Not. R. Astron. Soc.* **2025**, staf1247. [CrossRef]

61. Asplund, M.; Amarsi, A.M.; Grevesse, N. The chemical make-up of the Sun: A 2020 vision. *Astron. Astrophys.* **2021**, *653*, A141. [CrossRef]
62. Mashonkina, L.; Gehren, T.; Shi, J.R.; Korn, A.J.; Grupp, F. Non-LTE line formation for Fe and Ca in late-type stars–I. Statistical equilibrium of neutral and singly-ionised species. *Astron. Astrophys.* **2011**, *528*, A87. [CrossRef]
63. Przybilla, N.; Butler, K.; Becker, S.R.; Kudritzki, R.P.; Venn, K.A. Non-LTE line-formation for hydrogen and helium in early-type stars—II. The line spectrum of the B8 IV star HD 160762. *Astron. Astrophys.* **2001**, *369*, 1009. [CrossRef]
64. Ryabchikova, T.; Leone, F.; Kochukhov, O. Vertical abundance stratification in peculiar A-type stars: Silicon in 10 Aql. *Astron. Astrophys.* **2005**, *438*, 973. [CrossRef]
65. Romanovskaya, E.V.; Kochukhov, O.; Ryabchikova, T. Stratification and Non-LTE Effects in the Slowly Rotating Ap Star BD +00°1659. *Astron. Astrophys.* **2024**, *670*, A45.
66. Kochukhov, O.; Ryabchikova, T.; Weiss, W.W.; Piskunov, N. Discovery of a Magnetic Field in the Rapidly Oscillating Ap Star HD 99563. *Nature* **2007**, *450*, 633.
67. Hubeny, I.; Lanz, T. Non-LTE line-blanketed model atmospheres of hot stars. 1: Hybrid complete linearization/accelerated lambda iteration method. *Astrophys. J.* **1995**, *439*, 875. [CrossRef]
68. Butler, K.; Giddings, J. *Newsletter on Analysis of Astronomical Spectra, No. 9*; Technical Report; University of London: London, UK, 1985.
69. Bressan, A.; Marigo, P.; Girardi, L.; Salasnich, B.; Dal Cero, C.; Rubele, S.; Nanni, A. PARSEC: Stellar tracks and isochrones with the PAdova and TRieste Stellar Evolution Code. *Mon. Not. R. Astron. Soc.* **2012**, *427*, 127–145. [CrossRef]
70. Hubrig, S.; North, P.; Mathys, G. Magnetic AP Stars in the Hertzsprung-Russell Diagram. *Astrophys. J.* **2000**, *539*, 352–363. [CrossRef]
71. Torres, G. On the Use of Empirical Bolometric Corrections for Stars. *Astron. J.* **2010**, *140*, 1158–1162. [CrossRef]
72. Gaia Collaboration; Brown, A.G.A.; Vallenari, A.; Prusti, T.; de Bruijne, J.H.J.; Babusiaux, C.; Biermann, M.; Creevey, O.L.; Evans, D.W.; Eyer, L.; et al. Gaia Early Data Release 3. Summary of the contents and survey properties. *Astron. Astrophys.* **2021**, *649*, A1. [CrossRef]
73. McEvoy, C.M.; Smoker, J.V.; Dufton, P.L.; Smith, K.T.; Kennedy, M.B.; Keenan, F.P.; Lambert, D.L.; Welty, D.E.; Lauroesch, J.T. Early-type stars observed in the ESO UVES Paranal Observatory Project - V. Time-variable interstellar absorption. *Mon. Not. R. Astron. Soc.* **2015**, *451*, 1396–1412. [CrossRef]
74. Glagolevskij, Y.V. On Properties of Main Sequence Magnetic Stars. *Astrophys. Bull.* **2019**, *74*, 66–79. [CrossRef]
75. Borisov, S.B.; Chilingarian, I.V.; Rubtsov, E.V.; Ledoux, C.; Melo, C.; Grishin, K.A.; Katkov, I.Y.; Goradzhanov, V.S.; Afanasiev, A.V.; Kasparova, A.V.; et al. New Generation Stellar Spectral Libraries in the Optical and Near-infrared. I. The Recalibrated UVES-POP Library for Stellar Population Synthesis. *Astrophys. J. Suppl. Ser.* **2023**, *266*, 11. [CrossRef]
76. van Leeuwen, F. Validation of the new Hipparcos reduction. *Astron. Astrophys.* **2007**, *474*, 653–664. [CrossRef]
77. Bicz, K.; Falewicz, R.; Pietras, M.; Siarkowski, M.; Preś, P. Starspot Modeling and Flare Analysis on Selected Main-sequence M-type Stars. *Astrophys. J.* **2022**, *935*, 102. [CrossRef]
78. Notsu, Y.; Shibayama, T.; Maehara, H.; Notsu, S.; Nagao, T.; Honda, S.; Ishii, T.T.; Nogami, D.; Shibata, K. Superflares on Solar-type Stars Observed with Kepler II. Photometric Variability of Superflare-generating Stars: A Signature of Stellar Rotation and Starspots. *Astrophys. J.* **2013**, *771*, 127. [CrossRef]
79. Shibata, K.; Isobe, H.; Hillier, A.; Choudhuri, A.R.; Maehara, H.; Ishii, T.T.; Shibayama, T.; Notsu, S.; Notsu, Y.; Nagao, T.; et al. Can Superflares Occur on Our Sun? *Publ. Astron. Soc. Jpn.* **2013**, *65*, 49. [CrossRef]
80. Notsu, Y.; Maehara, H.; Honda, S.; Hawley, S.L.; Davenport, J.R.A.; Namekata, K.; Notsu, S.; Ikuta, K.; Nogami, D.; Shibata, K. Do Kepler Superflare Stars Really Include Slowly Rotating Sun-like Stars?—Results Using APO 3.5 m Telescope Spectroscopic Observations and Gaia-DR2 Data. *Astrophys. J.* **2019**, *876*, 58. [CrossRef]
81. Walkowicz, L.M.; Basri, G.; Valenti, J.A. The Information Content in Analytic Spot Models of Broadband Precision Light Curves. *Astrophys. J. Suppl. Ser.* **2013**, *205*, 17. [CrossRef]
82. Leone, F.; Catalano, F.A. The overall flux distribution of magnetic chemically peculiar stars. *Astron. Astrophys.* **1991**, *242*, 199.
83. Bailey, J.D.; Landstreet, J.D.; Bagnulo, S. Discovery of secular variations in the atmospheric abundances of magnetic Ap stars. *Astron. Astrophys.* **2014**, *561*, A147. [CrossRef]
84. Przybilla, N. Non-LTE line formation for neutral helium in early-type stars. *Astron. Astrophys.* **2005**, *443*, 293–303. [CrossRef]
85. Nieva, M.F.; Przybilla, N. Present-day cosmic abundances: A comprehensive study of nearby early B-type stars. *Astron. Astrophys.* **2012**, *539*, A143. [CrossRef]
86. Lind, K.; Bergemann, M.; Asplund, M. Non-LTE line formation of Fe in late-type stars—I. Standard stars with 1D and 3D model atmospheres. *Mon. Not. R. Astron. Soc.* **2012**, *427*, 50–60. [CrossRef]
87. Mashonkina, L.I.; Sitnova, T.N.; Pakhomov, Y.V. Non-LTE abundance determinations for silicon in A–B-type stellar atmospheres. *Astron. Lett.* **2016**, *42*, 606–617. [CrossRef]

88. Sitnova, T.N.; Mashonkina, L.I.; Pakhomov, Y.V. Non-LTE line formation for Sii–iii in A–B stars and the origin of Siii emission in *iota* Her. *Mon. Not. R. Astron. Soc.* **2020**, *493*, 6095–6108. [CrossRef]
89. Mashonkina, L.; Ryabchikova, T.; Ryabtsev, A. NLTE ionisation equilibrium of Nd II and Nd III in cool A and Ap stars. *Astron. Astrophys.* **2005**, *441*, 309–318. [CrossRef]
90. Ryabchikova, T.; Piskunov, N.; Kurucz, R.L. A database of rare-earth element line data and its application to Ap-star spectra. *Mon. Not. R. Astron. Soc.* **2015**, *447*, 2046–2055. [CrossRef]
91. Bailey, J.D.; Landstreet, J.D. Abundances determined using Si II and Si III in B-type stars: evidence for stratification. *Astron. Astrophys.* **2013**, *551*, A30. [CrossRef]

galaxies

MDPI

Article

Distant Resolved Spectroscopic Binaries: Orbital Parallaxes Contradict Trigonometric Parallaxes

Oleg Y. Malkov [1,*,†] and Arseniy M. Sachkov [1,2,†]

[1] Institute of Astronomy, 48 Pyatnitskaya St., Moscow 119017, Russia; asachkov2003@yandex.ru
[2] Faculty of Physics, Moscow State University, 1 Kolmogorova St., Moscow 119234, Russia
* Correspondence: malkov@inasan.ru
† These authors contributed equally to this work.

Abstract: Resolved spectroscopic binaries (RSB) are the only way (besides trigonometric parallax) to determine the dynamical, hypothesis-free distances to the stars of the galaxy. Analyzing the most comprehensive up-to-date data on RSB, we found that trigonometric parallaxes of all distant ($d >\approx 0.5$ kpc) binaries overestimate the distance by 10–50%. Such objects appear as single stars in Gaia and Hipparcos data, but their binarity can be detected/suspected by comparing trigonometric parallaxes in different data releases from these space missions.

Keywords: binaries: spectroscopic; binaries: visual; binaries: catalogues; stars: parameters; parallaxes

1. Introduction

Determining the distance to celestial objects is one of the most important and difficult problems in astronomy. Many methods have been devised to solve this problem: trigonometric parallaxes, assumptions about the absolute stellar magnitude of an object (the so-called photometric distance; this method is applicable to both Galactic stars and extragalactic objects like SN Ia supernovae), period-luminosity relations for some types of variable stars, HRD for clusters, redshift for galaxies, and others. All these methods allow us to estimate the distance to a large number of objects: from hundreds of thousands to billions (Gaia). However, all these methods, except the first one, require certain assumptions about the nature of the object and the characteristics of the media between the object and the observer (primarily the properties of the gas–dust component). In this paper, we discuss objects whose distance can be determined from dynamic considerations without making assumptions about their nature.

When a spectroscopic binary is visually resolved, the typical approach for deriving the parallax and masses consists of combining the independently obtained visual and spectroscopic orbits. Knowledge about both the visual and spectroscopic orbits in binary systems is very important for stellar astronomy as the combined analysis of astrometric and spectroscopic observations produces, without any additional assumptions, a complete 3D binary orbit, enabling precise distance, luminosity, and masses of the system components to be determined. Orbital parallax can only be determined for double-lined spectroscopic binaries with spectroscopic and visual orbits.

So, resolved spectroscopic binaries (RSB) provide us with the only method (apart from trigonometric parallax) to directly determine (rather than estimate) the distances to stars. Ref. [1] was one of the first to draw attention to this fact and compiled a list of about 40 RSB systems.

In a recently compiled comprehensive catalogue of resolved spectroscopic binary systems [2], we presented an analysis of 173 RSB, selected from the lists of binaries published by [1,3–5] and about 50 other publications, and supplied by data from external sources. We later revised our list and removed systems with very low-quality data and objects that were included by mistake. The catalog currently contains 153 RSB.

In this paper, we focus on comparing the trigonometric and orbital parallaxes of the catalogued stars (Section 2), and discuss the reasons they do not show agreement: inaccurate or wrong orbital (Section 3) and inaccurate or wrong trigonometric (Section 4) parallaxes. Finally, in Section 5, we draw our conclusions.

2. Comparison of Orbital and Trigonometric Parallaxes

Recall that the orbital parallax ϖ_{orb} can be deduced according to

$$\varpi_{orb} = a''/a, \tag{1}$$

where a'' and a are the semimajor axes of the visual orbit expressed in seconds of arc and AU, respectively. From the data of the spectroscopic orbit, we have $a \sin i$, where i is the inclination of the visual orbit. Thus, the analysis of the visual (a'', i) and spectroscopic ($a \sin i$) orbits allows us to obtain a ϖ_{orb} value for RSB.

A comparison of the orbital ϖ_{orb} and trigonometric ϖ_{tri} parallaxes (the SIMBAD database was used to obtain the latter) is shown in Figure 1. It can be seen that the data are in good agreement. For five stars, $|\varpi_{orb} - \varpi_{tri}|/\varpi_{tri}$ exceeds 0.2, they are marked with their HIP numbers. Having analyzed the characteristics of these outliers (see Section 3), we can draw preliminary conclusions about the region in the observational parameter space, where orbital parallaxes can be preferable to trigonometric parallaxes. We separately analyze the divergence in the parallaxes of the most distant ($\varpi_{orb} < 2$ mas) stars (see Section 4). The distribution of RSB over orbital parallaxes is shown in Figure 2.

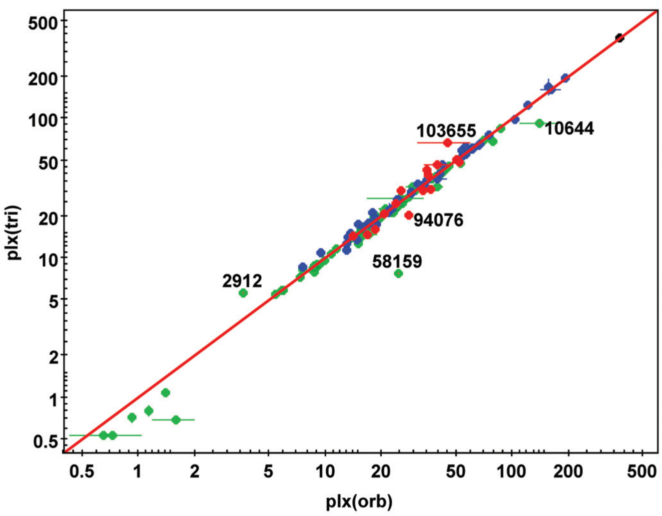

Figure 1. Trigonometric vs. orbital parallaxes (mas) of resolved spectroscopic binaries, with their observational errors. Sources for trigonometric parallaxes are Hip2007 [6] (blue), Gaia DR2 [7] (red), Gaia DR3 [8] (green). The black dot in the upper right corner is the faintest star in the catalogue GJ 65AB (V = 12.08 mag), which was not observed by Hipparcos or Gaia, its trigonometric parallax is taken from [9]. Five outliers are marked with their HIP numbers and are discussed in Section 3. A group of six low-parallax outliers are discussed in Section 4. The one-to-one relation is shown as a solid line, for reference. Note a logarithmic scale for both axes.

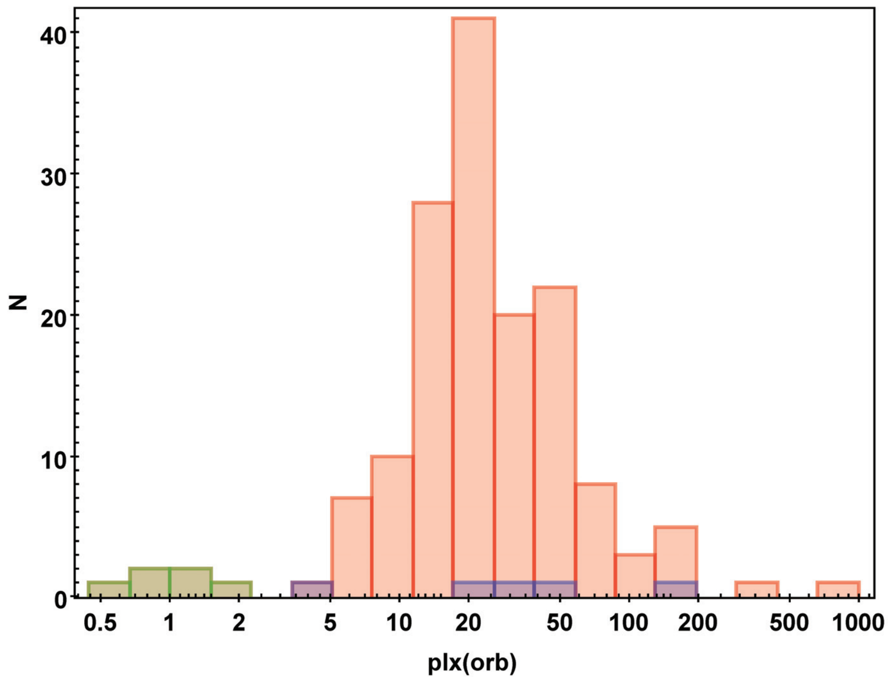

Figure 2. Distribution of RSB over orbital parallaxes (mas). Five outliers (see Section 3) and six distant objects (see Section 4) are marked with blue and green, respectively. In all 11 cases, trigonometric and orbital parallaxes differ by more than 20%. Note a logarithmic scale for the X axis.

3. Outliers

A number of stars in Figure 1 show a marked difference between orbital parallaxes and trigonometric parallaxes (recall that the axes in the figure are given on a logarithmic scale). It is interesting to look at other values of trigonometric parallaxes available for these stars in the literature. Table 1 includes parallaxes obtained for these stars by the Hipparcos mission (original version [10] and new reduction [6]), by the Gaia mission (DR2 [7] and DR3 [8] releases; none of the stars listed are found in the DR1 TGAS release [11]). Also included in Table 1 are the ground-based parallaxes from The General Catalogue of Trigonometric Stellar Parallaxes, Fourth Edition catalogue [12] and the orbital parallaxes presented in this paper.

Table 1. Parallaxes (mas) of five outliers labelled with their HIP numbers in Figure 1. Ground-based trigonometric parallaxes are taken from The General Catalogue of Trigonometric Stellar Parallaxes, Fourth Edition [12], the following columns contain the space-born trigonometric parallaxes from [6–8,10], respectively. Orbital parallaxes presented in this paper are given in the last column.

HIP	Grnd-Based	Hip1997	Hip2007	Gaia DR2	Gaia DR3	Orbital
2912	-04.6 ± 12.5	4.97 ± 0.82	5.45 ± 0.31	5.939 ± 0.3628	5.6563 ± 0.1474	3.615 ± 0.027
10644	$+96.5 \pm 03.7$	92.20 ± 0.84	92.73 ± 0.39	90.845 ± 0.3665	91.6504 ± 0.4271	139 ± 28
58159	-04.6 ± 11.1	5.82 ± 1.02	6.59 ± 0.29	7.44 ± 0.2695	7.7561 ± 0.2682	24.412 ± 0.081
94076	$+24.7 \pm 11.1$	20.42 ± 1.57	19.11 ± 2.35	20.2306 ± 0.3846		27.8 ± 1.1
103655	$+68.4 \pm 03.3$	66.21 ± 2.54	65.40 ± 1.84	66.8056 ± 0.0926		45 ± 14

It can be seen that the parallaxes of all releases from both space missions (i) differ very little from each other, and (ii) unanimously contradict the orbital parallaxes.

HIP 103655 is one of the faintest ($V = 10.12$ mag) objects in the sample, almost all of the others are brighter than $V = 9$ mag. HIP 10644 and HIP 2912 are one of the least massive ($M_1 + M_2$ = 0.25 $\pm$ 0.15 + 0.22 $\pm$ 0.14 $M_\odot$) and one of the most massive ($M_1 + M_2$ = 29.23 $\pm$ 0.93 + 11.83 $\pm$ 0.38 $M_\odot$) systems in the sample, respectively (see Figure 3). Obviously, the accuracy of determining the *trigonometric* parallax of a star does not depend on its mass. On the contrary, the *orbital* parallax of the system is determined simultaneously with the masses of the components; hence, these parameters can correlate. Thus, in these cases, the cause of the discrepancy should not be sought in the trigonometric paralax but in the orbital parallax.

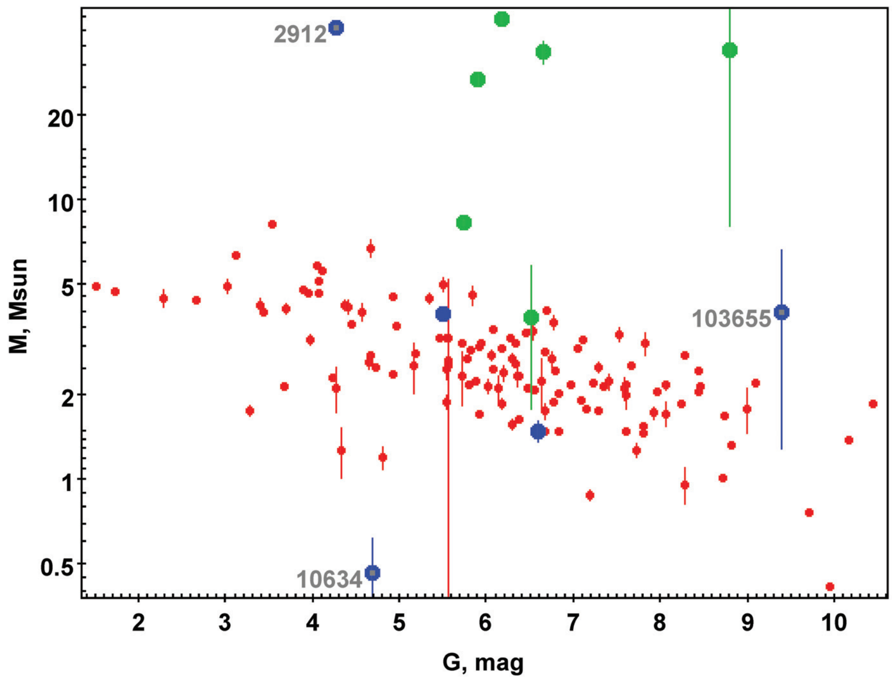

Figure 3. Gaia G-magnitude vs. total mass of the catalogued systems. Five outliers (see Section 3) and six distant objects (see Section 4) are marked with blue and green, respectively. Some of the outliers are labelled with their HIP numbers. Note a logarithmic scale for the Y axis.

These considerations suggest that the orbital parallaxes for this group of stars are not precise enough.

Let us add that [3] also noted that the orbital parallaxes of HIP 2912, HIP 10644, HIP 94076 differ markedly from the trigonometric parallaxes, and [1] drew attention to the divergence of the orbital parallax from the Hipparcos parallax for HIP 103655. In all cases, the authors explain this by the low quality of the visual and/or spectroscopic orbits.

The distribution of the catalogued objects by orbital period and semi-major axis is shown in Figure 4.

Concluding this section, we can say the following. There is good agreement between the trigonometric parallaxes obtained as a result of the work of different space missions (see Table 1) for the five studied stars. It suggests that the reason for their mismatch with the orbital parallaxes is, apparently, the inaccuracy of the latter. Other authors have also paid attention to this discrepancy. Some of these stars occupy a marginal place in terms of brightness or the mass of the components, which could also affect the quality of determining the orbital parallax. This question requires further investigation, and additional observations of these stars are required for more definite conclusions.

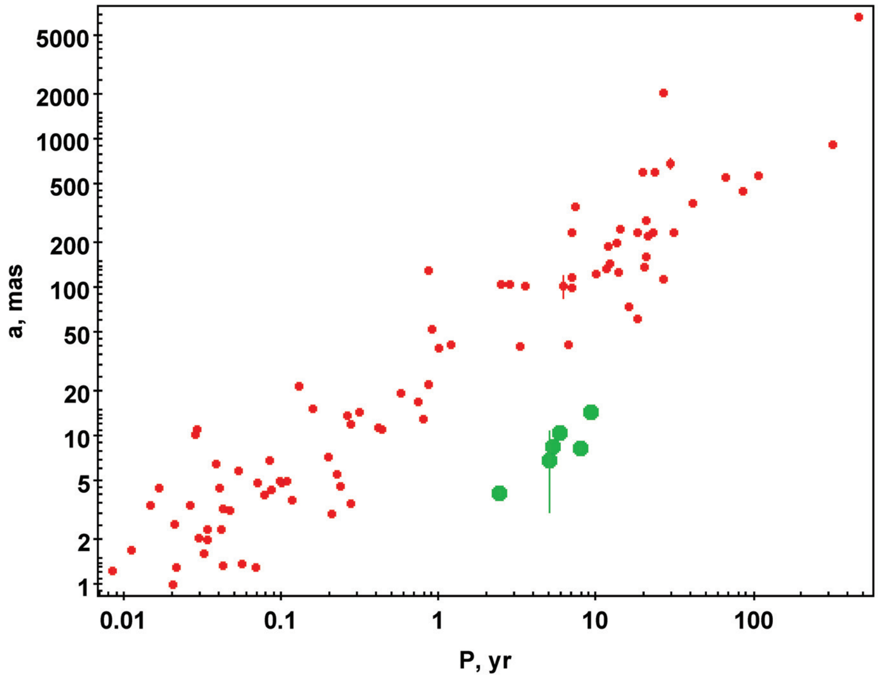

Figure 4. Orbital period vs. semi-major axis of the catalogued systems (red dots). Six distant objects (see Section 4) are marked with green. Note a logarithmic scale for both axes.

4. Distant Stars

The group of six low-parallax outliers (see Figure 1) irrefutably demonstrates that the space-born parallax values of all distant ($\varpi <\approx 2$ mas, $d >\approx 0.5$ kpc) orbital binaries are biased downward (i.e., the distances appear to be overestimated) due to orbital motion.

It is interesting to compare the different trigonometric parallaxes for these stars available in literature among themselves. According to The General Catalogue of Trigonometric Stellar Parallaxes, Fourth Edition [12] there are no ground-based parallaxes for these stars, except for HD 193793, which has a parallax of $\varpi = +12.2 \pm 8.8$ mas. Parallaxes published in different Gaia releases and different Hipparcos releases are presented in Table 2 and Figure 5. Unlike the outliers discussed in Section 3, here, the values of space-born parallaxes obtained by different telescopes and published in different releases differ (sometimes quite markedly). Apparently, the presence of such differences can be considered a sufficient (but not necessary) indicator of the hidden binarity of the object. Let us note, however, that the discrepancies between Gaia DR2 and DR3 are nowhere large enough that 2.5 σ, and the discrepancies with TGAS and Hipparcos are probably not that useful, given the very different quality of the astrometry. It is also interesting to note that the values of $\varpi_{DR3}/\varpi_{orb}$ (see Table 2) for all stars except HD 152233 (which has the largest value of the orbital parallax error) lie within fairly narrow limits: 0.70–0.83.

It makes sense to also look at some of the flags that explored stars have in space mission data releases; first of all, RUWE and `ipd_frac_mul_peak` parameters in Gaia (as indicators of unresolved binarity) and F2 value (goodness of fit) on Hipparcos.

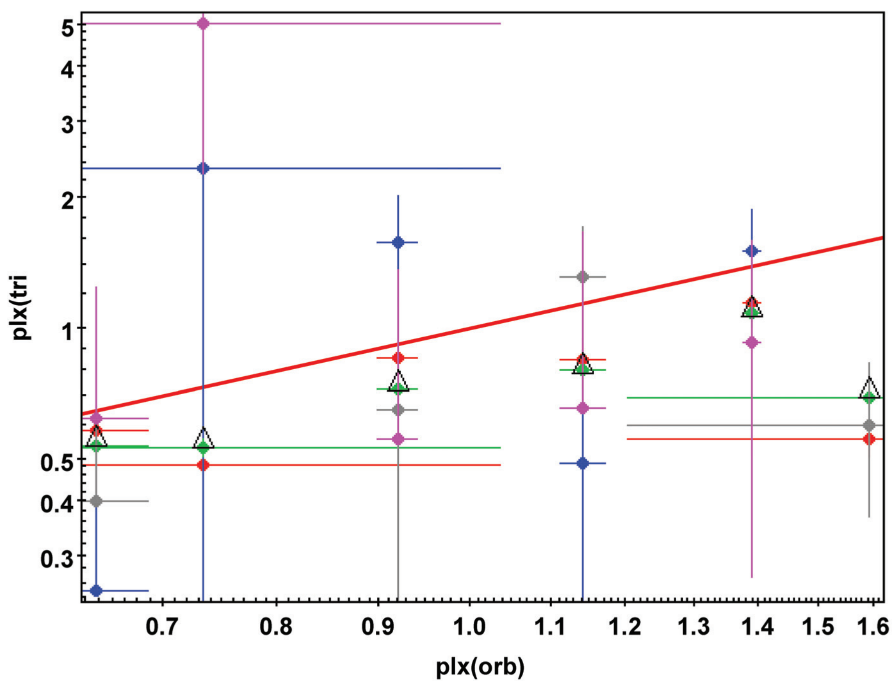

Figure 5. Trigonometric vs. orbital parallaxes (mas) of six most distant resolved spectroscopic binaries. Sources for trigonometric parallaxes are Hip1997 [10] (magenta), Hip2007 [6] (blue), Gaia DR1 TGAS [11] (grey), Gaia DR2 [7] (red), Gaia DR3 [8] (green). Open triangles represent Gaia DR3 parallaxes corrected for the VLBI data (see Equation (2)). The one-to-one relation is shown as a solid line, for reference. Note a logarithmic scale for both axes.

Table 2. Data for six distant RSB (lower left corner in Figure 1). Trigonometric parallaxes are, sequentially, from [6–8,10,11]. Second part: HD and HIP numbers are followed by $\varpi_{DR3}/\varpi_{orb}$ ratio, RUWE, IPDfmp, and F2 values, orbital period P (year); semi-major axis a (mas); and t-test statistics t for Gaia DR3 and orbital parallax.

HD	Gaia DR3	Gaia DR2	Gaia DR1 TGAS	Hip2007	Hip1997	Orbital		
54662	0.7238 ± 0.0526	0.8547 ± 0.0799	0.65 ± 0.52	1.58 ± 0.45	0.56 ± 0.81	0.920 ± 0.021		
152233	0.6965 ± 0.0379	0.5573 ± 0.0489	0.6 ± 0.23			1.59 ± 0.39		
164794	0.8001 ± 0.0728	0.8505 ± 0.0952	1.31 ± 0.39	0.49 ± 0.40	0.66 ± 1.01	1.14 ± 0.03		
168137	0.5316 ± 0.0256	0.4878 ± 0.0736		2.34 ± 2.24	5.02 ± 2.75	0.73 ± 0.30		
193793	0.5378 ± 0.0237	0.5815 ± 0.0286	0.4 ± 0.43	0.25 ± 0.42	0.62 ± 0.62	0.65 ± 0.04		
203156	1.0831 ± 0.0738	1.1506 ± 0.0663		1.51 ± 0.37	0.93 ± 0.66	1.388 ± 0.015		
HD	**HIP**	$\varpi_{DR3}/\varpi_{orb}$	**RUWE**	**IPDfmp**	**F2**	**P, yr**	**a, mas**	**t**
54662	34536	0.79	1.105	0	−0.1	5.79	10.5	3.46
152233		0.47	1.105	0		2.39	4.15	2.28
164794	88469	0.70	0.856	0	0.47	9.06	14.78	4.32
168137	89750	0.73	0.933	0	0.6	5.03	7.0	0.66
193793	100287	0.83	1.321	0	2.06	7.92	8.3	2.37
203156	105269	0.78	2.768	0	−0.95	5.29	8.54	0.05

Renormalised Unit Weight Error (RUWE) is associated with each source. RUWE is expected to be around 1.0 for sources where the single-star model provides a good fit to the astrometric observations. A value significantly greater than 1.0 (say, >1.4) could indicate that the source is non-single or otherwise problematic for the astrometric solution see also discussion in [13], Section 4.2.4.

`ipd_frac_multi_peak` (IPDfmp) is a percent of successful-IPD windows with more than one peak. This field provides information on the raw windows used for the astrometric processing of this source coming from the Image Parameters Determination (IPD) module in the core processing. It provides the fraction of windows (having a successful IPD result), as percentage (from 0 to 100), for which the IPD algorithm has identified a double peak, meaning that the detection may be a visually resolved double star (either just visual double or real binary). It should be noted, however, that if these RSBs are indeed all unresolved for Gaia, the `ipd_frac_multi_peak field` is not expected to be informative. Only for sources with angular separations above 0.2–0.3 arcseconds does this data quality indicator provide useful information on binarity.

F2, the goodness-of-fit statistic, indicates the goodness-of-fit of the astrometric solution to the accepted data (i.e., excluding the percentage of rejected data). For good fits, F2 should approximately follow a normal distribution with zero mean value and unit standard deviation. F2 values exceeding, say, 3, thus indicate a bad fit to the data.

RUWE, `ipd_frac_mul_peak`, and F2 values for the studied stars are presented in Table 2. It can be seen that (except for the RUWE value for HD 203156) they appear powerless to detect the binarity of distant RSBs, ref. [14] suggest a limit of RUWE = 1.25, but most of the objects in Table 2 are also below this limit.

Student's t-test statistics for Gaia DR3 and orbital parallax are also presented in Table 2. It can be seen that for all but HD 168137, the reliability of the difference in mean values can be considered proven.

In [15], a comparison was created between the trigonometric parallaxes of VLBI and Gaia DR3 for 126 radio stars. Based on their differences, an estimate of the systematic offset between the optical and radio reference frames was obtained, which can be expressed in mas units as

$$\varpi_{VLBI} = (\varpi_{Gaia} + 0.022)/1.001 \quad (2)$$

However, as can be seen in Figure 5, this correction cannot explain the discrepancy found between the orbital and trigonometric parallaxes.

In their recent study of Gaia data, ref. [14] explored how deviations from single object astrometry allowed the observer to infer the presence of an unresolved binary companion. They generated a catalogue of simulated binary systems and examined synthetic observations matching Gaia survey's scanning law and astrometric data processing routine. They showed how the unit weight error and proper motion anomaly varied as a function of period, as well as the properties of the binary. Ref. [14] limited their analysis to nearby systems, within 100 pc, and our distant objects had distances exceeding 500 pc. Perhaps this is why (and also because of the paucity of our data) we failed to find any dependence of the orbital/triginimetric parallax discrepancy on the object's orbital period, brightness, angular semi-major axis, or the parallax itself.

Concluding this section, we can say the following. In contrast with the conclusions at the end of the previous section, for these six stars, the cause of the mismatch of trigonometric and orbital parallaxes is the former. This is evidenced by the discrepancy between the trigonometric parallaxes obtained in different space experiments (see Table 2). We suggest using this discrepancy as an indicator of a possible hidden binarity of the object, especially as the indicators designed for this purpose (RUWE, `ipd_frac_mul_peak`, F2), as a rule, do not cope with this task. We also note that the relative errors in the trigonometric parallaxes of these objects are among the largest among catalogued stars (see Figure 6). Apparently the use of trigonometric parallaxes with high uncertainties is somewhat unhelpful.

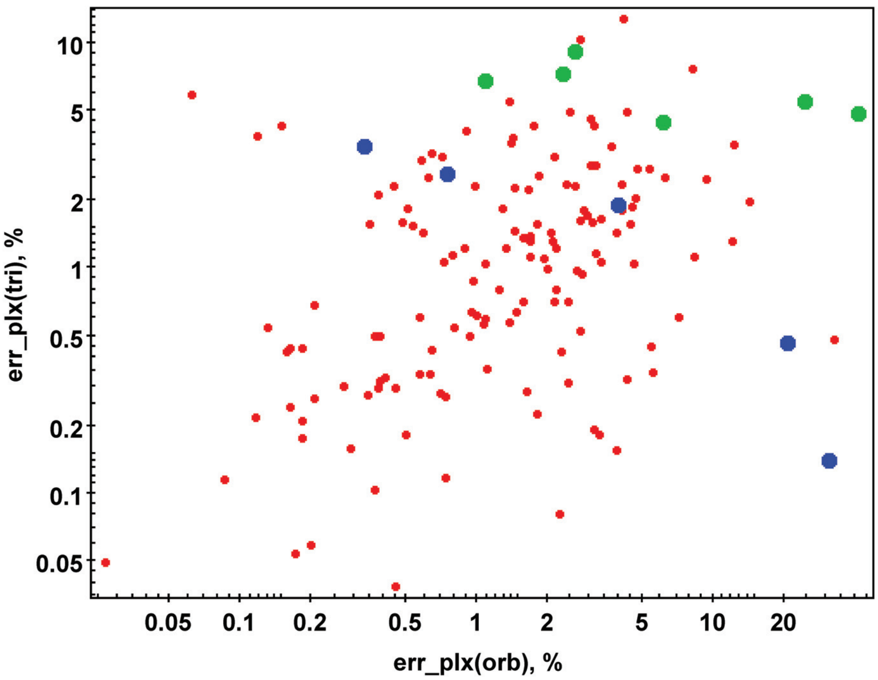

Figure 6. Relative errors of parallaxes (per cent) of the catalogued objects (red dots). Five outliers (see Section 3) and six distant objects (see Section 4) are marked with blue and green, respectively. Note a logarithmic scale for both axes.

5. Conclusions

We can draw the following conclusions.

Resolved spectroscopic binaries (RSB) are a powerful (and probably the only) tool for checking trigonometric parallaxes. A comparison of orbital parallaxes, presented in this paper, with parallaxes published in Gaia DR3 [8] for distant ($d >\approx 0.5$ kpc) stars shows that in all cases, the latter ones are overestimated by 10–50%. The assumption that it is the *trigonometric* parallaxes that are incorrect is based on the fact that the values of space-born parallaxes in different releases differ markedly from each other. The orbital motion, which helps determine the orbital parallax, is also a hindrance for the determination of the trigonometric parallax, since the orbital displacement can be confused with the parallactic displacement. Systems not resolved or barely resolved by the instrument determining the parallax will lead to uncertain parallaxes due to orbital motion, which is added to the parallactic motion and proper motion. Obviously, orbital motion makes quantitatively different contributions to the analysis of the data published in the first, second, and third Gaia releases (based on observations collected during the first 14, 22, and 34 months of Gaia's routine operational phase, respectively) and in two versions of the Hipparcos catalogue (41 months). We propose interpreting such a difference as an indicator of hidden binarity and the detection of new binary stars in the Gaia/Hipparcos data.

On the other hand, analyses of five other outliers showing the difference between orbital and trigonometric parallaxes show that it is the *orbital* parallaxes that are incorrectly determined for them. The reasons for this conclusion are as follows: (i) for some of them, the trigonometric parallax exceeds the orbital parallax, while for others, vice versa; (ii) all space-based parallaxes for these stars show unanimous agreement (in contrast to the stars discussed in the previous paragraph); (iii) at least parts of these outliers have rather marginal brightness values ($V = 10.12$ mag for HIP 103655) or component masses ($M_1 + M_2$ = 0.25 ± 0.15 + 0.22 ± 0.14 $M_\odot$ for HIP 10644 and $M_1 + M_2$ = 29.23 ± 0.93 + 11.83 ± 0.38 $M_\odot$ for HIP 2912), and the latter circumstance may affect the accuracy of the orbital parallaxes. All these stars require further investigation.

It is necessary to add that the main cause of the discrepancy between orbital and trigonometric parallaxes is that the orbits are not definitive. Some spectroscopic orbits need to be revised with new radial velocity measurements, as these are often missing in strategic locations within the orbit. The same can be said for visual orbits. So, we encourage observers to collect current observational data that would allow the orbits to be properly completed with maximum precision.

In this paper, we analyzed mainly data published before 2024. Since then, new data on orbital binaries have appeared (see, for example, compilations [16,17]). We will certainly use this information in our future work.

Author Contributions: O.Y.M. and A.M.S. contributed to the study conception and design. Material preparation, data collection, and analysis were performed by O.Y.M. and A.M.S. The first draft of the manuscript was written by O.Y.M., and O.Y.M. and A.M.S. commented on previous versions of the manuscript. All authors have read and agreed to the published version of the manuscript.

Funding: We thank the Foundation for the Advancement of Theoretical Physics and Mathematics "BASIS" for its support.

Institutional Review Board Statement: Not applicable.

Informed Consent Statement: Not applicable.

Data Availability Statement: Data are available upon request from the authors.

Acknowledgments: We are grateful to our anonymous reviewers whose constructive comments were very helpful in improving the paper. We thank V. Bobylev and A. Dambis for their valuable remarks. This research has made use of SAO/NASA Astrophysics Data System. and the SIMBAD database, operated at CDS, Strasbourg, France. This research made use of TOPCAT, an interactive graphical viewer and editor for tabular data [18] This work has made use of data from the European Space Agency (ESA) mission *Gaia* (https://www.cosmos.esa.int/gaia (accessed on 1 May 2025)), processed by the *Gaia* Data Processing and Analysis Consortium (DPAC, https://www.cosmos.esa.int/web/gaia/dpac/consortium (accessed on 1 May 2025)). Funding for the DPAC has been provided by national institutions, in particular the institutions participating in the *Gaia* Multilateral Agreement.

Conflicts of Interest: The authors declare no conflicts of interest.

References

1. Pourbaix, D. Resolved double-lined spectroscopic binaries: A neglected source of hypothesis-free parallaxes and stellar masses. *Astron. Astrophys. Suppl. Ser.* **2000**, *145*, 215–222. [CrossRef]
2. Zeleke, D.B.; Sachkov, A.M.; Malkov, O.Y.; Negu, S.H.; Tessema, S.B.; Grinenko, A.D. Resolved spectroscopic binaries: Orbital elements and parallaxes. *Astrophys. Space Sci.* **2025**, *370*, 1. [CrossRef]
3. Piccotti, L.; Docobo, J.Á.; Carini, R.; Tamazian, V.S.; Brocato, E.; Andrade, M.; Campo, P.P. A study of the physical properties of SB2s with both the visual and spectroscopic orbits. *Mon. Not. R. Astron. Soc.* **2020**, *492*, 2709–2721. [CrossRef]
4. Anguita-Aguero, J.; Mendez, R.A.; Clavería, R.M.; Costa, E. Orbital Elements and Individual Component Masses from Joint Spectroscopic and Astrometric Data of Double-line Spectroscopic Binaries. *Astron. J.* **2022**, *163*, 118. [CrossRef]
5. Gallenne, A.; Mérand, A.; Kervella, P.; Graczyk, D.; Pietrzyński, G.; Gieren, W.; Pilecki, B. The Araucaria project: High-precision orbital parallaxes and masses of binary stars. I. VLTI/GRAVITY observations of ten double-lined spectroscopic binaries. *Astron. Astrophys.* **2023**, *672*, A119. [CrossRef]
6. van Leeuwen, F. Validation of the new Hipparcos reduction. *Astron. Astrophys.* **2007**, *474*, 653–664. [CrossRef]
7. Brown, A.G.A. et al. [Gaia Collaboration] Gaia Data Release 2. Summary of the contents and survey properties. *Astron. Astrophys.* **2018**, *616*, A1. [CrossRef]
8. Vallenari, A. et al. [Gaia Collaboration] Gaia Data Release 3. Summary of the content and survey properties. *Astron. Astrophys.* **2023**, *674*, A1. [CrossRef]
9. Geyer, D.W.; Harrington, R.S.; Worley, C.E. Parallax, Orbit, and Mass of the Visual Binary L726-8. *Astron. J.* **1988**, *95*, 1841. [CrossRef]
10. Perryman, M.A.C.; Lindegren, L.; Kovalevsky, J.; Hoeg, E.; Bastian, U.; Bernacca, P.L.; Crézé, M.; Donati, F.; Grenon, M.; Grewing, M.; et al. The HIPPARCOS Catalogue. *Astron. Astrophys.* **1997**, *323*, L49–L52.

11. Prusti, T. et al. [Gaia Collaboration] The Gaia mission. *Astron. Astrophys.* **2016**, *595*, A1. [CrossRef]
12. van Altena, W.F.; Lee, J.T.; Hoffleit, E.D. *The General Catalogue of Trigonometric [Stellar] Parallaxes*; Yale University Observatory: New Haven, CT, USA, 1995.
13. Arenou, F. et al. [Gaia Collaboration] Gaia Data Release 3. Stellar multiplicity, a teaser for the hidden treasure. *Astron. Astrophys.* **2023**, *674*, A34. [CrossRef]
14. Penoyre, Z.; Belokurov, V.; Evans, N.W. Astrometric identification of nearby binary stars—I. Predicted astrometric signals. *Mon. Not. R. Astron. Soc.* **2022**, *513*, 2437–2456. [CrossRef]
15. Bobylev, V.V. Link between the Optical and Radio Frames from Gaia DR3 Data and VLBI Measurements. *Astron. Lett.* **2022**, *48*, 790–797. [CrossRef]
16. Groenewegen, M.A.T. Orbital parallax of binary systems compared to Gaia DR3 and the parallax zero-point offset at bright magnitudes. *Astron. Astrophys.* **2023**, *669*, A4. [CrossRef]
17. Ding, Y.; Liao, S.; Wen, S.; Qi, Z. Analysis of the Gaia Data Release 3 Parallax Bias at Bright Magnitudes. *Astron. J.* **2025**, *169*, 211. [CrossRef]
18. Taylor, M.B. TOPCAT and STIL: Starlink Table/VOTable Processing Software. In Proceedings of the Astronomical Data Analysis Software and Systems XIV, Pasadena, CA, USA, 24–27 October 2004; Astronomical Society of the Pacific Conference Series; Shopbell, P., Britton, M., Ebert, R., Eds.; Astronomical Society of the Pacific: San Francisco, CA, USA, 2005; Volume 347, p. 29.

galaxies

MDPI

Article

Light Variability from UV to Near-Infrared in the Ap Star CU Vir Induced by Chemical Spots

Yury Pakhomov *, Ilya Potravnov and Tatiana Ryabchikova

Institute of Astronomy of Russian Academy of Sciences, Pyatnitskaya Str., 48, 119017 Moscow, Russia; ilya.astro@gmail.com (I.P.); ryabchik@inasan.ru (T.R.)
* Correspondence: pakhomov@inasan.ru

Abstract: Multiwavelength modelling of the light variations in the chemically peculiar star CU Vir is presented. The modelling is based on the recent Doppler Imaging of CU Vir, which provides maps of the surface distribution of Si, Fe, He, and Cr. Intensity maps in both individual photometric filters and in the wide wavelength range from UV to NIR were calculated, taking into account the individual chemical abundances on the stellar surface. Comparison with observations revealed good agreement of both the light curves and their amplitude along the spectrum. Additionally, we analysed changes in the photometric period of the CU Vir from 1955 to 2022, including TESS measurements. The data of the last decades clearly indicate a gradual decrease in this period. Measurements of the CU Vir period over the next two decades will be crucial for verifying or refuting the periodic nature of its variations.

Keywords: Ap star; Si-star; CU Vir; synthetic photometry; UV

1. Introduction

Rotationally modulated spectroscopic and light variability is one of the key characteristics of chemically peculiar magnetic Ap/Bp stars. The reason for this variability is the inhomogeneous surface distribution of elements (chemical spots) [1], which is built up by selective atomic diffusion [2,3]. Such a patchy surface abundance pattern, in turn, affects the emergent flux via the effects of line blanketing, bound-free transitions, and modification of the local thermal structure of the atmosphere [4]. In the last few decades, the advances in surface imaging have made it possible to quantitatively model the light variability of some Ap/Bp stars and to reproduce quite successfully their photometric observations [5–9]. These results generally confirmed the concept of the Ap/Bp stars' variability. At the same time, the increasing accuracy of observations of the chemically peculiar stars allows the study of very fine effects, such as variations in low-amplitude variability of HgMn stars [10] due to the migration of spots or still unexplained changes in photometric periods of Ap/Bp stars (e.g., [11]). Proper interpretation of these phenomena also requires improved accuracy of light curve modelling and an understanding of all mechanisms underlying variability within a single rotational cycle.

The Ap star CU Vir (HD 124224) has been known to be spectroscopically variable since Deutsch [12]. Later, Hardie [13] discovered the periodic light variations of CU Vir. The star possesses one of the fastest axial rotation rates among the known Ap/Bp stars with a period of $P \approx 0.52^d$. Subsequent observations revealed unusual changes in the photometric period [11,14–18]. The first semi-quantitative model by Krivoseina et al. [5] allowed the reconstruction of the surface distribution of silicon in CU Vir, concentrated in three spots, and on its basis to reproduce satisfactorily the observed light curves in *vby* bands. Krtička et al. [8], using results of multi-element Doppler Imaging (DI) by Kuschnig et al. [19], performed modelling of the light curve of CU Vir from UV to the visual range. It was shown that the bulk of the photometric variability of the star is caused by the inhomogeneous distribution of silicon, as well as iron and chromium. Due to the flux redistribution, the photometric amplitude in UV grossly exceeds that in the visual spectrum. The synthetic light curves showed good agreement with observations except in the near-UV region. Various explanations for the remaining difference between model and observations have been proposed, including limitations of DI, unaccounted contributions from other elements, effects of vertical abundance stratification, deviations from LTE in the line formation region, effects of magnetic field, etc. In a subsequent study by Kochukhov et al. [20], the parameters of CU Vir were refined, and Zeeman–Doppler Imaging (ZDI) was performed on the basis of high-resolution NARVAL [21] spectra. These authors derived the topology of the magnetic field, which deviates significantly from the axisymmetric dipole, and also revealed the relation between magnetic and abundance structures. The chemical spot pattern was in general agreement with Kuschnig et al. [19] imaging. Krtička et al. [22] showed that employing DI maps by Kochukhov et al. [20] improved the theoretical representation of the flux-calibrated HST observations in far-UV. However, it is still of interest to examine how the employment of new surface maps, updated atomic data, and advanced atmospheric models will affect the theoretical representation of CU Vir's light variability over a wide wavelength range, including recent spacecraft TESS (Transiting Exoplanet Survey Satellite [23]) data. This is the aim of our study.

The paper consists of a description of observational data (Section 2), an analysis of the changes in the period of CU Vir (Section 3), modelling of the light curve (Section 4) and its results (Section 5), and a discussion in Section 6.

2. Observational Data

2.1. Doppler Imaging

For the modelling of light curves, we employed the results of multielement DI of CU Vir by Potravnov et al. [24]. This paper provides a detailed discussion of spectroscopic observations, DI technique, and derived surface abundance distributions for five elements—He, Mg, Si, Fe, Cr—which were reconstructed using the archival high-resolution ($R \approx 65,000$) spectroscopic timeseries obtained with the NARVAL echelle spectrograph. This is the same raw observational material used by Kochukhov et al. [20]. Thirteen spectra were obtained in a few runs during the 2009–2011 interval and cover the rotational period of CU Vir with good phase coverage (see Table 1 in [24] for the log of observations employed for DI). DI results in a strongly inhomogeneous surface distribution of the above-mentioned elements, with He and Mg varying roughly in antiphase with Si, Fe, and Cr. The abundance differences reached up to $[X/H] = \log(N_X/N_{tot}) - \log(N_X/N_{tot})_\odot \approx +2$ dex in the abundance scale for the element X relative to the Sun. The detailed discussion of spectroscopic observations, DI technique, and obtained surface abundance distributions is given in the paper by Potravnov et al. [24].

It is essential for light curve modelling that the resulting surface maps are presented in the form of the equi-element spherical grid of 3764 elements in total, with fixed abundances of the five considered elements in each grid cell.

2.2. Photometry

In our study, we analysed the publicly available photometric observations of CU Vir spanning the UV to red optical wavelengths. We used modern, accurate ground- and space-based optical photometry and UV spectrophotometry for light curve modelling and also employed historical photometric data to evaluate the period variations.

We used data from Sokolov [25], who analysed IUE spectra taken in January–March 1979 using the LWR (Long Wavelength Redudant 2000–3000 Å) and SWP (Short Wavelength Prime 1250–1900 Å) cameras and extracted a set of monochromatic fluxes. The 23 scans in the dataset provide uniform phase coverage over the stellar rotational period. Krtička et al. [8] reprocessed these IUE data to study the monochromatic light variations in UV.

In the optical range, we mainly focused on data by Pyper et al. [15] obtained in the Strömgren photometric system $uvby$. This is the longest series of homogeneous accurate observations of CU Vir, with 2820 measurements per filter. The typical photometric accuracy is 0.005^m , 0.004^m, 0.004^m, and 0.003^m for $uvby$ bands, respectively. The dataset spans the period from 1991 to 2012 and was obtained in 21 observational sets. We also used the extensive set of heterogeneous historical data available in the literature to discuss the period changes.

In our study, we also analysed the red optical photometry observed from 26 March 2022 to 22 April 2022 (over 14,000 measurements across 26 days with three data gaps) by the TESS space mission [23]. The dataset processed using the SPOC (Science Processing Operations Center) automatic software package was obtained via the MAST (Mikulski Archive for Space Telescopes) portal. The radiation flux was converted to the TESS magnitude scale using the formula $m_{TESS} = -2.5\, log(SAP\_FLUX) + 20.44$ as specified in the mission documentation (https://tess.mit.edu/public/tesstransients/pages/readme.html#flux-calibration accessed on 8 August 2025). The TESS dataset of CU Vir covers 50 rotational cycles, of which 37 have complete phase coverage.

3. Period Changes in CU Vir and Ephemeris

In contrast to the bulk of Ap/Bp stars with stable photometric periods, CU Vir demonstrates period variations that must be taken into account when phasing observational data. The first detection of these period changes was reported by Kuschnig et al. [26]. Subsequent analysis by Pyper et al. [14] revealed an abrupt period increase (indicative of the stellar spin-down) by $\sim$1.6 s occurring somewhere between 1983 and 1992. Continued photometric monitoring uncovered further period variations, which, within the model of discrete changes, are consistent with other glitches: one more period increase in $\sim$1992 and a subsequent decrease (acceleration of rotation) after 2012 [16]. The period between glitches is assumed to be constant. Alternatively, Mikulášek et al. [17,18] proposed the model with smooth period oscillations within $\approx$65 year cycle.

We collected photometric observations of CU Vir from 1955 to 2022 available in the literature and determined the period for annual observational seasons (excluding data from Pyper and Adelman [27], Adelman et al. [28], as well as Hoeg et al. [29], which were not split due to large uncertainties) using a Lomb–Scargle periodogram [30]. The complete list of observations with their detailed characteristics is presented in Table 1. The table includes the years of observations, the date range for each dataset, the number of measurements, the photometric band and the references. For a few datasets obtained before 1970, where the observational coverage was insufficient for reliable period determination, we adopted the period estimates reported in the original publications. The uncertainties of the period are estimated as $\sim \frac{1}{\Delta T\sqrt{N}}\sigma_m$, where ΔT is the duration of the observations (up to 365 days), N is the number of measurements, and σ_m is the uncertainty of magnitude measurements. Consequently, periods derived from shorter time series exhibit larger uncertainties, as evident in some of our results.

Table 1. List of observational time series employed to estimate the period of CU Vir.

Years	Range, Days	N_{obs}	Band	Reference
1955	99	54	UBV	Hardie [13]
1964–1966	836	235	UBV	Abuladze [31]
1980–1983	1139	23	*uvby*	Pyper and Adelman [27]
1987–1989	796	354	UBV	Adelman et al. [28]
1990–1993	1068	79	$B_T V_T$	Hoeg et al. [29]
2003–2010	2885	11,990	SMEI (4500–9500 Å)	Krtička et al. [22]
2011–2017	2016/2028	1059/995	B/V	Krtička et al. [22]
1991–2012	7710	2820	*uvby*	Pyper et al. [15]
2022	26	14,264	TESS (5800–11,000 Å)	MAST *
Literature values				
1966	3	18	B	Hardie et al. [32]
1968	120	85–105	UBV	Blanco and Catalano [33]

* https://mast.stsci.edu/portal/Mashup/Clients/Mast/Portal.html accessed on 8 August 2025.

The period determinations are plotted against data models by Pyper and Adelman [16] (P20) and Mikulášek et al. [18] (M19) (their Model 1 fitted by a cosine function and adopting the following model parameters: $P_0 = 0.52069404^d$, $A = 0.1611$, $T_0 = 2446604.4390$, and $\Pi = 24,110^d$ = 66 year) in Figure 1. At first glance, the plot can be roughly divided into two parts in terms of the density of observations. A significant increase in the number of observations was noticeable after ∼1990, when systematic observations of the star at FCAPT began [15]. Analysis of the pre-1990 data shows that, given their sparsity and errors, both interpretations, several constant periods and a smoothly changing one, are possible. The period found from Hardy's 1955 data seems to marginally favour the M19 model.

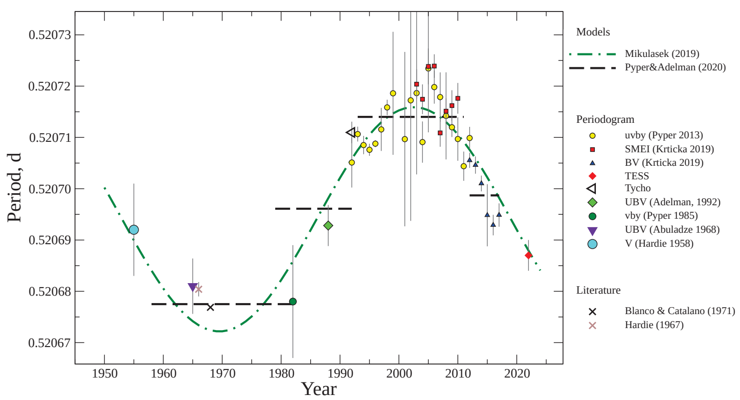

Figure 1. Period variations in CU Vir. The observational data and their references are described in the legend. Points with error bars correspond to our period determinations using the Lomb–Scargle method. The period values according to the Pyper and Adelman [16] model are marked by dashed lines, and the dashed–dotted line shows the Mikulášek et al. [18] cosine model.

The data are very sparse between 1980 and 1992; nevertheless, the drastic changes in the period are evident from Figure 1. The M19 model with continuous period changes reaches its extreme near 2005. The derivative of the period change tends to zero at this point, so the 1993–2012 data within the error limits are described well by both the models for the variable and the constant periods (the "tangent" at the maximum point). To quantify this, we used the so-called Bayesian information criterion (BIC) [34] for model selection (see details in Appendix A) . Accounting for the quality of data fitting and penalising the growing number of the model's free parameters, BIC allows for choosing an optimal model without overfitting. Generally, the models with a lower BIC are preferable. We have calculated the BIC for both models within four intervals: 1955–1983, 1983–1992, 1992–2012, and after 2012. We assume a number of free parameters of 2 and 6 for P20 and for the M19 cosine model, respectively, within each interval. The results are summarised in Table 2, together with the general root mean square (RMS). We also calculated the BIC parameter for the entire set of observations, where the combination of four discrete periods in P20 results in eight free parameters. The BIC= −2364.2 for P20 model and −2378.4 in the case of M19, as well as the data in Table 2, indicate a very similar formal quality of fit of the observations by both models, which is consistent with a similar conclusion by Pyper and Adelman Pyper and Adelman [16] based on O-C diagrams.

Table 2. Parameters of RMS and BIC for the approximation of CU Vir period changes in specified time intervals by the Pyper and Adelman [16] and Mikulášek et al. [18] models.

Period	P20		M19	
	RMS	BIC	RMS	BIC
1955–1983	6.62×10^{-6}	−309.8	8.45×10^{-6}	−291.6
1983–1992 *	1.46×10^{-5}	−56.1	1.28×10^{-5}	−52.5
1992–2012	5.73×10^{-6}	−1780.4	4.33×10^{-6}	−1809.8
2012–2022	5.34×10^{-6}	−231.1	2.82×10^{-6}	−235.5

* The values for this period are based on a very limited number of observations.

It can be seen from Table 2 that the estimates of RMS and BIC are quite close for these models, which is consistent with a similar conclusion by Pyper and Adelman [16] based on O-C diagrams. From a formal point of view, the models fit the data roughly equally, with M19 having a smaller RMS, excluding the period of 1955–1983, but a larger number of free parameters. An inspection of the data after 2012 reveals that a gradual decrease in the period is more likely than an abrupt change, in better agreement with the M19 model. This is particularly supported by the most recent TESS data. However, in our opinion, the final proof of the oscillatory model can be obtained in the next 5–10 years when the period will reach a minimum. Given the minor differences in the rotational phases according to the P20 and M19 models, we utilised the former to match the phases with the DI in the previous study. The TESS data were phased with the M19 ephemeris.

4. Light Curve Modelling

4.1. Calculation of Intensity Map

Based on the element distribution maps of silicon, iron, helium, and chromium revealed by DI [24], a grid of plane-parallel LTE models of stellar atmospheres was calculated with the LLMODELS code [35] , taking into account the individual chemical composition. In the latest version of the LLMODELS code, continuum opacity calculations were performed using blocks of Kurucz' ATLAS12 code [36,37]. The calculation of opacity in the LLMODELS also takes into account the individual absorption in spectral lines. Up-to-date data on atomic transitions are retrieved from the VALD3 [38,39] database. The grid consists of 120 models covering all combinations of abundances in the ranges given in Table 3. The parameters of the atmosphere ($T_{\rm eff}$= 12,800 K, $\log g$= 4.0) and the abundances of other elements remained unchanged. The surface maps contain 3764 unequally distributed cells across 53 latitude zones, ranging from 108 cells at the equator to 5 cells at each pole. Spectral energy distributions were calculated simultaneously with the models. Using the response curve of photometric filters (*uvby* and TESS), we calculated the flux and radiation intensity of 1 cm^2 of the stellar surface. The passbands of the Strömgren photometric system were adopted from [40] and for the TESS imaging receiver from [23].

Table 3. Elemental abundance ranges covered by the grid of models.

Element	[X/H]
Si	−6.5 −5.3 −4.1 −2.9 −1.7
Fe	−5.5 −4.5 −3.5 −2.5
He	−3.4 −1.8 −0.2
Cr	−6.4 −4.4

The calculated intensities converted to the magnitude scale were organised into two separate grids. The first one was designed for the broadband photometry (*uvby* and TESS). The second one was generated across the spectrum spanning 1000–12,000 Å and convolved with an instrumental profile corresponding to the spectral resolution $R = 1000$. The latter grid was used for analysis of monochromatic fluxes, in particular for ultraviolet IUE observations.

The logarithmic nature of the magnitude scale significantly reduces mesh gradients. For each surface stellar cell, in accordance with the abundances of Si, Fe, He, and Cr, the intensity was calculated using the grid interpolation method. This procedure generated maps of specific intensities $I_{l,b}$ for the photometric passbands and across the spectrum.

4.2. Synthetic Photometry Technique

The flux light curve was computed in matrix form:

$$F = G \times I$$

where F is the matrix product, is the flux column matrix for each rotational phase $(F_1, F_2, \dots, F_{Nph})^T$ of $[Nph\times 1]$ size (we use Nph = 36 phases), I is a 1D flattened intensity map of $[1 \times 3764]$ size created from map $I_{l,b}$ as a sequence of values, and G is the matrix of $[3764 \times 36]$ size accounting for cell visibility:

$$G = A \cdot L$$

where G is the product of matrix elements, $A = S\cos\vartheta$ is the $[3764 \times 36]$ matrix of apparent areas of each cell at an angle ϑ relative to the observer, S is the real areas of the cells of $[3764 \times 36]$ size with identical rows, and L is the $[3764 \times 36]$ matrix of the intensity damping due to the limb darkening effect. For cells on the invisible hemisphere of the star, $A_{ij} = 0$.

The limb darkening coefficients for a quadratic law

$$I_\mu = I_0[1 - a(1-\mu) - b(1-\mu)^2]$$

were calculated from intensities $I_{\mu,\lambda}$ of emergent radiation from stellar surface convolved with a specific passband T_λ for seven values of μ=cos ϑ using the Levenberg–Marquardt method [41,42] to approximate the function

$$\frac{I_\mu}{I_0} = \frac{\int I_{\mu,\lambda} T_\lambda d\lambda}{I_0 \int T_\lambda d\lambda} = 1 - a(1-\mu) - b(1-\mu)^2$$

The calculations were performed using a single stellar atmosphere model with mean Si, Fe, He, and Cr abundances. The effects of abundance variations (both over- and under-abundances) on the limb-darkening coefficients were found to be negligible, introducing deviations of less than 0.5%.

The vector of the relative synthetic magnitudes was calculated as

$$\Delta m^{syn} = -2.5\, log\, F/\overline{F}$$

where $\overline{F} = \sum F/Nph$ is the average flux. These values will be compared with the observational data.

4.3. Contribution of Different Elements to Light Variability

To model the light curves, we considered four elements with inhomogeneous surface distributions that significantly contribute to observable variability. Silicon was pointed out by Strom and Strom [43] as a principal element affecting opacity and flux redistribution when it is overabundant relative to the Sun. Later, Khan and Shulyak [4] searched for other elements whose overabundance affects the structure of the stellar atmosphere. Besides Si, these are Cr and Fe, the main elements that change the temperature distribution by more than 3 percent. Ti, Mg, and Ni have much smaller effects. And a very small effect is produced by He, C, N, O, Ca, Sr, Eu, and Hg. These authors also selected three key elements (Si, Cr, Fe) that affect the position of stars on the diagram: peculiarity index a (designed to measure the strength of the 5200 Å depression with respect to normal stars) vs. colour $b - y$. We checked the influence of elemental contribution to the Strömgren photometry for the stellar parameters of CU Vir. Using the LLmodels code [35], we computed stellar atmosphere models and spectral energy distributions with solar abundances as a reference. For each model, we increased the individual element abundances (from He to Zn) by 1 dex while holding others constant and then calculated corresponding $uvby$ magnitudes. Figure 2 presents the resulting magnitude differences relative to the reference. For CU Vir parameters, abundance changes of He, Fe, Si, and C produce the largest effect on the emergent flux. The effect is substantially smaller for Mg, Ca, N, and for the Fe-group, excluding iron itself.

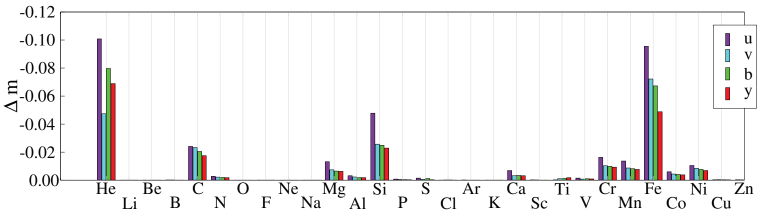

Figure 2. Contribution of different elements to photometric variability for the Strömgren photometric system.

In the case of CU Vir, the inhomogeneous carbon distribution can affect the light curve across UV to IR significantly. Unfortunately, mapping of carbon surface distribution is not possible because of the lack of suitable lines in the optical wavelength range at CU Vir's temperature. To estimate possible carbon abundance variations, we used Hubble Space Telescope (HST) spectral observations (STIS spectrograph, $R = 110,000$) of CU Vir obtained in five rotational phases in 2017 by Krtička et al. [22], program id 14737. Calibrated spectra were retrieved from the MAST portal. Figure 3 demonstrates behaviour of C II ion lines λ1334 Å in HST/STIS spectra. While the continuum level also varies, we normalised it using line-free regions to isolate the line profile variations. We estimated carbon abundances for minimal and maximal intensity of the lines ϵ(C) = [-4.50, ...-3.80]; i.e., carbon shows underabundance as in other Ap stars. Consequently, we expect negligible impact of carbon inhomogeneities to photometric variability, which does not exceed $0^m.0004$ by our estimations.

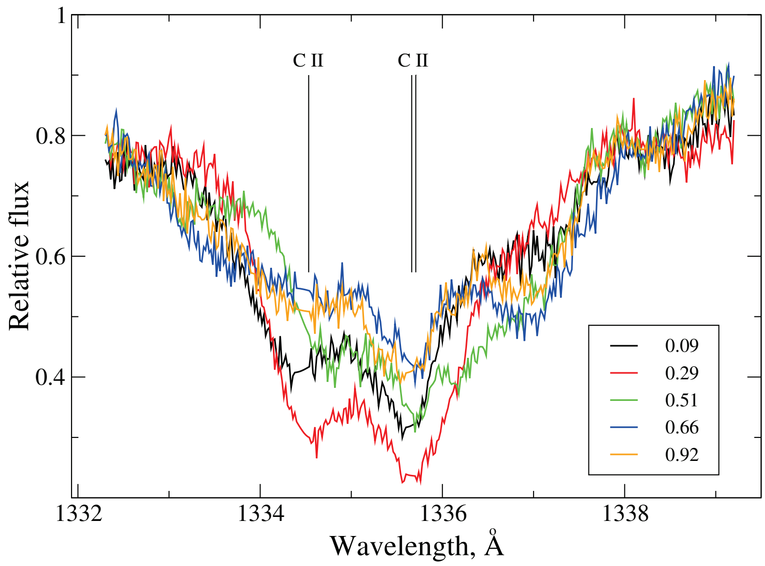

Figure 3. Variations of C II lines in the HST/STIS spectra of CU Vir. The phases are indicated in the legend. The interstellar lines were removed.

Using the Mg surface map, we also estimated the effect for this element as the difference between fluxes for maximal and minimal abundances. It is found to be $0^m.0064$, $0^m.0035$, $0^m.0035$, $0^m.0030$ for the *uvby* bands, respectively.

To summarise, we expect that, apart from Si, Fe, He, and Cr, only the joint effect of the iron peak and lighter elements may have a slight impact on the light curve.

5. Results

5.1. Visual Light Curve

Successful modelling of flux variability caused by the inhomogeneous surface distribution of elements in Ap/Bp stars requires adequate reproduction of both the amplitude of the variability in a wide wavelength range and the shape of the light curves in individual photometric bands.

The amplitude of photometric variability for a given by the DI surface distribution of elements in CU Vir is plotted in Figure 4 against the wavelength. The smoothed theoretical curve reproduces the observations well, capturing all major features. The largest amplitude, up to $\sim 0.9^m$, is observed in the far-UV, then rapidly decreases to the first "null-point" at 1800 Å, where the photometric variability is practically eliminated. There is some wavelength shift between our model curve and observations; the latter display this point ∼200 Å longward. The second "null-point" at 2400 Å also exists but is predicted by the model at a shorter wavelength than observed. However, we note that there is also an ambiguity in the determination of these points between Krtička et al. [8] and Sokolov [25], who utilised the same IUE observations. The amplitude of photometric variations is reproduced quite well. From 3500 Å onward, the theoretical curve precisely follows the observations.

Figure 5 shows a comparison of the phased synthetic light curves in *ubvy* Strömgren bands and observations of Pyper et al. [15], while Figure 6 is the same for TESS data. One can see that synthetic light curves fit observations very well in all filters, with only modest discrepancy in 0.5–0.7 phase interval for *u* and *v*. While the former shows a deficiency of flux in the theoretical curve, the latter shows an excess of it. Possible reasons for this discrepancy will be explored in the discussion. In the TESS passband, the amplitude of the synthetic light curve is also somewhat depleted, but given the small range of variability, the discrepancy itself is also negligible.

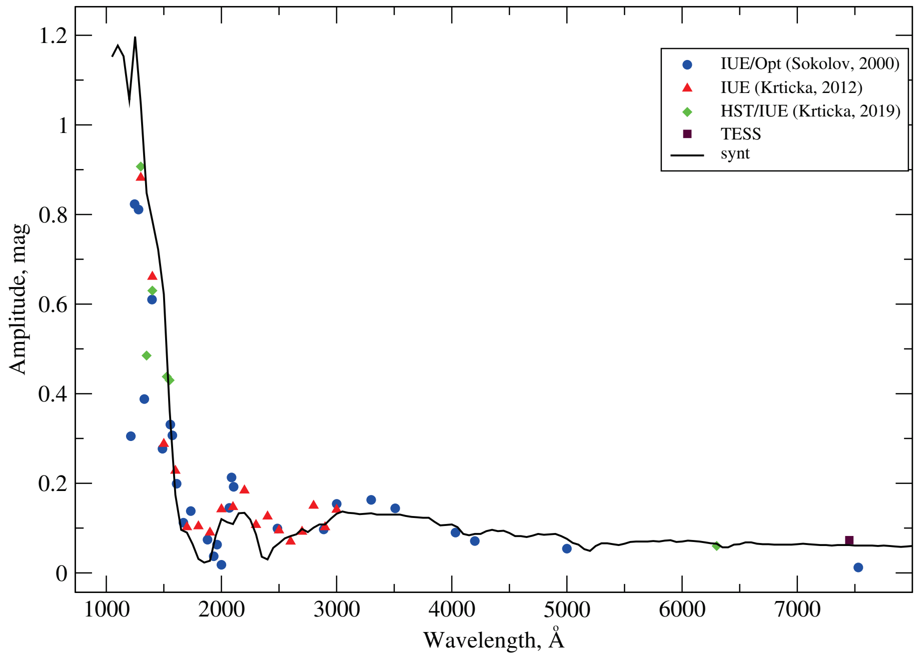

Figure 4. Amplitude of variability of CU Vir from FUV to NIR.

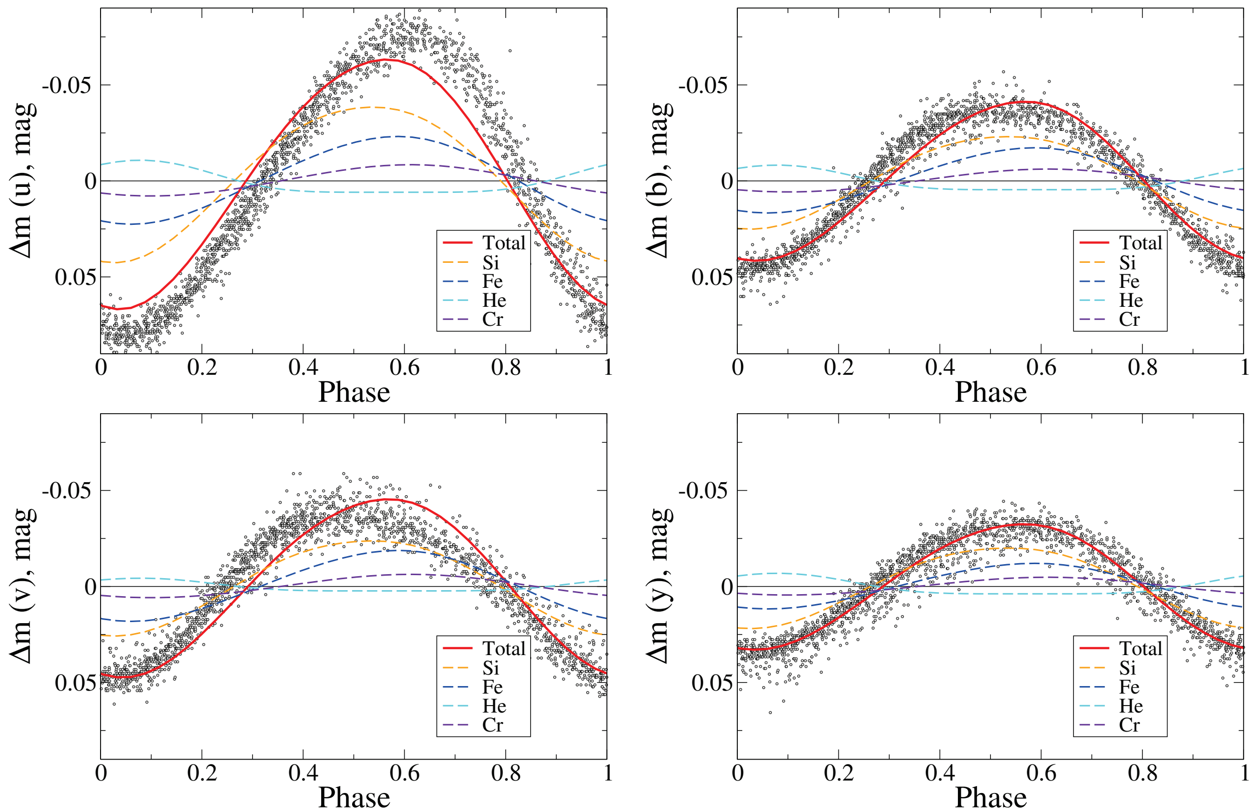

Figure 5. Comparison of the observed (black points) and synthetic (see in legend) light curves of CU Vir in different Strömgren bands.

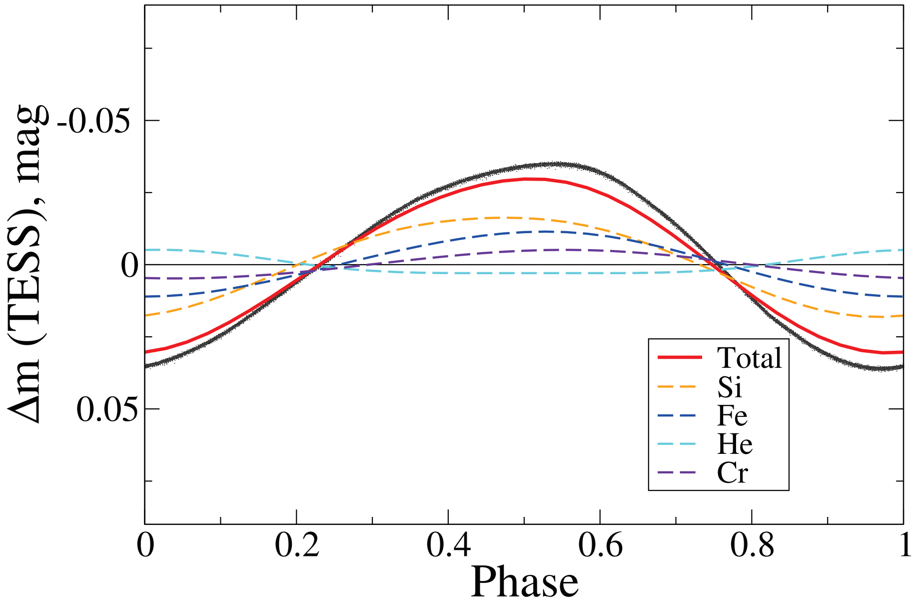

Figure 6. Comparison of the observed (black line) and synthetic (see in legend) light curves of CU Vir for TESS measurements.

Considering the individual contribution to flux variability, we note that the contribution of a large region depleted in Si, Fe and Cr defines the position of the primary light minimum at $\phi \approx 0$. Helium, varying in antiphase, acts as a "counterweight" and regulates the flux depth of the minimum and has almost no effect on the maximum. The wider and more asymmetrical maximum is caused by the transit via line of sight of the region with Si, Fe and Cr overabundance in the $\phi \approx 0.5$–0.6 phase range. The small phase shift of the maximum of observed light curves in different filters is possibly caused by the different relative contributions of the considered elements.

5.2. UV Variations

The ultraviolet spectral range is the most difficult to model due to the high density of strong spectral lines, ionisation edges of multiple atoms and ions, and physical effects like the influence of stellar wind [22].

In Figure 7, we show the comparison of our synthetic light curves with UV observations (1400–3500 Å) extracted from IUE spectra by [8,25]. Overall, the calculations successfully reproduce both the shapes and amplitudes of the observed light curves. The characteristic inversion of the light curve in the range 1400–2000 Å, caused by silicon absorption shortward 1600 Å, is clearly visible. At 1800 Å and 2400 Å, synthetic light curves possess "null-points" with very small amplitude. Observations nevertheless show a large amplitude of variability. The reason for this could be the contribution of some elements that change only the monochromatic flux or flux in narrow bands. We do not know their distribution over the surface and do not take them into account in the calculations.

At 2000 Å there is a notable difference in amplitude between observational data (different processing of the same IUE set) by Sokolov [25] and Krtička et al. [8]. Our synthetic light curve fits well with the latter.

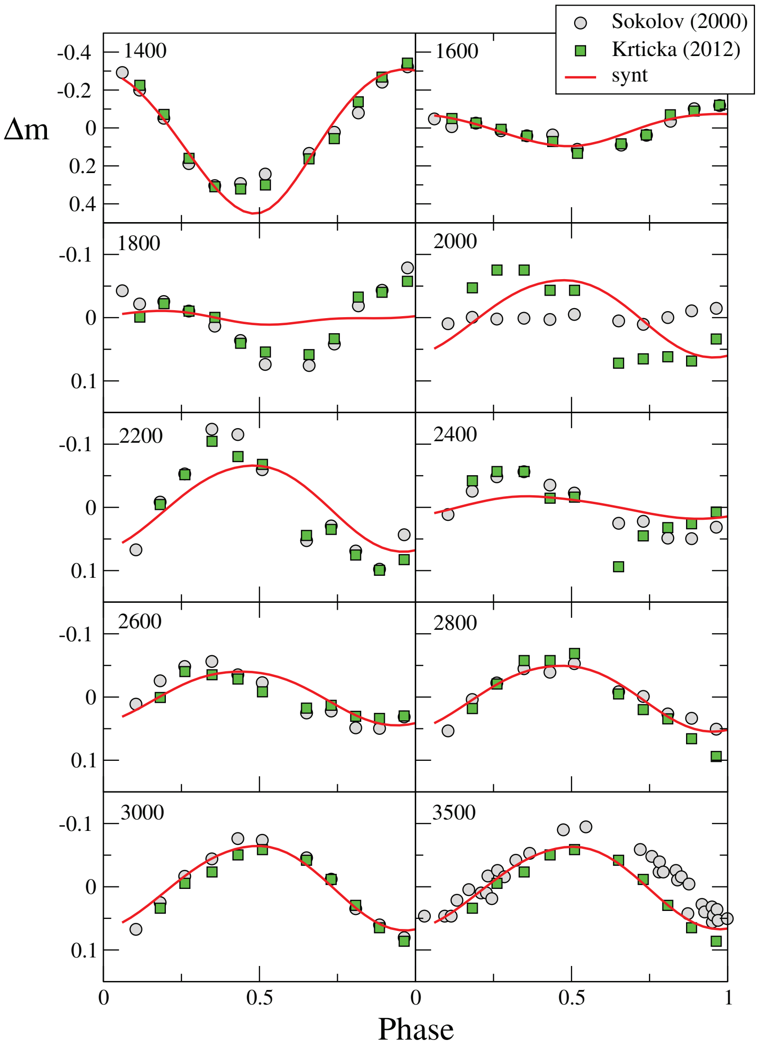

Figure 7. Comparison of the observed IUE spectrophotometry of CU Vir in UV with synthetic light curves. The corresponding wavelengths are given in the upper left corner.

6. Discussion

Photometric variability of CU Vir is one of the most intriguing cases among Ap/Bp stars. Despite the regularity and simple shape of the light curve, the star exhibits variations in its photometric period. In order to determine the physical mechanism responsible for these period changes, an accurate theoretical model of light variations within a single rotational cycle is desirable. Previously, the photometric variability of CU Vir was successfully explained by inhomogeneous surface distribution of a few elements and related effects of flux redistribution [5,8,22]. These simulations, based on horizontally inhomogeneous element distribution recovered by the DI technique, reproduce well the main observational features: the amplitude of the photometric variations, and, although less accurately, the shape of the light curves in different filters. However, the question about the reasons for the discrepancies remained open. Krtička et al. [8] suggested and discussed in detail several possible reasons such as limitations of abundance maps, influence of additional elements, vertical abundance stratification, surface temperature variations, the turbulent velocity, the effects of fast rotation, the magnetic field, the convection zone in helium-rich models, and the NLTE effects.

Employing the updated DI data [24] based on high-resolution NARVAL spectra, we revised the CU Vir light curve modelling. Our maps are in general agreement with those by Kuschnig et al. [19], which were used in previous light curve simulations. However, there are also modest differences in the spot geometry and abundance scales due to the different stellar rotation parameters we adopted (following [20]) and the higher spatial resolution of our maps, up to $\sim 3^\circ$ in latitude. The employment in our modelling of the atmospheric models grid with line-by-line opacity treatment (LL-models) based on up-to-date atomic line parameters from the VALD3 database [39] represents an important step forward.

Comparison with observations shows that we succeeded in the representation of the main features of the photometric variability of CU Vir over a range of wavelengths from the far-UV to red optical wavelengths. The synthetic light curves reproduce quite well the amplitude and shape of the light curves. The fit to the observations turns out to be generally better than in previous modelling [8]. The main discrepancies remaining between theory and observation are in the amplitude of "null-points" in UV, and amplitude in Strömgren u and v filters.

Discussing the reasons for deviations in the shape of the theoretical light curve from the observed one, Krtička et al. [8] noted the problem of "missing opacity" due to some element not accounted for in DI. We have estimated the possible contribution of several elements to the emergent flux for the atmospheric parameters of CU Vir. In addition to the elements He, Si, Mg, Cr, and Fe discussed above, the potential effect on photometric variability can be provided by the inhomogeneous surface distribution of light elements C and Ca and iron-peak elements Ti, Mn, Co, and Ni, which may produce significant but much more localised spectral features that manifested in monochromatic UV measurements. The DI of these elements is very difficult due to the lack of strong lines in the spectrum and severe line blending due to the rapid axial rotation of CU Vir. Thus, we can only hypothesise their contribution to the UV variability.

Another possibility is the effects of vertical abundance stratification. However, the rapid rotation of the star and corresponding severe line blending do not allow the direct investigation of the vertical elemental stratification in the atmosphere of CU Vir by existing methods. We were previously able to estimate the effect of vertical stratification on the photometric variability of the more slowly rotating star MX TrA [9], which is $\sim$1000 K cooler than CU Vir using the stratification profile of the slowly rotating Ap star BD+00°1659 as a benchmark [44]. It can be seen from Figure 5 in [9] that in the region of the Balmer discontinuity (u filter), the stratification leads to an increase in the emergent flux, while in the v band, the effect is reversed. Thus, the impact of vertical stratification of silicon suspected for CU Vir [20,24] qualitatively allows one to reconcile the amplitudes of theoretical light curves and observations in u, v filters.

When modelling the (spectro-) photometric observations obtained at different epochs from 1979 to 2022, we faced the change in the photometric period of CU Vir, which should be taken into account when constructing the phase curves. We performed a comparison of two models for period variations: a discrete model of the period change [14,16] and the model of the oscillating period [17,18]. Without attempting a comprehensive analysis, we utilised only publicly available photometric data from 1955 to 2022 and determined period values in individual seasons. One may say that within the errors, data up to $\sim$2012 are fitted by both models with similar accuracy. However, photometric observations after 2012 show a gradual decrease in the period, in better agreement with the model by Mikulášek et al. [18], which implies the continuous period variations in CU Vir. The next 5–10 years, are particularly intriguing as the period should reach its minimum in $\sim$2035 if the period oscillations are real. Further regular photometric and spectroscopic monitoring of CU Vir is highly desirable. As it was shown in our related paper [24], the structure of the chemical spots in CU Vir remains stable on a timescale of $\sim$26 year, while changes in the period are already apparent. Most probably, the changes in the period of CU Vir appear are caused by MHD effects: Alfven waves [45,46] or Tayler instability [24,47].

Accurate observational monitoring of future period changes in CU Vir are essential for understanding the mechanism.

7. Conclusions

We have made a new attempt to model the light curve of the Ap star CU Vir, whose variability is modulated with the axial rotation period $P \approx 0.52907$ d and is caused by the inhomogeneous surface distribution of chemical elements. Employing updated Doppler images, advanced LL-models of stellar atmospheres and up-to-date atomic data to properly account for opacity, we succeeded in reproducing the observed amplitude of variability and light curve shape over a wide wavelength range: from far-UV to NIR. Nevertheless, there remain some minor discrepancies between theory and observations in both the ultraviolet and u and v bands. Most likely, these discrepancies are caused by the effects of vertical elemental stratification in the CU Vir atmosphere. We also cannot exclude the "missed opacity" due to some elements not accounted for in our Doppler Imaging, as well as still incomplete knowledge of the structure of atomic transitions in the ultraviolet region. This motivates further theoretical and experimental research on atomic data and their applications in astrophysics for a more realistic modelling of spectroscopic and photometric data.

We also assessed the changes in the photometric period of CU Vir over the long baseline from 1955 to 2022 and compared them with models existing in the literature. Data from recent decades favour a gradual decrease in the period (acceleration of the apparent stellar rotation) in agreement with models [17,18]. However, firm evidence for the periodic character of the changes can be provided by observations in the next decade, when a period minimum will be reached. We encourage observers to continue monitoring CU Vir.

Author Contributions: Conceptualisation, Y.P. and T.R.; methodology, Y.P. and T.R.; software, Y.P.; formal analysis, Y.P. and I.P.; investigation, Y.P., I.P. and T.R.; resources, T.R. and Y.P.; data curation, Y.P.; writing—original draft preparation, Y.P.; writing—review and editing, Y.P., I.P. and T.R.; visualisation, Y.P.; supervision, I.P.; project administration, I.P. and T.R. All authors have read and agreed to the published version of the manuscript.

Funding: This research was funded by the grant of the Russian Science Foundation No. 24-22-00237, https://rscf.ru/en/project/24-22-00237/ accessed on 8 August 2025.

Data Availability Statement: The research is based on open data from the literature and the publicly available archives and databases. The software utilised is available upon reasonable request to the authors.

Acknowledgments: We are grateful to S. Savchenko for discussion on the model estimation methods and calling our attention to the Bayesian information criterion. We are very grateful to the reviewers for their valuable comments, which helped us improve the article.

Conflicts of Interest: The authors declare no conflicts of interest.

Abbreviations

The following abbreviations are used in this manuscript:

DI	Doppler Imaging
LTE	Local Thermodynamic Equilibrum
IUE	International Ultraviolet Explorer
HST	Hubble Space Telescope
TESS	Transiting Exoplanet Survey Satellite
MAST	Mikulski Archive for Space Telescopes

SMEI	Solar Mass Ejection Imager
FCATP	Four College Automated Photometric Telescope
UV	Ultraviolet
IR	Infrared
NIR	Near infrared
BIC	Bayesian information criterion
RMS	Root mean square
MHD	Magnetohydrodynamics

Appendix A. Bayesian Information Criterion

We define the Bayesian information criterion (BIC) introduced by Schwarz [34] via the following equation:

$$BIC = k \cdot \ln(n) - 2l, \tag{A1}$$

where k is the number of model parameters, n is the size of the sample, and l is the logarithmic likelihood function. For the calculation of the value of l, let us assume that we have n points (period determinations) with a standard deviation of each measurement σ_i. The model passes through the i-th point with deviation $\delta_i = Y_{obs} - Y_{mod}$. Assuming a Gaussian distribution of the probability of deviation of the observed point from the model prediction, then

$$f_i(Y) = \frac{1}{\sigma_i \cdot \sqrt{2\pi}} \cdot e^{-\frac{1}{2}(\frac{\delta_i}{\sigma_i})^2} \tag{A2}$$

The logarithmic likelihood function will be the product of the probabilities at each point:

$$l = \ln \prod_{i=1}^{n} \frac{1}{\sigma_i \cdot \sqrt{2\pi}} \cdot e^{-\frac{1}{2}(\frac{\delta_i}{\sigma_i})^2} = \sum_{i=1}^{n} \ln\left(\frac{1}{\sigma_i \cdot \sqrt{2\pi}} \cdot e^{-\frac{1}{2}(\frac{\delta_i}{\sigma_i})^2}\right) \tag{A3}$$

Taking the logarithm under the sum, we finally obtain

$$l = -\frac{1}{2}\left(n \ln 2\pi + 2\sum_{i=1}^{n} \ln\, \sigma_i + \sum_{i=1}^{n} (\frac{\delta_i}{\sigma_i})^2\right) \tag{A4}$$

References

1. Stibbs, D.W.N. A study of the spectrum and magnetic variable star HD 125248. *Mon. Not. R. Astron. Soc.* **1950**, *110*, 395. [CrossRef]
2. Michaud, G. Diffusion Processes in Peculiar a Stars. *Astrophys. J.* **1970**, *160*, 641. [CrossRef]
3. Michaud, G.; Alecian, G.; Richer, J. *Atomic Diffusion in Stars*; Springer: Berlin/Heidelberg, Germany, 2015. [CrossRef]
4. Khan, S.A.; Shulyak, D.V. Theoretical analysis of the atmospheres of CP stars. Effects of the individual abundance patterns. *Astron. Astrophys.* **2007**, *469*, 1083–1100. [CrossRef]
5. Krivoseina, A.A.; Ryabchikova, T.A.; Khokhlova, V.L. Distribution of SI on the Surface of the Silicon Ap-Star Cu-Virginis and Interpretation of the Lightcurves in the Vby Bands. *Nauchnye Informatsii* **1980**, *43*, 70.
6. Krtička, J.; Mikulášek, Z.; Zverko, J.; Žižňovský, J. The light variability of the helium strong star HD 37776 as a result of its inhomogeneous elemental surface distribution. *Astron. Astrophys.* **2007**, *470*, 1089–1098. [CrossRef]
7. Shulyak, D.; Krtička, J.; Mikulášek, Z.; Kochukhov, O.; Lüftinger, T. Modelling the light variability of the Ap star ε Ursae Majoris. *Astron. Astrophys.* **2010**, *524*, A66. [CrossRef]
8. Krtička, J.; Mikulášek, Z.; Lüftinger, T.; Shulyak, D.; Zverko, J.; Žižňovský, J.; Sokolov, N.A. Modelling of the ultraviolet and visual SED variability in the hot magnetic Ap star CU Virginis. *Astron. Astrophys.* **2012**, *537*, A14. [CrossRef]
9. Pakhomov, Y.; Potravnov, I.; Romanovskaya, A.; Ryabchikova, T. Modeling the TESS Light Curve of Ap Si Star MX TrA. *Universe* **2024**, *10*, 341. [CrossRef]
10. Prvák, M.; Krtička, J.; Korhonen, H. The nature of the photometric variability of HgMn stars: A test of simulated light curves of φ Phe against the TESS data. *Mon. Not. R. Astron. Soc.* **2020**, *492*, 1834–1840. [CrossRef]

11. Pyper, D.M.; Adelman, S.J. Light Curve Changes and Possible Precession in mCP Stars. *Publ. Astron. Soc. Pacific* **2021**, *133*, 084203. [CrossRef]
12. Deutsch, A.J. A New Spectrum Variable of Short Period, HD 124224. *Astrophys. J.* **1952**, *116*, 536. [CrossRef]
13. Hardie, R. Light-Variation of the Spectrum Variable HD 124224. *Astrophys. J.* **1958**, *127*, 620. [CrossRef]
14. Pyper, D.M.; Ryabchikova, T.; Malanushenko, V.; Kuschnig, R.; Plachinda, S.; Savanov, I. An abrupt decrease in the rotational period of the chemically peculiar magnetic star CU Virginis. *Astron. Astrophys.* **1998**, *339*, 822–830.
15. Pyper, D.M.; Stevens, I.R.; Adelman, S.J. An update on the rotational period of the magnetic chemically peculiar star CU Virginis. *Mon. Not. R. Astron. Soc.* **2013**, *431*, 2106–2110. [CrossRef]
16. Pyper, D.M.; Adelman, S.J. Newly Discovered Period Changes in Two mCP Stars and Updates for Previously Published Stars. *Publ. Astron. Soc. Pacific* **2020**, *132*, 024201. [CrossRef]
17. Mikulášek, Z.; Krtička, J.; Henry, G.W.; Janík, J.; Zverko, J.; Žižňovský, J.; Zejda, M.; Liška, J.; Zvěřina, P.; Kudrjavtsev, D.O.; et al. Surprising variations in the rotation of the chemically peculiar stars CU Virginis and V901 Orionis. *Astron. Astrophys.* **2011**, *534*, L5. [CrossRef]
18. Mikulášek, Z.; Krtička, J.; Henry, G.W.; Janík, J.; Pigulski, A. Towards Comprehension of the Variability of the mCP Star CU Virginis. In Proceedings of the Physics of Magnetic Stars, Nizhny Arkhyz, Russia, 1–5 October 2018; Volume 518, p. 125. [CrossRef]
19. Kuschnig, R.; Ryabchikova, T.A.; Piskunov, N.E.; Weiss, W.W.; Gelbmann, M.J. Multi element Doppler imaging of AP stars. I. He, Mg, Si, CR and Fe surface distribution for CU Virginis. *Astron. Astrophys.* **1999**, *348*, 924–932.
20. Kochukhov, O.; Lüftinger, T.; Neiner, C.; Alecian, E.; MiMeS Collaboration. Magnetic field topology of the unique chemically peculiar star CU Virginis. *Astron. Astrophys.* **2014**, *565*, A83. [CrossRef]
21. Aurière, M. Stellar Polarimetry with NARVAL. In *Setting a New Standard in the Analysis of Binary Stars*; European Astronomical Society Publications Series; Arnaud, J., Meunier, N., Eds.; Cambridge University Press: Cambridge, UK, 2003; Volume 9, p. 105.
22. Krtička, J.; Mikulášek, Z.; Henry, G.W.; Janík, J.; Kochukhov, O.; Pigulski, A.; Leto, P.; Trigilio, C.; Krtičková, I.; Lüftinger, T.; et al. HST/STIS analysis of the first main sequence pulsar CU Virginis. *Astron. Astrophys.* **2019**, *625*, A34. [CrossRef]
23. Ricker, G.R.; Winn, J.N.; Vanderspek, R.; Latham, D.W.; Bakos, G.Á.; Bean, J.L.; Berta-Thompson, Z.K.; Brown, T.M.; Buchhave, L.; Butler, N.R.; et al. Transiting Exoplanet Survey Satellite (TESS). *J. Astron. Telesc. Instruments Syst.* **2015**, *1*, 014003. [CrossRef]
24. Potravnov, I.; Ryabchikova, T.; Kitchatinov, L.; Pakhomov, Y. Long-term stability of chemical spots and reasons for the period variations in Ap star CU Vir. *Galaxies* **2025**, *13*, 90. [CrossRef]
25. Sokolov, N.A. Spectrophotometric behavior of CU Virginis. *Astron. Astrophys.* **2000**, *353*, 707–714.
26. Kuschnig, R.; Ryabchikova, T.; Piskunov, N.E.; Weiss, W.W. Ap-star mapping: He, Mg, Si, and Fe surface distributions on the CP2 star CU Virginis. In Proceedings of the IAU Symposium, Vienna, Austria, 9–13 October 1995; Volume 176, p. 135.
27. Pyper, D.M.; Adelman, S.J. Spectrophotometry of peculiar B and A stars. XVII. 63 Andromedae, HD 34452, epsilon Ursae Majoris, CQ Ursae Majoris, CU Virginis, CS Virginis and beta Coronae Borealis. *Astron. Astrophys Suppl. Ser.* **1985**, *59*, 369–397.
28. Adelman, S.J.; Dukes, R.J., Jr.; Pyper, D.M. Photometry of eight Magnetic Peculiar A Stars. *Astron. J.* **1992**, *104*, 314. [CrossRef]
29. Hoeg, E.; Bässgen, G.; Bastian, U.; Egret, D.; Fabricius, C.; Großmann, V.; Halbwachs, J.L.; Makarov, V.V.; Perryman, M.A.C.; Schwekendiek, P.; et al. The TYCHO Catalogue. *Astron. Astrophys.* **1997**, *323*, L57–L60.
30. Zechmeister, M.; Kürster, M. The generalised Lomb-Scargle periodogram. A new formalism for the floating-mean and Keplerian periodograms. *Astron. Astrophys.* **2009**, *496*, 577–584. [CrossRef]
31. Abuladze, O.P. Photoelectric observations of spectral binary variable star CU Vir. *Abastumanskaia Astrofiz. Obs. Byulleten* **1968**, *36*, 43–50.
32. Hardie, R.H.; Lieberman, L.; Reichmann, E. On the Period of HD 124224. *Publ. Astron. Soc. Pacific* **1967**, *79*, 74. [CrossRef]
33. Blanco, C.; Catalano, F.A. Photoelectric observations of magnetic stars. III. HD 124224, HD 140160, and HD 224801. *Astron. J.* **1971**, *76*, 630–633. [CrossRef]
34. Schwarz, G. Estimating the Dimension of a Model. *Ann. Stat.* **1978**, *6*, 461–464. [CrossRef]
35. Shulyak, D.; Tsymbal, V.; Ryabchikova, T.; Stütz, C.; Weiss, W.W. Line-by-line opacity stellar model atmospheres. *Astron. Astrophys.* **2004**, *428*, 993–1000. [CrossRef]
36. Kurucz, R.L. ATLAS12, SYNTHE, ATLAS9, WIDTH9, et cetera. *Mem. Della Soc. Astron. Ital. Suppl.* **2005**, *8*, 14.
37. Kurucz, R.L. *ATLAS12: Opacity Sampling Model Atmosphere Program*; Record ascl:1303.024; Astrophysics Source Code Library: College Park, MD, USA, 2013.
38. Piskunov, N.E.; Kupka, F.; Ryabchikova, T.A.; Weiss, W.W.; Jeffery, C.S. VALD: The Vienna Atomic Line Data Base. *Astron. Astrophys Suppl. Ser.* **1995**, *112*, 525.
39. Ryabchikova, T.; Piskunov, N.; Kurucz, R.L.; Stempels, H.C.; Heiter, U.; Pakhomov, Y.; Barklem, P.S. A major upgrade of the VALD database. *Physica Scripta* **2015**, *90*, 054005. [CrossRef]
40. Crawford, D.L.; Barnes, J.V. Standard stars for uvby photometry. *Astron. J.* **1970**, *75*, 978–998. [CrossRef]

41. Levenberg, K. A method for the solution of certain non-linear problems in least squares. *Q. Appl. Math.* **1944**, *2*, 164–168. [CrossRef]
42. Marquardt, D.W. An Algorithm for Least-Squares Estimation of Nonlinear Parameters. *J. Soc. Ind. Appl. Math.* **1963**, *11*, 431–441. [CrossRef]
43. Strom, S.E.; Strom, K.M. Effect of Silicon Opacity on b- and A-Star Atmospheres. *Astrophys. J.* **1969**, *155*, 17. [CrossRef]
44. Romanovskaya, A.; Ryabchikova, T.; Pakhomov, Y.; Potravnov, I.; Sitnova, T. Abundance and stratification analysis of slowly-rotating Si-star BD+00°1659 as a benchmark for ApSi-stars studies. *Galaxies* **2024**, *in preparation*.
45. Krtička, J.; Mikulášek, Z.; Henry, G.W.; Kurfürst, P.; Karlický, M. Torsional oscillations and observed rotational period variations in early-type stars. *Mon. Not. R. Astron. Soc.* **2017**, *464*, 933–939. [CrossRef]
46. Takahashi, K.; Langer, N. Standing torsional Alfvén waves as the source of the rotational period variation in magnetic early-type stars. *Astron. Astrophys.* **2025**, *696*, A129. [CrossRef]
47. Potravnov, I.S.; Kitchatinov, L.L. Tayler instability as possible reason for the period changes in Ap star 56 Ari. *arXiv* **2025**, arXiv:2504.08447. [CrossRef]

galaxies

MDPI

Article

Stark Broadening of O I Spectral Lines

Milan S. Dimitrijević [1,2,*] and Sylvie Sahal-Bréchot [2]

1 Astronomical Observatory, Volgina 7, 11060 Belgrade, Serbia
2 LUX, (Laboratoire d'étude de l'Univers et des Phénomènes Extrèmes) Observatoire de Paris, PSL (Paris Sciences & Lettres), CNRS (Centre National de la Recherche Scientifique), Sorbonne Université, F-92190 Meudon, France; sylvie.sahal-brechot@obspm.fr
* Correspondence: mdimitrijevic@aob.rs

Abstract: We do not know a priori chemical composition of a star. However, with more high resolution spectra becoming more abundant thanks to the development of space-born observations, atomic data including Stark broadening parameters for various spectral lines for elements in various ionisation stages are becoming more feasible. Particularly are important spectral lines of C-N-O peak in the distribution of abundances of chemical elements. For the calculation of Stark broadening parameters, spectral line full widths at half intensity maximum (FWHM) and shifts, we used semiclassical perturbation method. As the result, Stark widths and shifts for 36 spectral lines of neutral oxygen, broadened by the collisions with electrons, protons and helium ions, have been obtained and compared with other theoretical calculations. These data are of interest for a number of problems in astrophysics, plasma physics, as well as for inertial fusion and various plasmas in technology.

Keywords: Stark broadening; O I; spectral lines; line profiles

1. Introduction

With the development of space born telescopes and astronomical instrumentation, the need for atomic data, including Stark broadening parameters, for spectra of elements in different ionization stages, is permanently increasing, since a great number of high resolution spectra is produced. The analysis of profiles of spectral lines, broadened by fluctuating electric microfields of surrounding charged particles (Stark broadening), gives possibility to determine many useful quantities for investigation of cosmic plasma. For example Stark broadening parameters - line widths and shifts, are useful for investigations of Cepheides and stellar pairs producing supernovae of the first type (SN I), as well as for determination of abundances of oxygen and its variation during the chemical evolution of the Universe. Such data are also of interest for radiative transfer calculations, stellar spectra interpretation, synthesis and modelling. They may find applications in other topics such as fusion [1], laser produced plasma research [2], and in general, plasma science [3] and technology [4–6].

Oxygen belongs to the C-N-O peak in the distribution of abundances of chemical elements, so that data for its spectral lines are particularly important. For example neutral oxygen spectral lines are used in a study of chemical abundance variations in the globular cluster M4 (NGC 6121) [7], for oxygen abundance analysis in A-type stars γ Gem (HD 41705), o Peg (HD 214994), θ Vir (HD 114330), and ν Cap (HD 193432) [8], in 17 spectroscopic binary stars in 15 young open clusters [9], for seven very and extremely metal-poor stars in the Large Magellanic Cloud [10], for 311 metal poor stars [11], Cepheid variables [12], for investigation of oxygen rich supernova remnants [13], supernovas [14,15], SN2023ufx and its progenitor [16], and O I (7773 Å) line is observed in the spectrum of V1405 Cas [17].

Due to the importance of data on oxygen lines, a lot of experimental results have been published, as for example by Jung [18], Wiese and Murphy [19], Morris and Garrison [20], Miller and Bengtson [21], Assous [22], Goly et al. [23], Goly and Weniger [24], Sohns and Kock [25], Mijatović et al. [26], Gerhard et al. [27] and Burger and Hermann [28]. Numerous calculations, using different theoretical methods, exist as well. Stark line widths and shifts for O I have been calculated using different variants of semiclassical theory [29–31] by Griem [29], Ben Nessib et al. [32], Riviere [33] and by Alonizan et al. [34]. The Model Microfield (MMM) Method [35] has been used by Brissaud et al. [36], the computer simulation modeling [37], has been applied by Stambulchik et al. [38] for Stark broadening of O I 777 nm triplet, while in Johns et al. [39] a modified semiempirical method based on the works of Dimitrijevic and Konjevic [40,41] has been employed.

Recently, we calculated, using the semiclassical perturbation method [30,31,42], Stark widths and shifts of neutral oxygen spectral lines, for plasma conditions corresponding to experimental data in Jung [18], Wiese and Murphy [19], Morris and Garrison [20], Miller and Bengtson [21], Assous [22], Goly et al. [23], Goly and Weniger [24], Sohns and Kock [25], Mijatović et al. [26], Gerhard et al. [27], Burger and Hermann [28] and compared experiment and theory concluding that the accordance is within the error bars. Here, our objective is to calculate Stark broadening data for temperatures ranging from 2500 K to 80,000 K, for 36 O I spectral lines, in order to cover the needs for stellar spectra analysis and synthesis, oxygen abundance determination, stellar atmosphere modeling and other uses, as e.g., for laboratory, laser produced and technological plasma, where such data are useful for example for plama diagnostics, modelling, calculation of the corresponding absorption coefficient etc. We also compared our results with other theoretical calculations, when possible.

2. Theory

For the calculation of Stark full widths at half intensity maximum (FWHM) and shifts of spectral lines of neutral oxygen, the semiclassical perturbation theory [30,31,42] has been employed. It means that the radiating neutral atom is treated quantum mechanically, while perturbing particles, electrons and ions, are treated as classical particles. The connexion between these two systems is obtained using a time dependent potential. Besides the detailed description in above mentioned references, this theoretical approach has been presented many times, so that only basic expressions needed to understand how calculations have been performed, will be shown. The Stark FWHM (W) and shift (d) of an isolated, spectral line of a nonhydrogenic neutral atom, is:

$$W = N \int v f(v) dv \left(\sum_{i' \neq i} \sigma_{ii'}(v) + \sum_{f' \neq f} \sigma_{ff'}(v) + \sigma_{el} \right)$$

$$d = N \int v f(v) dv \int_{R_3}^{R_D} 2\pi\rho d\rho \sin(2\varphi_p), \quad (1)$$

where i and f are for the initial and final level of the corresponding transition; with i' and f' are denoted perturbing levels; N is perturber density; v perturber velocity, and $f(v)$ the Maxwellian distribution of electron velocities. The inelastic cross sections $\sigma_{kk'}(v)$, $k = i, f$ are calculated as an integral of the transition probability $P_{kk'}(\rho, v)$, over the impact parameter ρ:

$$\sum_{k' \neq k} \sigma_{kk'}(v) = \frac{1}{2}\pi R_1^2 + \int_{R_1}^{R_D} 2\pi\rho d\rho \sum_{k' \neq k} P_{kk'}(\rho, v). \quad (2)$$

The cross section for elastic collisions is given as:

$$\sigma_{el} = 2\pi R_2^2 + \int_{R_2}^{R_D} 2\pi\rho d\rho \sin^2 \delta,$$

$$\delta = (\varphi_p^2 + \varphi_q^2)^{\frac{1}{2}}. \quad (3)$$

Here, δ is the phase shift while φ_p (r^{-4}) and φ_q (r^{-3}), where r is the distance between the emitter and the perturber, are contributions due to polarization and quadrupole potentials. The calculation of cut-off parameters R_1, R_2, R_3, and the Debye cut-off R_D is presented in detail in Sahal-Bréchot [31].

We can see from Equation (1), that the line width W is an integral over the summ of cross sections for processes depopulating the initial and final levels of the transition forming the considered spectral line. Namely such processes decrease the lifetime of the optical electron and, it is easy to show that according to the Heisenberg's uncertainty principle, atomic energy levels and the corresponding spectral line become broader.

The Stark widths (W) and shifts (d) can be used to obtain the line profile $F(\omega)$ (where ω is the angular frequency), using the expression:

$$F(\omega) = \frac{W/(2\pi)}{(\omega - \omega_{if} - d)^2 + (W/2)^2}. \quad (4)$$

Here

$$\omega_{if} = \frac{E_i - E_f}{\hbar},$$

where E_i and E_f are the energies of the initial and final atomic energy levels, respectively.

3. Results and Discussion

Employing the semiclassical perturbation theory [30,31,42], Stark broadening parameters of 36 spectral lines of neutral oxygen, W and d, have been calculated for broadening caused by the collisions with electrons, protons and helium ions (He II), which are usually the main constituents of stellar atmospheres. Atomic energy levels of neutral oxygen, which are needed for the determination of Stark widths and shifts, have been taken from Moore [43], and the oscillator strengths have been calculated within the Coulomb approximation [44,45].

The obtained results are presented in Tables 1 and 2. In Table 1 are FWHM and shifts for 36 O I transitions for broadening by the collisions with electrons and protons. Results are given for a perturber density of 10^{16} cm^{-3} and temperatures ranging from 2500 K to 80,000 K. In Table 2, analogous results are given for spectral lines broadened by the collisions with ionized helium (He II). In [46] the results for Stark widths of helium lines, obtained by the semiclassical perturbation theory [30,31] have been compared with critically selected experimental data for spectral lines within 13 He I multiplets and it has been found that the disagreement is within the limits of 20 percent. Since O I is more complicated we assume that the error bars in the present case are within the limits of 30 percent. In the case of the shift, due to mutual cancellations of different contributions, which decreases the accuracy, one can adopt the error bars as 30 percent of the corresponding width.

Table 1. Stark broadening parameters, W and d, for spectral lines of neutral oxygen (O I), broadened by the collisions with electrons and protons, are presented. Wavelengths, calculated from the used atomic energy levels, and parameter C [47] are also given. Dividing C with the FWHM, one obtains the maximal pertuber density for which the line may be considered isolated. Results are presented for a perturber density of 10^{16} cm^{-3} and temperatures ranging from 2500 K to 80,000 K. A positive shift is towards the red part of the spectrum. An asterisk before a value indicates that this value is on the limit of validity of impact approximation.

Transition	T [K]	Electrons Width [Å]	Shift [Å]	Protons Width [Å]	Shift [Å]
Triplets					
O I 3S-3P	2500	0.686×10^{-2}	0.321×10^{-2}	0.357×10^{-2}	0.854×10^{-3}
	5000	0.721×10^{-2}	0.376×10^{-2}	0.358×10^{-2}	0.965×10^{-3}
8448.8 Å	10,000	0.822×10^{-2}	0.351×10^{-2}	0.361×10^{-2}	0.109×10^{-2}
C = 0.54×10^{19}	20,000	0.107×10^{-1}	0.306×10^{-2}	0.364×10^{-2}	0.122×10^{-2}
	40,000	0.145×10^{-1}	0.224×10^{-2}	0.368×10^{-2}	0.138×10^{-2}
	80,000	0.187×10^{-1}	0.180×10^{-2}	0.373×10^{-2}	0.155×10^{-2}
O I 3S-4P	2500	0.926×10^{-2}	0.355×10^{-2}	0.465×10^{-2}	0.967×10^{-3}
	5000	0.107×10^{-1}	0.425×10^{-2}	0.468×10^{-2}	0.110×10^{-2}
4369.5 Å	10,000	0.130×10^{-1}	0.478×10^{-2}	0.470×10^{-2}	0.125×10^{-2}
C = 0.42×10^{18}	20,000	0.161×10^{-1}	0.479×10^{-2}	0.473×10^{-2}	0.141×10^{-2}
	40,000	0.200×10^{-1}	0.372×10^{-2}	0.478×10^{-2}	0.159×10^{-2}
	80,000	0.236×10^{-1}	0.298×10^{-2}	0.485×10^{-2}	0.178×10^{-2}
O I 3S-5P	2500	0.202×10^{-1}	-0.684×10^{-2}	0.999×10^{-2}	-0.211×10^{-2}
	5000	0.238×10^{-1}	-0.581×10^{-2}	0.101×10^{-1}	-0.244×10^{-2}
3693.6 Å	10,000	0.297×10^{-1}	-0.392×10^{-2}	0.101×10^{-1}	-0.278×10^{-2}
C = 0.13×10^{18}	20,000	0.378×10^{-1}	-0.285×10^{-2}	0.102×10^{-1}	-0.315×10^{-2}
	40,000	0.459×10^{-1}	-0.200×10^{-2}	0.103×10^{-1}	-0.356×10^{-2}
	80,000	0.523×10^{-1}	-0.110×10^{-2}	0.104×10^{-1}	-0.401×10^{-2}
O I 3S-6P	2500	0.202×10^{-1}	-0.685×10^{-2}	0.999×10^{-2}	-0.210×10^{-2}
	5000	0.238×10^{-1}	-0.573×10^{-2}	0.101×10^{-1}	-0.243×10^{-2}
3693.6 Å	10,000	0.297×10^{-1}	-0.382×10^{-2}	0.101×10^{-1}	-0.277×10^{-2}
C = 0.13×10^{18}	20,000	0.378×10^{-1}	-0.272×10^{-2}	0.102×10^{-1}	-0.314×10^{-2}
	40,000	0.459×10^{-1}	-0.187×10^{-2}	0.103×10^{-1}	-0.355×10^{-2}
	80,000	0.523×10^{-1}	-0.100×10^{-2}	0.104×10^{-1}	-0.399×10^{-2}
O I 4S-4P	2500	0.452	−0.167	0.204	-0.434×10^{-1}
	5000	0.538	−0.196	0.205	-0.495×10^{-1}
28,935.2 Å	10,000	0.693	−0.196	0.206	-0.561×10^{-1}
C = 0.18×10^{20}	20,000	0.922	−0.177	0.208	-0.632×10^{-1}
	40,000	1.19	−0.138	0.210	-0.712×10^{-1}
	80,000	1.44	−0.112	0.213	-0.801×10^{-1}
O I 4S-5P	2500	0.280	−0.128	0.126	-0.324×10^{-1}
	5000	0.331	−0.135	0.128	-0.374×10^{-1}
13,082.2 Å	10,000	0.412	−0.126	0.129	-0.427×10^{-1}
C = 0.16×10^{19}	20,000	0.527	−0.111	0.131	-0.485×10^{-1}
	40,000	0.647	-0.928×10^{-1}	0.133	-0.549×10^{-1}
	80,000	0.741	-0.669×10^{-1}	0.135	-0.618×10^{-1}
O I 4S-6P	2500	0.280	−0.128	0.126	-0.323×10^{-1}
	5000	0.330	−0.134	0.128	-0.373×10^{-1}
13,082.2 Å	10,000	0.411	−0.125	0.129	-0.426×10^{-1}
C = 0.16×10^{19}	20,000	0.527	−0.110	0.130	-0.484×10^{-1}
	40,000	0.647	-0.915×10^{-1}	0.132	-0.548×10^{-1}
	80,000	0.741	-0.659×10^{-1}	0.135	-0.616×10^{-1}
O I 2P-3S	2500	0.895×10^{-4}	0.809×10^{-4}	0.248×10^{-4}	0.230×10^{-4}
	5000	0.104×10^{-3}	0.931×10^{-4}	0.278×10^{-4}	0.261×10^{-4}
1303.5 Å	10,000	0.124×10^{-3}	0.109×10^{-3}	0.312×10^{-4}	0.293×10^{-4}
C = 0.20×10^{18}	20,000	0.142×10^{-3}	0.124×10^{-3}	0.350×10^{-4}	0.330×10^{-4}
	40,000	0.153×10^{-3}	0.127×10^{-3}	0.393×10^{-4}	0.371×10^{-4}
	80,000	0.162×10^{-3}	0.116×10^{-3}	0.442×10^{-4}	0.417×10^{-4}

Table 1. *Cont.*

Transition	T [K]	Electrons Width [Å]	Shift [Å]	Protons Width [Å]	Shift [Å]
Triplets					
O I 2P-4S	2500	0.436×10^{-3}	0.332×10^{-3}	0.101×10^{-3}	0.908×10^{-4}
	5000	0.513×10^{-3}	0.389×10^{-3}	0.113×10^{-3}	0.104×10^{-3}
1040.1 Å	10,000	0.576×10^{-3}	0.451×10^{-3}	0.127×10^{-3}	0.118×10^{-3}
C = 0.37×10^{17}	20,000	0.608×10^{-3}	0.476×10^{-3}	0.143×10^{-3}	0.134×10^{-3}
	40,000	0.640×10^{-3}	0.444×10^{-3}	0.160×10^{-3}	0.150×10^{-3}
	80,000	0.689×10^{-3}	0.357×10^{-3}	0.180×10^{-3}	0.169×10^{-3}
O I 3P-4S	2500	0.714×10^{-1}	0.497×10^{-1}	0.168×10^{-1}	0.135×10^{-1}
	5000	0.821×10^{-1}	0.604×10^{-1}	0.184×10^{-1}	0.154×10^{-1}
13,168.2 Å	10,000	0.907×10^{-1}	0.674×10^{-1}	0.203×10^{-1}	0.175×10^{-1}
C = 0.60×10^{19}	20,000	0.102	0.683×10^{-1}	0.224×10^{-1}	0.198×10^{-1}
	40,000	0.116	0.549×10^{-1}	0.249×10^{-1}	0.223×10^{-1}
	80,000	0.138	0.436×10^{-1}	0.277×10^{-1}	0.251×10^{-1}
O I 2P-3D	2500	0.322×10^{-3}	0.229×10^{-3}	0.114×10^{-3}	0.618×10^{-4}
	5000	0.371×10^{-3}	0.264×10^{-3}	0.119×10^{-3}	0.704×10^{-4}
1026.6 Å	10,000	0.414×10^{-3}	0.293×10^{-3}	0.125×10^{-3}	0.799×10^{-4}
C = 0.23×10^{17}	20,000	0.453×10^{-3}	0.298×10^{-3}	0.132×10^{-3}	0.903×10^{-4}
	40,000	0.494×10^{-3}	0.271×10^{-3}	0.141×10^{-3}	0.102×10^{-3}
	80,000	0.542×10^{-3}	0.219×10^{-3}	0.151×10^{-3}	0.114×10^{-3}
O I 2P-4D	2500	0.588×10^{-2}	0.275×10^{-2}	* 0.157×10^{-2}	* 0.115×10^{-2}
	5000	0.575×10^{-2}	0.244×10^{-2}	* 0.177×10^{-2}	* 0.141×10^{-2}
972.5 Å	10,000	0.538×10^{-2}	0.202×10^{-2}	* 0.202×10^{-2}	* 0.167×10^{-2}
C = 0.57×10^{15}	20,000	0.497×10^{-2}	0.148×10^{-2}	* 0.235×10^{-2}	* 0.193×10^{-2}
	40,000	0.459×10^{-2}	0.928×10^{-3}	0.281×10^{-2}	0.222×10^{-2}
	80,000	0.421×10^{-2}	0.690×10^{-3}	0.345×10^{-2}	0.256×10^{-2}
O I 3P-3D	2500	0.371×10^{-1}	0.221×10^{-1}	0.151×10^{-1}	0.581×10^{-2}
	5000	0.411×10^{-1}	0.242×10^{-1}	0.154×10^{-1}	0.661×10^{-2}
11,289.9 Å	10,000	0.473×10^{-1}	0.232×10^{-1}	0.157×10^{-1}	0.749×10^{-2}
C = 0.28×10^{19}	20,000	0.573×10^{-1}	0.168×10^{-1}	0.162×10^{-1}	0.844×10^{-2}
	40,000	0.725×10^{-1}	0.115×10^{-1}	0.167×10^{-1}	0.951×10^{-2}
	80,000	0.869×10^{-1}	0.818×10^{-2}	0.174×10^{-1}	0.107×10^{-1}
O I 3P-4D	2500	0.306	0.143	* 0.812×10^{-1}	* 0.596×10^{-1}
	5000	0.299	0.128	* 0.918×10^{-1}	* 0.731×10^{-1}
7004.1 Å	10,000	0.280	0.102	* 0.105	* 0.865×10^{-1}
C = 0.29×10^{17}	20,000	0.260	0.744×10^{-1}	* 0.122	* 0.100
	40,000	0.243	0.493×10^{-1}	0.146	0.115
	80,000	0.225	0.312×10^{-1}	0.179	0.133
O I 4P-4D	2500	6.09	2.78	* 1.60	* 1.16
	5000	6.00	2.38	* 1.81	* 1.43
30,985.0 Å	10,000	5.76	1.87	* 2.06	* 1.69
C = 0.58×10^{18}	20,000	5.56	1.24	* 2.39	* 1.95
	40,000	5.41	0.796	2.86	2.24
	80,000	5.21	0.490	3.51	2.59
O I 3D-4P	2500	1.07	0.354×10^{-2}	0.567	-0.256×10^{-1}
	5000	1.28	0.305×10^{-1}	0.568	-0.289×10^{-1}
45,608.5 Å	10,000	1.64	0.518×10^{-1}	0.569	-0.326×10^{-1}
C = 0.46×10^{20}	20,000	2.15	0.439×10^{-1}	0.569	-0.366×10^{-1}
	40,000	2.74	0.421×10^{-1}	0.570	-0.412×10^{-1}
	80,000	3.27	0.293×10^{-1}	0.572	-0.463×10^{-1}
O I 3D-5P	2500	0.394	−0.163	0.185	-0.428×10^{-1}
	5000	0.466	−0.165	0.187	-0.494×10^{-1}
15,672.6 Å	10,000	0.580	−0.133	0.189	-0.564×10^{-1}
C = 0.24×10^{19}	20,000	0.738	−0.118	0.190	-0.640×10^{-1}
	40,000	0.899	-0.869×10^{-1}	0.193	-0.723×10^{-1}
	80,000	1.02	-0.630×10^{-1}	0.196	-0.814×10^{-1}
O I 3D-6P	2500	0.394	−0.166	0.185	-0.426×10^{-1}
	5000	0.466	−0.163	0.187	-0.492×10^{-1}
15,672.6 Å	10,000	0.580	−0.132	0.189	-0.562×10^{-1}
C = 0.24×10^{19}	20,000	0.738	−0.116	0.190	-0.638×10^{-1}
	40,000	0.899	-0.860×10^{-1}	0.193	-0.721×10^{-1}
	80,000	1.02	-0.613×10^{-1}	0.196	-0.812×10^{-1}

Table 1. *Cont.*

Transition	T [K]	Electrons Width [Å]	Shift [Å]	Protons Width [Å]	Shift [Å]
Triplets					
O I 4D-5P	2500	79.4	−35.3	19.8	* −13.4
	5000	81.0	−30.7	22.1	* −16.5
104,101.6 Å	10,000	81.6	−24.3	24.9	* −19.6
C = 0.65 × 10^{19}	20,000	83.3	−16.9	28.6	* −22.7
	40,000	85.7	−11.7	33.8	−26.0
	80,000	86.2	−8.12	41.1	−30.0
O I 4D-6P	2500	79.3	−34.7	* 19.8	* −13.4
	5000	81.0	−30.8	* 22.1	* −16.5
104,101.6 Å	10,000	81.6	−24.6	* 24.9	* −19.5
C = 0.65 × 10^{19}	20,000	83.3	−16.9	* 28.5	* −22.7
	40,000	85.7	−11.6	33.8	−26.0
	80,000	86.2	−8.11	41.1	−30.0
Quintets					
O I 3S-3P	2500	0.448 × 10^{-2}	0.153 × 10^{-2}	0.245 × 10^{-2}	0.414 × 10^{-3}
	5000	0.463 × 10^{-2}	0.169 × 10^{-2}	0.245 × 10^{-2}	0.466 × 10^{-3}
7775.5 Å	10,000	0.528 × 10^{-2}	0.167 × 10^{-2}	0.246 × 10^{-2}	0.525 × 10^{-3}
C = 0.53 × 10^{19}	20,000	0.694 × 10^{-2}	0.123 × 10^{-2}	0.247 × 10^{-2}	0.590 × 10^{-3}
	40,000	0.959 × 10^{-2}	0.917 × 10^{-3}	0.248 × 10^{-2}	0.663 × 10^{-3}
	80,000	0.125 × 10^{-1}	0.716 × 10^{-3}	0.249 × 10^{-2}	0.745 × 10^{-3}
O I 3S-4P	2500	0.704 × 10^{-2}	−0.795 × 10^{-3}	0.336 × 10^{-2}	−0.423 × 10^{-3}
	5000	0.815 × 10^{-2}	−0.188 × 10^{-4}	0.336 × 10^{-2}	−0.480 × 10^{-3}
3948.5 Å	10,000	0.100 × 10^{-1}	0.682 × 10^{-3}	0.337 × 10^{-2}	−0.543 × 10^{-3}
C = 0.26 × 10^{18}	20,000	0.124 × 10^{-1}	0.119 × 10^{-2}	0.338 × 10^{-2}	−0.611 × 10^{-3}
	40,000	0.151 × 10^{-1}	0.989 × 10^{-3}	0.340 × 10^{-2}	−0.687 × 10^{-3}
	80,000	0.177 × 10^{-1}	0.786 × 10^{-3}	0.343 × 10^{-2}	−0.773 × 10^{-3}
O I 3S-5P	2500	0.193 × 10^{-1}	−0.829 × 10^{-2}	0.775 × 10^{-2}	−0.248 × 10^{-2}
	5000	0.223 × 10^{-1}	−0.697 × 10^{-2}	0.787 × 10^{-2}	−0.287 × 10^{-2}
3349.2 Å	10,000	0.272 × 10^{-1}	−0.416 × 10^{-2}	0.801 × 10^{-2}	−0.329 × 10^{-2}
C = 0.85 × 10^{17}	20,000	0.339 × 10^{-1}	−0.250 × 10^{-2}	0.820 × 10^{-2}	−0.373 × 10^{-2}
	40,000	0.401 × 10^{-1}	−0.143 × 10^{-2}	0.845 × 10^{-2}	−0.423 × 10^{-2}
	80,000	0.451 × 10^{-1}	−0.409 × 10^{-3}	0.881 × 10^{-2}	−0.476 × 10^{-2}
O I 3S-6P	2500	0.496 × 10^{-1}	−0.274 × 10^{-1}	* 0.169 × 10^{-1}	* −0.695 × 10^{-2}
	5000	0.569 × 10^{-1}	−0.245 × 10^{-1}	* 0.175 × 10^{-1}	* −0.831 × 10^{-2}
3123.0 Å	10,000	0.680 × 10^{-1}	−0.170 × 10^{-1}	* 0.182 × 10^{-1}	* −0.969 × 10^{-2}
C = 0.39 × 10^{17}	20,000	0.836 × 10^{-1}	−0.122 × 10^{-1}	0.190 × 10^{-1}	−0.111 × 10^{-1}
	40,000	0.965 × 10^{-1}	−0.742 × 10^{-2}	0.199 × 10^{-1}	−0.127 × 10^{-1}
	80,000	0.106	−0.277 × 10^{-2}	0.211 × 10^{-1}	−0.144 × 10^{-1}
O I 4S-4P	2500	0.500	−0.254	0.172	−0.654 × 10^{-1}
	5000	0.572	−0.283	0.176	−0.748 × 10^{-1}
27,644.6 Å	10,000	0.680	−0.292	0.180	−0.849 × 10^{-1}
C = 0.13 × 10^{20}	20,000	0.840	−0.273	0.185	−0.962 × 10^{-1}
	40,000	1.04	−0.216	0.192	−0.108
	80,000	1.22	−0.176	0.201	−0.122
O I 4S-5P	2500	0.279	−0.144	0.105	* −0.371 × 10^{-1}
	5000	0.321	−0.147	0.107	* −0.431 × 10^{-1}
12,270.6 Å	10,000	0.389	−0.118	0.110	−0.494 × 10^{-1}
C = 0.11 × 10^{19}	20,000	0.491	−0.103	0.113	−0.562 × 10^{-1}
	40,000	0.592	−0.789 × 10^{-1}	0.117	−0.637 × 10^{-1}
	80,000	0.671	−0.510 × 10^{-1}	0.123	−0.717 × 10^{-1}
O I 4S-6P	2500	0.489	−0.265	* 0.163	* −0.682 × 10^{-1}
	5000	0.561	−0.258	* 0.170	* −0.816 × 10^{-1}
9697.5 Å	10,000	0.669	−0.189	* 0.177	* −0.951 × 10^{-1}
C = 0.38 × 10^{18}	20,000	0.828	−0.150	0.184	−0.109
	40,000	0.963	−0.963 × 10^{-1}	0.194	−0.125
	80,000	1.06	−0.427 × 10^{-1}	0.205	−0.141
O I 3P-4S	2500	0.490 × 10^{-1}	0.349 × 10^{-1}	0.115 × 10^{-1}	0.950 × 10^{-2}
	5000	0.569 × 10^{-1}	0.417 × 10^{-1}	0.126 × 10^{-1}	0.108 × 10^{-1}
11,302.5 Å	10,000	0.634 × 10^{-1}	0.485 × 10^{-1}	0.140 × 10^{-1}	0.123 × 10^{-1}
C = 0.46 × 10^{19}	20,000	0.694 × 10^{-1}	0.492 × 10^{-1}	0.155 × 10^{-1}	0.139 × 10^{-1}
	40,000	0.766 × 10^{-1}	0.414 × 10^{-1}	0.173 × 10^{-1}	0.157 × 10^{-1}
	80,000	0.900 × 10^{-1}	0.317 × 10^{-1}	0.193 × 10^{-1}	0.177 × 10^{-1}

Table 1. *Cont.*

Transition	T [K]	Electrons Width [Å]	Shift [Å]	Protons Width [Å]	Shift [Å]
Quintets					
O I 3P-3D	2500	0.314×10^{-1}	0.212×10^{-1}	0.105×10^{-1}	0.559×10^{-2}
	5000	0.358×10^{-1}	0.246×10^{-1}	0.109×10^{-1}	0.638×10^{-2}
9266.4 Å	10,000	0.396×10^{-1}	0.248×10^{-1}	0.114×10^{-1}	0.724×10^{-2}
$C = 0.14 \times 10^{19}$	20,000	0.442×10^{-1}	0.233×10^{-1}	0.121×10^{-1}	0.819×10^{-2}
	40,000	0.499×10^{-1}	0.182×10^{-1}	0.129×10^{-1}	0.921×10^{-2}
	80,000	0.563×10^{-1}	0.145×10^{-1}	0.140×10^{-1}	0.104×10^{-1}
O I 3P-4D	2500	0.193	0.111	* 0.469×10^{-1}	* 0.352×10^{-1}
	5000	0.197	0.101	* 0.526×10^{-1}	* 0.425×10^{-1}
6159.0 Å	10,000	0.192	0.868×10^{-1}	0.593×10^{-1}	0.499×10^{-1}
$C = 0.39 \times 10^{17}$	20,000	0.184	0.668×10^{-1}	0.677×10^{-1}	0.576×10^{-1}
	40,000	0.175	0.457×10^{-1}	0.788×10^{-1}	0.657×10^{-1}
	80,000	0.165	0.301×10^{-1}	0.945×10^{-1}	0.748×10^{-1}
O I 4P-4D	2500	3.75	2.06	* 0.885	* 0.653
	5000	3.87	1.91	* 0.990	* 0.791
26,514.7 Å	10,000	3.84	1.64	1.11	0.928
$C = 0.72 \times 10^{18}$	20,000	3.78	1.19	1.27	1.07
	40,000	3.74	0.815	1.47	1.22
	80,000	3.63	0.512	1.77	1.39
O I 3D-4P	2500	2.31	−1.13	0.903	−0.275
	5000	2.66	−1.09	0.913	−0.315
59,761.5 Å	10,000	3.16	−0.987	0.926	−0.357
$C = 0.60 \times 10^{20}$	20,000	3.91	−0.751	0.943	−0.404
	40,000	4.74	−0.624	0.968	−0.455
	80,000	5.44	−0.464	1.01	−0.512
O I 3D-5P	2500	0.746	−0.398	* 0.250	* −0.103
	5000	0.860	−0.384	* 0.260	* −0.123
11,950.4 Å	10,000	1.03	−0.294	* 0.270	* −0.144
$C = 0.58 \times 10^{18}$	20,000	1.26	−0.205	0.281	−0.165
	40,000	1.46	−0.131	0.296	−0.188
	80,000	1.60	-0.498×10^{-1}	0.313	−0.214
O I 3D-6P	2500	0.487	−0.231	0.186	-0.629×10^{-1}
	5000	0.568	−0.211	0.189	-0.730×10^{-1}
16,114.7 Å	10,000	0.686	−0.155	0.193	-0.836×10^{-1}
$C = 0.20 \times 10^{19}$	20,000	0.856	−0.130	0.198	-0.951×10^{-1}
	40,000	1.02	−0.101	0.205	−0.108
	80,000	1.14	-0.600×10^{-1}	0.215	−0.121
O I 4D-5P	2500	11.4	−6.00	* 2.63	* −1.46
	5000	12.4	−5.72	* 2.83	* −1.79
34,210.0 Å	10,000	13.5	−4.43	* 3.07	* −2.12
$C = 0.12 \times 10^{19}$	20,000	15.1	−3.13	* 3.35	* −2.46
	40,000	16.5	−2.06	3.73	−2.81
	80,000	17.2	−1.12	4.26	−3.20
O I 4D-6P	2500	111.	−56.9	* 25.2	* −17.0
	5000	118.	−53.2	* 27.7	* −20.6
131,456.1 Å	10,000	123.	−45.7	* 30.8	* −24.2
$C = 0.18 \times 10^{20}$	20,000	129.	−32.2	34.6	−27.9
	40,000	135.	−23.2	39.7	−31.8
	80,000	137.	−14.6	47.0	−36.2

Table 2. Stark broadening parameters, *W* and *d*, for spectral lines of neutral oxygen (O I), broadened by the collisions with He II ions, are presented. Wavelengths, calculated from the used atomic energy levels, and parameter *C* [47] are also given. Dividing *C* with the FWHM, one obtains the maximal pertuber density for which the line may be considered isolated. Results are presented for a perturber density of 10^{16} cm^{-3} and temperatures ranging from 2500 K to 80,000 K. A positive shift is towards the red part of the spectrum. An asterisk before a value indicates that this value is on the limit of validity of impact approximation. The empty places are because values for which the impact approximation is not valid are excluded.

Transition	**T [K]**	**He II Width [Å]**	**Shift [Å]**
Triplets			
O I 3S-3P	2500	0.355×10^{-2}	0.701×10^{-3}
	5000	0.356×10^{-2}	0.794×10^{-3}
8448.8 Å	10,000	0.357×10^{-2}	0.895×10^{-3}
C = 0.54×10^{19}	20,000	0.359×10^{-2}	0.101×10^{-2}
	40,000	0.362×10^{-2}	0.113×10^{-2}
	80,000	0.365×10^{-2}	0.127×10^{-2}
O I 3S-4P	2500	0.463×10^{-2}	0.790×10^{-3}
	5000	0.465×10^{-2}	0.903×10^{-3}
4369.5 Å	10,000	0.467×10^{-2}	0.103×10^{-2}
C = 0.42×10^{18}	20,000	0.469×10^{-2}	0.116×10^{-2}
	40,000	0.471×10^{-2}	0.131×10^{-2}
	80,000	0.474×10^{-2}	0.147×10^{-2}
O I 3S-5P	2500	* 0.989×10^{-2}	* -0.172×10^{-2}
	5000	* 0.100×10^{-1}	* -0.199×10^{-2}
3693.6 Å	10,000	0.101×10^{-1}	-0.228×10^{-2}
C = 0.13×10^{18}	20,000	0.101×10^{-1}	-0.259×10^{-2}
	40,000	0.102×10^{-1}	-0.293×10^{-2}
	80,000	0.102×10^{-1}	-0.330×10^{-2}
O I 3S-6P	2500	* 0.989×10^{-2}	* -0.171×10^{-2}
	5000	* 0.100×10^{-1}	* -0.198×10^{-2}
3693.6 Å	10,000	0.101×10^{-1}	-0.227×10^{-2}
C = 0.13×10^{18}	20,000	0.101×10^{-1}	-0.258×10^{-2}
	40,000	0.102×10^{-1}	-0.292×10^{-2}
	80,000	0.102×10^{-1}	-0.329×10^{-2}
O I 4S-4P	2500	0.203	-0.355×10^{-1}
	5000	0.204	-0.405×10^{-1}
28,935.2 Å	10,000	0.205	-0.460×10^{-1}
C = 0.18×10^{20}	20,000	0.206	-0.521×10^{-1}
	40,000	0.207	-0.586×10^{-1}
	80,000	0.208	-0.660×10^{-1}
O I 4S-5P	2500	* 0.125	* -0.262×10^{-1}
	5000	* 0.126	* -0.305×10^{-1}
13,082.2 Å	10,000	0.127	-0.350×10^{-1}
C = 0.16×10^{19}	20,000	0.128	-0.398×10^{-1}
	40,000	0.130	-0.451×10^{-1}
	80,000	0.131	-0.509×10^{-1}
O I 4S-6P	2500	* 0.125	* -0.261×10^{-1}
	5000	* 0.126	* -0.304×10^{-1}
13,082.2 Å	10,000	0.127	-0.349×10^{-1}
C = 0.16×10^{19}	20,000	0.128	-0.397×10^{-1}
	40,000	0.129	-0.450×10^{-1}
	80,000	0.131	-0.507×10^{-1}

Table 2. *Cont.*

Transition	T [K]	He II Width [Å]	Shift [Å]
Triplets			
O I 2P-3S	2500	0.204×10^{-4}	0.189×10^{-4}
	5000	0.229×10^{-4}	0.214×10^{-4}
1303.5 Å	10,000	0.257×10^{-4}	0.241×10^{-4}
$C = 0.20 \times 10^{18}$	20,000	0.289×10^{-4}	0.272×10^{-4}
	40,000	0.324×10^{-4}	0.306×10^{-4}
	80,000	0.364×10^{-4}	0.344×10^{-4}
O I 2P-4S	2500	0.831×10^{-4}	0.740×10^{-4}
	5000	0.932×10^{-4}	0.850×10^{-4}
1040.1 Å	10,000	0.105×10^{-3}	0.968×10^{-4}
$C = 0.37 \times 10^{17}$	20,000	0.118×10^{-3}	0.110×10^{-3}
	40,000	0.132×10^{-3}	0.124×10^{-3}
	80,000	0.148×10^{-3}	0.139×10^{-3}
O I 3P-4S	2500	0.145×10^{-1}	0.110×10^{-1}
	5000	0.158×10^{-1}	0.126×10^{-1}
13,168.2 Å	10,000	0.173×10^{-1}	0.143×10^{-1}
$C = 0.60 \times 10^{19}$	20,000	0.190×10^{-1}	0.163×10^{-1}
	40,000	0.209×10^{-1}	0.183×10^{-1}
	80,000	0.232×10^{-1}	0.206×10^{-1}
O I 2P-3D	2500	0.109×10^{-3}	0.504×10^{-4}
	5000	0.112×10^{-3}	0.577×10^{-4}
1026.6 Å	10,000	0.116×10^{-3}	0.656×10^{-4}
$C = 0.23 \times 10^{17}$	20,000	0.121×10^{-3}	0.743×10^{-4}
	40,000	0.127×10^{-3}	0.836×10^{-4}
	80,000	0.135×10^{-3}	0.941×10^{-4}
O I 2P-4D	2500	* 0.129×10^{-2}	* 0.896×10^{-3}
	5000	* 0.144×10^{-2}	* 0.113×10^{-2}
972.5 Å	10,000	* 0.161×10^{-2}	* 0.135×10^{-2}
$C = 0.57 \times 10^{15}$	20,000	* 0.181×10^{-2}	* 0.158×10^{-2}
	40,000	* 0.203×10^{-2}	* 0.181×10^{-2}
	80,000	0.230×10^{-2}	0.206×10^{-2}
O I 3P-3D	2500	0.148×10^{-1}	0.475×10^{-2}
	5000	0.150×10^{-1}	0.542×10^{-2}
11,289.9 Å	10,000	0.152×10^{-1}	0.615×10^{-2}
$C = 0.28 \times 10^{19}$	20,000	0.155×10^{-1}	0.695×10^{-2}
	40,000	0.158×10^{-1}	0.783×10^{-2}
	80,000	0.163×10^{-1}	0.881×10^{-2}
O I 3P-4D	2500	* 0.669×10^{-1}	* 0.464×10^{-1}
	5000	* 0.748×10^{-1}	* 0.584×10^{-1}
7004.1 Å	10,000	* 0.836×10^{-1}	* 0.700×10^{-1}
$C = 0.29 \times 10^{17}$	20,000	* 0.936×10^{-1}	* 0.817×10^{-1}
	40,000	* 0.105	* 0.939×10^{-1}
	80,000	0.119	0.107
O I 4P-4D	2500	* 1.32	* 0.906
	5000	* 1.48	* 1.14
30,985.0Å	10,000	* 1.65	* 1.36
$C = 0.58 \times 10^{18}$	20,000	* 1.84	* 1.59
	40,000	* 2.07	* 1.83
	80,000	2.34	2.08

Table 2. *Cont.*

Transition	T [K]	He II Width [Å]	Shift [Å]
Triplets			
O I 3D-4P	2500	0.566	-0.210×10^{-1}
	5000	0.568	-0.238×10^{-1}
45,608.5 Å	10,000	0.568	-0.268×10^{-1}
C = 0.46×10^{20}	20,000	0.569	-0.302×10^{-1}
	40,000	0.569	-0.339×10^{-1}
	80,000	0.569	-0.381×10^{-1}
O I 3D-5P	2500	* 0.183	* -0.347×10^{-1}
	5000	* 0.185	* -0.403×10^{-1}
15,672.6 Å	10,000	0.187	-0.462×10^{-1}
C = 0.24×10^{19}	20,000	0.188	-0.525×10^{-1}
	40,000	0.189	-0.595×10^{-1}
	80,000	0.191	-0.670×10^{-1}
O I 3D-6P	2500	* 0.183	* -0.346×10^{-1}
	5000	* 0.185	* -0.401×10^{-1}
15,672.6 Å	10,000	0.187	-0.460×10^{-1}
C = 0.24×10^{19}	20,000	0.188	-0.523×10^{-1}
	40,000	0.189	-0.593×10^{-1}
	80,000	0.191	-0.668×10^{-1}
O I 4D-5P	2500		
	5000	* 18.5	* −13.2
104,101.6 Å	10,000	* 20.3	* −15.8
C = 0.65×10^{19}	20,000	* 22.5	* −18.5
	40,000	* 24.9	* −21.2
	80,000	* 28.0	* −24.2
O I 4D-6P	2500		
	5000	* 18.5	* −13.2
104,101.6 Å	10,000	* 20.3	* −15.8
C = 0.65×10^{19}	20,000	* 22.5	* −18.5
	40,000	* 24.9	* −21.2
	80,000	* 28.0	* −24.2
Quintets			
O I 3S-3P	2500	0.244×10^{-2}	0.340×10^{-3}
	5000	0.245×10^{-2}	0.384×10^{-3}
7775.5 Å	10,000	0.245×10^{-2}	0.432×10^{-3}
C = 0.53×10^{19}	20,000	0.245×10^{-2}	0.486×10^{-3}
	40,000	0.246×10^{-2}	0.546×10^{-3}
	80,000	0.247×10^{-2}	0.614×10^{-3}
O I 3S-4P	2500	0.335×10^{-2}	-0.347×10^{-3}
	5000	0.336×10^{-2}	-0.394×10^{-3}
3948.5 Å	10,000	0.336×10^{-2}	-0.447×10^{-3}
C = 0.26×10^{18}	20,000	0.337×10^{-2}	-0.503×10^{-3}
	40,000	0.337×10^{-2}	-0.566×10^{-3}
	80,000	0.338×10^{-2}	-0.637×10^{-3}
O I 3S-5P	2500	* 0.760×10^{-2}	* -0.200×10^{-2}
	5000	0.772×10^{-2}	-0.234×10^{-2}
3349.2 Å	10,000	0.782×10^{-2}	-0.269×10^{-2}
C = 0.85×10^{17}	20,000	0.793×10^{-2}	-0.306×10^{-2}
	40,000	0.806×10^{-2}	-0.347×10^{-2}
	80,000	0.824×10^{-2}	-0.392×10^{-2}

Table 2. *Cont.*

Transition	T [K]	He II Width [Å]	Shift [Å]
Quintets			
O I 3S-6P	2500		
	5000	* 0.167×10^{-1}	* -0.669×10^{-2}
3123.0 Å	10,000	* 0.172×10^{-1}	* -0.788×10^{-2}
C = 0.39×10^{17}	20,000	* 0.178×10^{-1}	* -0.909×10^{-2}
	40,000	0.185×10^{-1}	-0.104×10^{-1}
	80,000	0.193×10^{-1}	-0.118×10^{-1}
O I 4S-4P	2500	0.169	-0.533×10^{-1}
	5000	0.171	-0.612×10^{-1}
27,644.6 Å	10,000	0.174	-0.697×10^{-1}
C = 0.13×10^{20}	20,000	0.177	-0.790×10^{-1}
	40,000	0.181	-0.891×10^{-1}
	80,000	0.187	−0.100
O I 4S-5P	2500	0.103	* -0.300×10^{-1}
	5000	0.105	* -0.351×10^{-1}
12,270.6 Å	10,000	0.106	-0.404×10^{-1}
C = 0.11×10^{19}	20,000	0.108	-0.461×10^{-1}
	40,000	0.111	-0.523×10^{-1}
	80,000	0.114	-0.591×10^{-1}
O I 4S-6P	2500		
	5000	* 0.162	* -0.657×10^{-1}
9697.5 Å	10,000	* 0.167	* -0.773×10^{-1}
C = 0.38×10^{18}	20,000	* 0.173	* -0.893×10^{-1}
	40,000	0.179	−0.102
	80,000	0.187	−0.116
O I 3P-4S	2500	0.980×10^{-2}	0.775×10^{-2}
	5000	0.107×10^{-1}	0.888×10^{-2}
11,302.5 Å	10,000	0.118×10^{-1}	0.101×10^{-1}
C = 0.46×10^{19}	20,000	0.131×10^{-1}	0.115×10^{-1}
	40,000	0.145×10^{-1}	0.129×10^{-1}
	80,000	0.161×10^{-1}	0.145×10^{-1}
O I 3P-3D	2500	0.998×10^{-2}	0.457×10^{-2}
	5000	0.103×10^{-1}	0.523×10^{-2}
9266.4 Å	10,000	0.106×10^{-1}	0.594×10^{-2}
C = 0.14×10^{19}	20,000	0.111×10^{-1}	0.674×10^{-2}
	40,000	0.116×10^{-1}	0.758×10^{-2}
	80,000	0.123×10^{-1}	0.854×10^{-2}
O I 3P-4D	2500	* 0.391×10^{-1}	* 0.277×10^{-1}
	5000	* 0.435×10^{-1}	* 0.341×10^{-1}
6159.0 Å	10,000	* 0.484×10^{-1}	* 0.405×10^{-1}
C = 0.39×10^{17}	20,000	* 0.540×10^{-1}	* 0.470×10^{-1}
	40,000	0.603×10^{-1}	0.538×10^{-1}
	80,000	0.678×10^{-1}	0.612×10^{-1}
O I 4P-4D	2500	* 0.742	* 0.514
	5000	* 0.823	* 0.634
26,514.7 Å	10,000	* 0.913	* 0.753
C = 0.72×10^{18}	20,000	* 1.02	* 0.873
	40,000	1.13	1.00
	80,000	1.27	1.14

Table 2. *Cont.*

Transition	T [K]	He II Width [Å]	Shift [Å]
Quintets			
O I 3D-4P	2500	0.892	−0.224
	5000	0.900	−0.258
59,761.5 Å	10,000	0.908	−0.293
C = 0.60 × 10^{20}	20,000	0.917	−0.332
	40,000	0.930	−0.374
	80,000	0.947	−0.422
O I 3D-5P	2500		
	5000	* 0.248	
11,950.4 Å	10,000	* 0.255	* −0.117
C = 0.58 × 10^{18}	20,000	* 0.264	* −0.135
	40,000	0.274	−0.154
	80,000	0.286	−0.175
O I 3D-6P	2500	* 0.182	* −0.508 × 10^{-1}
	5000	* 0.185	* −0.594 × 10^{-1}
16,114.7 Å	10,000	0.188	−0.684 × 10^{-1}
C = 0.20 × 10^{19}	20,000	0.191	−0.780 × 10^{-1}
	40,000	0.195	−0.885 × 10^{-1}
	80,000	0.200	−0.100
O I 4D-5P	2500		
	5000		
34,210.0 Å	10,000	* 2.70	* −1.71
C = 0.12 × 10^{19}	20,000	* 2.89	* −2.00
	40,000	* 3.11	* −2.30
	80,000	* 3.37	* −2.62
O I 4D-6P	2500	* 21.8	* −13.3
	5000	* 23.8	* −16.5
131,456.1 Å	10,000	* 25.9	* −19.6
C = 0.18 × 10^{20}	20,000	* 28.4	* −22.8
	40,000	31.2	−26.1
	80,000	34.6	−29.7

Concerning the behavior of the electron-impact widths with temperature (see e.g., [48,49], one can see from Equation (1) that the width is a sum of cross sections for collisions which depopulate the initial and final levels of the transition from which the considered spectral line originates. The behavior of cross sections for electron – neutral atom collisions with temperature is the following: They start from zero and increase with temperature until a maximum depending on the Maxwellian distribution of electron velocities and then slowly decrease. The behavior of electron-impact line width with temperature depends on the temperature behavior of the sum of the corresponding cross sections. If the temperature is in the increasing part, the width increases with temperature, if it is in the decreasing part, the width decreases. If the temperature range includes the maximum, the width will first increase and after the maximum decrease.

In Table 3, our results for Stark widths are compared for temperatures ranging from 5000 K to 40,000 K and a density of 10^{17} cm^{-3}, with Stark widths for 11 multiplets calculated by Griem [29] and 4 by Alonizan et al. [34]. Namely, their calculations cover temperatures only up to 40,000 K, which is not enough for the modelling of stellar atmospheres and other purposes like laser produced and fusion plasma diagnostics and investigation. In

Table 4, the same comparison is presented for the shifts. For these three calculations, the semiclassical perturbation theory has been used. The main differences between the version used here [30,31,42] and the version of Griem, presented in his book on spectral line broadening by plasmas [29], are the calculation of elastic collisions, cut-offs in integration and symmetrization of perturber velocities before and after collision. Alonizan et al. [34] used in their study on Stark broadening of neutral oxygen spectral lines the version applied in our work, but their oscillator strengths have been taken from TOP database [50]. Moreover they calculated data for nine O I transitions for temperatures ranging from 5000 K to 40,000 K while here are presented data for 36 transitions for temperatures ranging from 2500 K to 80,000 K covering especially needs for investigations of stellar atmospheres. We note that for the comparison we did not used linear interpolation from our results for the density of 10^{16} cm^{-3}, but we made calculations for the density of 10^{17} cm^{-3}, used in Griem [29] and Alonizan et al. [34]. Namely the linear interpolation is less accurate due to the influence of Debye shielding. This influence can be taken into account using the correction given in Griem [29].

In order to better see the similarities and differences of three calculations, in Tables 5 and 6 are given the ratios of Stark widths (Table 5) and shifts (Table 6) of Griem [29] and Alonizan et al. [34] with Stark widths and shifts from this work, for the lowest temperature of 5000 K and the highest from Tables 3 and 4, of 40,000 K. We took into account only transitions where all three calculations exist. We can see that for the widths (Table 3), in the case of Griem [29], the agreement is very good for lower temperatures except for the 1303.5 Å line where it is on the limit of theoretical error bars. For higher temperatures, the agreement is not so good but within the theoretical error bars. These differences arise due to different method for calculating elastic collisions, different integration cut-offs and the symmetrization of perturber velocities before and after collision. In the case of Alonizan et al. [34], practically there is no difference between the lowest and highest temperature. The ratios are very close both for collisions with electron and protons, or in the case of 7775.5 Å transition, they are within the theoretical error bars. Here, the differences arise only due to different methods for the calculation of oscillator strengths. In this paper, the Coulomb approximation [44,45] has been used, while Alonizan et al. [34] use oscillator strengths from the TOP database [50], calculated employing close coupling non relativistic R-matrix method [51,52]. One can see that in spite of differences in oscillator strengths the final results are very close.

The ratios for the shift are given in Table 6. One can see that the Griem's values are slightly smaller than ours, but the differences are within the theoretical error bars. The unique case with an extreme disagreement is for the lowest temperatue (5000 K) for 3948.5 Å transition. Namely, Griem's result is -0.00683 and ours is -0.000188 which is very small and in both cases much smaller than the corresponding width value. We draw attention that in the case of the width all cross sections entering in Equation (1) are positive, while in the case of the line shift, contributions to the phase shift ϕ_p in Equation (1) are positive for virtual transitions to the perturbing levels above the considered atomic energy level and negative for perturbing levels below it. If these contributions are comparable, the shift will be much smaller than the width and the resulting accuracy will be poor.

Table 3. In this table, electron-impact widths from this work (W_{TW}) are compared with the semi-classical results of Griem [29] (W_G) and of Alonizan et al. [34] (W_A). The electron density is 10^{17} cm^{-3}.

Transition	T [K]	W_{TW} [Å]	W_G [Å]	W_A [Å]
Triplets				
O I 3S-3P	5000	0.721×10^{-1}	0.788×10^{-1}	
8448.8 Å	10,000	0.822×10^{-1}	0.103	
C = 0.54×10^{20}	20,000	0.107	0.139	
	40,000	0.145	0.181	
O I 3S-4P	5000	0.107	0.117	0.116
4369.5 Å	10,000	0.130	0.160	0.141
C = 0.42×10^{19}	20,000	0.161	0.214	0.175
	40,000	0.200	0.262	0.217
O I 2P-3S	5000	0.104×10^{-2}	0.144×10^{-2}	0.112×10^{-2}
1303.5 Å	10,000	0.124×10^{-2}	0.164×10^{-2}	0.133×10^{-2}
C = 0.20×10^{19}	20,000	0.142×10^{-2}	0.185×10^{-2}	0.151×10^{-2}
	40,000	0.153×10^{-2}	0.216×10^{-2}	0.162×10^{-2}
O I 3P-4S	5000	0.821	0.918	
13,168.2 Å	10,000	0.907	1.094	
C = 0.60×10^{20}	20,000	1.02	1.32	
	40,000	1.16	1.59	
O I 2P-3D	5000	0.371×10^{-2}	0.418×10^{-2}	
1026.6 Å	10,000	0.414×10^{-2}	0.488×10^{-2}	
C = 0.23×10^{18}	20,000	0.453×10^{-2}	0.570×10^{-2}	
	40,000	0.494×10^{-2}	0.646×10^{-2}	
O I 3P-4D	5000	2.85	3.50	
7004.1 Å	10,000	2.70	3.30	
C = 0.29×10^{18}	20,000	2.53	3.08	
	40,000	2.38	2.84	
Quintets				
O I 3S-3P	5000	0.463×10^{-1}	0.456×10^{-1}	0.552×10^{-1}
7775.5 Å	10,000	0.528×10^{-1}	0.630×10^{-1}	0.630×10^{-1}
C = 0.53×10^{20}	20,000	0.694×10^{-1}	0.894×10^{-1}	0.825×10^{-1}
	40,000	0.959×10^{-1}	0.121	0.113
O I 3S-4P	5000	0.815×10^{-1}	0.906×10^{-1}	0.901×10^{-1}
3948.5 Å	10,000	0.100	0.125	0.110
C = 0.26×10^{19}	20,000	0.124	0.164	0.137
	40,000	0.151	0.197	0.167
O I 3P-4S	5000	0.569	0.644	
11,302.5 Å	10,000	0.634	0.752	
C = 0.46×10^{20}	20,000	0.694	0.894	
	40,000	0.766	1.04	
O I 3P-3D	5000	0.358	0.384	
9266.4 Å	10,000	0.396	0.444	
C = 0.14×10^{20}	20,000	0.442	0.516	
	40,000	0.499	0.588	
O I 3P-4D	5000	1.95	2.34	
6159.0 Å	10,000	1.90	2.32	
C = 0.39×10^{18}	20,000	1.83	2.22	
	40,000	1.75	2.08	

Table 4. In this table, electron-impact shifts from this work (d_{TW}) are compared with the semiclassical results of Griem [29] (d_G) and of Alonizan et al. [34] (d_A). The electron density is 10^{17} cm^{-3}.

Transition	T [K]	d_{TW} [Å]	d_G [Å]	d_A [Å]
Triplets				
O I 3S-3P	5000	0.374×10^{-1}	0.358×10^{-1}	
8448.8 Å	10,000	0.350×10^{-1}	0.373×10^{-1}	
C = 0.54×10^{20}	20,000	0.306×10^{-1}	0.356×10^{-1}	
	40,000	0.224×10^{-1}	0.310×10^{-1}	
O I 3S-4P	5000	0.419×10^{-1}	0.331×10^{-1}	0.480×10^{-1}
4369.5 Å	10,000	0.475×10^{-1}	0.356×10^{-1}	0.527×10^{-1}
C = 0.42×10^{19}	20,000	0.479×10^{-1}	0.358×10^{-1}	0.532×10^{-1}
	40,000	0.371×10^{-1}	0.330×10^{-1}	0.414×10^{-1}
O I 2P-3S	5000	0.927×10^{-3}	0.872×10^{-3}	0.975×10^{-3}
1303.5 Å	10,000	0.108×10^{-2}	0.100×10^{-2}	0.115×10^{-2}
C = 0.20×10^{19}	20,000	0.124×10^{-2}	0.110×10^{-2}	0.130×10^{-2}
	40,000	0.127×10^{-2}	0.110×10^{-2}	0.134×10^{-2}
O I 3P-4S	5000	0.596	0.548	
13,168.2 Å	10,000	0.669	0.597	
C = 0.60×10^{20}	20,000	0.683	0.594	
	40,000	0.548	0.532	
O I 2P-3D	5000	0.259×10^{-2}	0.256×10^{-2}	
1026.6 Å	10,000	0.291×10^{-2}	0.273×10^{-2}	
C = 0.23×10^{18}	20,000	0.297×10^{-2}	0.270×10^{-2}	
	40,000	0.271×10^{-2}	0.248×10^{-2}	
O I 3P-4D	5000	1.03	1.20	
7004.1 Å	10,000	0.869	0.999	
C = 0.29×10^{18}	20,000	0.693	0.805	
	40,000	0.482	0.628	
Quintets				
O I 3S-3P	5000	0.168×10^{-1}	0.144×10^{-1}	0.182×10^{-1}
7775.5 Å	10,000	0.167×10^{-1}	0.143×10^{-1}	0.181×10^{-1}
C = 0.53×10^{20}	20,000	0.123×10^{-1}	0.130×10^{-1}	0.135×10^{-1}
	40,000	0.917×10^{-2}	0.108×10^{-1}	0.102×10^{-1}
O I 3S-4P	5000	-0.188×10^{-3}	-0.683×10^{-2}	-0.443×10^{-6}
3948.5 Å	10,000	0.688×10^{-2}	-0.172×10^{-2}	0.735×10^{-2}
C = 0.26×10^{19}	20,000	0.119×10^{-1}	0.298×10^{-2}	0.127×10^{-1}
	40,000	0.989×10^{-2}	0.597×10^{-2}	0.108×10^{-1}
O I 3P-4S	5000	0.410	0.377	
11,302.5 Å	10,000	0.481	0.416	
C = 0.46×10^{20}	20,000	0.491	0.419	
	40,000	0.414	0.379	
O I 3P-3D	5000	0.243	0.223	
9266.4 Å	10,000	0.246	0.228	
C = 0.14×10^{20}	20,000	0.233	0.214	
	40,000	0.182	0.184	
O I 3P-4D	5000	0.891	0.945	
6159.0 Å	10,000	0.791	0.813	
C = 0.39×10^{18}	20,000	0.646	0.668	
	40,000	0.452	0.527	

Table 5. In this table, ratios of Stark widths of Griem [29] (W_G) and of Alonizan et al. [34] (W_A) with Stark widths from this work (W_{TW}) are presented. The electron density is 10^{17} cm^{-3}.

Transition	T [K]	Electrons W_G/W_{TW}	W_A/W_{TW}	Protons W_A/W_{TW}
Triplets				
O I 3S-4P	5000	1.09	1.08	1.05
4369.5 A	40,000	1.31	1.08	1.05
O I 2P-3S	5000	1.38	1.08	1.05
1303.5 A	40,000	1.41	1.06	1.05
Quintets				
O I 3S-3P	5000	0.98	1.19	1.28
7775.5 A	40,000	1.26	1.18	1.27
O I 3S-4P	5000	1.11	1.11	1.17
3948.5 A	40,000	1.30	1.11	1.16

Table 6. In this table, ratios of Stark shifts of Griem [29] (d_G) and of Alonizan et al. [34] (d_A) with Stark shifts from this work (d_{TW}) are presented. The electron density is 10^{17} cm^{-3}.

Transition	T [K]	Electrons d_G/d_{TW}	d_A/d_{TW}	Protons d_A/d_{TW}
Triplets				
O I 3S-4P	5000	0.79	1.15	1.12
4369.5 A	40,000	0.89	1.12	1.11
O I 2P-3S	5000	0.94	1.05	1.05
1303.5 A	40,000	0.87	1.06	1.05
Quintets				
O I 3S-3P	5000	0.86	1.08	1.09
7775.5 A	40,000	1.18	1.11	1.09
O I 3S-4P	5000	36	0.06	1.06
3948.5 A	40,000	0.60	1.09	1.06

4. Conclusions

Electron-, proton-, and ionized helium-impact broadening parameters, FWHM, and shifts, for 36 O I transitions have been calculated with the help of the impact semiclassical perturbation theory [30,31,42]. We note that in previous calculations number of considered transitions is smaller, 23 in Griem [29], 4 in Ben Nessib et al. [32] and 9 in Alonizan et al. [34], while here, it is 36. Moreover, in the mentioned articles, the temperature range is from 5000 K to 40,000 K while here, it is from 2500 K to 80,000 K, so that the obtained data cover the needs of modern space-based spectroscopy. The results are compared with the theoretical calculations of Griem [29] and Alonizan et al. [34] and in general, a good agreement between the values obtained from the different calculations is observed.

The presented Stark broadening data are of interest for stellar spectra interpretation, analysis and synthesis, stellar abundance of oxygen determination and its variation during the evolution of the Universe, for modelling of stellar atmospheres, for laboratory plasma diagnostics and investigation and modelling of various plasmas in technology anf fusion experiments.

Author Contributions: M.S.D. and S.S.-B. were involved in the preparation of the manuscript. All authors have read and agreed to the published version of the manuscript.

Funding: This research received no external funding.

Institutional Review Board Statement: Not applicable.

Data Availability Statement: All obtained data are in the paper.

Acknowledgments: This article is based upon work from COST Action CA21136 Addressing observational tensions in cosmology with systematics and fundamental physics (CosmoVerse) supported by COST (European Cooperation in Science and Technology).

Conflicts of Interest: The authors declare no conflicts of interest.

References

1. Iglesias, E.; Griem, H.; Welch, B.; Weaver, J. UV Line Profiles of B IV from a 10-Ps KrF-Laser-Produced Plasma. *Astrophys. Space Sci.* **1997**, *256*, 327–331. [CrossRef]
2. Sorge, S.; Wierling, A.; Röpke, G.; Theobald, W.; Sauerbrey, R.; Wilhein, T. Diagnostics of a laser-induced dense plasma by hydrogen-like carbon spectra. *J. Phys. B At. Mol. Phys.* **2000**, *33*, 2983–3000. [CrossRef]
3. Konjević, N. Plasma broadening and shifting of non-hydrogenic spectral lines: Present status and applications. *Phys. Rep.* **1999**, *316*, 339–401. [CrossRef]
4. Hoffman, J.; Szymański, Z.; Azharonok, V. Plasma Plume Induced During Laser Welding of Magnesium Alloys. In Proceedings of the PLASMA-2005 Conference on Research and Application of Plasmas, Opole-Turawa, Poland, 6–9 September 2005; Sadowski, M.J., Dudek, M., Hartfuss, H.J., Pawelec, E., Eds.; American Institute of Physics Conference Series; American Institute of Physics: College Park, MD, USA, 2006; Volume 812, pp. 469–472. [CrossRef]
5. Dimitrijević, M.; Sahal-Bréchot, S. On the Application of Stark Broadening Data Determined with a Semiclassical Perturbation Approach. *Atoms* **2014**, *2*, 357–377. [CrossRef]
6. Yilbas, B.S.; Patel, F.; Karatas, C. Laser controlled melting of H12 hot-work tool steel with B_4C particles at the surface. *Opt. Laser Technol.* **2015**, *74*, 36–42. [CrossRef]
7. Nordlander, T.; Gruyters, P.; Richard, O.; Korn, A.J. Atomic diffusion and mixing in old stars - VIII. Chemical abundance variations in the globular cluster M4 (NGC 6121). *Mon. Not. R. Astron. Soc.* **2024**, *527*, 12120–12139. [CrossRef]
8. Romanovskaya, A.M.; Ryabchikova, T.A.; Pakhomov, Y.V.; Korotin, S.A.; Sitnova, T.M. Non-LTE abundance analysis of A-B stars with low rotational velocities - II. Do A-B stars with normal abundances exist? *Mon. Not. R. Astron. Soc.* **2023**, *526*, 3386–3399. [CrossRef]
9. Ramos, A.A.; Holanda, N.; Drake, N.A.; Rain, M.J.; Maia, F.F.S.; Daflon, S.; Pereira, C.B. A study of chemical abundances, rotational velocities, and orbital elements in single-lined spectroscopic binary stars in open clusters. *Mon. Not. R. Astron. Soc.* **2024**, *527*, 6211–6226. [CrossRef]
10. Oh, W.S.; Nordlander, T.; Da Costa, G.S.; Bessell, M.S.; Mackey, A.D. High-resolution spectroscopic study of extremely metal-poor stars in the Large Magellanic Cloud. *Mon. Not. R. Astron. Soc.* **2024**, *528*, 1065–1080. [CrossRef]
11. Mittal, S.; Roederer, I.U. New Stellar Parameters, Metallicities, and Elemental Abundance Ratios for 311 Metal-poor Stars. *Astron. J.* **2025**, *169*, 172. [CrossRef]
12. Takeda, Y.; Kang, D.I.; Han, I.; Lee, B.C.; Kim, K.M. C, N, O and Na abundances of Cepheid variables: Implications on the mixing process in the envelope. *Mon. Not. R. Astron. Soc.* **2013**, *432*, 769–792. [CrossRef]
13. Kravtsov, T.; Anderson, J.P.; Kuncarayakti, H.; Maeda, K.; Mattila, S. Discovery of young, oxygen-rich supernova remnants in PHANGS-MUSE galaxies. *Astron. Astrophys.* **2025**, *700*, A223. [CrossRef]
14. Dastidar, R.; Misra, K.; Valenti, S.; Sand, D.J.; Pastorello, A.; Reguitti, A.; Pignata, G.; Benetti, S.; Bose, S.; Gangopadhyay, A.; et al. SN 2018is: A low-luminosity Type IIP supernova with narrow hydrogen emission lines at early phases. *Astron. Astrophys.* **2025**, *694*, A260. [CrossRef]
15. Andrews, J.E.; Shrestha, M.; Bostroem, K.A.; Dong, Y.; Pearson, J.; Fausnaugh, M.M.; Sand, D.J.; Valenti, S.; Ravi, A.P.; Hoang, E.; et al. Asymmetries and Circumstellar Interaction in the Type II SN 2024bch. *Astrophys. J.* **2025**, *980*, 37. [CrossRef]
16. Ravi, A.P.; Valenti, S.; Dong, Y.; Hiramatsu, D.; Barmentloo, S.; Jerkstrand, A.; Bostroem, K.A.; Pearson, J.; Shrestha, M.; Andrews, J.E.; et al. Luminous Type II Short-plateau SN 2023ufx: Asymmetric Explosion of a Partially Stripped Massive Progenitor. *Astrophys. J.* **2025**, *982*, 12. [CrossRef]
17. Taguchi, K.; Maeda, K.; Maehara, H.; Tajitsu, A.; Yamanaka, M.; Arai, A.; Isogai, K.; Shibata, M.; Tampo, Y.; Kojiguchi, N.; et al. Spectra of V1405 Cas at the Very Beginning Indicate a Low-mass ONeMg White Dwarf Progenitor. *Astrophys. J.* **2023**, *958*, 156. [CrossRef]
18. Jung, M. Verbreiterung von Spektrallinien des neutralen Sauerstoffs durch Mikrofelder. Mit 5 Textabbildungen. *Z. Astrophys.* **1963**, *58*, 93.

19. Wiese, W.L.; Murphy, P.W. Shifts and Widths of Some Stark-Broadened Oxygen Lines in an Arc Plasma. *Phys. Rev.* **1963**, *131*, 2108–2115. [CrossRef]
20. Morris, J.C.; Garrison, R.L. Measurement of the Radiation Emitted f Values and Stark Half-Widths for the Strong Vacuum Ultraviolet Lines of O I and N I. *Phys. Rev.* **1969**, *188*, 112–118. [CrossRef]
21. Miller, M.H.; Bengtson, R.D. Measured Stark Widths and Shifts for Neutral Atomic Lines. *Phys. Rev. A* **1970**, *1*, 983–990. [CrossRef]
22. Assous, R. Elargissement et déplacement par effet Stark de raies de l'atome neutre d'oxygène. *J. Quant. Spectrosc. Radiat. Transf.* **1970**, *10*, 975–990. [CrossRef]
23. Goly, A.; Rakotoarijimy, D.; Weniger, S. Experimental Stark parameters for some lines of neutral carbon, oxygen, and sulfur. *J. Quant. Spectrosc. Radiat. Transf.* **1983**, *30*, 417–431. [CrossRef]
24. Goly, A.; Weniger, S. Widths and shifts of some plasma-broadened oxygen and carbon multiplets. *J. Quant. Spectrosc. Radiat. Transf.* **1987**, *38*, 225–230. [CrossRef]
25. Sohns, E.; Kock, M. Plasma diagnostics based on self-reversed lines. II. Application to nitrogen, carbon and oxygen arc measurements in the vacuum ultraviolet. *J. Quant. Spectrosc. Radiat. Transf.* **1992**, *47*, 335–343. [CrossRef]
26. Mijatović, Z.; Konjević, N.; Kobilarov, R.; Djurović, S. Search for ion dynamics effects on the shift and width of plasma-broadened C i and O i spectral lines. *Phys. Rev. E* **1995**, *51*, 613–618. [CrossRef]
27. Gerhard, C.; Hermann, J.; Mercadier, L.; Loewenthal, L.; Axente, E.; Luculescu, C.R.; Sarnet, T.; Sentis, M.; Viöl, W. Quantitative analyses of glass via laser-induced breakdown spectroscopy in argon. *Spectrochim. Acta-Part B At. Spectrosc.* **2014**, *101*, 32–45. [CrossRef]
28. Burger, M.; Hermann, J. Stark broadening measurements in plasmas produced by laser ablation of hydrogen containing compounds. *Spectrochim. Acta-Part B At. Spectrosc.* **2016**, *122*, 118–126. [CrossRef]
29. Griem, H.R. *Spectral Line Broadening by Plasmas*; Academic Press: Cambridge, MA, USA, 1974.
30. Sahal-Bréchot, S. Impact Theory of the Broadening and Shift of Spectral Lines due to Electrons and Ions in a Plasma. *Astron. Astrophys.* **1969**, *1*, 91.
31. Sahal-Bréchot, S. Impact Theory of the Broadening and Shift of Spectral Lines due to Electrons and Ions in a Plasma (Continued). *Astron. Astrophys.* **1969**, *2*, 322.
32. Ben Nessib, N.; Ben Lakhdar, Z.; Sahal-Bréchot, S. Stark broadening of neutral oxygen lines in the impact and quasistatic approximations. *Phys. Scr.* **1996**, *54*, 608–613. [CrossRef]
33. Riviere, P. Systematic semi-classical calculations of Stark broadening parameters of NI, OI, NII, OII multiplets for modelling the radiative transfer in atmospheric air mixture plasmas. *J. Quant. Spectrosc. Radiat. Transf.* **2002**, *73*, 91–110. [CrossRef]
34. Alonizan, N.; Qindeel, R.; Nessib, N.B.; Sahal-Bréchot, S.; Dimitrijević, M.S. Stark Broadening Parameters for Neutral Oxygen Spectral Lines. *J. Astrophys. Astron.* **2015**, *36*, 661–669. [CrossRef]
35. Brissaud, A.; Goldbach, C.; Leorat, J.; Mazure, A.; Nollez, G. On the validity of the model microfield method as applied to Stark broadening of neutral lines. *J. Phys. B At. Mol. Phys.* **1976**, *9*, 1129–1146. [CrossRef]
36. Brissaud, A.; Goldbach, C.; Leorat, J.; Mazure, A.; Nollez, G. Application of the model microfield method to Stark profiles of overlapping and isolated neutral lines. *J. Phys. B At. Mol. Phys.* **1976**, *9*, 1147–1162. [CrossRef]
37. Stambulchik, E.; Maron, Y. Plasma line broadening and computer simulations: A mini-review. *High Energy Density Phys.* **2010**, *6*, 9–14. [CrossRef]
38. Stambulchik, E.; Kroupp, E.; Maron, Y.; Malka, V. On the Stark Effect of the O I 777-nm Triplet in Plasma and Laser Fields. *Atoms* **2020**, *8*, 84. [CrossRef]
39. Johns, H.M.; Kilcrease, D.P.; Colgan, J.; Judge, E.J.; Barefield II, J.E.; Wiens, R.C.; Clegg, S.M. Improved electron collisional line broadening for low-temperature ions and neutrals in plasma modeling. *J. Phys. B At. Mol. Opt. Phys.* **2015**, *48*, 224009. [CrossRef]
40. Dimitrijevic, M.S.; Konjevic, N. Simple formulae for estimating Stark widths and shifts of neutral atom lines. *Astron. Astrophys.* **1986**, *163*, 297–300.
41. Dimitrijevic, M.S.; Konjevic, N. Simple estimates for Stark broadening of ion lines in stellar plasmas. *Astron. Astrophys.* **1987**, *172*, 345–349.
42. Sahal-Bréchot, S.; Dimitrijević, M.; Ben Nessib, N. Widths and Shifts of Isolated Lines of Neutral and Ionized Atoms Perturbed by Collisions With Electrons and Ions: An Outline of the Semiclassical Perturbation (SCP) Method and of the Approximations Used for the Calculations. *Atoms* **2014**, *2*, 225–252. [CrossRef]
43. Moore, C.E. *Tables of Spectra of Hydrogen, Carbon, Nitrogen, and Oxygen Atoms and Ions*; CRC Press: Boca Raton, FL, USA, 1993.
44. Bates, D.R.; Damgaard, A. The Calculation of the Absolute Strengths of Spectral Lines. *Philos. Trans. R. Soc. Lond. Ser. A* **1949**, *242*, 101–122. [CrossRef]
45. Oertel, G.K.; Shomo, L.P. Tables for the Calculation of Radial Multipole Matrix Elements by the Coulomb Approximation. *Astrophys. J. Suppl. Ser.* **1968**, *16*, 175. [CrossRef]

46. Dimitrijevic, M.S.; Sahal-Bréchot, S. Comparison of measured and calculated Stark broadening parameters for neutral-helium lines. *Phys. Rev. A* **1985**, *31*, 316–320. [CrossRef]
47. Dimitrijević, M.S.; Sahal-Bréchot, S. Stark broadening of neutral helium lines. *J. Quant. Spectrosc. Radiat. Transf.* **1984**, *31*, 301–313. [CrossRef]
48. Dimitrijevic, M.S.; Christova, M.; Sahal-Bréchot, S. Stark broadening of visible Ar I spectral lines. *Phys. Scr.* **2007**, *75*, 809–819. [CrossRef]
49. Dimitrijević, M.S.; Christova, M.D.; Sahal-Bréchot, S. Stark broadening of B I spectral lines. *Mon. Not. R. Astron. Soc.* **2022**, *509*, 3203–3208. [CrossRef]
50. Cunto, W.; Mendoza, C. The Opacity Project—The Topbase Atomic Database. *Rev. Mex. Astron. AstrofíSica* **1992**, *23*, 107–118.
51. Seaton, M.J.; Zeippen, C.J.; Tully, J.A.; Pradhan, A.K.; Mendoza, C.; Hibbert, A.; Berrington, K.A. The Opacity Project—Computation of Atomic Data. *Rev. Mex. Astron. AstrofíSica* **1992**, *23*, 19.
52. Berrington, K.A.; Burke, P.G.; Butler, K.; Seaton, M.J.; Storey, P.J.; Taylor, K.T.; Yan, Y. Atomic data for opacity calculations. II. Computational methods. *J. Phys. At. Mol. Phys.* **1987**, *20*, 6379–6397. [CrossRef]

galaxies

MDPI

Article

Estimation of Host Galaxy Extinction for SNe Ia

Oleg Malkov [1,*], Alexey Sytov [1,†], Gang Zhao [2,3,†] and Zehao Zhong [3,†]

[1] Institute of Astronomy, 48 Pyatnitskaya St., Moscow 119017, Russia; sytov@inasan.ru
[2] National Astronomical Observatories, Chinese Academy of Sciences, Beijing 100101, China; gzhao@nao.cas.cn
[3] School of Astronomy and Space Science, University of Chinese Academy of Sciences, Beijing 100049, China; zhzhong@nao.cas.cn
* Correspondence: malkov@inasan.ru
† These authors contributed equally to this work.

Abstract: Type Ia supernovae are used as fundamental probes of the cosmological parameters, based on a tight empirical relation between their peak luminosity and the width of their light curve. However, it has been recognized that SNe Ia are not "standard" candles, since important variations in their peak luminosities are observed, as a function of the metallicity, age, environment, and morphological type of the supernova hosts. The largest correction in the standardization scheme is related to extinction. While extinction in the Milky Way (MW) Galaxy is usually known and extinction between galaxies can be assumed to be zero, the value of extinction in the SN Ia host galaxy (A_{host}) is determined with much more uncertainty. In this paper, we provide an estimate of the A_{host} value based on statistical modeling. To do this, we generate, based on MaNGA data, a set of galaxies in the vicinity of the MW, and distribute the parameters of the galaxies and the positions of SNe Ia in them. As a result, using a simplified model for the distribution of interstellar matter, which is the same for all the sampled galaxies, we can estimate the probability that A_{host} exceeds a certain value. Our estimates show, in particular, that in almost all cases, $A_{host} >$ 0.10 mag V, and in 25% of cases, $A_{host} > 0.25$ mag V.

Keywords: supernovae; interstellar extinction

1. Introduction

A Type Ia supernova (SN Ia) represents one of the most powerful explosions in the Universe. These events occur when a white dwarf star—the dense, carbon-rich core left behind after a medium-sized star exhausts its nuclear fuel—reaches a critical mass threshold known as the Chandrasekhar limit, about 1.4 $m_\odot$ (strictly speaking, the explosion mechanism is more complex; for details, see, for example, [1]). In many cases, the extra material required to push the star over its critical mass threshold can be pulled from a companion star or merger with another white dwarf in a binary system. Once the white dwarf crosses this mass threshold, it triggers a nuclear fusion reaction that releases a huge amount of energy. Unlike regular Type II supernovae, which occur every fifty years in the MW, SNe Ia have been detected once every two hundred years [2,3]. The largest SN Ia release to date [4] contains several thousand spectroscopically classified SNe Ia discovered by the Zwicky Transient Facility survey.

What makes SNe Ia particularly valuable is their consistent peak brightness, allowing them to serve as "standard candles" for measuring distances across the Universe. By comparing their apparent brightness in the sky with their known luminosity, their distance can be calculated. These explosions allow astronomers to measure the distances to objects millions or billions of light-years away, and this is vital to measuring the rate at which the Universe is expanding. It should be noted, however, that important variations in SNe Ia peak luminosities are observed, as a function of the metallicity, age, environment, and morphological type of the supernovae hosts (see, e.g., discussion in [1]), which makes them a bit difficult to use as "standard candles".

SNe Ia became the basis for the construction of a distance ladder used to compare cosmological models, and they have a rich history in revolutionizing the field [5,6]. Modern methods for standardizing SNe Ia light curves use the SALT2 fitting algorithm [7,8], as used by the Pantheon+ Type Ia Supernovae spectroscopic data set [9], and, more recently, SALT3 [10] used by the Dark Energy Survey 5-year release [11]. A new, cosmologically model-independent, statistical analysis of the Pantheon+, improving a standard methodology, was presented in [12], where it was found that the timescape cosmology is not only a viable contender to the ΛCDM framework but may also provide new insights to the astrophysics of modeling SNe Ia. Thus, the study of reasons that can influence the observed brightness of SNe is quite relevant.

SNe Ia are known to suffer from extinction along the line of sight. It is assumed that interstellar dust in the MW Galaxy and host galaxy are primarily responsible for making some objects redder than others. The problem of restoring the intrinsic color and absolute stellar magnitude is complicated by a number of circumstances. The situation is complicated by the fact that different sub-types of SNe Ia may have different intrinsic colors [13], that the low R_V (the ratio of total-to-selective extinction) is due to the presence of a circumstellar medium around the progenitor system [14,15], or the angle from which we view the explosion [13,16]. The problem of the separation of intrinsic and extrinsic components, which both contribute to the observed variability, was recently discussed in [17–19].

In this paper, we investigate the possibility of statistically estimating the magnitude of interstellar extinction in the host galaxy, A_{host}. We assume that the magnitude of extinction in the MW is relatively well known [20–22] and the extinction between galaxies (intergalactic extinction) can be neglected.

In Section 2, we describe the method for calculating interstellar extinction in the host galaxy and describe the principles of simulating an ensemble of galaxies with SNe Ia in them. The results and conclusions are presented in Sections 3 and 4, respectively.

2. Description of the Model

2.1. Distribution of Interstellar Medium in A Galaxy

The classical model of a homogeneous, semi-infinite absorbing layer with a density exponentially distributed over the height provides the so-called cosecant law (Parenago formula [23]) for visual extinction A_{V}:

$$A_{\mathrm{V}}(d,b) = \frac{a_0\beta}{\sin|b|}\left(1 - e^{\frac{-d\sin|b|}{\beta}}\right) \quad (1)$$

where d is distance (kpc), b is galactic latitude, parameter β (kpc) is the height scale, and a_0 (mag kpc^{-1}) is the extinction value per unit distance in the Galactic plane.

At infinity, for $d \to \infty$, the expression (1) degenerates into a simpler form:

$$A_{\mathrm{V}}(b) = \frac{a_0\beta}{\sin|b|} \quad (2)$$

To estimate the extinction value, we will use Formula (1), and expression (2) within the framework of the problem can be useful for quickly estimating the A_{V} scale. Note that more complete and complex models of interstellar extinction can be found in the literature [24–30], but for our purposes, the relatively simple Formula (1) is sufficient.

2.2. *Estimating the Interstellar Extinction of Light from a Star in a Distant Galaxy*

We assume that the supernova is located in the galactic disk and calculate distance d to which the absorbing material extends (let us call this the "boundary" of the galaxy). For simplicity, we will assume that the shape of the "boundary" of the host galaxy is a conical surface with radius R and height h. In this case, the distance d from a point located in the galactic disk $z = 0$ at a distance r from the center of the galaxy, in the direction determined by the galactic latitude b and longitude l of the observer, to the "boundary" of the galaxy (see Figure 1) will be determined by the expression

$$d_{1,2} = \frac{-2h(R^2 \sin b - rh \cos b \cos l)}{2(h^2 \cos^2 b - R^2 \sin^2 b)} \pm \\ \pm \frac{\sqrt{[2h(R^2 \sin b - rh \cos b \cos l)]^2 - 4(h^2 \cos^2 b - R^2 \sin^2 b)(h^2(r^2 - R^2))}}{2(h^2 \cos^2 b - R^2 \sin^2 b)} \quad (3)$$

where the value of d is chosen as $d = \min(\max(d_1, 0), \max(d_2, 0))$. In the degenerate case, when $h^2 \cos^2 b = R^2 \sin^2 b$, the distance is found from the expression

$$d = \frac{-h^2(r^2 - R^2)}{2h(R^2 \sin b - rh \cos b \cos l)} \quad (4)$$

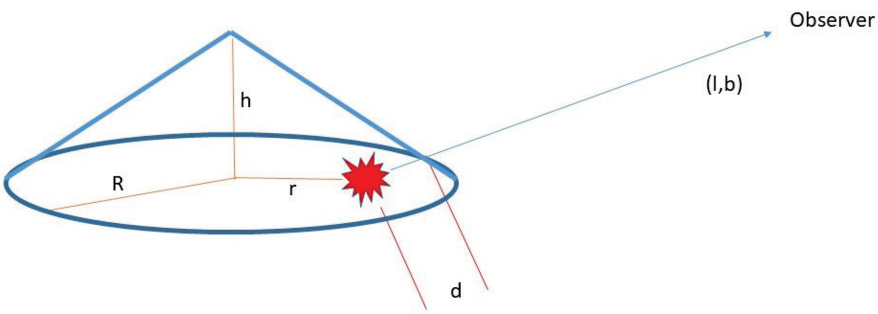

Figure 1. Schematic for the calculation of distance d from an SN to the "boundary" of the host galaxy (see text for details).

A similar approach, but for fixed values of $R = 15$ kpc and $r = 8.5$ kpc, was used in [31] (see their Equation (5)).

To find the law of distribution of interstellar extinction, we conduct statistical modeling. Let us assume that the distance from the supernova to the center of the host galaxy r is distributed exponentially $f(r) \sim e^{-r/R}$, the galactic latitude of the observer b is distributed as $f(b) \sim sin(b)$, and the galactic longitude of the observer l is distributed uniformly $f(l) \sim 1$.

Using inverse transform sampling, we obtain the following expressions for r, l, and b:

$$r = -R \log_2(1 - x_1) \qquad l = 2\pi x_2 \qquad b = \arccos(1 - x_3) \quad (5)$$

where $x_1 \in [0, 1]$, $x_2 \in [0, 1]$, and $x_3 \in [0, 1]$ are random uniformly distributed variables $f(x_1) = 1$, $f(x_2) = 1$, and $f(x_3) = 1$.

2.3. *The Distribution of Spiral Galaxy Radii and Heights from Observational Survey and Numerical Simulations*

In this section, we describe the procedure for obtaining the values R and h needed to calculate the distance d.

The size distribution of spiral galaxies can be derived from observational surveys. The Mapping Nearby Galaxies at Apache Point Observatory [32], call the MaNGA survey, is one of the most advanced and widely used integral field spectroscopic surveys. MaNGA provides spatially resolved spectra that include the kinematics of galaxies and information on stellar populations. It can not only describe the various properties of galaxies well, but the stellar population can also help accurately calculate the stellar mass of galaxies [33]. In addition to spectroscopy, image-based morphological analysis is also important. Because the observed galaxies are two-dimensional images projected at different inclination angles, it is difficult to obtain the galaxy height in the direction of the rotation axis for face-on galaxies. In this regard, morphological analysis based on deep learning helps us select edge-on galaxies and calculate the ratio of the galaxy's height to radius [34]. Ref. [35] provides both traditional photometry analysis and deep learning-based morphological analysis of MaNGA DR17. Here, we use the MaNGA PyMorph photometric Value Added Catalogue (MPP-VAC-DR17) and the MaNGA Deep Learning Morphological Value Added Catalogue (MDLM-VAC-DR17) from [35] to select edge-on late-type galaxies (LTGs) and calculate the distribution of the corresponding heights and radii. We selected samples with edge-on and LTG probabilities both larger than 0.95 in MaNGA DR17 and excluded dwarf galaxies with logarithmic stellar mass $\log(M/M_{\odot})$ less than 9.5. The redshift range of our sample galaxies from the MaNGA survey is around $0.013 \lesssim z \lesssim 0.083$. The corresponding distribution of galaxy radius and height is shown in Figure 2 (left panel, blue dots), and histograms of their uncertainties, which are derived from the above Value Added Catalogue and error propagation, are shown in the same figure, right panel.

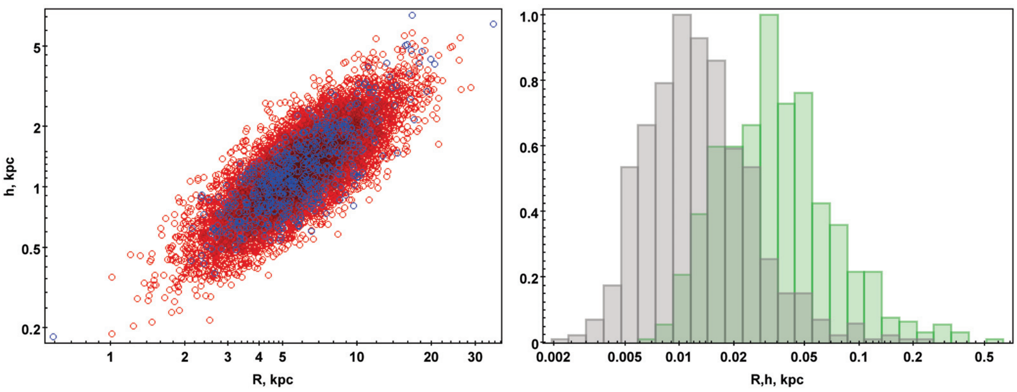

Figure 2. Left panel: the distributions of observational (blue) and model (red) sets of galaxies by R and h. Note that both axes follow a logarithmic scale. Right panel: normalized histograms of errors in the observational set of galaxies by R (green) and h (grey). Note that the X-axis follows a logarithmic scale.

Generally, there exist some selection effects in the observational spectroscopic surveys, which may cause certain deviations in the size distribution of spiral galaxies. However, correcting the selection effects is time-consuming and beyond the scope of the research, since the goal here is to obtain an approximate size distribution of spiral galaxies.

Statistical modeling of the population of galaxies with sizes corresponding to the observed distribution was performed as follows. The size of each galaxy in the modeled ensemble is determined by the values of R and h, which are statistically independent:

$$(\log R, \log h) = (\langle \log R_{\mathrm{M}} \rangle, \langle \log h_{\mathrm{M}} \rangle) + \mathbf{L}_{\mathrm{M}}(x_0, x_1) \quad (6)$$

where $\langle \log R_{\mathrm{M}} \rangle, \langle \log h_{\mathrm{M}} \rangle$ are the mean observed values, $\mathbf{L}_{\mathrm{M}}$ is the Cholesky decomposition of the covariance matrix corresponding to the observed values, and x_i are normally distributed random variables $x_i \sim \mathcal{N}(0,1)$.

The Cholesky decomposition $\mathbf{L}_\mathrm{M}$ of the covariance matrix $\mathbf{\Sigma}_\mathrm{M} = \mathbf{L}_\mathrm{M}\mathbf{L}_\mathrm{M}{}^T$ for the two-dimensional case is

$$\mathbf{L}_\mathrm{M} = \begin{pmatrix} \sqrt{\sigma_{11}} & 0 \\ \frac{\sigma_{21}}{\sqrt{\sigma_{11}}} & \frac{\sqrt{\sigma_{11}\sigma_{22} - \sigma_{21}^2}}{\sqrt{\sigma_{11}}} \end{pmatrix} \quad (7)$$

where σ_{ij} denotes the components of the covariance matrix $\mathbf{\Sigma}_\mathrm{M}$, which has the following structure:

$$\mathbf{\Sigma}_\mathrm{M} = \begin{pmatrix} \sigma_\mathrm{RR} & \sigma_\mathrm{Rh} \\ \sigma_\mathrm{Rh} & \sigma_\mathrm{hh} \end{pmatrix}, \quad \begin{aligned} \sigma_\mathrm{RR} &= \langle (\log R_\mathrm{M} - \langle \log R_\mathrm{M} \rangle)^2 \rangle \\ \sigma_\mathrm{Rh} &= \langle (\log R_\mathrm{M} - \langle \log R_\mathrm{M} \rangle)(\log h_\mathrm{M} - \langle \log h_\mathrm{M} \rangle) \rangle \\ \sigma_\mathrm{hh} &= \langle (\log h_\mathrm{M} - \langle \log h_\mathrm{M} \rangle)^2 \rangle \end{aligned} \quad (8)$$

The distributions of the observational and model sets of galaxies with R and h are shown in Figure 2, and there is good agreement between them. Both quantities, R and h, are well described by the lognormal distribution.

By substituting these values of R and h, as well as the values of r, l, and b from (5) into (3), we find the distance d. Finally, by substituting b and d into the expression (1), we find the value of the interstellar extinction A_V. The distributions of the model set of SNe Ia in galaxies with r and d are shown in Figure 3.

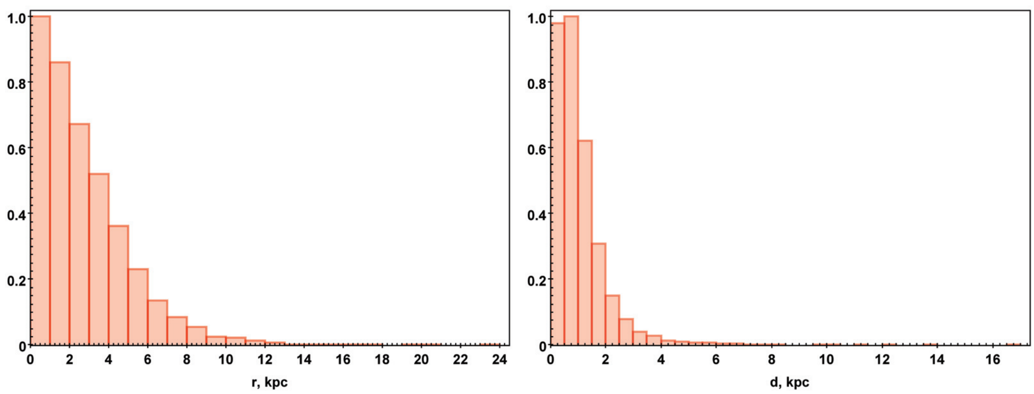

Figure 3. Distributions of the model set of galaxies with r (**left**) and d (**right**).

3. Results

When calculating A_V, we used the value $a_0 = 1.6$ mag kpc^{-1} and $\beta = 0.114$ kpc [36]. The distribution $f(A_\mathrm{V})$ obtained from the simulation is shown in Figure 4, left panel. The average value is $A_\mathrm{V} = 0.26$ mag. Uncertainty can be estimated as Poisson noise level $\sigma_i/N = \pm\sqrt{(n_i)}/N$ (normalized). It seems useful to approximate the resulting distribution with a function. The left part of distribution $f(A_\mathrm{V})$ on the interval $\log A_\mathrm{V} \in [-8, -0.75]$ could be approximated by the following expression:

$$\log f(\log A_\mathrm{V}) = 0.348 \log^{-4} A_\mathrm{V} + \log A_\mathrm{V} - 1.059 \quad (9)$$

And the right part on the interval $\log A_\mathrm{V} \in [-0.75, 1.65]$ could be approximated with another expression:

$$\log f(\log A_\mathrm{V}) = -0.795 \log^3 A_\mathrm{V} - 9.494 \log A_\mathrm{V} - 51.073 \quad (10)$$

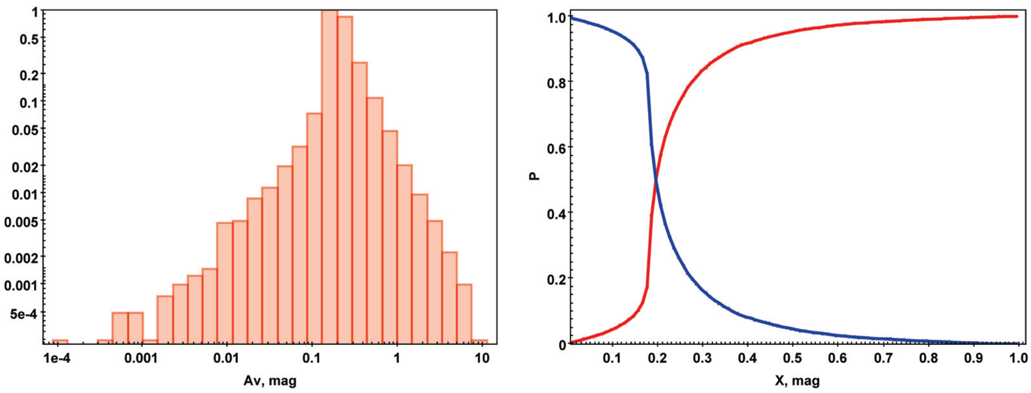

Figure 4. Left panel: the distribution of the model set of SNe Ia with A_V. Note that both axes follow a logarithmic scale. Right panel: the probability P that A_V will take a value less than or equal to X (red curve) and a value larger than X (blue curve).

Cumulative distribution functions are shown in Figure 4, right panel. This is the probability P that A_V will take a value less than or equal to X (red curve) and a value larger than X (blue curve). One can see that, e.g.,

- $P(A_V > 0.10$ mag) = 0.95;
- $P(A_V > 0.15$ mag) = 0.90;
- $P(A_V > 0.20$ mag) = 0.46;
- $P(A_V > 0.25$ mag) = 0.25;
- $P(A_V > 0.35$ mag) = 0.11.

Our results are in qualitative agreement with the results of [37], which obtained the distribution of the total extinction A_V for different host galaxy inclination angles and different values of bulge-to-total luminosity ratios (see their Figure 3), as well as with the results of [38], which explored the dependence of A_V on four observables: the inclination of the host galaxy disk, radial position of the supernova, redshift of the supernova and host, and the level of star formation in the host galaxy.

4. Conclusions

We can draw the following conclusions. Assuming that SNe Ia are located in the plane of spiral galaxies and the distribution of absorbing matter in galaxies corresponds to that in the MW, we investigated the question of the value of interstellar extinction in the host galaxy. We generated 10^9 spiral galaxies (their sizes correspond to the sizes of galaxies from the MaNGA set), each of which hosts SN Ia at some distance from the center. We calculated the A_V values for them and, based on their distribution, found the probability that, when observing a random supernova, the A_{host} value for it exceeds a certain value. In particular, $A_{host} > 0.15$ mag with a probability of 90%, and $A_{host} > 0.25$ mag with a probability of 25%. These results can be useful for calculating the distance to SN Ia. It is worth comparing our results with those of intergalactic extinction ($A_V \sim 0.1$ mag [39]).

It should be noted that several simplifications were made in the modeling described here. The model does not include the distribution of SNe with the height above the galactic plane. It may be noted that [40] found that SNe Ia in spiral galaxies are located in thick disks, which in our galaxy has a height scale of about 0.7–0.9 kpc. In addition, SNe Ia may also be found in the bulge population of spirals. Also, a supernova can be located in a spiral arm or between arms, but in the current version of the model, we do not distinguish between these two cases.

The model does not include the difference in the extinction coefficient with the radius of the galaxy and morphological type. Also, extended dust halos are rather common in spiral galaxies, as demonstrated by edge-on galaxies (see, e.g, case NGC891). We also neglect circumstellar extinction. Last but not least, the space between the host galaxy and the MW Galaxy may not be empty at all. In particular, the model presented in [41] predicts a total of about 300 MW satellites within 300 kpc. All these considerations will be taken into account in further research.

Author Contributions: All authors contributed to the study conception and design. Material preparation, data collection, and analysis were performed by all authors. The first draft of the manuscript was written by O.M., and all authors commented on previous versions of the manuscript. All authors have read and agreed to the published version of the manuscript.

Funding: G.Z. and Z.Z. acknowledge the support of the National Natural Science Foundation of China (NSFC) under grant No. 12588202, National Key R&D Program of China No. 2024YFA1611900. Z.Z. acknowledges the support of the fellowship from the China Postdoctoral Science Foundation (Certificate Number: 2024M763214).

Data Availability Statement: Data are available on request from the authors.

Acknowledgments: The authors thanks Maria Pruzhinskaya for her valuable comments. The work was performed using computing resources of the Joint Supercomputing Center of the Russian Academy of Sciences. This research made use of the SAO/NASA Astrophysics Data System and the SIMBAD database, operated at CDS, Strasbourg, France. This research made use of TOPCAT, an interactive graphical viewer and editor for tabular data [42] The acknowledgments were compiled using the Astronomy Acknowledgement Generator.

Conflicts of Interest: The authors have no relevant financial or non-financial interests to disclose.

References

1. Livio, M.; Mazzali, P. On the progenitors of Type Ia supernovae. *Phys. Rep.* **2018**, *736*, 1–23. [CrossRef]
2. Li, W.; Chornock, R.; Leaman, J.; Filippenko, A.V.; Poznanski, D.; Wang, X.; Ganeshalingam, M.; Mannucci, F. Nearby supernova rates from the Lick Observatory Supernova Search—III. The rate-size relation, and the rates as a function of galaxy Hubble type and colour. *Mon. Not. R. Astron. Soc.* **2011**, *412*, 1473–1507. [CrossRef]
3. Palicio, P.A.; Matteucci, F.; Della Valle, M.; Spitoni, E. Cosmic Type Ia supernova rate and constraints on supernova Ia progenitors. *Astron. Astrophys.* **2024**, *689*, A203. [CrossRef]
4. Rigault, M.; Smith, M.; Goobar, A.; Maguire, K.; Dimitriadis, G.; Johansson, J.; Nordin, J.; Burgaz, U.; Dhawan, S.; Sollerman, J.; et al. ZTF SN Ia DR2: Overview. *Astron. Astrophys.* **2025**, *694*, A1. [CrossRef]
5. Riess, A.G.; Filippenko, A.V.; Challis, P.; Clocchiatti, A.; Diercks, A.; Garnavich, P.M.; Gilliland, R.L.; Hogan, C.J.; Jha, S.; Kirshner, R.P.; et al. Observational Evidence from Supernovae for an Accelerating Universe and a Cosmological Constant. *Astron. J.* **1998**, *116*, 1009–1038. [CrossRef]
6. Perlmutter, S.; Aldering, G.; Goldhaber, G.; Knop, R.A.; Nugent, P.; Castro, P.G.; Deustua, S.; Fabbro, S.; Goobar, A.; Groom, D.E.; et al. Measurements of Ω and Λ from 42 High-Redshift Supernovae. *Astrophys. J.* **1999**, *517*, 565–586. [CrossRef]
7. Guy, J.; Astier, P.; Baumont, S.; Hardin, D.; Pain, R.; Regnault, N.; Basa, S.; Carlberg, R.G.; Conley, A.; Fabbro, S.; et al. SALT2: Using distant supernovae to improve the use of type Ia supernovae as distance indicators. *Astron. Astrophys.* **2007**, *466*, 11–21. [CrossRef]
8. Taylor, G.; Lidman, C.; Tucker, B.E.; Brout, D.; Hinton, S.R.; Kessler, R. A revised SALT2 surface for fitting Type Ia supernova light curves. *Mon. Not. R. Astron. Soc.* **2021**, *504*, 4111–4122. [CrossRef]
9. Scolnic, D.; Brout, D.; Carr, A.; Riess, A.G.; Davis, T.M.; Dwomoh, A.; Jones, D.O.; Ali, N.; Charvu, P.; Chen, R.; et al. The Pantheon+ Analysis: The Full Data Set and Light-curve Release. *Astrophys. J.* **2022**, *938*, 113. [CrossRef]
10. Kenworthy, W.D.; Jones, D.O.; Dai, M.; Kessler, R.; Scolnic, D.; Brout, D.; Siebert, M.R.; Pierel, J.D.R.; Dettman, K.G.; Dimitriadis, G.; et al. SALT3: An Improved Type Ia Supernova Model for Measuring Cosmic Distances. *Astrophys. J.* **2021**, *923*, 265. [CrossRef]
11. DES Collaboration; Abbott, T.M.C.; Acevedo, M.; Aguena, M.; Alarcon, A.; Allam, S.; Alves, O.; Amon, A.; Andrade-Oliveira, F.; Annis, J.; et al. The Dark Energy Survey: Cosmology Results with ∼1500 New High-redshift Type Ia Supernovae Using the Full 5 yr Data Set. *Astrophys. J. Lett.* **2024**, *973*, L14. [CrossRef]
12. Seifert, A.; Lane, Z.G.; Galoppo, M.; Ridden-Harper, R.; Wiltshire, D.L. Supernovae evidence for foundational change to cosmological models. *Mon. Not. R. Astron. Soc.* **2025**, *537*, L55–L60. [CrossRef]
13. Foley, R.J.; Kasen, D. Measuring Ejecta Velocity Improves Type Ia Supernova Distances. *Astrophys. J.* **2011**, *729*, 55. [CrossRef]

14. Wang, L. Dust around Type Ia Supernovae. *Astrophys. J. Lett.* **2005**, *635*, L33–L36. [CrossRef]
15. Goobar, A. Low R_V from Circumstellar Dust around Supernovae. *Astrophys. J. Lett.* **2008**, *686*, L103. [CrossRef]
16. Maeda, K.; Leloudas, G.; Taubenberger, S.; Stritzinger, M.; Sollerman, J.; Elias-Rosa, N.; Benetti, S.; Hamuy, M.; Folatelli, G.; Mazzali, P.A. Effects of the explosion asymmetry and viewing angle on the Type Ia supernova colour and luminosity calibration. *Mon. Not. R. Astron. Soc.* **2011**, *413*, 3075–3094. [CrossRef]
17. Chotard, N.; Gangler, E.; Aldering, G.; Antilogus, P.; Aragon, C.; Bailey, S.; Baltay, C.; Bongard, S.; Buton, C.; Canto, A.; et al. The reddening law of type Ia supernovae: Separating intrinsic variability from dust using equivalent widths. *Astron. Astrophys.* **2011**, *529*, L4. [CrossRef]
18. Meldorf, C.; Palmese, A.; Brout, D.; Chen, R.; Scolnic, D.; Kelsey, L.; Galbany, L.; Hartley, W.G.; Davis, T.M.; Drlica-Wagner, A.; et al. The Dark Energy Survey Supernova Program results: Type Ia supernova brightness correlates with host galaxy dust. *Mon. Not. R. Astron. Soc.* **2023**, *518*, 1985–2004. [CrossRef]
19. Smadja, G.; Copin, Y.; Hillebrandt, W.; Saunders, C.; Tao, C. Intrinsic and extinction colour components in SNe Ia and the determination of R_V. *Astron. Astrophys.* **2024**, *682*, A121. [CrossRef]
20. Gontcharov, G.A.; Marchuk, A.A.; Khovrichev, M.Y.; Mosenkov, A.V.; Savchenko, S.S.; Il'in, V.B.; Poliakov, D.M.; Smirnov, A.A. New Interstellar Extinction Maps Based on Gaia and Other Sky Surveys. *Astron. Lett.* **2023**, *49*, 673–696. [CrossRef]
21. Malkov, O.; Avdeeva, A.; Kovaleva, D. LAMOST Spectroscopy and Gaia Photo-Astrometry for an Interstellar Extinction Study. *Galaxies* **2024**, *12*, 65. [CrossRef]
22. Zhang, X.; Green, G.M. Three-dimensional maps of the interstellar dust extinction curve within the Milky Way galaxy. *Science* **2025**, *387*, 1209–1214. [CrossRef]
23. Parenago, P.P. On interstellar extinction of light. *Astron. Zh.* **1940**, *13*, 3.
24. Fitzgerald, M.P. The Distribution of Interstellar Reddening Material. *Astron. J.* **1968**, *73*, 983. [CrossRef]
25. Neckel, T.; Klare, G. The spatial distribution of the interstellar extinction. Astronomy and Astrophysics Supplement Series **1980**, *42*, 251.
26. Pandey, A.K.; Mahra, H.S. Interstellar extinction and Galactic structure. *Mon. Not. R. Astron. Soc.* **1987**, *226*, 635–643. [CrossRef]
27. Arenou, F.; Grenon, M.; Gomez, A. 16. A tridimensional model of the galactic interstellar extinction. *Astron. Astrophys.* **1992**, *258*, 104–111.
28. Sale, S.E.; Drew, J.E.; Barentsen, G.; Farnhill, H.J.; Raddi, R.; Barlow, M.J.; Eislöffel, J.; Vink, J.S.; Rodríguez-Gil, P.; Wright, N.J. A 3D extinction map of the northern Galactic plane based on IPHAS photometry. *Mon. Not. R. Astron. Soc.* **2014**, *443*, 2907–2922. [CrossRef]
29. Green, G.M.; Schlafly, E.F.; Finkbeiner, D.P.; Rix, H.-W.; Martin, N.; Burgett, W.; Draper, P.W.; Flewelling, H.; Hodapp, K.; Kaiser, N. A Three-dimensional Map of Milky Way Dust. *Astrophys. J.* **2015**, *810*, 25. [CrossRef]
30. Lallement, R.; Babusiaux, C.; Vergely, J.L.; Katz, D.; Arenou, F.; Valette, B.; Hottier, C.; Capitanio, L. Gaia-2MASS 3D maps of Galactic interstellar dust within 3 kpc. *Astron. Astrophys.* **2019**, *625*, A135. [CrossRef]
31. Hakkila, J.; Myers, J.M.; Stidham, B.J.; Hartmann, D.H. A Computerized Model of Large-Scale Visual Interstellar Extinction. *Astron. J.* **1997**, *114*, 2043. [CrossRef]
32. Bundy, K.; Bershady, M.A.; Law, D.R.; Yan, R.; Drory, N.; MacDonald, N.; Wake, D.A.; Cherinka, B.; Sánchez-Gallego, J.R.; Weijmans, A.M.; et al. Overview of the SDSS-IV MaNGA Survey: Mapping nearby Galaxies at Apache Point Observatory. *Astrophys. J.* **2015**, *798*, 7. [CrossRef]
33. Sánchez, S.F.; Barrera-Ballesteros, J.K.; Lacerda, E.; Mejía-Narvaez, A.; Camps-Fariña, A.; Bruzual, G.; Espinosa-Ponce, C.; Rodríguez-Puebla, A.; Calette, A.R.; Ibarra-Medel, H.; et al. SDSS-IV MaNGA: PyPipe3D Analysis Release for 10,000 Galaxies. *Astrophys. J. Suppl. Ser.* **2022**, *262*, 36. [CrossRef]
34. Fischer, J.L.; Domínguez Sánchez, H.; Bernardi, M. SDSS-IV MaNGA PyMorph Photometric and Deep Learning Morphological Catalogues and implications for bulge properties and stellar angular momentum. *Mon. Not. R. Astron. Soc.* **2019**, *483*, 2057–2077. [CrossRef]
35. Domínguez Sánchez, H.; Margalef, B.; Bernardi, M.; Huertas-Company, M. SDSS-IV DR17: Final release of MaNGA PyMorph photometric and deep-learning morphological catalogues. *Mon. Not. R. Astron. Soc.* **2022**, *509*, 4024–4036. [CrossRef]
36. Sharov, A.S. A Reappraisal of Interstellar Light Absorption in the Galaxy. *Astron. Rep.* **1963**, *40*, 900.
37. Riello, M.; Patat, F. Extinction correction for Type Ia supernova rates - I. The model. *Mon. Not. R. Astron. Soc.* **2005**, *362*, 671–680. [CrossRef]
38. Holwerda, B.W.; Reynolds, A.; Smith, M.; Kraan-Korteweg, R.C. SN Ia host galaxy properties and the dust extinction distribution. *Mon. Not. R. Astron. Soc.* **2015**, *446*, 3768–3775. [CrossRef]
39. Ménard, B.; Kilbinger, M.; Scranton, R. On the impact of intergalactic dust on cosmology with Type Ia supernovae. *Mon. Not. R. Astron. Soc.* **2010**, *406*, 1815–1820. [CrossRef]

40. Hakobyan, A.A.; Barkhudaryan, L.V.; Karapetyan, A.G.; Mamon, G.A.; Kunth, D.; Adibekyan, V.; Aramyan, L.S.; Petrosian, A.R.; Turatto, M. Supernovae and their host galaxies - V. The vertical distribution of supernovae in disc galaxies. *Mon. Not. R. Astron. Soc.* **2017**, *471*, 1390–1400. [CrossRef]
41. Santos-Santos, I.M.E.; Frenk, C.S.; Navarro, J.F.; Cole, S.; Helly, J. The unabridged satellite luminosity function of Milky Way-like galaxies in ΛCDM: The contribution of 'orphan' satellites. *Mon. Not. R. Astron. Soc.* **2025**, *540*, 1107–1123. [CrossRef]
42. Taylor, M.B. TOPCAT & STIL: Starlink Table/VOTable Processing Software. In *Proceedings of the Astronomical Data Analysis Software and Systems XIV*; Astronomical Society of the Pacific Conference Series; Shopbell, P.; Britton, M.; Ebert, R., Eds.; Astronomical Society of the Pacific: San Francisco, CA, USA, 2005; Volume 347, p. 29.

MDPI AG
Grosspeteranlage 5
4052 Basel
Switzerland
Tel.: +41 61 683 77 34

Galaxies Editorial Office
E-mail: galaxies@mdpi.com
www.mdpi.com/journal/galaxies

MDPI

Academic Open
Access Publishing

mdpi.com

ISBN 978-3-7258-8118-5